Elastic magnetic electron scattering from nuclei

T. William Donnelly

Center for Theoretical Physics, Laboratory for Nuclear Science, and Department of Physics, Massachusetts Institute of Technology, Cambridge, Massachusetts 02139

Ingo Sick

Department of Physics, University of Basel, CH-4056 Basel, Switzerland

This paper is focused mainly on the subject of elastic magnetic electron scattering and how it has come to be a useful tool for studying the spatial distributions of convection and magnetization currents in the nuclear ground state. Using such a probe, emphasis is clearly placed on the electromagnetic currents provided by the valence nucleons in the nucleus, indeed, by neutrons as well as protons. These do not yield a complete description of the problem, however, and more complex nuclear many-body configurations are generally required. Various models are employed (shell-model configuration mixing, core-polarization effects, models of deformed nuclei, for instance), giving rise to quantitative comparisons with experimental measurements. Moreover, to achieve such successful descriptions, especially at high momentum transfers, it is frequently necessary to go beyond a purely one-body nucleonic reaction mechanism and to include the effects of two-body meson-exchange currents based on non-nucleonic degrees of freedom ($\pi,\rho,\Delta,\ldots$). The authors discuss all of these various facets of the problem, beginning with surveys of the historical development of the field and of the experimental techniques employed in such studies. They present a detailed treatment of the formalism needed in discussions of elastic electron scattering, including an introduction to the density-matrix approach to the nuclear many-body problem, with simple examples to clarify the ideas involved. For the nonspecialist a separate section of illustrative examples is supplied in which qualitative discussions of various aspects of the physics accessible in such (e,e') studies are highlighted. Experimental and theoretical results for a large number of nuclei ranging from $A=2$ to 209 are described in detail; this represents a compilation of virtually all of the high-quality data that are available at present. The paper concludes with projections as to which directions may be followed in the future, in particular, with a relatively complete discussion of the use of polarization in elastic electron scattering.

CONTENTS*

*In order to guide the reader, we have indicated by the symbol ▲ sections which treat more specialized topics and which can be skipped in a first reading.

I. INTRODUCTION

This paper deals with elastic scattering of high-energy electrons from the nuclear convection and magnetization distributions. Significant progress in the use of this tool for investigations of nuclear structure has been made over the past 15 years, and we feel that a review of both experimental and theoretical achievements is appropriate at this time.

For a number of reasons, electron-nucleus scattering in general turns out to be an excellent tool for the study of nuclei. The main asset of the electron as a probe resides in the weakness of the electromagnetic force by means of which the electron interacts with the nucleus. The coupling constant $\alpha=1/137$ is much smaller than the characteristic strength of the nuclear force which is responsible for most of the properties of the nucleus. Therefore, the electron hardly perturbs the nucleus under investigation. Moreover, the electromagnetic interaction is well known and described by an exact theory, quantum electrodynamics. As a consequence, the nuclear properties can be extracted from data in a quantitative way. In fact, the same comments pertain more generally to the larger subject of electroweak interaction studies of nuclei.

The weakness of the electromagnetic interaction has additional consequences: calculations performed in the impulse and plane-wave approximation are already quite close to reality; hence the refinements needed for a quantitative calculation of electron-nucleus scattering are of manageable complexity. The one-step nature of the electron-nucleus scattering process implies that a given momentum transfer to the nucleus is a direct measure of the spatial resolution of the "electron microscope." Due to the weak absorption of the electron, this probe is nearly the only practical way to investigate the interior of nuclei. These unique properties of electrons explain why a considerable effort in experimental and theoretical work has been expended in this field.

Over the years it has become increasingly possible to overcome many of the difficulties closely linked to the advantageous features cited above. In particular, the construction of accelerators that provide electrons of several hundred MeV energy has led to considerable progress. This high energy is required in order to achieve a small wavelength for the electron despite its small mass. The technology of accelerators and beam optical systems today allows one to work with the excellent relative energy resolution $\Delta E/E < 10^{-4}$ needed to obtain the absolute energy resolution ΔE imposed by nuclear level spacings. The high-intensity beams (of order 50 μA) required to overcome the small cross sections also are within range of today's technology.

With these tools, extensive work on the scattering of electrons by the nuclear charge distribution has been performed. Experiments at low momentum transfer provide us with accurate nuclear radii and transition probabilities. Data taken at large momentum transfer measure ground-state and transition charge densities with 0.5 fm spatial resolution. The results and their interpretation have been summarized in a number of review papers (Hofstadter, 1957; de Forest and Walecka, 1966; Überall, 1971; Barrett, 1974; Donnelly and Walecka, 1975; Ciofi Degli Atti, 1980). The main characteristics of the results obtained concern collective properties of nuclei. In general, the information deduced refers almost exclusively to the charged constituents, i.e., protons.

While the bulk of the work is devoted to the investigation of (transition) charge densities, this does not cover all aspects of coherent electron-nucleus scattering. High-energy electrons also scatter from the nuclear electromagnetic current distributions. The experimental observation of this process provides valuable information on the spatial distribution of intrinsic magnetism and convection currents within the nucleus. This is the topic we shall concentrate upon in this review. In order to keep the size of the review manageable, and in order not to discuss things in too superficial a way, we limit ourselves to *elastic* magnetic scattering.

The process of magnetic scattering has the same advantages and drawbacks as the electromagnetic probe mentioned above. The physics studied, however, is quite different. Four main differences from charge scattering merit attention.

(1) According to the shell model, most of the nucleon spins and orbital momenta pair off to yield zero contribution to the magnetic scattering. The nuclear magnetism thus is determined by a few valence nucleons. As a consequence, magnetic scattering mainly provides information on the single-particle properties of nuclear wave functions; the collective aspects that dominate charge scattering show up only in special cases.

(2) It is the intrinsic magnetization that dominates magnetic scattering cross sections, and the intrinsic magnetic moments of protons and neutrons are quite similar in magnitude. Magnetic electron scattering, therefore, will provide information on both protons and neutrons; it does not suffer from the inherent drawback of charge scattering, which (basically) is blind to more than half of the nuclear constituents.

(3) The information obtained via magnetic electron scattering is very directly related to the main body of data gathered using strongly interacting probes. Much of what has been learned from hadronic probes of (most often)

low energy concerns the outermost, least-bound shells. Magnetic scattering deals with these same shells, although with a different emphasis. Due to the different radial sensitivity—surface domination for strongly interacting probes, volume domination for electrons—electron and hadron scattering complement each other in a nice way. The connection of magnetic electron scattering to the main body of theoretical calculations concerning valence nucleons very much enhances the relationship between the physics learned from electron scattering and that learned from other probes.

(4) Electrons also scatter from the convection current distributions within nuclei. While this contribution in general provides little additional insight, it becomes crucial for the study of exchange currents. The exchange of mesons between nucleons, the process we picture to be responsible for the nucleon-nucleon force, creates currents observable in magnetic scattering. These effects of meson-exchange currents (MEC) represent both a complication and an asset of magnetic scattering. In selected cases, the MEC contribution can be very large; then experiments on magnetic scattering represent the best and cleanest tool available for the study of non-nucleonic constituents of the nucleus. The results obtained in this field are most relevant for modern nuclear physics, which increasingly has to cope with the internal degrees of freedom of the nuclear constituents.

For these reasons, magnetic electron scattering is a topic of high current interest and represents a domain in its own right; this paper tries to present a first reasonably complete review. Our goal is to describe both the experimental and the theoretical methods relevant for this field and to discuss the most important physics results obtained.

The organization of this paper is as follows: Sec. II traces the historical development of magnetic electron scattering, in order to put into perspective the ideas and their connection to traditional charge scattering. We then discuss in Sec. III some experimental aspects of the subject; in this we mention some of the typical high-energy facilities in order to describe, without much detail, the state of the art. In Sec. IV the formalism needed to understand magnetic scattering in terms of the simplest theoretical framework, the plane-wave Born approximation, is presented; this section develops the understanding to a point where explicit expressions for magnetic form factors can be calculated starting from nuclear wave functions characterized by density-matrix elements. In this regard, both one-body and two-body meson-exchange-current contributions are considered and framed in the density-matrix language. To demonstrate the results and the physics contained in magnetic form factors, Sec. V presents a number of illustrative cases that have been particularly striking; this section is intended explicitly for the reader who is not interested in more detailed aspects of the theory or in going through a nucleus-by-nucleus discussion of the results obtained. For this reader, Secs. I and V give an adequate, though superficial, summary of the field.

In Sec. VI we summarize many of the results obtained by magnetic electron scattering from nuclei with $A > 4$; here we discuss in a fairly detailed way the physical problems addressed by experiment and calculation. Since this section is by no means exhaustive of the work performed, a table of work arranged by nucleus follows; in this table, we present what we hope is a reasonably up to date and complete bibliography of experimental work. The magnetic form factors of the few-body nuclei ($A = 2,3$) are covered in Sec. VII; they are discussed separately, since they deal with nuclear structure phenomena of a quite different type. Section VIII discusses the new possibilities opened up by the use of polarized electrons and targets.

In order to guide the reader through the paper, we have indicated by the symbol ▲ sections that treat more specialized topics that can be skipped in a first reading (viz., Secs. IV.D, IV.E, VI, and VIII). The reader who wishes to get a general flavor of the physics involved in magnetic scattering is encouraged to proceed directly to Sec. V, where a few illustrative cases are qualitatively discussed.

II. HISTORICAL PERSPECTIVES

In this section we try to trace some of the important developments that determined the directions taken by the field of magnetic electron scattering. To do so, we emphasize here the appearance of new ideas; a systematic account of actual results obtained will be given in later sections. While many of the ideas discussed did develop during the time the authors were actively involved in the field, our account of the earlier developments is based largely on published material. The recollections of several individuals involved in magnetic electron scattering from its very beginning have been very helpful in putting the early ideas into proper perspective.

Electron nucleus scattering actually is quite an old field; it got its start with the historical work of Sir Nevill Mott, who applied the new wave equation of Dirac (Dirac, 1928) in 1929 to the problem of "scattering of fast electrons by atomic nuclei" (Mott, 1929). Much of the activity in this field during the following years was devoted to an experimental check of the Mott scattering cross section (for pointlike charge Ze) using 0.5—3-MeV electrons. The sizeable discrepancies observed led to calculations of scattering not only by the nuclear charge, but also by the nuclear magnetic moments. In particular, the work of Massey (1930) dealt with "scattering of fast electrons and nuclear magnetic moments." In the publication of Jauch (1940), the different angular dependences of the incoherent charge and magnetic scattering cross sections, expressed today by the "Rosenbluth formula," were already clearly presented. These authors found that for electrons of a few MeV energy the magnetic cross section was orders of magnitude smaller than the charge cross section, and hence unobservable.

With the improvement of experimental data the discrepancies with the Mott scattering formula largely disappeared; the field of electron-nucleus scattering with

electrons of wavelength much larger than the nuclear size ceased to receive much attention. The investigation of nuclear properties got its start through the use of hadronic probes, which achieve small wavelength at much lower energy.

The field of electron scattering took a new turn once higher-energy electrons started to become an experimental possibility. Now, electrons could be used as a probe of nuclear properties, rather than as a vehicle to test quantum mechanics and the Dirac equation. In its early phase, the work on electron-nucleus scattering was devoted entirely to charge scattering; magnetic scattering was ignored.

The potential of electron-nucleus scattering for nuclear structure investigations was brought into focus by an early paper by Guth (1934). Guth showed that large effects due to finite nuclear size could be expected if the momentum transfer q of the electron to the nucleus became comparable to the inverse of the expected size of the nucleus. Using the Dirac theory and plane-wave Born approximation, Guth derived the low-q expansion of the elastic form factor. He pointed out the possibility of obtaining by electron scattering a Fourier analysis of the electrostatic potential produced by the nucleus. This paper foreshadowed the application of electrons as a probe of nuclei and anticipated by about 15 years the first experiments, as well as the exact calculations by Rose (1948) and Elton (1950).

The first experiment sensitive to nuclear size was published in 1951 by Lyman, Hanson, and Scott. Working with the external beam of the University of Illinois betatron, these authors scattered 15.7-MeV electrons off five nuclei ranging from ^{12}C to ^{197}Au. The ratio between the experimental and the Mott cross section, reaching 0.5 at the highest scattering angle, clearly measured the nuclear size. The implication of the differences between experiment and prediction—a nuclear radius 20% smaller than the accepted value 1.45 $A^{1/3}$ determined using hadronic probes—was a first sign of the information to be gathered using the electron as a probe. This pioneering experiment on elastic (charge) scattering was the beginning of a beautiful series of ingenious experiments and sophisticated interpretations started in 1953 by Hofstadter and collaborators using the (initially) 200-MeV Stanford accelerator.

Nuclear magnetic electron scattering, the topic of main interest in this review, was largely neglected during the early phase of electron-nucleus scattering. Schiff (1949), in a report on the physics potential of the Stanford accelerator then under construction, mentioned that for electron-proton scattering the magnetic moment should be expected to contribute, and gave numerical estimates for the magnetic cross sections. While this report on scattering off nucleons presented a strikingly clear foresight of the things to come, no mention was made of nuclear magnetic scattering; the cross sections were presumably estimated to be much too small. The first observation of the finite size of nuclear magnetization densities subsequently was made via the Bohr-Weisskopf effect (1950), i.e., the hyperfine splitting of atomic energy levels.

The work of Rosenbluth (1950) was an important step towards the exploitation of magnetic electron scattering. In a remarkably modern calculation Rosenbluth derived the cross section for scattering off a nucleus with charge and both normal and anomalous magnetic moment contributions. The familiar form of the total elastic cross section as it is now used up to very large momentum transfer, the equation identified today with Rosenbluth's name, was introduced and its numerical consequences for e-p scattering discussed.

In 1955, finally, the first experiment on electron scattering off a magnetization distribution was published. Hofstadter and McAllister (1955), during an experiment on electron-proton scattering between 100- and 236-MeV energy, found at backward scattering angles a cross section exceeding the Mott cross section. They correctly identified the origin of this effect, where the finite size of the charge distribution necessarily leads to a cross section smaller than the Mott cross section: "Deviations from the Mott formula such as we have found may be anticipated at large angles because of additional scattering from the magnetic moment of the proton. We have observed this additional scattering, but in an amount smaller than predicted by theory." To explain the deviation found, some speculation was required: "If we make the naive assumption that the proton charge cloud and its magnetic moment are both spread out in the same proportions, we can calculate simple form factors for various values of the proton 'size.' When these calculations are carried out we find that the experimental curves can be represented very well by the following choices of size .... A comparison value fitting all the experimental results is [an rms radius of] $7.4\pm2.4\times10^{-14}$ cm" (Hofstadter and McAllister, 1955). This observation was to withstand later scrutiny remarkably well.

A calculation of considerable importance for magnetic scattering in general and the understanding of the two-body system in particular was published in 1956. Jankus (1956) calculated the cross section for $C0,M1,C2$ scattering off the deuteron by including the deuteron D state. A calculation of the breakup cross section featuring an exact treatment of the ($l=0$) final-state n-p interaction was presented as well. (The then justified neglect of the D state in calculation of the magnetic breakup cross section was to influence significantly our early perception of the role of meson-exchange currents in electron scattering.) This calculation was very useful for the study of nucleon form factors and deuteron properties, two topics that represent some of the most remarkable achievements of early electron scattering work.

The study of magnetic scattering from "real" nuclei ($A>2$) got started at Stanford after Peterson and Barber (1962) built a magnet system to measure cross sections at 180° scattering angle. The construction of this 180° system paved the way for measurements of magnetic cross sections for heavier nuclei. The motivation for building the first 180° scattering system actually was not the measurement of elastic magnetic scattering, but rather the measurement of inelastic transitions which could be per-

formed more cleanly above the greatly suppressed radiation tail associated with the elastic charge scattering. Moreover, magnetic transitions could be measured in the relative absence of most electric transitions (Peterson and Barber, 1962). The first application of the 180° scattering method was to the low-momentum-transfer magnetic dipole ($M1$) electrodisintegration of the deuteron.

In 1962, Peterson published results from the first experiment, which measured the ^{6}Li and ^{7}Li magnetic cross sections at 41 MeV and $\theta=180°$. In accordance with the relative size of the magnetic moments, ^{7}Li was found to have a ~ 10 times larger magnetic cross section. At the same time the theoretical basis for elastic magnetic electron scattering at 180° from complex nuclei was beginning to be established (Pratt *et al.*, 1965).

With the progress of experimental techniques, further experiments on magnetic scattering quickly reached a high level of performance. This was documented best by the work on p-shell nuclei by Rand *et al.* (1965). These experiments covered a large range of momentum transfer (up to 2.4 fm^{-1}) and revealed the important contribution of the magnetic octupole form factor. The shape of the octupole distribution turned out to agree reasonably well with expectations, while the overall value of the octupole moment was too small. These data were interpreted using the shell-model calculations of Griffy and Yu (1965), which clearly pointed out the sensitivity of magnetic form factors to the assumed coupling—jj, LS, intermediate—of the valence nucleons. This demonstrated one of the main assets of magnetic scattering, its usefulness as an excellent configuration analyzer.

Two experiments in the mid sixties were, in retrospect, to provide the clearest evidence for the role of meson-exchange currents (MEC). The magnetic transition to the singlet-S state of the deuteron was measured by Rand *et al.* (1967), and the $A=3$ elastic magnetic form factor was determined by Collard *et al.* (1965). Both experiments reached a momentum transfer of $q\sim 3$ fm^{-1}, at which MEC effects are much more important than at $q\sim 0$, where a very early calculation of Villars (1947) had already indicated an observable contribution to the magnetic dipole moment. The dominating contribution of MEC at high q was not realized, however, despite the fact that MEC were repeatedly alluded to in discussions of the experimental results. Due to the neglect of S- to D-state transitions, impulse-approximation calculations neglecting the contribution of MEC satisfactorily explained the data; there seemed no need to introduce the "complications" due to non-nucleonic degrees of freedom.

With the work of Li *et al.* (1970) the potential of magnetic electron scattering really began to be realized. From earlier experiments (Stovall *et al.*, 1967) it seemed that higher multipole magnetic form factors were beyond experimental capabilities, and that the observation of $M3$ contributions remained a singularity only accessible for p-shell nuclei. Li *et al.* found that the $M5$ form factor of ^{27}Al could be measured even at scattering angles $<180°$, and they showed that for ^{209}Bi magnetic scattering from the 2^9 pole moment could be observed. Together with the calculations of Donnelly and Walecka (1973a) this work pointed out some of the important simplifications that occur in the study of high multipole form factors and paved the way for the use of magnetic scattering for the determination of accurate valence nucleon radial wave functions.

The field of magnetic elastic scattering at low q was greatly extended through the work done with the 180° facility at the EVA accelerator (Van Niftrik *et al.*, 1971a). The measurement of very accurate cross sections of neighboring even-even and even-odd nuclei allowed one to deal with the dominant charge contributions at low q, and led to a systematic investigation of $M1$ form factors for medium-heavy nuclei (for a review see Lapikás, 1978).

An important step in the understanding of magnetic form factors was taken with the work of Hockert *et al.* (1973) and Brandenburg *et al.* (1974). For the case of the deuteron magnetic transition to the singlet-S state, the triplet-D to singlet-S transition had previously been neglected. This term leads to the appearance of a very pronounced diffraction minimum in the form factor, in complete disagreement (by a factor of 10) with experiment. Agreement with the experimental cross sections can be achieved only once meson-exchange currents (the pair and pionic currents in particular) are allowed for. A similar situation occurred for the ^{3}He magnetic form factor, in which Brandenburg *et al.* found a large effect of the elastic S-D transition. With those new calculations the great importance of non-nucleonic degrees of freedom in nuclei became obvious. These two magnetic form factors today provide perhaps the best and cleanest testing ground for mesonic-exchange-current effects. The theoretical work done for light nuclei has paved the way for more systematic applications to complex nuclei, such as those of Suzuki (1978) and Dubach (1980).

The complementary role of magnetic and charge scattering by electrons was brought to bear most clearly by the work of Sick *et al.* (1977) and Platchkov *et al.* (1979), which led to the determination of accurate radial wave functions for neutrons. While previously information on neutrons was obtained only by hadronic probes and so was affected by uncertainties in the reaction mechanism, now valence neutron rms radii accurate to $\pm 1\%$ could be obtained from magnetic electron scattering. This became feasible once scattering off the 2^7 and 2^9 pole distributions could be measured with the necessary experimental accuracy. Recently the theory of magnetic form factors has been extended to very deformed nuclei by Moya de Guerra and Dieperink (1978). For a deformed nucleus the magnetic form factor differs drastically from the one for a spherical nucleus. Both the coupling of the unpaired nucleon to the deformed core and the currents connected with the collective rotation play a role. With the improvement of experimental capabilities the study of the magnetic form factors of deformed nuclei is becoming a realistic possibility. A first experiment (Rad *et al.*, 1980) has already been performed, but only the surface has been scratched. For the lighter nuclei, in the p and s/d shell, magnetic electron scattering has now been es-

tablished as a standard spectroscopic tool. The systematic work done at Bates Linear Accelerator Laboratory (Peterson, 1983) shows the great variety of questions on nuclear structure that can be addressed with magnetic scattering.

III. EXPERIMENT

The experimental facilities used for electron scattering experiments obviously are of considerable diversity. Descriptions of various installations have been given by Hofstadter (1956), Ehrenberg *et al.* (1972), De Vries *et al.* (1984), Bertozzi *et al.* (1979), and Leconte *et al.* (1980). In this paper we can only describe a "typical" setup by discussing selected aspects of the apparatuses used at the three highest-energy facilities, at Amsterdam, Bates, and Saclay. We shall give a general overview of the complete system, but shall emphasize the special features important for magnetic electron scattering.

The electron accelerators presently in use for the investigation of nuclear physics deliver electron beams of energies up to about 700 MeV. These linear accelerators produce beams with an average intensity of up to a few hundred μA, a relative energy resolution $\Delta E/E$ of a few times 10^{-3}, an emittance of a few tenths of mm mrad, and a duty cycle of up to a few percent. For the experiments to be described here the beam intensity is often marginal. The relative energy resolution is more than an order of magnitude worse than that desired for most nuclear physics experiments. The duty cycle is of little concern for the noncoincidence experiments of interest in this paper.

Two considerations governing the choice of the experimental setup for beam preparation and detection of the scattered electron are as follows:

(1) The electromagnetic interaction is very weak. This main asset of the electron as a probe of nuclei has to be paid for by the fact that cross sections are very small, typically α^2 times smaller than the ones for hadronic probes. Experimentally, this smallness can be compensated for to a very limited degree only through the use of thicker targets or spectrometers of larger solid angle. In order to obtain sensible counting rates, the experimental setup therefore must be designed to allow for the maximum beam intensity on target.

(2) The momentum transfer q one would like to reach in an electron scattering experiment is imposed by the desire to observe the smallest features present in nuclear wave functions. These features are of the size of a few tenths of a fermi for nuclei with $A > 4$. This spatial resolution of the "electron microscope" amounts to roughly $1.5/q$ (full width at half maximum). This dictates momentum transfers of the order of 4 fm^{-1}, which implies electron energies of more than 500 MeV. The energy resolution, on the other hand, is fixed by the spacing of nuclear levels one wishes to separate. Even to observe the lowest states of deformed nuclei (let alone higher-lying levels) an energy resolution of the order of 50 keV is required. The resulting relative energy resolution $\Delta E/E$ of 10^{-4} or better represents a formidable challenge.

The desire to perform experiments with a very good relative energy resolution and with the full beam intensity delivered by the accelerator has led to the general use of so-called energy-loss spectrometer systems. In order to use the full beam despite its wide energy band, the beam is energy dispersed on target in such a way that electrons differing in energy by ΔE are separated by a distance $x = D\Delta E$. The magnetic spectrometer used to energy-analyze the scattered electrons is designed to have, for a given point in the focal plane, an energy dispersion dx/dE identical to $-D$. In this case a measurement of the coordinates of an electron trajectory in the focal plane yields directly the quantity of interest, the electron energy loss, which amounts to the sum of nuclear excitation plus recoil energy, independent of the absolute energy.

The energy-loss systems used are special cases of a more general setup where the coordinate x, together with the absolute energy of the scattered electron, is measured. This more general system actually provides more freedom in optimizing solid angle, etc., at the expense of little additional complexity in the detectors.

Usually the system that distributes electrons to the different experimental halls deflects the beam in the horizontal plane, for obvious reasons. An energy dispersion in the horizontal plane is thus easily available. The spectrometers are built to deflect in the vertical plane so as to achieve the largest range in scattering angles (a consideration most important for magnetic scattering). A magnetic device that moves the dispersion from the horizontal to the vertical plane is thus required.

Moreover, spectrometers with the energy dispersion in the plane orthogonal to the scattering plane are advantageous. In general the scattering angle has to be known with an accuracy 10 times that given by the solid angle defining spectrometer slits. Only then can the variation of the recoil nucleus kinetic energy with scattering angle be corrected for, and the excitation energy determined with the resolution desired. The decoupling of scattering angle and energy dispersion is achieved easily if they occur in orthogonal planes.

With these general considerations in mind, we can now discuss the various elements of the apparatus used.

A. Beam transport system

The beam transport systems used at different laboratories are quite different, and specific to the particular sites. For this subject, we shall therefore discuss only one specific setup in any detail: we take as an example the Saclay ALS accelerator and the HE1 experimental hall shown in Fig. 1 (Leconte, 1976).

Downstream of the last cavity of the accelerator the beam is brought to a focus in the horizontal direction. This focus forms the object point for the beam transport system. A collimator of 0.5 mm width, useable only at low average beam intensity (low repetition rate) allows one to check the fraction of the beam that is within the

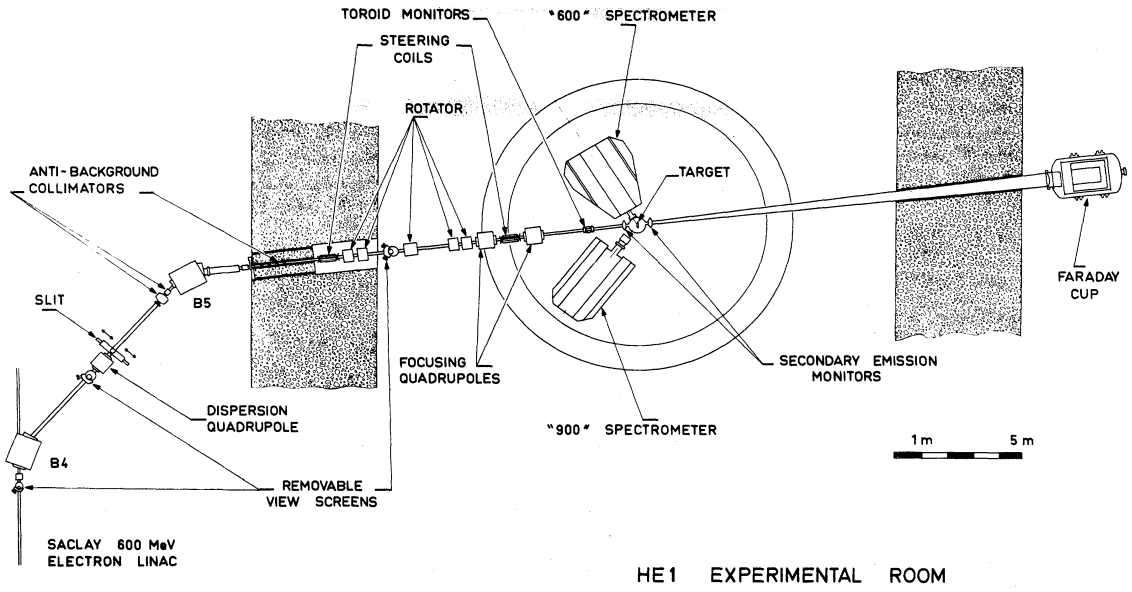

FIG. 1. Beam switchyard and HE1 experimental end station at the Saclay linear accelerator (Leconte, 1976).

desired spot. The location of the beam is constantly measured by a position-sensitive ferrite monitor. A fast switching magnet (not shown) allows one, on a time basis of tens of ms, to switch the beam from the main to parasitic users. The magnet $B4$ deflects the beam $\sim 45°$; its magneto-optical properties, adjusted by the inclination of entrance and exit pole tip angles, are such that it focuses electrons of a given energy, originating from the "point" object, to a vertical line at the location of the energy-defining slit. These slits are set to select from the beam a given band ΔE in energy; for the energy-loss mode operation $\Delta E/E$ is typically 10—20 times the final energy resolution desired. Electrons outside this band, up to a maximum lost beam power of 50 kW, are energy degraded by the slits and ultimately removed.

The quadrupole lens situated in front of the energy slits has a double function. In the conventional achromatic beam transport mode it refocuses the beam; electrons of different energies, separated spatially at the location of the slit, then form a single beam at the exit of magnet $B5$. In the energy-loss mode, the quadrupole defocuses the beam in the horizontal plane in order to increase the energy dispersion produced by $B4$ by a factor of ~ 2. In this mode, the quadrupole allows one to tune the dispersion to the value imposed by the spectrometer. The magnet $B5$ bends the beam by another 45° and sends it towards the experimental hall HE1. The main function of $B5$ is to clean up the beam by removing all electrons energy degraded by the energy slits. Various collimators before and after $B5$ absorb these showers of low-energy electrons.

At the entrance to the experimental hall HE1 the energy dispersion is shifted from the horizontal to the vertical plane. The rotator consists of five quadrupole magnets tilted by 45° relative to the normal quadrupole orientation. This tilt introduces a coupling of horizontal and vertical phase space; by appropriate choice of strength and distance of the five magnetic elements, the exchange of horizontal and vertical coordinates is obtained without further change of the optical properties of the beam. The pair of quadrupole lenses upstream of the target produces, for a monochromatic beam, a horizontal line focus at the target. For an energy-dispersed beam of $\Delta E/E \simeq 10^{-3}$ the vertical dispersion amounts to ~ 1 cm. The decoupling of various parameters, dispersion, rotation, and monochromatic image, helps to adjust the beam properties desired efficiently.

A zinc sulfide screen at the end of the accelerator allows one to adjust the beam position visually. The focus to a vertical line required by beam transport optics can be checked by using the removable slit mentioned above. Another screen near $B4$ allows one to align the beam along the optical axis of the transport system. Screens near the center of the rotator and at the location of the target determine the alignment of the beam along the 0° axis of the spectrometer. Various horizontal and vertical steering magnets at the end of the accelerator, near $B4$, R, and QF, allow various small corrections to the beam position.

Downstream of the target, the beam is stopped in a Faraday cup. This beamstop is located in a well-shielded separate hall in order to avoid excessive background due to neutrons produced via (γ,n) reactions by the large flux of bremsstrahlung gammas. The particular cup used at Saclay has a useful aperture of 60 cm and is able to dissipate up to 100 kW of beam power.

The primary measurement for the integrated beam current is also provided by the Faraday cup. Cooling with very pure water ensures that leak currents are of the order of a few nA only; these residual currents are compensated for by injecting a current of opposite polarity.

Unless the electrons are refocused after the target, as is done at lower-energy facilities where this problem is much more severe, a few percent of the electrons miss the cup due to multiple scattering in the target. Using a nonintercepting toroid beam intensity monitor placed upstream of the target, one can determine the losses of the Faraday cup from toroid to Faraday ratios with and without target. The overall precision of the absolute integrated charge derived from the Faraday cup is better than 1%.

B. Targets

For most magnetic scattering experiments the targets are solid ones. Liquid or gas targets require rather special techniques, which are discussed in the literature cited in Sec. VII for $A=2,3$. The solid targets used have thicknesses of 20—100 mg/cm^2 and sizes of 5—10 cm^2 determined by the energy dispersion on target. The targets are fabricated by rolling, pressing, electroplating, or casting, depending on the mechanical and thermal properties of the isotope of interest.

The maximum target thickness is imposed by the energy resolution desired; energy straggling in the target gives a contribution of approximately 0.4 keV/mg cm^2. Target homogeneity is restricted by the accuracy of the cross sections one intends to achieve, since in general the intensity distribution of the beam over the target is poorly known. Absorption of γ or β rays has proven to be the best method for measuring the relative density profile of the target. The combination of relative density profiles with the average areal density obtained from weight and surface area yields absolute target thicknesses for the area covered by the beam to an accuracy of $<1\%$.

The removal of heat deposited in the target by the high-intensity electron beam requires additional apparatus. This is particularly important for experiments at medium to large q, i.e., for small cross sections. The vertical dispersion of the beam required by energy-loss systems is very helpful in this respect, but additional horizontal movement of the target is often required to spread the heat further. The most efficient way to remove heat is to cool the target with a jet of H_2 gas of ~ 1 Torr pressure. Circulating the H_2 gas with Roots pumps at high speed through nozzles pointing at the target (Kowald, 1976) allows a very high heat extraction rate. The thin windows needed to separate the scattering chamber from accelerator and spectrometer vacuums can be made thin enough to have no disturbing effects upon the energy resolution or multiple scattering.

C. 180° scattering

For experiments aiming at a determination of magnetic form factors, scattering at $\theta=180°$ is of special importance. As we shall discuss in more detail in Sec. IV, the electron scattering cross section can be separated into longitudinal (charge) and transverse (magnetic) parts. In the plane-wave Born approximation, and for electron energies much larger than the electron rest mass, the elastic cross section is given by

$$\frac{d\sigma}{d\Omega}(\theta)=4\pi\sigma_M(\theta,\varepsilon)[F_L^2(q)+(\tfrac{1}{2}+\tan^2\theta/2)F_T^2(q)] .$$

At a given momentum transfer q, the transverse form factor F_T that contains the information on nuclear magnetic properties can be determined by measurements at different scattering angles θ and different energies ε, but constant $q\approx 2\varepsilon\sin\theta/2$. The ratio of the term containing F_T to the one containing F_L is largest at $\theta=180°$, where σ_M tends towards zero while $\sigma_M\tan^2\theta/2$ remains nonzero.

For many cases, it is indispensable experimentally to enhance as much as possible the ratio of magnetic to charge scattering. Charge form factors depend basically on collective nuclear properties; for elastic scattering, F_L^2 thus contains a factor Z^2, while magnetic form factors are basically single-particle observables that lack this factor. At low and medium momentum transfer, and for all but the lightest nuclei, F_T can be measured only if the charge contribution is minimized by taking data at $\theta=180°$.

The first 180° system was built at Stanford (Peterson and Barber, 1962). It consisted of a rectangular magnet placed directly upstream of the target to bend the incoming and backscattered electrons by 10° in such a way that the 180° scattered electrons could be observed with the 18″ spectrometer placed at an angle of 160° relative to the beam. Downstream of the target the (low-intensity) electron beam was directed to a beam dump using a permanent magnet. Over the years, the setup for 180° scattering has been vastly improved and various drawbacks removed. The system developed for the EVA facility at Amsterdam (Van Niftrik *et al.*, 1971a) and reused with the new NIKHEF accelerator (Donné *et al.*, 1984) already showed most of the features of modern 180° systems.

The most sophisticated 180° system in use at present is the one installed at the Bates accelerator (Peterson *et al.*, 1979); it is shown in Fig. 2. It consists of four magnets upstream of the target; an additional magnet of very small deflection angle between target and Faraday cup (not shown) keeps electrons backscattered by the cup from reaching the target and spectrometer. With this system no special beam line for "normal" and 180° scattering is needed; for both types of experiments the incident and outgoing electron beams have the same direction and use

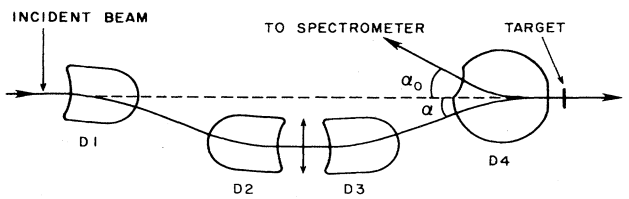

FIG. 2. 180° scattering system used at the Bates accelerator (Peterson *et al.*, 1979).

the same beamstop and beam monitoring equipment. The passage from normal to 180° scattering requires only that magnet $D4$, together with the 180° scattering chamber, be shifted over onto the spectrometer pivot. For any inelasticity of the scattering process an angle of $\theta=180°$ can be maintained by appropriate tuning of magnets $D1$—$D4$. This results in a constant spectrometer solid angle, independent of inelasticity. The optical properties of $D1$—$D4$ have been designed to be compatible with the large extension of the beam required by the energy-loss system. The operation of this 180° system has shown that the high-resolution capability of the energy-loss system can be maintained, the degradation being a contribution of $<10^{-4}$ to $\Delta E/E$.

With such 180° systems the contribution of charge scattering can be suppressed to a very high degree. It cannot be eliminated completely, since multiple scattering in the target and finite spectrometer angular acceptance and, at low energy, finite electron mass lead to an effective average scattering angle of 178°—179°. In this case the cross section around $\theta=180°$ is a quadratic function of the angle $180°-\theta$. A measurement of the quadratic term, as shown in the experimental result of Fig. 3, allows one to remove the nonmagnetic contribution to a large degree. In general this is sufficient to remove charge scattering almost completely, and magnetic form factors have been measured down to $q\sim 0.5$ fm^{-1} even for heavy nuclei.

The availability of 180° facilities does not imply that all magnetic form factors are indeed measured at 180°. The overall energy resolution of an experiment is often dominated by the energy loss in the target. This contribution amounts to twice the electron energy loss in the target at 180°. For "normal" scattering, with the target plane bisecting the incident and scattered electron direction, the corresponding contribution is due to straggling and amounts to 20% of the energy loss in the target only. If the ratio of magnetic to charge contributions is not too low, and if cross sections are very small—both of these conditions occur at large momentum transfer—then scattering at, say, $\theta=160°$ increases the counting rate by a factor of 10 for the same energy resolution. For gas targets and high momentum transfer, measurements at $\theta=180°$ hardly allow one to move the windows of the target outside the spectrometer acceptance. In this case, scattering under "normal" angles again might be advantageous, despite the increased difficulty in removing the charge contribution.

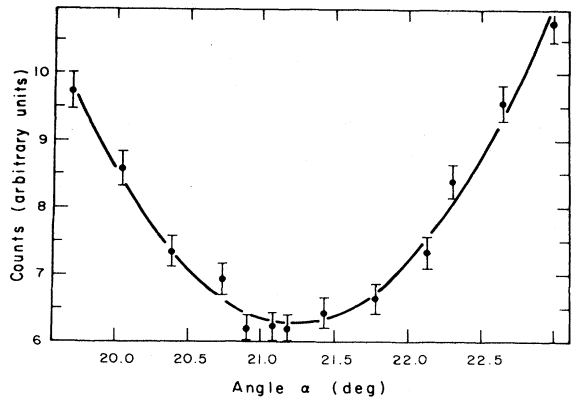

FIG. 3. Angular dependence of the cross section around the scattering angle $\theta=180°$ (Peterson *et al.*, 1979).

D. Spectrometers

For an energy-loss spectrometer, the magnetic systems for beam transport and scattered electron analysis form a single unit. They differ only in the emittance of the "beam" with which they have to deal.

The design of the magnetic spectrometer is governed by a number of considerations, chief among which are the desired energy resolution, the solid angle, and, for certain applications, the momentum acceptance. Additional criteria such as large angular range, smallness of background, or shape of the focal plane are often considered as secondary.

The spectrometer most widely used in electron scattering features a deflection of the scattered electron in an inhomogeneous field by $\sim 180°$. This type of spectrometer was introduced to electron scattering by the pioneering experiments performed at Stanford. A modern version, used at the Saclay ALS (Leconte, 1976), features curved entrance and exit pole faces and achieves an intrinsic resolution of $\Delta E/E\sim 1.5\times 10^{-4}$ with a 5 msr solid angle and a 10% momentum acceptance. With corrections of aberrations, feasible since the trajectory of the electron in the focal plane is measured, the resolution reaches $<10^{-4}$. This type of spectrometer is very compact. With its large deflection angle and narrow focal plane, resulting from the double-focusing property, it provides for excellent background suppression.

The spectrometer used at the Bates accelerator (Bertozzi *et al.*, 1979) differs in several respects. Two separate 45° bending magnets with a homogeneous field are used to energy-analyze the scattered electrons. The four curved pole faces are used to achieve focusing and to correct higher-order aberrations. In particular, aberrations due to finite source (target) extension can be controlled. The Bates spectrometer features properties similar to those used at Saclay, as far as solid angle and momentum acceptance go. Its momentum resolution is superior, due to the better control of higher-order aberration, and has reached $<5\times 10^{-5}$. This type of split-pole spectrometer has a rather large distance from target to focal plane and is not very compact, a feature which, together with a bending angle of only 90°, complicates shielding and makes background suppression more difficult.

The spectrometer installed at the NIKHEF accelerator in Amsterdam (De Vries *et al.*, 1984) features a quadrupole—two-dipole (QDD) system (Fig. 4) similar to the ones used in hadron spectrometers. The dipoles, with a homogeneous field and curved pole faces, deflect the electrons by 75° each. The quadrupole focuses the electrons in the nondispersive plane, thereby creating a crossover of

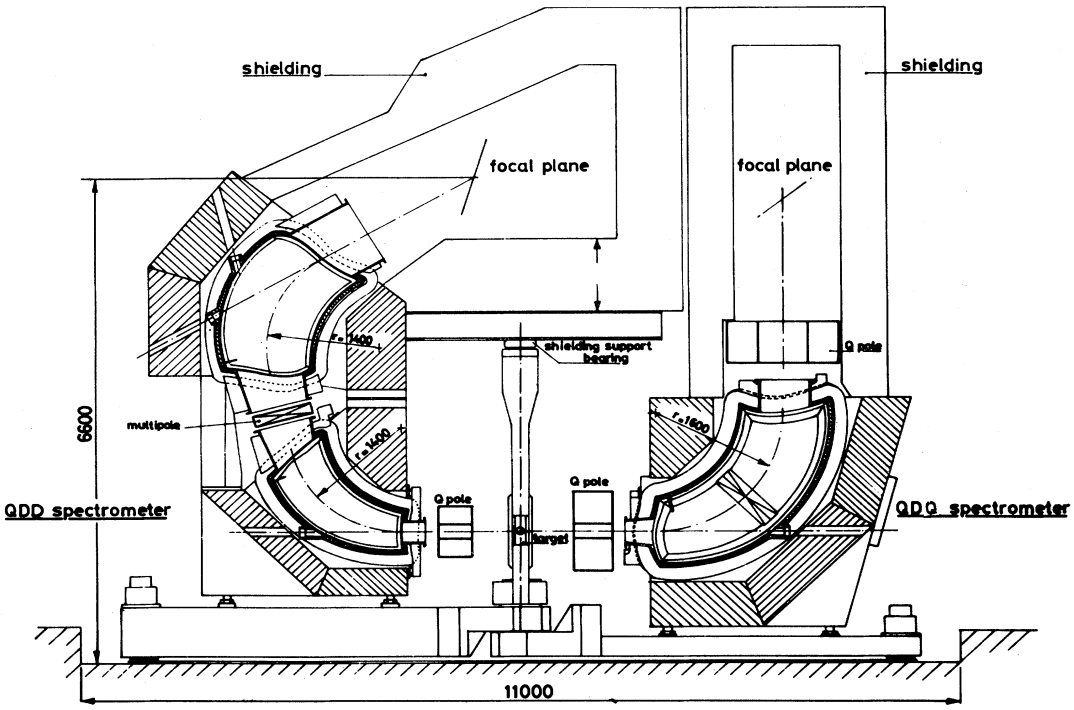

FIG. 4. QDD and QDQ spectrometers at the NIKHEF accelerator (De Vries *et al.*, 1984).

electron trajectories; for a given solid angle this leads to an important decrease of dipole gap (i.e., cost). The defocusing of the quadrupole in the dispersive plane has no detrimental effects, since in this direction the spectrometer acceptance is very large anyway due to the large momentum acceptance. An additional multipole element between the two dipoles can serve to correct optical imperfections.

This QDD system achieves a solid angle of 6 msr, a momentum acceptance of 10%, and an energy resolution, at the present time, of $<6\times10^{-5}$. The degrees of freedom offered by pole face curvature and the use of the quadrupole have permitted the creation of a flat focal plane, a feature that is very helpful in reducing the complexity of the focal plane detector and/or on-line data reduction system. The compactness of the QDD design, together with the good possibilities for shielding, leads to very low backgrounds.

All of the spectrometers described above are true energy-loss spectrometers, with identical energy dispersion of switchyard and spectrometer. The next generation of spectrometers probably will no longer respect this condition, but will feature one additional element, a position-sensitive detector after the first dipole, at a place where an intermediate image of the target is formed. In such an arrangement (Zeidmann, 1982) the first part of the spectrometer serves to measure the target coordinates, while the second part serves to measure the scattered electron energy. Decoupling these two quantities introduces new degrees of freedom and promises excellent resolution (a few times 10^{-5}) with large ($\sim$20 msr) solid angle.

High-resolution spectrometers in general have field maps measured with good precision for the verification of the optical properties required for good energy resolution. Using the field map, one can calculate the electron energy if the absolute field is measured during the experiment at one point using a nuclear-magnetic-resonance probe. This allows one to determine the energy of scattered (hence incident) electrons to an accuracy of a few times 10^{-4} in $\delta E/E$. This type of measurement in general is more reliable than the determination of energy via recoil energy differences or floating wire measurements.

The spectrometer solid angle is defined by accurately machined collimators of various sizes. The collimators determine the solid angle with an accuracy of $<1\%$. For the largest solid angle the accuracy in general is worse, since ill-determined pieces of the vacuum chamber and the like define the solid angle.

Due to the large amount of radiation produced by a high-intensity electron beam, the spectrometers involve large amounts of shielding. Typically 0.5—1 m of heavy material (iron, loaded concrete, lead) is used to surround the focal plane in order to protect it from the neutrons produced via (γ,n) reactions by bremsstrahlung.

E. Focal plane detectors

The detector system located in the spectrometer focal plane has a double function. Identification of the scattered particle as an electron allows one to suppress the large amount of radiation present despite good shielding.

Measurement of the coordinates and direction of the scattered electron in the focal plane yields accurate energy-(loss) measurements.

The identification of the particle detected is generally performed using signals provided by plastic scintillators and a Čerenkov counter. The fast coincidence between these signals also serves as a trigger for the more complex localization detector readout. The plastic scintillators, of the order of 1 cm thick, are often segmented into many individual units and are arranged in one or two planes in order to reduce pileup and increase directionality. The Čerenkov counter is used to identify the particle via its velocity v. When using Lucite or some liquid-hydrocarbon compound as a material, the index of refraction is such that one accepts particles with $v/c > 0.8$; such a detector does not eliminate the pions that are abundant at the higher incident energies and at large energy loss. Gas Čerenkov counters using a gas of high molecular weight (freon) at atmospheric pressure, as utilized for example in the Saclay spectrometer, allow one to eliminate all particles but electrons.

The detector used for the localization of the electron trajectory varies in complexity according to the type of spectrometer used and the number of aberrations to be corrected. The minimum number of measurements required occurs with spectrometers that have no residual aberrations and a focal "plane" which is a plane indeed. In this case one needs to measure the localization of the track only along the dispersive direction. The track position has to be measured with a resolution of a fraction of a millimeter, in order to define a peak of width $\Delta E/E \sim 10^{-4}$ by a number of points. For light nuclei it is important to determine the nuclear recoil energy, i.e., the scattering angle, with equivalent resolution. To this end a second measurement of either trajectory angle or transverse position of the track in or after the focal plane is required. Often spectrometers have a focal plane of complicated shape with residual aberrations; in this case two coordinates in the focal plane plus two angles have to be measured. With this information one can extrapolate the trajectory measured at the location of the detector to the focal plane or target, and a number of known aberrations can be removed.

Drift chambers have found general acceptance as localization detectors and replace the scintillation or solid-state counter ladders used previously. In such a multiwire proportional chamber, the secondary electrons produced by the high-energy electron drift to one or several collection wires before proportional gas amplification. The drift time is used to locate the track accurately. This provides an economical measurement, since a spatial resolution of ~ 0.1 mm can be obtained with a wire density of a few wires per cm (Bertozzi *et al.*, 1977). Since this detector causes little multiple scattering of the high-energy electron, successive measurements of several coordinates of the track are possible. Such drift chambers require a fraction of a microsecond to process one track, a time that has become acceptable with modern electron accelerators of duty cycle $> 10^{-2}$. The readout electronics and interface to the data acquisition computer have to be rather fast, in order to deal with the high data rates that can occur at very low momentum transfer. The dynamical range of cross sections measured with a given installation then can reach a factor of $\sim 10^{11}$.

For the determination of accurate cross sections, a number of factors, as discussed above, must be known. In this respect, the quantity which is usually most difficult to measure is the focal plane detector efficiency. It is often determined via a measurement of an accurately known reference cross section; the ^{12}C and ^{1}H elastic cross sections are generally used for this purpose. An independent determination of absolute efficiency is possible if the detector has enough elements to overdetermine electron identification and track measurement. In this case the redundancy of the detection system can be exploited to determine the efficiency of every individual element. With today's combinations of several multiwire proportional counters, plastic scintillators, and Čerenkov counters, this redundancy is available at low momentum transfer, where background rejection is of no concern. This procedure can be expected to provide in the future the standard method for determining absolute efficiencies to within $\sim 1\%$ accuracy. An alternative procedure, using a special spectrometer with a particularly simple detector, has been developed at Mainz (Reuter *et al.*, 1982). For experimental parameters determined with the accuracies quoted above, cross sections can be measured with systematical uncertainties of one to several percent. The most precise experiments, aiming at the determination of absolute reference cross sections, have reached 0.5% systematical error (Cardman *et al.*, 1980).

F. Data reduction

The raw data furnished by the experimental hardware require considerable manipulation during the transformation to publishable cross sections. A number of corrections have to be applied, imperfections of the apparatus removed, spectra decomposed into contributions of individual nuclear levels, target impurities eliminated, etc. Many of these corrections can be applied on-line during the experiment; others have to be performed after a detailed study of the results has revealed some unwanted effect. These procedures require considerable effort, and they are specific to the given installation and experiment. Since they are of little interest to the reader who wants to obtain a general idea of the state of the art of electron scattering experiments, we shall not discuss them further. We will, however, mention two particularly large "corrections."

Due to the small electron mass, the scattering of an electron is accompanied by emission of bremsstrahlung. Every peak in the energy spectrum corresponding to a well-defined nuclear level, therefore, has a radiative tail that extends to higher excitation energies. The cross sections required for a theoretical understanding have these radiative effects removed.

The radiative correction method commonly used is a rather simple one for the (magnetic) elastic scattering of interest here. For the highest-energy (elastically scattered) electrons all we need to know is the fraction of electrons that have radiated more than the energy cutoff used to integrate the elastic peak; this energy in general is imposed by the excitation energy of the first excited state. The fraction of electrons radiated outside can be calculated reliably using the work of Mo and Tsai (1969) and Tsai (1971). These radiative corrections have in principle been calculated using QED, an exact theory; in practice, some approximations have been made. Unfortunately, there is little information available on the uncertainty of this procedure. Experimentally, one can check radiative corrections by extrapolating form factors to momentum transfer zero, where $F(0)$ is known. Such checks lead to an estimate that the radiative corrections for elastic scattering—they amount to a correction of the order of $\sim 30\%$—have a reliability such that the final cross section is accurate to significantly better than 1%.

The second correction concerns the effects of Coulomb distortion. For the interpretation of experimental data on magnetic scattering, the plane-wave Born approximation (PWBA) offers great advantages; the connection between observable and underlying physical quantities is much more transparent, and calculations are much easier. Therefore it is desirable to convert magnetic cross sections to plane-wave form factors that can be used in a PWBA interpretation.

The effects of Coulomb distortion can be treated in a quantitative way using the distorted-wave Born approximation (DWBA). The theory of DWBA and calculations for a number of practical cases have been given by Überall (1971) and Prewitt and Wright (1974). The second-order Born approximation has been discussed by Bergstrom (1975). Here, we do not discuss DWBA in detail. For the combination of q range and atomic numbers of interest for magnetic electron scattering experiments available today, the effect of Coulomb distortion is not very large. A conversion from cross-section to plane-wave form factors can therefore be performed in a quantitative way.

The most important effect of distortion is a change of the q scale. The effective energy of the electron when being scattered is larger than the c.m. energy, due to the attraction in the nuclear Coulomb field. The increase in energy, by roughly the factor $1+\frac{4}{3}(Z\alpha/R_{eq}\varepsilon)$, leads to a corresponding increase in the effective momentum transfer $q_{\rm eff}$, and to a shift of diffraction minima and maxima. This dominant effect of Coulomb distortion can be accounted for by defining $F_{\rm exp}(q_{\rm eff})=d\sigma/d\Omega_{\rm exp}/\sigma_{\rm Mott}$ as a function of $q_{\rm eff}$ rather than q.

For heavier nuclei, or low q, the use of $q_{\rm eff}$ does not represent the distortion effects with sufficient accuracy. In this case a second step in the removal of distortion effects can be used. Starting from a model wave function, one calculates magnetic scattering cross sections both in PWBA and in DWBA, using one of the DWBA programs like DUELS (Tuan *et al.*, 1968) or HEINEL (Heisenberg, 1981). If the model wave function is reasonably close to reality, the distortion effects calculated with it are precise enough to be used for a conversion of the data to PWBA. The ratio $\sigma^{\rm DWBA}_{\rm model}$ and $\sigma^{\rm PWBA}_{\rm model}=F^2_{\rm model}(q_{\rm eff})\sigma_{\rm Mott}$ then can be used to convert experimental cross sections $\sigma_{\rm exp}$ to experimental PWBA form factors $F^2_{\rm exp}(q_{\rm eff})$.

The above procedure has been shown to work with satisfactory precision for the data available at present. It might fail once very precise data covering diffraction minima in F_M become available. This will not occur too often, though. As long as no polarization observables are measured, magnetic form factors for $J_0>\frac{1}{2}$ are incoherent sums over different multipolarities; minima in one multipolarity are filled in by maxima of others, and for form factors without too much structure the above recipe works well.

The form factors shown in this review in Sec. VI are displayed as functions of effective momentum transfer.

IV. FORMALISM

In this section the basic formalism for discussing electron scattering from nuclei is summarized and applied to a few illustrative cases. Our approach is based on the paper of Donnelly and Walecka (1973a), in which much of the required formalism is presented. For further discussions of electron scattering in general the reader is referred to several review articles or books on the subject (de Forest and Walecka, 1966; Überall, 1977; Donnelly and Walecka, 1975). Much of the past work has been presented somewhat piecemeal, and here we attempt to bring together the several different parts of the problem in a more coherent whole. We stress the density-matrix formalism as a common thread running through the discussions of the nuclear many-body problem.

Let us begin by considering electron scattering in the one-photon-exchange approximation, as shown in Fig. 5. Here an incident electron with four momentum[1] $k_\mu=(\mathbf{k},\varepsilon)$ is scattered through an angle θ to four momentum $k'_\mu=(\mathbf{k}',\varepsilon')$. In the process a virtual photon with four momentum $q_\mu=(\mathbf{q},\omega)$ is exchanged with the nucleus. Conservation of four momentum implies that $q_\mu=k_\mu-k'_\mu$; that is, we have energy transfer

$$\omega=\varepsilon-\varepsilon' \tag{4.1}$$

and three-momentum transfer

$$q=|\mathbf{q}|=(k^2+k'^2-2kk'\cos\theta)^{1/2} \tag{4.2}$$

to the nuclear system. Generally speaking, we have $\varepsilon=(k^2+m_e^2)^{1/2}$ and $\varepsilon'=(k'^2+m_e^2)^{1/2}$, where m_e is the

[1]We indicate four vectors by $A_\mu=(\mathbf{A},A_0)$, $B_\mu=(\mathbf{B},B_0)$, etc. Then we have for the scalar product $A\cdot B=A_\mu B_\mu=\mathbf{A}\cdot\mathbf{B}-A_0B_0$, where the summation convention is employed. Furthermore, the magnitude of a three vector is indicated by $A=|\mathbf{A}|$.

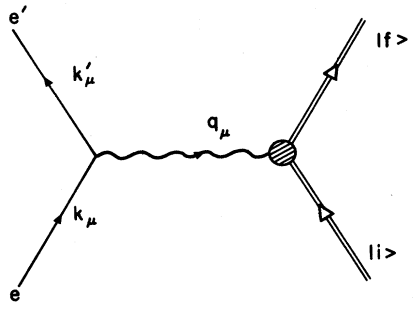

FIG. 5. Electron scattering in the one-photon exchange or first Born approximation.

electron mass, although at energies of interest (hundreds of MeV) the extreme relativistic limit (ERL) may be taken:

$$k=|\mathbf{k}|=\varepsilon,\quad k'=|\mathbf{k}'|=\varepsilon' . \tag{4.3}$$

In this limit Eq. (4.2) may be rewritten (for ERL)

$$q=\left[\omega^2+4\varepsilon\varepsilon'\sin^2\frac{\theta}{2}\right]^{1/2} . \tag{4.4}$$

The four-momentum transfer is then given by (for ERL)

$$q_\mu^2=q^2-\omega^2=4\varepsilon\varepsilon'\sin^2\frac{\theta}{2} . \tag{4.5}$$

For convenience of notation we also use $Q\equiv(q_\mu^2)^{1/2}$. We note that the four momentum transferred in the scattering must be spacelike:

$$q_\mu^2\geq 0,\quad q\geq\omega . \tag{4.6}$$

This is true whether or not the extreme relativistic limit is taken. In the special case of real-photon interactions with the nucleus, such as gamma decay, photoexcitation, etc. (see de Forest and Walecka, 1966; Überall, 1971; Donnelly and Walecka, 1975, for discussions of these processes in the context of electron scattering), one has $q_\mu^2=0$ ($q=\omega$).

In the general situation the nucleus may absorb the energy ω and momentum q transferred from the electron and proceed from initial ground state $|i\rangle$ to some (in general excited) state $|f\rangle$. In this paper our focus is on *elastic electron scattering,* in which case the state $|f\rangle$ refers to the ground state as well, now recoiling with momentum $\mathbf{q}$. If we denote the target mass by $M_{\rm tg}$, then the energy transfer for elastic scattering must be

$$\omega=(q^2+M_{\rm tg}^2)^{1/2}-M_{\rm tg} , \tag{4.7}$$

and the four-momentum transfer is given by

$$q_\mu^2=2M_{\rm tg}\omega . \tag{4.8}$$

Alternatively, we may eliminate the variables q and ω (and hence q_μ^2) in favor of the incident electron energy ε and scattering angle θ:

$$q_\mu^2=f_{\rm rec}^{-1}\left[2\varepsilon\sin\frac{\theta}{2}\right]^2 , \tag{4.9}$$

where

$$f_{\rm rec}=1+\frac{2\varepsilon}{M_{\rm tg}}\sin^2\frac{\theta}{2} , \tag{4.10}$$

$$\omega=q_\mu^2/2M_{\rm tg} , \tag{4.11}$$

$$q=\left[2M_{\rm tg}\omega\left[1+\frac{\omega}{2M_{\rm tg}}\right]\right]^{1/2} , \tag{4.12}$$

and

$$\varepsilon'=f_{\rm rec}^{-1}\varepsilon . \tag{4.13}$$

Typically, for all but the lightest targets at very high momentum transfers, we shall be interested in $q\ll M_{\rm tg}$, in which case we have

$$\omega\cong q^2/2M_{\rm tg}\cong 0 , \tag{4.14}$$

$$Q\cong q\cong 2\varepsilon\sin\frac{\theta}{2} . \tag{4.15}$$

Of course it is not necessary to use these approximations, and Eqs. (4.9)–(4.13) will generally be applied in this paper.

Returning now to the general situation of elastic or inelastic scattering, if the electrons in Fig. 5 are considered to be plane waves, then we have the plane-wave Born approximation. The cross section for unpolarized electron scattering,[2] involving a transition from state $|i\rangle$ to state $|f\rangle$, may be written (de Forest and Walecka, 1966; Überall, 1971; Donnelly and Walecka, 1975)

$$\left[\frac{d\sigma}{d\Omega}\right]_{i\to f}=4\pi\sigma_M f_{\rm rec}^{-1}F^2(q,\theta) . \tag{4.16}$$

Here, for a given momentum transfer q and scattering angle θ, the energy transfer ω is fixed by the excitation energy E_f-E_i and the recoil energy. The elementary cross section is given by

$$\sigma_M=\left[\frac{\alpha\cos\frac{\theta}{2}}{2\varepsilon\sin^2\frac{\theta}{2}}\right]^2 , \tag{4.17}$$

the Mott cross section, where α is the fine-structure constant.[3] The recoil correction is given in Eq. (4.10). The electron scattering form factor is given by

$$F^2(q,\theta)=(Q/q)^4F_L^2(q)+\left[\tfrac{1}{2}(Q/q)^2+\tan^2\frac{\theta}{2}\right]F_T^2(q) , \tag{4.18}$$

[2]Polarization in electron scattering is discussed in Sec. VIII.

[3]The reader is cautioned about the presence of the factors 4π in Eq. (4.16) and α instead of $Z\alpha$ in Eq. (4.17); while these are exactly the conventions used in some of the basic published works on the general subject of electron scattering from nuclei (e.g., de Forest and Walecka, 1966; Donnelly and Walecka, 1975, used here), they are not uniformly adopted by everyone in the field.

where $F_L(q)$ and $F_T(q)$ are the longitudinal and transverse form factors, respectively. By fixing q and ω (and so q_μ^2) and varying θ it is possible to separate $F_L^2(q)$ from $F_T^2(q)$ (a Rosenbluth separation). Alternatively, by working at $\theta=180°$ one ensures that only the transverse form factor contributes and so may be isolated. In this latter case note that the combination of $\sigma_M \tan^2(\theta/2)$ is well behaved as $\theta\rightarrow 180°$:

$$\sigma_M \tan^2\frac{\theta}{2} \underset{\theta\rightarrow 180°}{\rightarrow} \left[\frac{\alpha}{2\varepsilon}\right]^2 . \tag{4.19}$$

This discussion has been made within the context of the ERL: for low electron energies and for extreme angles ($\theta\approx 0°$ or 180°) corrections due to the finite mass of the electron should be retained. These form factors are in turn related to matrix elements of the nuclear electromagnetic current operator[4] $\hat{J}_\mu$ taken between states $|i\rangle$ and $|f\rangle$. The nuclear electromagnetic current-density operator $\hat{J}_\mu(\mathbf{x})=[\hat{\mathbf{J}}(\mathbf{x}),\hat{\rho}(\mathbf{x})]$ contains a "time" component ($\mu=0$), the charge-density operator

$$\hat{J}_0(\mathbf{x})=\hat{\rho}(\mathbf{x}) , \tag{4.20}$$

and three spatial components making up the three-vector current-density operator

$$\hat{\mathbf{J}}(\mathbf{x})=\hat{\mathbf{J}}_c(\mathbf{x})+\hat{\mathbf{J}}_m(\mathbf{x}) , \tag{4.21}$$

where the latter has been further subdivided into a convection current $\hat{\mathbf{J}}_c$ and a magnetization current $\hat{\mathbf{J}}_m$. The magnetization current-density operator may be rewritten in terms of the nuclear magnetization density operator $\hat{\boldsymbol{\mu}}(\mathbf{x})$:

$$\hat{\mathbf{J}}_m(\mathbf{x})=\boldsymbol{\nabla}\times\hat{\boldsymbol{\mu}}(\mathbf{x}) . \tag{4.22}$$

It is more convenient when plane-wave electrons are assumed to work in momentum space, and so we shall consider the Fourier transforms of the components of the electromagnetic current-density operator,

$$\hat{J}_\mu(\mathbf{q})=\int d\mathbf{x}\, e^{i\mathbf{q}\cdot\mathbf{x}}\hat{J}_\mu(\mathbf{x}) . \tag{4.23}$$

Furthermore, as we shall deal with states $|i\rangle$ and $|f\rangle$ having definite angular momenta J_i and J_f, respectively, it is useful to expand the exponential in a multipole series (Edmonds, 1960) and consider specific electromagnetic multipole operators. The multipole projections of the charge-density operator are the Coulomb multipole operators

$$\hat{M}^{\text{Coul}}_{JM_J}(q)\equiv\int d\mathbf{x}\, M_J^{M_J}(q\mathbf{x})\hat{\rho}(\mathbf{x}) , \tag{4.24}$$

with $J=0,1,2,\ldots$, where J is the multipole order, M_J is the z projection of angular momentum, and where

$$M_J^{M_J}(q\mathbf{x})\equiv j_J(qx)Y_J^{M_J}(\Omega_x) \tag{4.25}$$

is defined in terms of spherical Bessel functions and spherical harmonics. The three-vector current-density operator may be written in terms of two components orthogonal to the momentum transfer $\mathbf{q}$ (i.e., two transverse components, say J_x and J_y) and a component along $\mathbf{q}$ (i.e., a longitudinal component, say J_z), where we have chosen a coordinate system with the z axis along $\mathbf{q}$. The latter is eliminated using current conservation:

$$\partial_\mu\langle f|\hat{J}_\mu(\mathbf{x})|i\rangle=0 \tag{4.26a}$$

$$\Rightarrow q_\mu\langle f|\hat{J}_\mu(\mathbf{q})|i\rangle=0 \tag{4.26b}$$

$$\Rightarrow\langle f|\hat{J}_z(\mathbf{q})|i\rangle=\frac{\omega}{q}\langle f|\hat{\rho}(\mathbf{q})|i\rangle . \tag{4.26c}$$

The remaining two transverse projections may be expressed in terms of the electric and magnetic multipole operators (de Forest and Walecka, 1966; Überall, 1971; Donnelly and Walecka, 1975):

$$\hat{T}^{\text{el}}_{JM_J}(q)\equiv\int d\mathbf{x}\left[\frac{1}{q}\boldsymbol{\nabla}\times\mathbf{M}_{JJ}^{M_J}(q\mathbf{x})\right]\cdot\hat{\mathbf{J}}(\mathbf{x}) , \tag{4.27}$$

$$\hat{T}^{\text{mag}}_{JM_J}(q)\equiv\int d\mathbf{x}\,\mathbf{M}_{JJ}^{M_J}(q\mathbf{x})\cdot\hat{\mathbf{J}}(\mathbf{x}) \tag{4.28}$$

with $J=1,2,3,\ldots$, where

$$\mathbf{M}_{JL}^{M_J}(q\mathbf{x})\equiv j_L(qx)\mathbf{Y}_{JL1}^{M_J}(\Omega_x) \tag{4.29}$$

is defined in terms of spherical Bessel functions and vector spherical harmonics. A useful identity permits the curl to be rewritten (Edmonds, 1960)

$$\frac{1}{q}\boldsymbol{\nabla}\times\mathbf{M}_{JJ}^{M_J}(q\mathbf{x})=i\{-J^{1/2}\mathbf{M}_{JJ+1}^{M_J}(q\mathbf{x}) +(J+1)^{1/2}\mathbf{M}_{JJ-1}^{M_J}(q\mathbf{x})\}/[J] , \tag{4.30}$$

where $[J]\equiv\sqrt{2J+1}$.

The cross section may then be expressed directly in terms of matrix elements of these multipole operators. Since we are dealing with states with well-defined angular momenta, we may use the Wigner-Eckart theorem (Edmonds, 1960),

$$\langle J_f M_{J_f}|\hat{T}_{JM_J}(q)|J_i M_{J_i}\rangle=(-)^{J_f-M_{J_f}}\begin{pmatrix} J_f & J & J_i \\ -M_{J_f} & M_J & M_{J_i}\end{pmatrix}\langle J_f||\hat{T}_J(q)||J_i\rangle , \tag{4.31}$$

[4] A circumflex over a symbol, e.g., $\hat{J}_\mu$, is used to denote a second-quantized operator operating in the nuclear Hilbert space.

where the M dependence is all contained in the 3-j symbol and the detailed dynamics are contained in the reduced matrix element. Here $\hat{T}$ is any one of $\hat{M}^{\rm Coul}$, $\hat{T}^{\rm el}$, or $\hat{T}^{\rm mag}$. Once the M dependence has been made explicit, using Eq. (4.31) it is straightforward to perform the average over initial substates and sum over final substates (for the unpolarized cross section),

$$\overline{\sum_{if}} \leftrightarrow \frac{1}{2J_i+1}\sum_{M_{J_i}}\sum_{M_{J_f}} ,$$

to express the result in the form given in Eqs. (4.16)—(4.18) (see de Forest and Walecka, 1966; Überall, 1971; Donnelly and Walecka, 1975, for further details):

$$F_L^2(q)=\frac{1}{2J_i+1}\sum_{J\geq 0}|\langle J_f||\hat{M}_J^{\rm Coul}(q)||J_i\rangle|^2 , \tag{4.32}$$

$$F_T^2(q)=\frac{1}{2J_i+1}\sum_{J\geq 1}\{|\langle J_f||\hat{T}_J^{\rm el}(q)||J_i\rangle|^2 + |\langle J_f||\hat{T}_J^{\rm mag}(q)||J_i\rangle|^2\} . \tag{4.33}$$

Thus the cross section may be expressed directly in terms of Coulomb ($C0, C1, C2, \ldots$), electric ($E1, E2, \ldots$), and magnetic ($M1, M2, \ldots$) multipole matrix elements. Note that in general both electric and magnetic multipoles have convection and magnetization current contributions; indeed, using Eq. (4.22), we may write

$$\hat{T}^{\rm el}_{JM_J}(q)=\int d\mathbf{x}\left[\left[\frac{1}{q}\nabla\times\mathbf{M}^{M_J}_{JJ}(q\mathbf{x})\right]\cdot\hat{\mathbf{J}}_c(\mathbf{x}) + q\mathbf{M}^{M_J}_{JJ}(q\mathbf{x})\cdot\hat{\boldsymbol{\mu}}(\mathbf{x})\right] , \tag{4.34}$$

$$\hat{T}^{\rm mag}_{JM_J}(q)=\int d\mathbf{x}\left[\mathbf{M}^{M_J}_{JJ}(q\mathbf{x})\cdot\hat{\mathbf{J}}_c(\mathbf{x}) + q\left[\frac{1}{q}\nabla\times\mathbf{M}^{M_J}_{JJ}(q\mathbf{x})\right]\cdot\hat{\boldsymbol{\mu}}(\mathbf{x})\right] , \tag{4.35}$$

where Eq. (4.30) may be used for the curl terms.

As we frequently consider the nuclear states to have well-defined isospin, it is useful to employ Eq. (4.31) again, now in isospin space as well as angular momentum:

$$\langle J_fM_{J_f};T_fM_{T_f}|\hat{T}_{JM_J;TM_T}(q)|J_iM_{J_i};T_iM_{T_i}\rangle = (-)^{J_f-M_{J_f}}\begin{pmatrix} J_f & J & J_i \\ -M_{J_f} & M_J & M_{J_i}\end{pmatrix}(-)^{T_f-M_{T_f}}\begin{pmatrix} T_f & T & T_i \\ -M_{T_f} & M_T & M_{T_i}\end{pmatrix}\langle J_f;T_f::\hat{T}_{J;T}(q)::J_i;T_i\rangle . \tag{4.36}$$

Here the symbols :: denote matrix elements reduced both in angular momentum and isospin. Now for electromagnetic interactions $T=0,1$ and $M_T=0$, so we have from Eqs. (4.32) and (4.33)

$$F_L^2(q)=\frac{1}{2J_i+1}\sum_{J\geq 0}\left|\sum_{T=0,1}\begin{pmatrix} T_f & T & T_i \\ -M_{T_0} & 0 & M_{T_0}\end{pmatrix}\langle J_f;T_f::\hat{M}^{\rm Coul}_{J;T}(q)::J_i;T_i\rangle\right|^2 , \tag{4.37}$$

$$F_T^2(q)=\frac{1}{2J_i+1}\sum_{J\geq 1}\left[\left|\sum_{T=0,1}\begin{pmatrix} T_f & T & T_i \\ -M_{T_0} & 0 & M_{T_0}\end{pmatrix}\langle J_f;T_f::\hat{T}^{\rm el}_{J;T}(q)::J_i;T_i\rangle\right|^2 + \left|\sum_{T=0,1}\begin{pmatrix} T_f & T & T_i \\ -M_{T_0} & 0 & M_{T_0}\end{pmatrix}\langle J_f;T_f::\hat{T}^{\rm mag}_{J;T}(q)::J_i;T_i\rangle\right|^2\right] , \tag{4.38}$$

where $M_{T_f}=M_{T_i}\equiv M_{T_0}$, since $M_T=0$. The 3-j symbols may be evaluated (Edmonds, 1960) to yield

$$F_L^2(q)=\frac{1}{(2J_i+1)(2T_i+1)}\sum_{J\geq 0}\left|\delta_{T_fT_i}\left[\langle J_f;T_f::\hat{M}^{\rm Coul}_{J;0}(q)::J_i;T_i\rangle+\frac{M_{T_0}}{(T_i(T_i+1))^{1/2}}\langle J_f;T_f::\hat{M}^{\rm Coul}_{J;1}(q)::J_i;T_i\rangle\right] - \delta_{T_f,T_i+1}\frac{(T_f^2-M_{T_0}^2)^{1/2}}{(T_f)^{1/2}[T_f]}\langle J_f;T_f::\hat{M}^{\rm Coul}_{J;1}(q)::J_i;T_i\rangle\right|^2 , \tag{4.39}$$

where of course the second term vanishes when $T_i=0$. There is an additional term with $T_f=T_i-1$ which we have omitted; generally the ground state has the lowest isospin allowed. Analogous expressions are obtained for the electric and magnetic contributions to $F_T^2(q)$ using Eq. (4.38).

Next let us consider the parity and time-reversal properties of the multipole operators. The former is obtained by examining the behavior of the spherical harmonics under the transformation $\mathbf{x}\rightarrow-\mathbf{x}$, along with the nature of the electromagnetic current itself, which is a polar vector. From Eqs. (4.24), (4.25), and (4.27)—(4.29) it is

straightforward to show that the Coulomb and electric multipoles are of natural parity, while the magnetic multipoles have non-natural parity:

$$\begin{aligned} &CJ,EJ:\ \pi=(-)^J\ , \\ &MJ:\ \pi=(-)^{J+1}\ . \end{aligned} \tag{4.40}$$

Thus, for elastic scattering where $\pi=\pi_f\pi_i=+$, conservation of parity implies that only even-J Coulomb and electric multipoles and odd-J magnetic multipoles survive. The consequences of time-reversal invariance are less easy to demonstrate. Details on T invariance are presented in the review article by de Forest and Walecka (1966) and expanded upon in Donnelly and Walecka (1976). The implications for our purposes are that, for elastic scattering, time-reversal invariance permits only even-J Coulomb and odd-J electric and magnetic multipoles to survive. Thus for elastic electron scattering we have the following situation:

$$\begin{aligned} &CJ,\ J=\text{even only} \\ &EJ,\ \text{absent} \\ &MJ,\ J=\text{odd only}\ . \end{aligned} \tag{4.41}$$

In summary, for *elastic electron scattering* from a state with $J_f=J_i\equiv J_0$, $T_f=T_i\equiv T_0$, and $M_{T_f}=M_{T_i}\equiv M_{T_0}$ we have

$$F_L^2(q)=\frac{1}{(2J_0+1)(2T_0+1)}\sum_{\substack{J\geq 0\\ \text{even}}}\left|\langle J_0;T_0::\hat{M}^{\text{Coul}}_{J;0}(q)::J_0;T_0\rangle+\frac{M_{T_0}}{(T_0(T_0+1))^{1/2}}\langle J_0;T_0::\hat{M}^{\text{Coul}}_{J;1}(q)::J_0;T_0\rangle\right|^2\ , \tag{4.42}$$

$$F_T^2(q)=\frac{1}{(2J_0+1)(2T_0+1)}\sum_{\substack{J\geq 1\\ \text{odd}}}\left|\langle J_0;T_0::\hat{T}^{\text{mag}}_{J;0}(q)::J_0;T_0\rangle+\frac{M_{T_0}}{(T_0(T_0+1))^{1/2}}\langle J_0;T_0::\hat{T}^{\text{mag}}_{J;1}(q)::J_0;T_0\rangle\right|^2\ . \tag{4.43}$$

Of course it is this latter result, elastic magnetic electron scattering, which is the focus of the present paper.

Before turning to a more detailed discussion of the matrix elements themselves, let us end this subsection by discussing the low-q or long-wavelength limit of the expressions in Eqs. (4.42) and (4.43). The scale for momentum transfers in scattering from nuclei is set roughly by the nuclear radius R. Thus a characteristic scale of momentum transfer appropriate for nuclear physics is approximately $Q_N\sim\pi/R$. The long-wavelength limit then pertains when $q\ll Q_N$. Let us write Eqs. (4.42) and (4.43) as sums of multipoles:

$$F_L^2(q)\equiv\frac{1}{4\pi}\sum_{\substack{J\geq 0\\ \text{even}}}|\mathscr{F}_J(q)|^2\ , \tag{4.44}$$

$$F_T^2(q)\equiv\frac{1}{4\pi}\sum_{\substack{J\geq 1\\ \text{odd}}}|\mathscr{F}_J(q)|^2\ , \tag{4.45}$$

where $\mathscr{F}_J(q)$ is defined using Eqs. (4.42) and (4.43)

$$\mathscr{F}_J(q)=\frac{\sqrt{4\pi}}{[J_0][T_0]}\times\begin{cases}\langle J_0;T_0::\hat{M}^{\text{Coul}}_{J;0}(q)::J_0;T_0\rangle+\dfrac{M_{T_0}}{(T_0(T_0+1))^{1/2}}\langle J_0;T_0::\hat{M}^{\text{Coul}}_{J;1}(q)::J_0;T_0\rangle, & J=\text{even}\\ \langle J_0;T_0::[-i\hat{T}^{\text{mag}}_{J;0}(q)]::J_0;T_0\rangle+\dfrac{M_{T_0}}{(T_0(T_0+1))^{1/2}}\langle J_0;T_0::[-i\hat{T}^{\text{mag}}_{J;1}(q)]::J_0;T_0\rangle, & J=\text{odd}\ ,\end{cases} \tag{4.46}$$

and where, with the inclusion of the factor $-i$ in the magnetic terms, all $\mathscr{F}_J(q)$ may be considered to be real (de Forest and Walecka, 1966; Donnelly and Walecka, 1976). Focusing on $\mathscr{F}_0(q)$ for the moment, we note that this multipole projection involves $M_0^0(q\mathbf{x})=(1/\sqrt{4\pi})j_0(qx)$ [see Eqs. (4.24) and (4.25)]. When $q\ll Q_N$ we may take the leading term in the small-argument expansion of the spherical Bessel function $j_0(qx)\to 1$; thus in the long-wavelength limit (LWL) the Coulomb monopole operator simply becomes proportional to the integral of the charge-density operator, that is, becomes the charge operator $\hat{Z}$ itself with eigenvalue Z. Equivalently, examining the isoscalar and isovector pieces of Eq. (4.46), one finds in the low-q limit

$$\langle J_0;T_0::\hat{M}^{\text{Coul}}_{0;0}(q)::J_0;T_0\rangle\underset{\text{LWL}}{\to}\frac{1}{\sqrt{4\pi}}[J_0][T_0]\tfrac{1}{2}A\ , \tag{4.47a}$$

$$\langle J_0;T_0::\hat{M}^{\text{Coul}}_{0;1}(q)::J_0;T_0\rangle\underset{\text{LWL}}{\to}\frac{1}{\sqrt{4\pi}}[J_0][T_0]\times(T_0(T_0+1))^{1/2}\ , \tag{4.47b}$$

where the fact is used that the nuclear state involved is considered to be an eigenstate of the total baryon number

operator $\hat{A}$, with eigenvalue A, and of the z component of isospin $\hat{T}_z$, with eigenvalue M_{T_0}. Thus we find that

$$\mathcal{F}_0(q) \underset{\text{LWL}}{\rightarrow} \tfrac{1}{2}A + M_{T_0} = Z \ . \tag{4.48}$$

Similar arguments can be applied to the rest of the even-J Coulomb multipoles. Following Überall (1971), we define electric (really Coulomb) multipole operators

$$\hat{Q}_{JM_J} \equiv \frac{\sqrt{4\pi}}{[J]} \int d\mathbf{x}\, x^J Y_J^{M_J}(\Omega_x) \hat{\rho}(\mathbf{x}) \ , \tag{4.49}$$

with the ground-state moments being defined as the expectation values of these operators in the state with $M_{J_0} = J_0$:

$$Q_J \equiv \langle J_0, M_{J_0} = J_0 \,|\, \hat{Q}_{J0} \,|\, J_0, M_{J_0} = J_0 \rangle \ . \tag{4.50}$$

With our definition of the Coulomb operators in Eqs. (4.24) and (4.25) we have, using the long-wavelength expansion of the spherical Bessel function

$$j_J(qx) \underset{\text{LWL}}{\rightarrow} (qx)^J/(2J+1)!! \ , \tag{4.51}$$

the following relationships:

$$\hat{M}_{JM_J}^{\text{Coul}}(q) \underset{\text{LWL}}{\rightarrow} \frac{[J]}{\sqrt{4\pi}(2J+1)!!} q^J \hat{Q}_{JM_J} \ . \tag{4.52}$$

This implies that the low-q limits of the Coulomb form factors are proportional to the corresponding moments,

$$\mathcal{F}_J(q) \underset{\text{LWL}}{\rightarrow} \frac{[J]}{(2J+1)!!} \left[\frac{(2J_0+J+1)!(2J_0-J)!}{(2J_0+1)!(2J_0)!} \right]^{1/2} q^J Q_J \ , \tag{4.53}$$

where J = even and satisfies $0 \le J \le 2J_0$. Since $Q_0 = Z$, we recover Eq. (4.48); also for $J=2$ ($C2$ moment) we find

$$\mathcal{F}_2(q) \underset{\text{LWL}}{\rightarrow} \frac{1}{3\sqrt{5}} \left[\frac{J_0+1}{J_0} \right]^{1/2} \frac{[J_0+1]}{[J_0-1]} q^2 Q_2 \ , \tag{4.54}$$

where $J_0 \ge 1$ for this expression to be applicable and where $2Q_2$ is the usual ground-state electric quadrupole moment. Similarly, all moments $C0, C2, C4, \ldots$, up to a maximum $J \le 2J_0$ occur as the low-q limits of the Coulomb form factors. Likewise for the odd-J magnetic multipoles, we may make use of an alternative way of writing the magnetic operators (Donnelly and Walecka, 1973):

$$-i\hat{T}_{JM_J}^{\text{mag}}(q) = q \int d\mathbf{x} \left[\frac{1}{\sqrt{J(J+1)}} \left[\frac{1}{q} \nabla M_J^{M_J}(q\mathbf{x}) \right] \cdot \hat{\mathbf{L}}_c(\mathbf{x}) + \left[-\frac{i}{q} \nabla \times \mathbf{M}_{JJ}^{M_J}(q\mathbf{x}) \right] \cdot \hat{\boldsymbol{\mu}}(\mathbf{x}) \right] \ , \tag{4.55}$$

where we have used the identity (Edmonds, 1960)

$$\mathbf{M}_{JJ}^{M_J}(q\mathbf{x}) = \frac{-i}{\sqrt{J(J+1)}} (\mathbf{x} \times \nabla) M_J^{M_J}(q\mathbf{x}) \tag{4.56}$$

and have introduced the orbital angular momentum density operator $\hat{\mathbf{L}}_c(\mathbf{x})$ corresponding to the convection current-density operator $\mathbf{J}_c(\mathbf{x})$,

$$\hat{\mathbf{L}}_c(\mathbf{x}) = \mathbf{x} \times \hat{\mathbf{J}}_c(\mathbf{x}) \ . \tag{4.57}$$

The curl term in Eq. (4.55) may be re-expressed using the identity in Eq. (4.30); furthermore, the gradient terms may be rewritten using (Edmonds, 1960)

$$\frac{1}{q} \nabla M_J^{M_J}(q\mathbf{x}) = \{ (J+1)^{1/2} \mathbf{M}_{JJ+1}^{M_J}(q\mathbf{x}) + J^{1/2} \mathbf{M}_{JJ-1}^{M_J}(q\mathbf{x}) \} / [J] \ . \tag{4.58}$$

Now if we define odd-J magnetic multipole operators (Überall, 1971)

$$\hat{\mu}_{JM_J} \equiv \frac{\sqrt{4\pi}}{[J]} \int d\mathbf{x} \{ \nabla [x^J Y_J^{M_J}(\Omega_x)] \} \times \left[\frac{1}{J+1} \hat{\mathbf{L}}_c(\mathbf{x}) + \hat{\boldsymbol{\mu}}(\mathbf{x}) \right] \ , \tag{4.59}$$

then we find in the long-wavelength limit that

$$-i\hat{T}_{JM_J}^{\text{mag}}(q) \underset{\text{LWL}}{\rightarrow} \frac{\sqrt{J+1}[J]}{\sqrt{4\pi}\sqrt{J}(2J+1)!!} q^J \hat{\mu}_{JM_J} \ . \tag{4.60}$$

Indeed, this was the reason that the factor $-i$ was chosen in Eq. (4.46), since we have the usual definition of the magnetic moments as expectation values of the operators $\hat{\mu}_{JM_J}$ in the state with $M_{J_0} = J_0$, multiplied by $2M_N$, where M_N is the nucleon mass (from the nuclear magneton $e\hbar/2M_pc$; Überall, 1971):

$$\mu_J \equiv 2M_N \langle J_0, M_{J_0} = J_0 \,|\, \hat{\mu}_{J0} \,|\, J_0, M_{J_0} = J_0 \rangle \ . \tag{4.61}$$

Thus we find that the low-q limits of the magnetic form factors are proportional to the corresponding moments:

$$\mathcal{F}_J(q) \underset{\text{LWL}}{\rightarrow} \frac{[J]}{(2J+1)!!} \left[\frac{(J+1)(2J_0+J+1)!(2J_0-J)!}{J(2J_0+1)!(2J_0)!} \right]^{1/2} \times \frac{q^J}{2M_N} \mu_J \ , \tag{4.62}$$

where J = odd and satisfies $0 \le J \le 2J_0$. For example, for $J=1$ we obtain

$$\mathcal{F}_1(q) \underset{\text{LWL}}{\rightarrow} \sqrt{2/3} \left[\frac{J_0+1}{J_0} \right]^{1/2} \left[\frac{q}{2M_N} \right] \mu_1, \quad J_0 \ge \tfrac{1}{2} \ , \tag{4.63}$$

where $\mu_1 = \mu$ is the usual ground-state magnetic dipole moment, so that we find

$$F_T^2(q) \underset{\text{LWL}}{\rightarrow} \frac{1}{6\pi} \left[\frac{J_0+1}{J_0} \right] \left[\frac{q}{2M_N} \right]^2 \mu^2 \ , \tag{4.64}$$

since the $M1$ moment dominates at low momentum

transfer. Similarly, all moments $M1, M3, M5, \ldots$, up to a maximum $J \leq 2J_0$ occur as the low-q limits of the respective magnetic form factors.

A. Nuclear many-body problem

Having summarized the basic formalism required in describing electron scattering from nuclei, including the low-q relationships of the elastic form factors to the static ground-state moments, we now turn to questions of nuclear dynamics. We wish to establish a connection between, say, a shell-model description of the nuclear states involved and the resulting electromagnetic form factors. We shall work in second quantization, where the nuclear states are represented as sums of A-fold products of nucleon creation operators acting on the vacuum. That is, our many-body description will be in terms of nuclear degrees of freedom, with only implicit dependence on nonnucleonic degrees of freedom (see, for example, Sec. IV.E, where meson-exchange currents are discussed). We assume that some single-particle basis set of wave functions has been specified

$$\{\phi_\alpha(\mathbf{x})\} ,$$

where α labels the single-particle quantum numbers appropriate for the chosen basis. For example, in many cases Hartree-Fock wave functions provide a good starting point for such many-body descriptions. We shall generally assume that $\{\alpha\}$ refers to the set of single-particle quantum numbers.

$$\{\alpha\} \leftrightarrow \{nlj, m_j; \tfrac{1}{2} m_t\} ,$$

where $n = 1,2,3,\ldots$ is a node number (note that the convention $n = 0,1,2,\ldots$ is alternatively used by some authors), l is the orbital angular momentum, j is the total single-particle angular momentum [we couple orbital angular momentum l and spin-$\frac{1}{2}$ in the order $(l\frac{1}{2})j$], and m_j is the z projection of angular momentum. Also useful is the principal quantum number defined by $N \equiv 2(n-1)+l = 0,1,2,\ldots$. In addition we have isospin-$\frac{1}{2}$ with projection m_t, where $m_t = +\frac{1}{2}$ corresponds to a proton and $m_t = -\frac{1}{2}$ to a neutron.[5] Thus the single-particle wave functions $\phi_\alpha(\mathbf{x})$ are two-component spinors in both spin and isospin spaces:

$$\phi_{nlj,m_j;1/2,m_t}(\mathbf{x}) = R_{nlj}(x)[Y_l(\Omega_x) \otimes \chi_{1/2}]_j^{m_j} \xi_{1/2}^{m_t} , \tag{4.65}$$

where the $R_{nlj}(x)$ are radial wave functions normalized according to

$$\int_0^\infty x^2 dx \, | R_{nlj}(x) |^2 = 1 . \tag{4.66}$$

In fact we shall assume that a phase convention has been chosen in which the radial wave functions are real and begin positive at the origin. The spin-$\frac{1}{2}$ spinors are denoted $\chi_{1/2}^{m_s}$ and the isospin-$\frac{1}{2}$ spinors $\xi_{1/2}^{m_t}$. We have used a condensed notation for the coupling of two quantities with good angular momentum quantum numbers:

$$[A_{j_1} \otimes B_{j_2}]_{j_3}^{m_3} \equiv \sum_{m_1 m_2} \langle j_1 m_1 j_2 m_2 \,|\, (j_1 j_2) j_3 m_3 \rangle A_{j_1}^{m_1} B_{j_2}^{m_2} . \tag{4.67}$$

Furthermore, it will prove useful to define $\{-\alpha\}$ to stand for the same single-particle quantum numbers, but with $-m_j$ and $-m_t$,

$$\{-\alpha\} \leftrightarrow \{nlj, -m_j; \tfrac{1}{2}, -m_t\}$$

and to let $\{a\}$ stand for the set of quantum numbers other than m_j and m_t:

$$\{a\} \leftrightarrow \{nlj; \tfrac{1}{2}\} .$$

Now it is useful to perform a canonical transformation from a second-quantized description in terms of particles only to one in terms of particles and holes with respect to some chosen Fermi surfaces (Fetter and Walecka, 1971),

$$c_\alpha = \theta(\varepsilon_\alpha - \varepsilon_F) a_\alpha + \theta(\varepsilon_F - \varepsilon_\alpha) S_\alpha b_{-\alpha}^\dagger , \tag{4.68a}$$

$$c_\alpha^\dagger = \theta(\varepsilon_\alpha - \varepsilon_F) a_\alpha^\dagger + \theta(\varepsilon_F - \varepsilon_\alpha) S_\alpha b_{-\alpha} . \tag{4.68b}$$

Here ε_α is the single-particle energy corresponding to the quantum numbers α, ε_F is the Fermi energy, and

$$S_\alpha \equiv (-)^{j-m_j} (-)^{1/2-m_t} \tag{4.69}$$

is a phase factor chosen so that c_α transforms as an irreducible tensor operator (Fetter and Walecka, 1971). Thus in Eq. (4.68a), the first term destroys particles above the Fermi sea, while the second creates holes below the Fermi sea. Equation (4.68b) is interpreted similarly.

A general operator may then be expanded in the following manner:

$$\hat{T} = T^{(0)} + \hat{T}^{(1)} + \hat{T}^{(2)} + \cdots , \tag{4.70}$$

where the various terms correspond to a zero-body (c-number) piece, a one-body piece, a two-body piece, and so on. The c-number piece contains no c_α or $c_\alpha^\dagger$ and is trivial to handle. The one-body contribution appears as

$$\hat{T}^{(1)} = \sum_{\alpha' \alpha} \langle \alpha' \,|\, T^{(1)} \,|\, \alpha \rangle c_{\alpha'}^\dagger c_\alpha , \tag{4.71}$$

where the c numbers multiplying the creation and destruction operators, that is, the factors $\langle \alpha' \,|\, T^{(1)} \,|\, \alpha \rangle$, are single-particle matrix elements. Let us suppose that in first quantization we have

$$T^{(1)} = \sum_{i=1}^{A} T^{(1)}(\mathbf{x}_i) . \tag{4.72}$$

Here we have made explicit the dependence on the nucleon coordinates $\mathbf{x}_i$ one at a time; of course it should be understood that in general there will also be dependence on the discrete coordinates, spin and isospin, as well, which has been suppressed for the time being. The

[5] Of course it should be noted that the opposite convention is also frequently used in nuclear physics.

single-particle matrix elements in Eq. (4.71) are then

$$\langle\alpha'\,|\,T^{(1)}\,|\,\alpha\rangle=\int d\mathbf{r}\,\phi^\dagger_{\alpha'}(\mathbf{r})T^{(1)}(\mathbf{r})\phi_\alpha(\mathbf{r})\,, \tag{4.73}$$

where $\mathbf{r}$ is any coordinate from the set $\{\mathbf{x}_1,\ldots,\mathbf{x}_A\}$. With discrete degrees of freedom, such as spin or isospin, the product $\phi^\dagger T^{(1)}\phi$ may be understood to be a matrix product (row vector×square matrix×column vector) in each space. Similar considerations hold for the two-body piece of Eq. (4.70). In first quantization we have

$$T^{(2)}=\sum_{i,j=1}^{A}T^{(2)}(\mathbf{x}_i,\mathbf{x}_j)\,, \tag{4.74}$$

yielding in second quantization the two-body operator

$$\hat{T}^{(2)}=\sum_{\substack{\alpha'\alpha\\ \beta'\beta}}\langle\alpha'\beta'\,|\,T^{(2)}\,|\,\alpha\beta\rangle c^\dagger_{\alpha'}c^\dagger_{\beta'}c_\beta c_\alpha\,, \tag{4.75}$$

where the two-particle matrix elements are given by

$$\langle\alpha'\beta'\,|\,T^{(2)}\,|\,\alpha\beta\rangle=\int d\mathbf{r}\int d\mathbf{r}'\phi^\dagger_{\alpha'}(\mathbf{r})\phi^\dagger_{\beta'}(\mathbf{r}')\times T^{(2)}(\mathbf{r},\mathbf{r}')\phi_\alpha(\mathbf{r})\phi_\beta(\mathbf{r}')\,. \tag{4.76}$$

Succeeding terms in Eq. (4.70), involving three-body, etc., terms, may be handled following the same procedures. For more discussion of the transition from first to second quantization see one of the standard books in many-body theory, such as Fetter and Walecka (1971, especially Chaps. 1 and 15).

Fortunately (because of the great complexity of handling multibody operators in practice), electromagetic interactions with nuclei are usually dominated by one-body contributions. This, however, is not a general statement: we shall see when we return to discuss two-body meson-exchange-current contributions, in Sec. IV.E below, that under some conditions a one-body analysis would be inadequate. For the present let us focus on the one-body pieces of the various multipole operators discussed in the preceding section.

Let us begin this one-body discussion by generalizing Eqs. (4.71)—(4.73) to include density operators:

$$T^{(1)}(\mathbf{x})=\sum_{i=1}^{A}T^{(1)}(\mathbf{x};\mathbf{x}_i)\,, \tag{4.77}$$

$$\hat{T}^{(1)}(\mathbf{x})=\sum_{\alpha'\alpha}\langle\alpha'\,|\,T^{(1)}(\mathbf{x})\,|\,\alpha\rangle c^\dagger_{\alpha'}c_\alpha\,, \tag{4.78}$$

$$\langle\alpha'\,|\,T^{(1)}(\mathbf{x})\,|\,\alpha\rangle=\int d\mathbf{r}\,\phi^\dagger_{\alpha'}(\mathbf{r})T^{(1)}(\mathbf{x};\mathbf{r})\phi_\alpha(\mathbf{r})\,. \tag{4.79}$$

Note that the coordinate $\mathbf{x}$ specifies the density dependence, whereas $\mathbf{x}_i$, $i=1,\ldots,A$ and $\mathbf{r}$ specify the dependence on the nucleon coordinates. To help clarify this, let us consider a specific example, that of the charge density. If we take the nucleons to be point particles (see Sec. IV.B for a discussion of this point), then we have

$$\rho^{(1)}(\mathbf{x})=\sum_{i=1}^{A}e(i)\delta(\mathbf{x}-\mathbf{x}_i)\,, \tag{4.80}$$

where

$$e(i)=\tfrac{1}{2}[1+\tau_3(i)]=\begin{cases}1 & \text{for protons}\\ 0 & \text{for neutrons.}\end{cases} \tag{4.81}$$

Then the single-particle matrix elements [Eq. (4.79)] become

$$\langle\alpha'\,|\,\rho^{(1)}(\mathbf{x})\,|\,\alpha\rangle=\int d\mathbf{r}\,\phi^\dagger_{\alpha'}(\mathbf{r})\tfrac{1}{2}(1+\tau_3)\delta(\mathbf{x}-\mathbf{r})\phi_\alpha(\mathbf{r}) \tag{4.82a}$$

$$=\delta_{m_t,+1/2}\phi^\dagger_{\alpha'}(\mathbf{x})\phi_\alpha(\mathbf{x}) \tag{4.82b}$$

$$=\delta_{m_t,+1/2}\delta_{m'_t m_t}R^*_{n'l'j'}(x)R_{nlj}(x)\sum_{\substack{m'_l m_l\\ m'_s m_s}}\langle l'm'_l\,\tfrac{1}{2}m'_s\,|\,(l'\tfrac{1}{2})j'm_{j'}\rangle\langle lm_l\,\tfrac{1}{2}m_s\,|\,(l\tfrac{1}{2})jm_j\rangle \times Y^{m'_l}_{l'}(\Omega_x)^*Y^{m_l}_{l}(\Omega_x)\delta_{m'_s m_s}\,. \tag{4.82c}$$

Note that matrix elements in spin and isospin spaces (of the unit matrix and of τ_3) have been taken, resulting in factors $\delta_{m'_s m_s}$ and $\delta_{m_t,+1/2}\delta_{m_t m'_t}$. These single-particle matrix elements may then be inserted in Eq. (4.78) to obtain the second-quantized one-body charge-density operator $\hat{\rho}^{(1)}(\mathbf{x})$.

Now we wish to exploit the multipole projections that were discussed in the preceding section. Let us suppose that the general one-body operator in Eq. (4.78) is characterized by definite angular momentum and isospin quantum numbers JM_J and TM_T and multipole projected as in Eqs. (4.24), (4.27), and (4.28):

$$\hat{T}^{(1)}_{JM_J;TM_T}(q)=\sum_{\alpha'\alpha}\langle\alpha'\,|\,T^{(1)}_{JM_J;TM_T}(q)\,|\,\alpha\rangle c^\dagger_{\alpha'}c_\alpha\,. \tag{4.83}$$

By reducing the single-particle matrix element [using the Wigner-Eckart theorem, cf. Eq. (4.36)], this may be written

$$\hat{T}^{(1)}_{JM_J;TM_T}(q)=\sum_{a'a}\langle a'::T^{(1)}_{J;T}(q)::a\rangle\hat{\psi}^\dagger_{JM_J;TM_T}(a'a)\,, \tag{4.84}$$

where we have defined a one-body creation operator built by coupling the $c^\dagger_{\alpha'}$ and c_α to total angular momentum and isospin, JM_J and TM_T,

$$\hat{\psi}^\dagger_{JM_J;TM_T}(a'a)\equiv\frac{1}{[J][T]}[c^\dagger_{a'}\otimes\tilde{c}_a]^{M_J;M_T}_{J;T}\,, \tag{4.85}$$

and where we also define $\tilde{c}_\alpha\equiv S_\alpha c_{-\alpha}$. Reduced matrix elements of such one-body multipole operators between nuclear many-body states having definite angular momen-

tum and isospin quantum numbers, $J_nM_{J_n}$ and $T_nM_{T_n}$ $n=1,2$ are then given by

$$\langle J_1;T_1::\hat{T}^{(1)}_{J;T}(q)::J_2;T_2\rangle=\sum_{a'a}\langle a'::T^{(1)}_{J;T}(q)::a\rangle \times\psi^{(12)}_{J;T}(a'a)\,, \tag{4.86}$$

where we have defined one-body density-matrix elements

$$\psi^{(12)}_{J;T}(a'a)\equiv\langle J_1;T_1::\hat{\psi}^{\dagger}_{J;T}(a'a)::J_2;T_2\rangle\,. \tag{4.87}$$

Thus all of the single-particle dependence (and q dependence) has been isolated in the single-particle reduced matrix elements, $\langle a'::T^{(1)}_{J;T}(q)::a\rangle$, while the complexities of the nuclear many-body problem have been isolated in the one-body density-matrix elements.

So far we have discussed the basic formalism as it pertains to one-body operators. Let us now turn to Eqs. (4.75) and (4.76) and conclude this subsection by summarizing the extensions which occur when two-body operators must be handled. Specifically we shall be interested in two-body meson-exchange currents and return to discuss these in Sec. IV.E. As in the one-body operator development, we wish to exploit the multipole projections of the current operators, and so we suppose that the general two-body operator is characterized by definite angular momentum and isospin quantum numbers JM_J and TM_T, respectively [cf. Eq. (4.83)]:

$$\hat{T}^{(2)}_{JM_J;TM_T}(q)=\sum_{\substack{\alpha'\beta'\\ \alpha\beta}}\langle\alpha'\beta'\,|\,T^{(2)}_{JM_J;TM_T}(q)\,|\,\alpha\beta\rangle c^{\dagger}_{\alpha'}c^{\dagger}_{\beta'}c_{\beta}c_{\alpha}\,. \tag{4.88}$$

As before, we have Fourier-transformed to momentum space. Using the Wigner-Eckart theorem and working with matrix elements reduced in angular momentum and isospin, we have [cf. Eq. (4.84)]

$$\hat{T}^{(2)}_{JM_J;TM_T}(q)=\sum_{\substack{a'b'\\ ab}}\langle(a'b')\mathscr{J}'\mathscr{T}'::T^{(2)}_{J;T}(q)::(ab)\mathscr{J}\mathscr{T}\rangle \times\hat{\Psi}^{\dagger}_{JM_J;TM_T}((a'b')\mathscr{J}'\mathscr{T}';(ab)\mathscr{J}\mathscr{T})\,, \tag{4.89}$$

where the two-particle configurations have been coupled to total angular momentum and isospin, e.g.,

$$|(ab)\mathscr{J}\mathscr{M}_{\mathscr{J}};\mathscr{T}\mathscr{M}_{\mathscr{T}}\rangle =\sum_{\substack{m_{j_\alpha}m_{j_\beta}\\ m_{t_\alpha}m_{t_\beta}}}\langle j_a m_{j\alpha}j_b m_{j_\beta}\,|\,(j_aj_b)\mathscr{J}\mathscr{M}_{\mathscr{J}}\rangle \times\langle\tfrac{1}{2}m_{t_\alpha}\tfrac{1}{2}m_{t_\beta}\,|\,(\tfrac{1}{2}\tfrac{1}{2})\mathscr{T}\mathscr{M}_{\mathscr{T}}\rangle\,|\,\alpha\beta\rangle\,. \tag{4.90}$$

Thus in Eq. (4.89) we have two-particle double-reduced matrix elements multiplying a two-body creation operator defined by

$$\hat{\Psi}^{\dagger}_{JM_J;TM_T}((a'b')\mathscr{J}'\mathscr{T}';(ab)\mathscr{J}\mathscr{T})\equiv-\frac{1}{[J][T]}[[c^{\dagger}_{a'}\otimes c^{\dagger}_{b'}]_{\mathscr{J}';\mathscr{T}'}\otimes[\tilde{c}_a\otimes\tilde{c}_b]_{\mathscr{J};\mathscr{T}}]^{M_J;M_T}_{J;T}\,, \tag{4.91}$$

to be compared with Eq. (4.85). The reduced matrix elements of this general two-body operator between nuclear many-body states, as required for instance in calculating MEC contributions to the electromagnetic form factors, are then given by [cf. Eq. (4.86)]

$$\langle J_1,T_1::\hat{T}^{(2)}_{J;T}(q)::J_2;T_2\rangle=\sum_{\substack{(a'b')\mathscr{J}'\mathscr{T}'\\ (ab)\mathscr{J}\mathscr{T}}}\langle(a'b')\mathscr{J}'\mathscr{T}'::T^{(2)}_{J;T}(q)::(ab)\mathscr{J}\mathscr{T}\rangle\Psi^{(12)}_{J;T}((a'b')\mathscr{J}'\mathscr{T}';(ab)\mathscr{J}\mathscr{T})\,. \tag{4.92}$$

We now have the two-particle dependence (and the q dependence) isolated in two-particle reduced matrix elements, while the complexities of the nuclear many-body problem have been isolated in two-body density-matrix elements defined by

$$\Psi^{(12)}_{J;T}((a'b')\mathscr{J}'\mathscr{T}';(ab)\mathscr{J}\mathscr{T})\equiv\langle J_1;T_1::\hat{\Psi}^{\dagger}_{J;T}((a'b')\mathscr{J}'\mathscr{T}';(ab)\mathscr{J}\mathscr{T})::J_2;T_2\rangle\,, \tag{4.93}$$

in close analogy to the one-body density matrix defined in Eq. (4.87). Of course this formulation of the nuclear many-body problem may alternatively be handled using coefficients of fractional parentage [see, for example, de Shalit and Talmi (1963)].

We turn next to the relevant single-particle currents and multipole matrix elements. Only after completing the discussion of analyses based on one-body operators will we return to summarize the treatment of two-body meson-exchange currents in Sec. IV.E.

B. Single-particle matrix elements

We begin by discussing the general form for the single-nucleon electromagnetic current (de Forest and Walecka, 1966; Überall, 1971; Donnelly and Walecka, 1975); the conventions used here for Dirac γ matrices and spinors are those of de Forest and Walecka (1966) and Donnelly and Walecka (1975):

$$\langle\mathbf{p}'m_s'm_t'\,|\,J_\mu(0)\,|\,\mathbf{p}m_sm_t\rangle=i\bar{u}(\mathbf{p}',m_s')\xi^{m_t'\,\dagger}_{1/2} \times(F_1\gamma_\mu-F_2\sigma_{\mu\nu}q_\nu) \times\xi^{m_t}_{1/2}u(\mathbf{p},m_s)\,. \tag{4.94}$$

Here the single-nucleon states are labeled with linear momentum $\mathbf{p}$ ($\mathbf{p}'$), spin projection (helicity really) m_s (m_s'), and isospin projection m_t (m_t'). The momentum transfer is $q_\mu=p'_\mu-p_\mu$. The two terms in Eq. (4.94)

involve the Dirac contribution ($\sim\gamma_\mu$) and the anomalous magnetic moment contribution ($\sim\sigma_{\mu\nu}q_\nu$), each multiplied by its corresponding form factor

$$F_{1,2}=F_{1,2}(q_\mu^2)\ .$$

In turn these depend on whether the single nucleon is a proton or a neutron:

$$F_{1,2}=F_{1,2}^p\tfrac{1}{2}(1+\tau_3)+F_{1,2}^n\tfrac{1}{2}(1-\tau_3)\ , \tag{4.95}$$

where the operators $\frac{1}{2}(1\pm\tau_3)$ project protons and neutrons, respectively.

Since we shall only be dealing with isoscalar and isovector operators ($T=0,1$ only), it is convenient to define the following general isospin operators:

$$I_T^{M_T}\equiv\frac{1}{2}\times\begin{cases}1, & T=0,\ M_T=0\\ \tau_0=\tau_3, & T=1,\ M_T=0\\ \tau_{\pm1}=\mp\dfrac{1}{\sqrt{2}}(\tau_1\pm i\tau_2), & T=1,\ M_T=\pm1\ .\end{cases} \tag{4.96}$$

While we need only the $M_T=0$ operators in considering electromagnetic interactions with nuclei, in fact it is little extra work to extend the analysis to include $M_T=\pm1$ pieces, which occur, for example, when considering the charge-changing weak interaction (O'Connell *et al.*, 1972; Walecka, 1975; Donnelly and Peccei, 1979). The form factors in Eq. (4.95) may be rewritten in terms of isoscalar and isovector single-nucleon form factors, $F_{1,2}^{(T)}(q_\mu^2), T=0,1$:

$$F_{1,2}=F_{1,2}^{(0)}I_0^0+F_{1,2}^{(1)}I_1^0\ , \tag{4.97}$$

where

$$F_{1,2}^{(0)}=F_{1,2}^p+F_{1,2}^n\ , \tag{4.98a}$$

$$F_{1,2}^{(1)}=F_{1,2}^p-F_{1,2}^n\ . \tag{4.98b}$$

Instead of $F_2^{(T)}$, we shall in general use the combination

$$\mu^{(T)}\equiv F_1^{(T)}+2M_NF_2^{(T)}\ . \tag{4.99}$$

At zero four-momentum transfer we have

$$F_1^{(0)}(0)=F_1^{(1)}(0)=1\ , \tag{4.100}$$

since $F_1^p(0)=1$ and $F_1^n(0)=0$, the proton and neutron charges, respectively, and

$$\mu^{(0)}(0)=\mu^p+\mu^n=0.8798\ , \tag{4.101a}$$

$$\mu^{(1)}(0)=\mu^p-\mu^n=4.7059\ , \tag{4.101b}$$

the isoscalar and isovector single-nucleon magnetic moments, respectively. The q_μ^2 dependences of the four basic single-nucleon form factors are in general different; however, for simplicity in dealing with complex nuclei at moderate momentum transfers we shall frequently take as an approximation an overall universal dependence,

$$f_N(q_\mu^2)=[1+q_\mu^2/(855\ \text{MeV})^2]^{-2}\ , \tag{4.102}$$

although this is not a necessary assumption. (For better parametrizations see Gourdin, 1974.) Naturally, in making comparisons with experimental data better parametrizations of the single-nucleon electromagnetic form factors are used, including the neutron electric form factor. This inclusion, for example, is especially important in the convection current contributions for odd-neutron nuclei and can amount to a few percent change in the form factors.

To make contact with the usual nonrelativistic descriptions of the nuclear many-body problem we next reduce the spinor matrix element in Eq. (4.94) through order $p^2/M_N^2\approx(v/c)^2_{\text{nucleon}}$. To do this we write the four-component nucleon spinors in the form

$$u(\mathbf{p},m_s)=\left[\frac{E_p+M_N}{2E_p}\right]^{1/2}\begin{bmatrix}\chi_{1/2}^{m_s}\\ \left[\dfrac{\boldsymbol{\sigma}\cdot\mathbf{p}}{E_p+M_N}\right]\chi_{1/2}^{m_s}\end{bmatrix}\ , \tag{4.103}$$

where $E_p=(p^2+M_N^2)^{1/2}$ is the nucleon's energy and where $\chi_{1/2}^{m_s}$ is an ordinary two-component Pauli spinor [$\chi_{1/2}^{+1/2}=\binom{1}{0}, \chi_{1/2}^{-1/2}=\binom{0}{1}$], as used in Sec. IV.A. Substituting into Eq. (4.94), using the explicit forms for the γ matrices, and keeping terms to order M_N^{-2}, we find the resulting single-nucleon current to be (McVoy and Van Hove, 1962; de Forest and Walecka, 1966; Donnelly and Walecka, 1975)

$$\langle\mathbf{p}'m_s'm_t'\,|\,J_\mu(0)\,|\,\mathbf{p}m_sm_t\rangle = \chi_{1/2}^{m_s'\dagger}\xi_{1/2}^{m_t'\dagger}(\mathscr{M}_\mu^{(0)}I_0^0+\mathscr{M}_\mu^{(1)}I_1^0)\xi_{1/2}^{m_t}\chi_{1/2}^{m_s}\ , \tag{4.104}$$

where $\mathscr{M}_\mu^{(T)}=(\boldsymbol{\mathscr{M}}^{(T)},\mathscr{M}_0^{(T)})$, $T=0,1$ and we have

$$\mathscr{M}_0^{(T)}=F_1^{(T)}+[q_\mu^2/8M_N^2+i\mathbf{q}\cdot(\boldsymbol{\sigma}\times\mathbf{q})/4M_N^2](F_1^{(T)}-2\mu^{(T)}), \tag{4.105a}$$

$$\boldsymbol{\mathscr{M}}^{(T)}=[(\mathbf{p}+\mathbf{p}')/2M_N]F_1^{(T)}+(i\boldsymbol{\sigma}\times\mathbf{q}/2M_N)\mu^{(T)}\ . \tag{4.105b}$$

In arriving at these results we have assumed that $F_2^{(T)}$ is already of $O(M_N^{-1})$ and that $q_0=\omega$, which for a free nucleon is $q_0=(p'^2-p^2)/2M_N=(q^2+2\mathbf{p}\cdot\mathbf{q})/2M_N$, is also of $O(M_N^{-1})$. Thus q_0 does not appear above. In addition to the leading term of $O(M_N^0)$, Eq. (4.105a) contains corrections of $O(M_N^{-2})$. These are the well-known Darwin-Foldy and spin-orbit terms. The three-vector part of the current in Eq. (4.105b), on the other hand, contains no terms of $O(M_N^{-2})$. Let us ignore the $O(M_N^{-2})$ terms in Eq. (4.105a) and assume that an overall universal single-nucleon form factor $f_N(q_\mu^2)$ [Eq. (4.102)] has been extracted to represent all of the q_μ^2 dependence in these currents (these are not necessary assumptions; rather they are made to help clarify the analysis). Then it follows from these results that the appropriate single-particle nuclear densities to be considered in first quantization are[6]

[6]We shall hereafter omit the (1) to indicate single-particle or one-body operators; in the rest of this section they are assumed always to be so.

$$\rho(\mathbf{x})=\sum_{i=1}^{A}[I_0^0(i)+I_1^0(i)]\delta(\mathbf{x}-\mathbf{x}_i)\ , \tag{4.106a}$$

$$\mathbf{J}_c(\mathbf{x})=\sum_{i=1}^{A}[I_0^0(i)+I_1^0(i)]\left[\delta(\mathbf{x}-\mathbf{x}_i)\left[-\frac{i}{M_N}\boldsymbol{\nabla}^{(i)}\right]\right]_{\text{sym}}\ , \tag{4.106b}$$

$$\boldsymbol{\mu}(\mathbf{x})=\sum_{i=1}^{A}[\mu^{(0)}(0)I_0^0(i)+\mu^{(1)}(0)I_1^0(i)]\delta(\mathbf{x}-\mathbf{x}_i)\frac{1}{2M_N}\boldsymbol{\sigma}^{(i)}\ . \tag{4.106c}$$

Note that, having removed the single-nucleon q_μ^2 dependence, which takes into account the finite size of the nucleon, as an overall factor, we are left in Eqs. (4.106) effectively with point nucleons to consider. Furthermore, at this juncture we mention another effect which we shall treat throughout this paper in a rather simplified way without detailed elaboration, viz., center-of-mass corrections. The use of shell-model degrees of freedom involves many-body wave functions specified by $3A$ coordinates $\mathbf{x}_i$. In fact three of these, $\mathbf{R}\equiv\sum_i\mathbf{x}_i/A$, are just the coordinates of the center of mass and do not reflect true (internal) nuclear structure. In general, the problem cannot be separated into internal and center-of-mass dependence, but for a few special cases it can. One in particular is the shell-model problem using harmonic-oscillator wave functions as a single-particle basis on which to build the many-body wave functions. In that case the problem is separable, and it can be shown that the calculated shell-model form factors for any nonspurious ground state should be multiplied by a center-of-mass correction $f_{\text{c.m.}}(q)=\exp(y/A)$ where $y\equiv(bq/2)^2$ and b is the oscillator parameter (Tassie and Barker, 1958; see also de Forest and Walecka, 1966). We shall assume that this is done in all of the following examples.

We are now in a position to bring into play the developments thus far to obtain the requisite single-particle multipole matrix elements. First the isospin dependence is all displayed in Eqs. (4.106) and can be handled immediately. Let us write the isospin dependence of a general single-particle operator [e.g., one of those in Eqs. (4.106)] in the form

$$T^{(1)}_{TM_T}(\mathbf{x})=\sum_{i=1}^{A}T^{(1)}_{(T)}(\mathbf{x};\mathbf{x}_i)I_T^{M_T}(i)\ , \tag{4.107}$$

where the subscript (T) is to remind us that, while the explicit isospin operator dependence is in the factors $I_T^{M_T}(i)$, the remaining space-spin dependence may be different for isoscalar and isovector contributions. Since the isospin reduction is simply

$$\langle\tfrac{1}{2}||I_T||\tfrac{1}{2}\rangle=[T]/\sqrt{2}\ , \tag{4.108}$$

we have

$$\langle a'::T^{(1)}_{J;T}(q)::a\rangle=\frac{[T]}{\sqrt{2}}\langle n'l'j'||T^{(1)}_{J;(T)}(q)||nlj\rangle\ , \tag{4.109}$$

where only matrix elements reduced in angular momentum remain to be considered.

With the remaining space-spin dependence $\sim(1,\ \boldsymbol{\nabla},$ or $\boldsymbol{\sigma})\times\delta(\mathbf{x}-\mathbf{x}_i)$ in Eqs. (4.106) we need to make the multipole projections discussed above [Eqs. (4.24), (4.34), and (4.35)]. This leads us to define the following five single-particle multipole operators (O'Connell *et al.*, 1972; Donnelly and Peccei, 1979; Donnelly and Haxton, 1979, 1980):

$$M_J^{M_J}(q\mathbf{x}), \tag{4.110a}$$

$$\Delta_J^{M_J}(q\mathbf{x})\equiv\mathbf{M}_{JJ}^{M_J}(q\mathbf{x})\cdot\frac{1}{q}\boldsymbol{\nabla}\ , \tag{4.110b}$$

$$\Delta'_J{}^{M_J}(q\mathbf{x})\equiv-i\left[\frac{1}{q}\boldsymbol{\nabla}\times\mathbf{M}_{JJ}^{M_J}(q\mathbf{x})\right]\cdot\frac{1}{q}\boldsymbol{\nabla}\ , \tag{4.110c}$$

$$\boldsymbol{\Sigma}_J^{M_J}(q\mathbf{x})\equiv\mathbf{M}_{JJ}^{M_J}(q\mathbf{x})\cdot\boldsymbol{\sigma}\ , \tag{4.110d}$$

$$\boldsymbol{\Sigma}'_J{}^{M_J}(q\mathbf{x})\equiv-i\left[\frac{1}{q}\boldsymbol{\nabla}\times\mathbf{M}_{JJ}^{M_J}(q\mathbf{x})\right]\cdot\boldsymbol{\sigma}\ , \tag{4.110e}$$

where Eq. (4.110a) is defined in Eq. (4.25). The curl terms may be rewritten using Eq. (4.30), so that projections $\mathbf{M}_{JJ\pm1}^{M_J}$ occur for Δ' and for Σ'. For completeness let us note that two other multipole operators also enter when a similar analysis is made for the entire electroweak interaction (O'Connell *et al.*, 1972; Donnelly and Peccei, 1979; Donnelly and Haxton, 1979, 1980):

$$\boldsymbol{\Sigma}''{}_J^{M_J}(q\mathbf{x})\equiv\left[\frac{1}{q}\boldsymbol{\nabla}M_J^{M_J}(q\mathbf{x})\right]\cdot\boldsymbol{\sigma}\ , \tag{4.110f}$$

$$\Omega_J^{M_J}(q\mathbf{x})\equiv M_J^{M_J}(q\mathbf{x})\boldsymbol{\sigma}\cdot\frac{1}{q}\boldsymbol{\nabla}\ . \tag{4.110g}$$

The gradient term [Eq. (4.110f)] may be reexpressed using Eq. (4.58). The isoscalar and isovector single-particle electromagnetic multipole operators may then be written in terms of these basic operators:

$$M^{\text{Coul}}_{JM_J;TM_T}(q\mathbf{x})=F_1^{(T)}(0)M_J^{M_J}(q\mathbf{x})I_T^{M_T}\ , \tag{4.111a}$$

$$T^{\text{el}}_{JM_J;TM_T}(q\mathbf{x})=\frac{q}{M_N}[F_1^{(T)}(0)\Delta'_J{}^{M_J}(q\mathbf{x})+\tfrac{1}{2}\mu^{(T)}(0)\boldsymbol{\Sigma}_J^{M_J}(q\mathbf{x})]I_T^{M_T}\ , \tag{4.111b}$$

$$iT^{\text{mag}}_{JM_J;TM_T}(q\mathbf{x})=\frac{q}{M_N}[F_1^{(T)}(0)\Delta_J^{M_J}(q\mathbf{x})-\tfrac{1}{2}\mu^{(T)}(0)\boldsymbol{\Sigma}'_J{}^{M_J}(q\mathbf{x})]I_T^{M_T}\ . \tag{4.111c}$$

[The axial-vector current multipole operators which occur when considering the weak interaction are discussed by O'Connell *et al.* (1972), Donnelly and Peccei (1979), and Donnelly and Haxton (1979,1980).]

General expressions and tables of these single-particle matrix elements have been made available by Donnelly and Haxton (1979,1980). Here we shall restrict our attention to elastic scattering, and so must deal only with M, Δ, and Σ'. In Donnelly and Haxton (1980) the single-particle matrix elements we require are written

$$(4\pi)^{1/2}\langle n'l'j'||M_J(q\mathbf{x})||nlj\rangle = A_J(l'j';lj)\langle n'l'j' \mid j_J(\rho) \mid nlj\rangle \ , \tag{4.112a}$$

$$(4\pi)^{1/2}\langle n'l'j'||\Delta_J(q\mathbf{x})||nlj\rangle = B_J(l'j';lj)\left\langle n'l'j' \left| \frac{1}{\rho} j_J(\rho) \right| nlj \right\rangle$$

$$= [J]^{-2} B_J(l'j';lj)[\langle n'l'j' \mid j_{J+1}(\rho) \mid nlj\rangle + \langle n'l'j' \mid j_{J-1}(\rho) \mid nlj\rangle] \ , \tag{4.112b}$$

$$(4\pi)^{1/2}\langle n'l'j'||\Sigma'_J(q\mathbf{x})||nlj\rangle = -J^{1/2} D_J^+(l'j';lj)\langle n'l'j' \mid j_{J+1}(\rho) \mid nlj\rangle + (J+1)^{1/2} D_J^-(l'j';lj)\langle n'l'j' \mid j_{J-1}(\rho) \mid nlj\rangle \ , \tag{4.112c}$$

where $\rho \equiv qx$ and where the radial matrix elements of the spherical Bessel functions,

$$\langle n'l'j' \mid j_L(\rho) \mid nlj\rangle = \int_0^\infty x^2 dx \, R^*_{n'l'j'}(x) j_L(qx) R_{nlj}(x) \ , \tag{4.113}$$

with $L = J$ for Coulomb multipoles and $L = J \pm 1$ for magnetic multipoles, have been left quite general—arbitrary single-particle radial functions labeled by nlj may be used here. The coefficients A_J, B_J, and $D_J^\pm$ may be written explicitly in terms of 3-j, 6-j, and 9-j symbols (Donnelly and Haxton, 1979; see also de Forest and Walecka, 1966):

$$A_J(l'j';lj) = (-)^J(-)^{j+1/2}[l'][l][j'][j][J] \begin{Bmatrix} l' & j' & \frac{1}{2} \\ j & l & J \end{Bmatrix} \begin{bmatrix} l' & l & J \\ 0 & 0 & 0 \end{bmatrix} \ , \tag{4.114a}$$

$$B_J(l'j';lj) = (-)^{J+1}(-)^{j+1/2}[l'][l][j'][j][J] \begin{Bmatrix} l' & j' & \frac{1}{2} \\ j & l & J \end{Bmatrix} \begin{bmatrix} l' & l & J-1 \\ 0 & 0 & 0 \end{bmatrix} \left[\frac{\{(l'+l+1)^2 - J^2\}\{J^2 - (l'-l)^2\}}{4J(J+1)} \right]^{1/2} \ , \tag{4.114b}$$

$$D_J^\pm(l'j';lj) = (-)^{l'}\sqrt{6}[l'][l][j'][j][J\pm 1] \begin{Bmatrix} l' & l & J\pm 1 \\ \frac{1}{2} & \frac{1}{2} & 1 \\ j' & j & J \end{Bmatrix} \begin{bmatrix} l' & l & J\pm 1 \\ 0 & 0 & 0 \end{bmatrix} . \tag{4.114c}$$

Several constraints on these coefficients may be deduced immediately. We summarize below the allowed values of the angular momentum quantum numbers for which in elastic electron scattering the coefficients may be nonzero:

$$J \geq 0, \text{ even for } A_J \ , \tag{4.115a}$$

$$J \geq 1, \text{ odd for } B_J \text{ and } D_J^\pm \ , \tag{4.115b}$$

$$l'+l = \text{even for } A_J, B_J, \text{ and } D_J^\pm \ , \tag{4.115c}$$

$$|j'-j| \leq J \leq j'+j \text{ for } A_J, B_J, \text{ and } D_J^\pm \ , \tag{4.115d}$$

$$|l'-l| \leq J \leq l'+l \text{ for } A_J \ , \tag{4.115e}$$

$$|l'-l|+1 \leq J \leq l'+l-1 \text{ for } B_J \ , \tag{4.115f}$$

$$|l'-l|-1 \leq J \leq l'+l-1 \text{ for } D_J^+ \ , \tag{4.115g}$$

$$|l'-l|+1 \leq J \leq l'+l+1 \text{ for } D_J^- \ . \tag{4.115h}$$

Of course the above conditions all must be satisfied simultaneously. Under interchange of primed and unprimed arguments, a common phase factor occurs for A_J, B_J, and $D_J^\pm$:

$$l'j' \leftrightarrow lj \Longrightarrow (-)^{j'-j} \ . \tag{4.116}$$

Since the radial matrix elements in Eq. (4.113) are symmetrical under this interchange, this implies that the overall single-particle matrix elements in Eqs. (4.112) also have the same phase relationship (Donnelly and Haxton, 1979,1980),

$$\langle nlj||T_J(q\mathbf{x})||n'l'j'\rangle = (-)^{j'-j}\langle n'l'j'||T_J(q\mathbf{x})||nlj\rangle \tag{4.117}$$

for $T_J = M_J$, Δ_J, and Σ'_J.

Note that when $l = 0$ and $j = \frac{1}{2}$ we have

$$l' = J \text{ for } A_J \ , \tag{4.118a}$$

$$B_J = 0 \ , \tag{4.118b}$$

for $j' = l' + \frac{1}{2}$

$$l' = J-1 \text{ for } D_J^- \text{ and } D_J^+ = 0 \tag{4.118c}$$

for $j' = l' - \frac{1}{2}$

$$l' = J+1 \text{ for } D_J^+ \text{ and } D_J^- = 0 \ . \tag{4.118d}$$

Similarly, the case where $l' = 0$ and $j' = \frac{1}{2}$ can be obtained from this by using the turnaround relations in Eq. (4.116).

Two cases that will be of special interest later may be obtained in simple form. First, for the Coulomb monopole ($C0$) we require

$$A_0(l'j';lj) = \delta_{l'l}\delta_{j'j}[j] \ . \tag{4.119}$$

Second, for the magnetic dipole ($M1$) we require

$$B_1(l'j';lj)=-\sqrt{3}\delta_{l'l}\frac{\sqrt{l(l+1)}}{[l]}\times\begin{cases}\sqrt{l}\,[l+1], & j'=j=l+\frac{1}{2}\\ 1, & j'=l+\frac{1}{2},\ j=l-\frac{1}{2}\\ -1, & j'=l-\frac{1}{2},\ j=l+\frac{1}{2}\\ \sqrt{l+1}[l-1], & j'=j=l-\frac{1}{2}\ ,\end{cases} \tag{4.120}$$

$$D_1^-(l'j';lj)=\sqrt{2/3}\delta_{l'l}\frac{1}{[l]}\times\begin{cases}\sqrt{l+1}[l+1], & j'=j=l+\frac{1}{2}\\ -2\sqrt{l(l+1)}, & j'=l+\frac{1}{2},\ j=l-\frac{1}{2}\\ +2\sqrt{l(l+1)}, & j'=l-\frac{1}{2},\ j=l+\frac{1}{2}\\ -\sqrt{l}\,[l-1], & j'=j=l-\frac{1}{2}\ .\end{cases} \tag{4.121}$$

In addition, there are coefficients $D_1^+(l'j';lj)$ which may be evaluated, although some of them yield more complicated expressions than those above. We shall not require these D_1^+ cases except when specific values of $l'j'$ and lj are known, and under those circumstances the tables of Donnelly and Haxton (1979,1980) may be employed (see below). It is worth noting in passing, however, that some of these coefficients may simply be obtained from the D_J^- results using (Donnelly and Haxton, 1980)

$$\begin{aligned}&(J+1)^{1/2}[\eta_{j'l'}+\eta_{jl}-(J+2)]D_J^+(l'j';lj)\\ &\quad=J^{1/2}[\eta_{j'l'}+\eta_{jl}+(J+1)]D_J^-(l'j';lj)\ ,\end{aligned} \tag{4.122}$$

where

$$\eta_{jl}=\begin{cases}-l, & j=l+\frac{1}{2}\\ l+1, & j=l-\frac{1}{2}\ .\end{cases} \tag{4.123}$$

C. One-body density-matrix elements

Having dealt with the single-particle matrix elements required for descriptions of elastic electron scattering in the preceding section, we turn now to a discussion of the many-body content in the nuclear matrix elements, namely, the one-body density-matrix elements defined in Eqs. (4.85) and (4.87) and rewritten here for elastic matrix elements:[7]

$$\psi_{J;T}(a'a)=\frac{1}{[J][T]}\langle J_0;T_0::[c_{a'}^\dagger\otimes\tilde{c}_a]_{J;T}::J_0;T_0\rangle\ . \tag{4.124}$$

With the phase conventions chosen here it may be shown that the density-matrix elements are real (Donnelly and Walecka, 1975). This further implies for the matrix elements that

$$\psi_{J;T}(aa')=(-)^{j'-j}\psi_{J;T}(a'a)\ . \tag{4.125}$$

Since the same phase enters when the single-particle matrix elements are turned around [Eq. (4.117)], effectively we need consider only one order for the quantum numbers $a'a$ and use symmetrized one-body density-matrix elements, indicated by curly brackets:

$$\psi_{J;T}\{a'a\}\equiv\begin{cases}\psi_{J;T}(a^2), & a'=a\\ 2\psi_{J;T}(a'a), & a'\neq a\ .\end{cases} \tag{4.126}$$

Several special constraints on the ground-state density matrix may be derived by considering the basic one-body operator matrix element equation [Eq. (4.86)]:

$$\begin{aligned}&\langle J_0;T_0::\hat{T}_{J;T}(q)::J_0;T_0\rangle\\ &\quad=\sum_{a'a}\langle a'::T_{J;T}(q)::a\rangle\psi_{J;T}(a'a)\\ &\quad=\sum_{a'\geq a}\langle a'::T_{J;T}(q)::a\rangle\psi_{J;T}\{a'a\}\ ,\end{aligned} \tag{4.127}$$

where in the latter form we use the symmetrized one-body density-matrix elements and indicate by $\sum_{a'\geq a}$ that only one ordering[8] (say, by single-particle energies) of $a'a$ is to be considered here. The ground state has been assumed to be an eigenstate of the total nucleon number operator $\hat{A}$, of the z component of isospin $\hat{T}_z$ (i.e., equivalently, of the charge and neutron number operators, $\hat{Z}$ and $\hat{N}$, respectively) and of the z component of angular momentum $\hat{J}_z$. Inserting these in succession for the one-body operator $\hat{T}_{J;T}$, with $J=T=0$ for $\hat{A}$, $J=0$, $T=1$ and $\hat{T}_z$, and $J=1$, $T=0$ for J_z, and using the known single-particle matrix elements in each case, we obtain three identities involving the diagonal matrix elements:

$$\sum_a[j]\psi_{0;0}\{a^2\}=\frac{1}{\sqrt{2}}[J_0][T_0]A\ , \tag{4.128a}$$

[7] We shall suppress the labels (12) on the ψ's, since only the ground state is involved here.

[8] One choice for this ordering is suggested by Donnelly and Haxton (1979), but any consistent convention will suffice.

$$\sum_a [j]\psi_{0;1}\{a^2\} = \sqrt{2/3}[J_0][T_0][T_0(T_0+1)]^{1/2} , \quad (4.128b)$$

$$\sum_a \sqrt{j(j+1)}[j]\psi_{1;0}\{a^2\} = \frac{1}{\sqrt{2}}[J_0(J_0+1)]^{1/2}[J_0][T_0] . \quad (4.128c)$$

These were obtained previously (Donnelly and Walecka, 1976) for the special case of $T_0 = \frac{1}{2}$ [also compare Eqs. (4.47) above].

Now let us return to the elastic electron scattering form factors defined in Eq. (4.46). These may be recast in terms of integrals containing products of spherical Bessel functions and specific proton or neutron coordinate space multipole densities (denoted by $m_t = \pm\frac{1}{2}$ as usual). We obtain

$$\mathcal{F}_J(q) = \begin{cases} \int_0^\infty r^2 dr\, j_J(qr)\rho_J(r)_{+1/2}, & J = \text{even} \\ \dfrac{q}{M_N}\int_0^\infty r^2 dr \left[\dfrac{1}{qr} j_J(qr)\alpha_J(r)_{+1/2} + \dfrac{1}{2}\displaystyle\sum_{m_t=\pm 1/2} [j_{J+1}(qr)\beta_J^+(r)_{m_t} + j_{J-1}(qr)\beta_J^-(r)_{m_t}] \right], & J = \text{odd} , \end{cases} \quad (4.129)$$

(4.130)

where

$$\rho_J(r)_{m_t} \equiv \sum_{a'a} A_J(l'j';lj)\psi_J(a'a)_{m_t}\rho_{a'a}(r)_{m_t}/[J_0] , \quad (4.131a)$$

$$\alpha_J(r)_{m_t} \equiv -\sum_{a'a} B_J(l'j';lj)\psi_J(a'a)_{m_t}\rho_{a'a}(r)_{m_t}/[J_0] , \quad (4.131b)$$

$$\beta_J^+(r)_{m_t} \equiv -\sqrt{J}\,(\delta_{m_t,+1/2}\mu^p + \delta_{m_t,-1/2}\mu^n)\sum_{a'a} D_J^+(l'j';lj)\psi_J(a'a)_{m_t}\rho_{a'a}(r)_{m_t}/[J_0] , \quad (4.131c)$$

$$\beta_J^-(r)_{m_t} \equiv \sqrt{J+1}\,(\delta_{m_t,+1/2}\mu^p + \delta_{m_t,-1/2}\mu^n)\sum_{a'a} D_J^-(l'j';lj)\psi_J(a'a)_{m_t}\rho_{a'a}(r)_{m_t}/[J_0] , \quad (4.131d)$$

with

$$\rho_{a'a}(r)_{m_t} \equiv R^*_{n'l'j';m_t}(r)R_{nlj;m_t}(r) \quad (4.132)$$

and

$$\psi_J(a'a)_{m_t} \equiv \frac{1}{\sqrt{2}[T_0]}\left[\psi_{J;0}(a'a) + \frac{2\sqrt{3}m_t M_{T_0}}{[T_0(T_0+1)]^{1/2}}\psi_{J;1}(a'a)\right] . \quad (4.133)$$

In obtaining these expressions we have defined linear combinations of the basic one-body density-matrix elements in Eq. (4.133), where specific mixtures of the isoscalar and isovector pieces occur. Note that if $+M_{T_0} \to -M_{T_0}$, then $\psi_J(a'a)_{m_t} \to \psi_J(a'a)_{-m_t}$; i.e., the proton density matrix for $+M_{T_0}$ is equal to the neutron density matrix for $-M_{T_0}$. In Eqs. (4.131) we have defined proton (charge) and neutron multipole densities ρ_J, convection-current multipole densities α_J, and two contributions to magnetization-current multipole densities $\beta_J^\pm$. These involve the coefficients A_J, B_J, and $D_J^\pm$, which were discussed in the preceding section. Finally the elementary densities $\rho_{a'a}(r)_{m_t}$ defined in Eq. (4.132) enter into these expressions weighted with the nuclear structure factors. Any radial wave function can be used here. Of course, for special analytic forms such as harmonic-oscillator wave functions, the results given here may be simplified. General expressions and tables of single-particle harmonic-oscillator matrix elements are available (Donnelly and Haxton, 1979).

In passing, let us mention the long-wavelength limit for the $J = 1$ case, where, by Eq. (4.63), we have an expression for the magnetic moment of the ground state:

$$\mu = \frac{1}{[J_0]}\left[\frac{2J_0}{J_0+1}\right]^{1/2}\sum_{a'a}\delta_{n'n}\left[-\frac{1}{\sqrt{3}}B_1(l'j';lj)\psi_1(a'a)_{+1/2} + \sqrt{3/2}D_1^-(l'j';lj)[\mu^p\psi_1(a'a)_{+1/2} + \mu^n\psi_1(a'a)_{-1/2}]\right] , \quad (4.134a)$$

where explicit results were given in Eqs. (4.120) and (4.121) for the coefficients B_1 and D_1^-. To obtain this result we have used the fact that

$$\int_0^\infty r^2 dr\, j_J(qr)\rho_{a'a}(r)_{m_t} \underset{\text{LWL}}{\to} \delta_{J0}\delta_{n'n} . \quad (4.134b)$$

Thus for a given ground state having $J_0 \geq \frac{1}{2}$, where the dipole moment is known, we have another relationship involving

one-body density-matrix elements to be considered together with the three basic identities discussed above [Eqs. (4.128)]. This magnetic dipole momentum identity was obtained previously (Donnelly and Walecka, 1976) for the special case of $T_0=\frac{1}{2}$.

It is also possible to define a magnetic radius in analogy with the familiar charge radius that comes from elastic charge scattering. Following the form found in the latter case (see Überall, 1971) and using the above results for the magnetic moment, let us write

$$\mathscr{F}_1(q)\underset{\text{LWL}}{\rightarrow}\sqrt{2/3}\left[\frac{J_0+1}{J_0}\right]^{1/2}\left[\frac{q}{2M_N}\right]\mu[1-\tfrac{1}{6}q^2\langle r^2\rangle_{\text{mag}}+O(q^4)]\ . \tag{4.135a}$$

Then the basic expressions in Eqs. (4.130)—(4.133) allow us to write for the square of the magnetic radius

$$\langle r^2\rangle_{\text{mag}}=\frac{1}{\mu}\left[\frac{6J_0}{J_0+1}\right]^{1/2}\int_0^\infty r^4dr\left[\tfrac{1}{5}\alpha_1(r)_{+1/2}+\sum_{m_t=\pm1/2}[\tfrac{1}{2}\beta_1^-(r)_{m_t}-\tfrac{1}{5}\beta_1^+(r)_{m_t}]\right]\ . \tag{4.135b}$$

This contains contributions from integrals containing both j_0 and j_2 spherical Bessel functions. Magnetic radii are discussed in more detail and collected together in the compilation of de Jager *et al.* (1974). In passing we note that complementary information on $M1$ moments and radii can be obtained from hyperfine splittings of energy levels of muonic atoms (Hüfner *et al.*, 1977).

Another special low-q result involving the one-body density-matrix elements may be obtained for the special case of $T_0=\frac{1}{2}$ (Donnelly and Walecka, 1976). Then the ground state of interest is a member of an isospin mirror pair. In this situation there will also be a β decay from one member of the isospin doublet to the other. Since we consider the nuclear states to be eigenstates of isospin and have cast the formalism in terms of matrix elements reduced in isospin as well as angular momentum, it is straightforward to incorporate semileptonic weak interactions into the present electromagnetic analysis (O'Connell *et al.*, 1972; Walecka, 1975; Donnelly and Peccei, 1979). Here we shall not discuss this general analysis, but rather quote only the results for the mirror β decay. From Donnelly and Walecka (1976) we have for the β-decay rate

$$\omega_{\beta^\pm}=\frac{G^2}{2\pi^3}\int_{m_e}^{W_0^\pm}\beta\varepsilon^2(W_0^\pm-\varepsilon)^2F^\pm(Z,\varepsilon)d\varepsilon\left[1+\frac{4\pi}{[J_0]^2}\langle J_0;T_0=\tfrac{1}{2}::i\hat{T}^{\text{el}_5}_{1;1}(0)::J_0;T_0=\tfrac{1}{2}\rangle^2\right]\ . \tag{4.136}$$

Here G is the Fermi weak-interaction coupling constant, $GM_p^2=1.023\times10^{-5}$, with M_p the proton mass. $W_0^\pm$ is the maximum electron energy, and the integral over the electron energy ε extends from m_e to $W_0^\pm$. The integrand contains the factors $\beta=[1-(m_e/\varepsilon)^2]^{1/2}$ and $F^\pm(Z,\varepsilon)$, where the latter accounts for the distortion of the electron in the Coulomb field of the daughter nucleus (see Donnelly and Walecka, 1976, for an approximation for this Coulomb factor). We have assumed that the momentum transfer in such mirror β decays is so low that the nuclear matrix elements may be taken from under the integral and evaluated at $q=0$. The factor 1 in Eq. (4.136) accounts for the Fermi contribution, whereas the term involving the axial-vector multipole operator $-i\hat{T}^{\text{el}_5}_{1;1}$ accounts for the Gamow-Teller contribution (Donnelly and Walecka, 1976). This in turn simply involves the same magnetization-current Σ_1' discussed above, now multiplied by the axial-vector coupling constant $F_A^{(1)}(0)=-1.23$ instead of vector couplings as before. Specifically, we have

$$4\pi\langle J_0;T_0=\tfrac{1}{2}::i\hat{T}^{\text{el}_5}_{1;1}(0)::J_0;T_0=\tfrac{1}{2}\rangle^2=3\left[F_A^{(1)}(0)\sum_{a'a}\delta_{n'n}D_1^-(l'j';lj)\psi_{1;1}(a'a)\right]^2\ , \tag{4.137}$$

where once again the coefficient D_1^- is given in Eq. (4.121). Thus, given the β-decay rate in such a $T_0=\frac{1}{2}$ case, we obtain yet another relationship involving one-body density-matrix elements.

At this point it is perhaps useful to discuss some simple examples of the one-body density-matrix elements. Let us begin with a closed-shell 0^+0 $N=Z$ configuration to define the Fermi surface and add or subtract a single particle to form one-particle ($1p$) or one-hole ($1h$) states, respectively. Indicating the closed shell by $|\tilde{0}\rangle$, we have

$$|\,1p:J_0M_{J_0};T_0M_{T_0}\rangle=a^\dagger_{\alpha_p}|\,\tilde{0}\rangle\ , \tag{4.138a}$$

$$|\,1h:J_0M_{J_0};T_0M_{T_0}\rangle=b^\dagger_{\alpha_h}|\,\tilde{0}\rangle\ , \tag{4.138b}$$

where $\{\alpha_p\}=\{n_pl_pj_p,m_{jp};\frac{1}{2},m_{tp}\}$ with $\varepsilon_p>\varepsilon_F$ and $\{\alpha_h\}=\{n_hl_hj_h,m_{jh}:\frac{1}{2},m_{th}\}$ with $\varepsilon_h\le\varepsilon_F$. For a $1p$ state we must have $J_0=j_p$, $M_{J_0}=m_{jp}$, $T_0=\frac{1}{2}$, and $M_{T_0}=m_{tp}$, whereas for the $1h$ state we must have $J_0=j_h$, $M_{J_0}=m_{jh}$, $T_0=\frac{1}{2}$, and $M_{T_0}=m_{th}$. To obtain the one-body density-matrix elements using Eq. (4.124), we evaluate the matrix elements

$$\left\langle\begin{bmatrix}1p\\1h\end{bmatrix}:J_0M_{J_0};T_0M_{T_0}\middle|[c^\dagger_{a'}\otimes\tilde{c}_a]^{0;0}_{J;T}\middle|\begin{bmatrix}1p\\1h\end{bmatrix}:J_0M_{J_0};T_0M_{T_0}\right\rangle=\left\langle\tilde{0}\middle|\begin{bmatrix}a_{\alpha_p}\\b_{\alpha_h}\end{bmatrix}[c^\dagger_{a'}\otimes\tilde{c}_a]^{0;0}_{J;T}\begin{bmatrix}a^\dagger_{\alpha_p}\\b^\dagger_{\alpha_h}\end{bmatrix}\middle|\tilde{0}\right\rangle \tag{4.139}$$

using the anticommutation relations for the a's and b's (Fetter and Walecka, 1971) and using the fact that

$$a_{\alpha_p}\,|\,\tilde{0}\rangle = b_{\alpha_h}\,|\,\tilde{0}\rangle = 0\ . \tag{4.140}$$

The Wigner-Eckart theorem and the general expression for the one-body density-matrix elements [Eq. (4.124)] then yield immediately

$$\psi^{1p}_{J;T}(a'a) = \delta_{a'a} \times \begin{cases} \delta_{aa_p}, & \varepsilon_a > \varepsilon_F \\ 2\delta_{J0}\delta_{T0}[j][J_0], & \varepsilon_a \le \varepsilon_F\ , \end{cases} \tag{4.141a}$$

$$\psi^{1h}_{J;T}(a'a) = \delta_{a'a} \times \begin{cases} 0, & \varepsilon_a > \varepsilon_F \\ 2\delta_{J0}\delta_{T0}[j][J_0] - (-)^{J+T}\delta_{aa_h}, & \varepsilon_a \le \varepsilon_F\ . \end{cases} \tag{4.141b}$$

Thus, for elastic magnetic electron scattering where J is odd (and so cannot be zero), we have

$$\psi^{1p}_{J;T}(a'a) = \delta_{a'a}\delta_{aa_p}\ ,$$
$$\psi^{1h}_{J;T}(a'a) = \pm\delta_{a'a}\delta_{aa_h}\ , \tag{4.142}$$

where the $+$ $(-)$ sign in the $1h$ case occurs for $T=0$ (1) density-matrix elements. Similar results hold for Coulomb scattering, with the $+$ $(-)$ sign in the $1h$ case now occurring when $T=1$ (0), except when $J=T=0$. Then the extra core terms in Eq. (4.141a) and (4.141b) enter (i.e., a term $2[j][J_0]$ for each nucleon below the Fermi surface). This leads immediately to the coherent Z^2 effect found for the Coulomb monopole cross section [see Eq. (4.48)].

These ideas may be generalized to the situation where a single particle or single hole is added to an $N>Z$ even-even core having closed neutron and proton shells. Let us denote the core by $|\,C\rangle$ and presume that it has N_c neutrons and Z_c protons giving angular momentum and isospin quantum numbers $J_c=M_{Jc}=0$, $T_c=-M_{Tc}=\frac{1}{2}(N_c-Z_c)$. By applying single-particle or single-hole creation operators to this core and ensuring that the resulting state has good angular momentum and isospin quantum numbers, we may obtain approximations to the odd-A ground states. Let us assume that the single particle or hole is added in a valence orbit characterized by the single-particle quantum numbers

$$a_V \rightarrow \{n_V l_V j_V; \tfrac{1}{2}\}\ .$$

Then we have

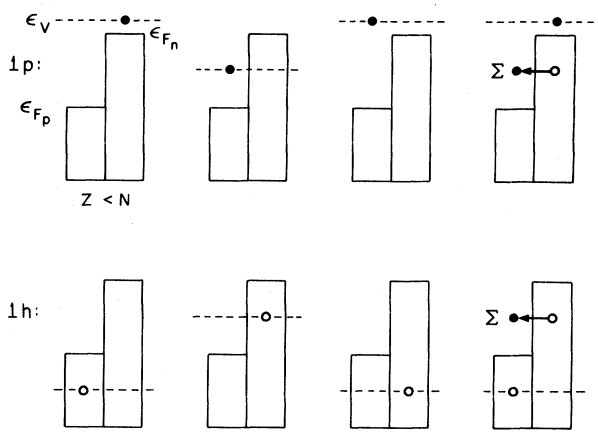

FIG. 6. Configurations contributing to one-particle and one-hole states built on an $N>Z$ closed-shell core.

$$|\,1p{:}J_0M_{J_0};T_0M_{T_0}\rangle = \begin{cases} a^\dagger_{a_V;m_{jV},-1/2}\,|\,C\rangle, & T_0=-M_{T_0}=T_c+\frac{1}{2},\ \varepsilon_V > \varepsilon_{F_n} \quad (4.143a) \\ a^\dagger_{a_V;m_{jV},+1/2}\,|\,C\rangle, & T_0=-M_{T_0}=T_c-\frac{1}{2},\ \varepsilon_{F_n} \ge \varepsilon_V > \varepsilon_{F_p} \quad (4.143b) \\ \left[\dfrac{2T_c}{2T_c+1}\right]^{1/2} a^\dagger_{a_V;m_{jV},+1/2}\,|\,C\rangle - \dfrac{1}{(2T_c+1)^{1/2}} a^\dagger_{a_V;m_{jV},-1/2}\,|\,C_+\rangle\ , \\ \qquad T_0=-M_{T_0}=T_c-\frac{1}{2},\ \varepsilon_V > \varepsilon_{F_n}\ , \quad (4.143c) \end{cases}$$

where the $\pm\frac{1}{2}$ refers to m_{tV} as before and where we have denoted the neutron and proton Fermi levels by ε_{F_n} and ε_{F_p}, respectively. We have defined the state

$$|\,C_+\rangle \equiv \frac{1}{(2T_c)^{1/2}}\hat{T}_+\,|\,C\rangle \tag{4.144}$$

by applying the isospin raising operator to the core state $|\,C\rangle$. In all cases we have $J_0=j_V$ and $M_{J_0}=m_{jV}$. Likewise when adding a single hole we have

$$|\,1h{:}J_0M_{J_0};T_0M_{T_0}\rangle = \begin{cases} b^\dagger_{a_V;m_{jV},-1/2}\,|\,C\rangle, & T_0=-M_{T_0}=T_c+\frac{1}{2},\ \varepsilon_{F_p} \ge \varepsilon_V \quad (4.145a) \\ b^\dagger_{a_V;m_{jV},+1/2}\,|\,C\rangle, & T_0=-M_{T_0}=T_c-\frac{1}{2},\ \varepsilon_{F_n} \ge \varepsilon_V > \varepsilon_{F_p} \quad (4.145b) \\ \left[\dfrac{2T_c}{2T_c+1}\right]^{1/2} b^\dagger_{a_V;m_{jV},+1/2}\,|\,C\rangle - \dfrac{1}{(2T_c+1)^{1/2}} b^\dagger_{a_V;m_{jV},-1/2}\,|\,C_+\rangle\ , \\ \qquad T_0=-M_{T_0}=T_c-\frac{1}{2},\ \varepsilon_{F_p} \ge \varepsilon_V\ . \quad (4.145c) \end{cases}$$

These configurations are indicated pictorially in Fig. 6. Once again using these states in the general definition [Eq. (4.124)], we obtain the one-body density-matrix elements. When $T_0=-M_{T_0}=T_c+\frac{1}{2}$ and $\varepsilon_V>\varepsilon_{F_n}$ we have

$$\psi^{1p}_{J;T}(a'a)=\delta_{a'a}K_T(T_0)\times\begin{cases}\delta_{aa_V}, & \varepsilon_a>\varepsilon_{F_n} & (4.146a)\\ \delta_{J0}[j][J_0], & \varepsilon_{F_n}\geq\varepsilon_a>\varepsilon_{F_p} & (4.146b)\\ 2\delta_{J0}\delta_{T0}[j][J_0], & \varepsilon_{F_p}\geq\varepsilon_a\ , & (4.146c)\end{cases}$$

where we have defined the function

$$K_T(T_0)\equiv(T_0+\tfrac{1}{2})^{1/2}\times\begin{cases}1, & T=0\\ \left[\dfrac{T_0+1}{3T_0}\right]^{1/2}, & T=1\ .\end{cases} \quad (4.147)$$

When $T_0=-M_{T_0}=T_c-\frac{1}{2}$ and $\varepsilon_{F_n}\geq\varepsilon_V>\varepsilon_{F_p}$ we have

$$\psi^{1p}_{J;T}(a'a)=\delta_{a'a}K_T(T_0)\times\begin{cases}0, & \varepsilon_a>\varepsilon_{F_n} & (4.148a)\\ (-)^T\delta_{aa_V}+\delta_{J0}[j][J_0], & \varepsilon_{F_n}\geq\varepsilon_a>\varepsilon_{F_p} & (4.148b)\\ 2\delta_{J0}\delta_{T0}[j][J_0], & \varepsilon_{F_p}\geq\varepsilon_a & (4.148c)\end{cases}$$

and finally, when $T_0=-M_{T_0}=T_c-\frac{1}{2}$ and $\varepsilon_V>\varepsilon_{F_n}$ we have

$$\psi^{1p}_{J;T}(a'a)=\delta_{a'a}K_T(T_0)\times\begin{cases}\left[\delta_{T0}-\dfrac{T_0}{T_0+1}\delta_{T1}\right]\delta_{aa_V}, & \varepsilon_a>\varepsilon_{F_n} & (4.149a)\\ \left[\delta_{T0}+\dfrac{T_0}{T_0+1}\left[\dfrac{2T_0+3}{2T_0+1}\right]\delta_{T1}\right]\delta_{J0}[j][J_0], & \varepsilon_{F_n}\geq\varepsilon_a>\varepsilon_{F_p} & (4.149b)\\ 2\delta_{J0}\delta_{T0}[j][J_0], & \varepsilon_{F_p}\geq\varepsilon_a\ . & (4.149c)\end{cases}$$

Specifically, for elastic magnetic electron scattering where J is odd (and so cannot be zero), we have

$$\psi^{1p}_{J;T}(a'a)=\delta_{a'a}\delta_{aa_V}K_T(T_0)\times\begin{cases}1, & T_0=-M_{T_0}=T_c+\frac{1}{2},\ \varepsilon_V>\varepsilon_{F_n}\\ (-)^T, & T_0=-M_{T_0}=T_c-\frac{1}{2},\ \varepsilon_{F_n}\geq\varepsilon_V>\varepsilon_{F_p}\ .\\ \delta_{T0}-\dfrac{T_0}{T_0+1}\delta_{T1}, & T_0=-M_{T_0}=T_c-\frac{1}{2},\ \varepsilon_V>\varepsilon_{F_n}\ .\end{cases} \quad (4.150)$$

Following the same procedures for the case where a single hole is added to the core, using the states in Eqs. (4.145), we obtain for the $T_0=-M_{T_0}=T_c+\frac{1}{2}$, $\varepsilon_{F_p}\geq\varepsilon_V$ configuration

$$\psi^{1h}_{J;T}(a'a)=\delta_{a'a}K_T(T_0)\times\begin{cases}\delta_{J0}[j][J_0], & \varepsilon_{F_n}\geq\varepsilon_a>\varepsilon_{F_p} & (4.151a)\\ 2\delta_{J0}\delta_{T0}[j][J_0]-(-)^{J+T}\delta_{aa_V}, & \varepsilon_{F_p}\geq\varepsilon_a & (4.151b)\end{cases}$$

and for the $T_0=-M_{T_0}=T_c-\frac{1}{2}$, $\varepsilon_{F_n}\geq\varepsilon_V>\varepsilon_{F_p}$ configuration

$$\psi^{1h}_{J;T}(a'a)=\delta_{a'a}K_T(T_0)\times\begin{cases}\delta_{J0}[j][J_0]-(-)^J\delta_{aa_V}, & \varepsilon_{F_n}\geq\varepsilon_a>\varepsilon_{F_p} & (4.152a)\\ 2\delta_{J0}\delta_{T0}[j][J_0], & \varepsilon_{F_p}\geq\varepsilon_a & (4.152b)\end{cases}$$

and finally for the $T_0=-M_{T_0}=T_c-\frac{1}{2}$, $\varepsilon_{F_p}\geq\varepsilon_V$ configuration

$$\psi^{1h}_{J;T}(a'a)=\delta_{a'a}K_T(T_0)\times\begin{cases}\left[\delta_{To}+\dfrac{T_0}{T_0+1}\left[\dfrac{2T_0+3}{2T_0+1}\right]\delta_{T1}\right]\delta_{J0}[j][J_0], & \epsilon_{F_n}\geq\varepsilon_a>\varepsilon_{F_p} \quad (4.153a)\\ 2\delta_{J0}\delta_{T0}[j][J_0]-(-)^{J+T}\left[\delta_{T0}-\dfrac{T_0}{T_0+1}\delta_{T1}\right]\delta_{aa_V}, & \varepsilon_{F_p}\geq\varepsilon_a\ . \quad (4.153b)\end{cases}$$

As above, for the specific situation of elastic magnetic electron scattering where J is odd (and so cannot be zero), we have

$$\psi^{1h}_{J;T}(a'a)=\delta_{a'a}\delta_{aa_V}K_T(T_0)\times\begin{cases}(-)^T, & T_0=-M_{T_0}=T_c+\frac{1}{2},\ \varepsilon_{F_p}\geq\varepsilon_V\\ 1, & T_0=-M_{T_0}=T_c-\frac{1}{2},\ \varepsilon_{F_n}\geq\varepsilon_V>\varepsilon_{F_p}\\ (-)^T\left[\delta_{T0}-\dfrac{T_0}{T_0+1}\delta_{T1}\right], & T_0=-M_{T_0}=T_c-\frac{1}{2},\ \varepsilon_{F_p}\geq\varepsilon_V\ .\end{cases} \quad (4.154)$$

Using the specific $1p$ and $1h$ results in Eqs. (4.146)—(4.149) and Eqs. (4.151)—(4.153), it is straightforward to verify that the general density-matrix identities [Eqs. (4.128)] are satisfied.

To illustrate more complicated situations, let us conclude this section by considering the following $2p$-$1h$ and $1p$-$2h$ states (i.e., with respect to an $N=Z$ core):

$$|\,2p\text{-}1h:\gamma;J_0M_{J_0};T_0M_{T_0}\rangle=\mathcal{N}_{a_{p_1}a_{p_2}}[[a^\dagger_{a_{p_1}}\otimes a^\dagger_{a_{p_2}}]_{J_p;T_p}\otimes b^\dagger_{a_h}]^{M_{J_0};M_{T_0}}_{J_0;T_0}|\,\tilde{0}\rangle\ , \quad (4.155a)$$

$$|\,1p\text{-}2h:\gamma;J_0M_{J_0};T_0M_{T_0}\rangle=\mathcal{N}_{a_{h_1}a_{h_2}}[a^\dagger_{a_p}\otimes[b^\dagger_{a_{h_1}}\otimes b^\dagger_{a_{h_2}}]_{J_h;T_h}]^{M_{J_0};M_{T_0}}_{J_0;T_0}|\,\tilde{0}\rangle\ , \quad (4.155b)$$

where the normalization factors are given by

$$\mathcal{N}_{a_1a_2}\equiv(1+\delta_{a_1a_2})^{-1/2}\ . \quad (4.156)$$

Thus, for the $2p$-$1h$ states, two particles with single-particle quantum numbers α_{p_1} and α_{p_2} (a_{p_1} and a_{p_2} without the magnetic quantum numbers) are coupled to $J_p;T_p$, and then this combination is coupled to the single hole with quantum numbers α_h to the total $J_0M_{J_0};T_0M_{T_0}$. We choose the orderings to be the ones in Eqs. (4.155a) and (4.155b). Of course, in the usual way, if $a_{p_1}=a_{p_2}$, then J_p+T_p must be odd. Since now there may be many configurations, all with the same values of $J_0M_{J_0};T_0M_{T_0}$, we include another label γ to summarize the rest of the quantum numbers. Thus for the $2p$-$1h$ states γ stands for $(a_{p_1}a_{p_2})a_h$ and $J_p;T_p$. Clearly the nomenclature for the $1p$-$2h$ states in Eq. (4.155b) is interpreted in an analogous manner.

Suppose now we represent the entire ground state as a combination of $1p$ and $2p$-$1h$ configurations (with real coefficients),

$$|\,J_0M_{J_0};T_0M_{T_0}\rangle=A^{1p}|\,1p:J_0M_{J_0};T_0M_{T_0}\rangle+\sum_\gamma A^{2p\text{-}1h}_\gamma|\,2p\text{-}1h:\gamma;J_0M_{J_0};T_0M_{T_0}\rangle\ , \quad (4.157)$$

where

$$(A^{1p})^2+\sum_\gamma(A^{2p\text{-}1h}_\gamma)^2=1\ . \quad (4.158)$$

If this is inserted into Eq.(4.124), we obtain for the one-body density-matrix elements

$$\psi_{J;T}(a'a)=(A^{1p})^2\psi^{\rm I}_{J;T}(a'a)+A^{1p}\sum_\gamma A^{2p\text{-}1h}_\gamma\psi^{{\rm II};\gamma}_{J;T}(a'a)+\sum_{\gamma'\gamma}A^{2p\text{-}1h}_{\gamma'}A^{2p\text{-}1h}_\gamma\psi^{{\rm III};\gamma'\gamma}_{J;T}(a'a)\ , \quad (4.159)$$

where $\psi^{\rm I}_{J;T}(a'a)=\psi^{1p}_{J;T}(a'a)$ [see Eq. (4.141a)], and

$$\psi^{\rm I}_{J;T}=\begin{cases}\delta_{aa_p}, & \varepsilon_a>\varepsilon_F\\ 2\delta_{J0}\delta_{T0}[j][J_0], & \varepsilon_a\leq\varepsilon_F\ ,\end{cases} \quad (4.160a)$$

$$\psi^{{\rm II},\gamma}_{J;T}(a'a)=\mathcal{N}_{a_{p_1}a_{p_2}}(-)^{j_h+1/2}(-)^{j_{p_1}-j_{p_2}}[J_0][T_0][J_p][T_p]\begin{Bmatrix}J_0 & J_0 & J\\ j' & j & J_p\end{Bmatrix}\begin{Bmatrix}T_0 & T_0 & T\\ \frac{1}{2} & \frac{1}{2} & T_p\end{Bmatrix}\times\delta_{aa_h}[\delta_{a'a_{p_2}}\delta_{a_pa_{p_1}}-(-)^{j_{p_1}-j_{p_2}}(-)^{J_p+T_p}\delta_{a'a_{p_1}}\delta_{a_pa_{p_2}}]\ ,\ \varepsilon_a\leq\varepsilon_F,\ \varepsilon_{a'}>\varepsilon_F\ , \quad (4.160b)$$

$$\psi^{\mathrm{III},\gamma'\gamma}_{J;T}(a'a)=\mathcal{N}_{a_{p_1'}a_{p_2'}}\mathcal{N}_{a_{p_1}a_{p_2}}(-)^{j_h+1/2}(-)^{j_{p_1}-j_{p_2}}[J_0]^2[T_0]^2$$

$$\times[J_p'][T_p'][J_p][T_p](-)^{J_0+T_0}\begin{Bmatrix}J_0 & J_0 & J\\ J_p' & J_p & j_h\end{Bmatrix}\begin{Bmatrix}T_0 & T_0 & T\\ T_p' & T_p & \frac{1}{2}\end{Bmatrix}\begin{Bmatrix}T_p' & T_p & T\\ \frac{1}{2} & \frac{1}{2} & \frac{1}{2}\end{Bmatrix}$$

$$\times\delta_{a_h'a_h}\sum_{a''}\begin{Bmatrix}J_p' & J_p & J\\ j & j' & j''\end{Bmatrix}$$

$$\times[\delta_{a_{p_1}a''}\delta_{a_{p_2}a}\delta_{a_{p_1'}a''}\delta_{a_{p_2'}a'}-(-)^{j_{p_1}-j_{p_2}}(-)^{J_p+T_p}\delta_{a_{p_1}a}\delta_{a_{p_2}a''}\delta_{a_{p_1'}a''}\delta_{a_{p_2'}a'}$$

$$-(-)^{j_{p_1'}-j_{p_2'}}(-)^{J_p'+T_p'}\delta_{a_{p_1}a''}\delta_{a_{p_2}a}\delta_{a_{p_1'}a'}\delta_{a_{p_2'}a''}$$

$$+(-)^{j_{p_1}-j_{p_2}}(-)^{j_{p_1'}-j_{p_2'}}(-)^{J_p+T_p}(-)^{J_p'+T_p'}\delta_{a_{p_1}a}\delta_{a_{p_2}a''}\delta_{a_{p_1'}a'}\delta_{a_{p_2'}a''}]\quad\text{when } \varepsilon_a>\varepsilon_F,\ \varepsilon_{a'}>\varepsilon_F\ , \tag{4.160c}$$

and

$$\psi^{\mathrm{III},\gamma'\gamma}_{J;T}(a'a)=\sqrt{2}\delta_{a'a}\delta_{\gamma'\gamma}\delta_{J0}\delta_{T0}[j][J_0][T_0]$$

$$-(-)^{j_h+1/2}(-)^{J_0+T_0}(-)^{J_p+T_p}\delta_{J_p'J_p}\delta_{T_p'T_p}[J_0]^2[T_0]^2\begin{Bmatrix}J_0 & J_0 & J\\ j_{h'} & j_h & J_p\end{Bmatrix}\begin{Bmatrix}T_0 & T_0 & T\\ \frac{1}{2} & \frac{1}{2} & T_p\end{Bmatrix}\delta_{a'a_h}\delta_{aa_{h'}}\delta_{a_{p_1'}a_{p_1}}\delta_{a_{p_2'}a_{p_2}}$$

$$\text{when } \varepsilon_a\le\varepsilon_F,\ \varepsilon_{a'}\le\varepsilon_F\ . \tag{4.160d}$$

Naturally, applying the same ideas to the situation where a combination of $1h$ [Eq. (4.138b)] and $1p$-$2h$ [Eq. (4.155b)] states occur, we may obtain similar expressions for the density matrix (Donnelly and Gökalp, 1981). Rather than discuss this situation in detail we shall end this section with a specific example of the $1p/2p$-$1h$ problem. Let us consider ^{13}C with $J_0=T_0=-M_{T_0}=\frac{1}{2}$ to be of the following form:

$$(1-\eta^2)^{1/2}\,|\,1p:(1p_{1/2})\rangle$$
$$+\eta\,|\,2p\text{-}1h:(1p_{1/2}1p_{1/2})_{1;0}1p_{3/2}^{-1}\rangle\ . \tag{4.161a}$$

That is, we have the above situation with

$$A^{1p}=(1-\eta^2)^{1/2}\ ,$$
$$A^{2p\text{-}1h}=\eta\ \text{ with }\ -1\le\eta\le+1\ , \tag{4.161b}$$

where the $1p$ state has a single $1p_{1/2}$ neutron added to the $(1s_{1/2})^4(1p_{3/2})^8$ closed core, while the $2p$-$1h$ state has two $1p_{1/2}$ particles coupled to $J_p=1, T_p=0$ and these in turn coupled with a $1p_{3/2}$ hole to form the total state with $J_0=T_0=-M_{T_0}=\frac{1}{2}$. In the $1p$ model space only this one $2p$-$1h$ configuration can occur. Using Eqs. (4.159) and (4.160), we then have the following nonzero density-matrix elements:

$$\psi_{0;0}(a'a)=\begin{cases}1+\eta^2, & a'=a=1p_{1/2}\\ 4\sqrt{2}-\dfrac{1}{\sqrt{2}}\eta^2, & a'=a=1p_{3/2}\\ 4, & a'=a=1s_{1/2}\ ,\end{cases}$$

$$\psi_{0;1}(a'a)=\begin{cases}1-\eta^2, & a'=a=1p_{1/2}\\ \dfrac{1}{\sqrt{2}}\eta^2, & a'=a=1p_{3/2}\ ,\end{cases}$$

$$\psi_{1;0}(a'a)=\begin{cases}1-\frac{5}{3}\eta^2, & a'=a=1p_{1/2}\\ \dfrac{\sqrt{5}}{3\sqrt{2}}\eta^2, & a'=a=1p_{3/2}\\ \sqrt{2/3}\eta(1-\eta^2)^{1/2}, & a'=1p_{1/2},\ a=1p_{3/2}\ ,\end{cases}$$

$$\psi_{1;1}(a'a)=\begin{cases}1-\eta^2, & a'=a=1p_{1/2}\\ -\dfrac{5}{3\sqrt{2}}\eta^2, & a'=a=1p_{3/2}\\ -\sqrt{2/3}\eta(1-\eta^2)^{1/2}, & a'=1p_{1/2},\ a=1p_{3/2}\ .\end{cases} \tag{4.162}$$

To help bring the ideas presented in this section into

better focus, let us consider one very simple specific example. Let us treat the ground state of ^{27}Al with $J_0=\frac{5}{2}$, $T_0=\frac{1}{2}$, and $M_{T_0}=-\frac{1}{2}$ as a single $1d_{5/2}$ proton hole in a closed $(1s_{1/2})^4(1p_{3/2})^8(1p_{1/2})^4(1d_{5/2})^{12}$ shell (a naive model for ^{28}Si). Then the ground state of ^{27}Al is of the form given in Eq. (4.138b) and yields one-body density-matrix elements as in Eq. (4.141b):

$$\psi_{J;T}(a'a)=\delta_{a'a}\{2\delta_{J0}\delta_{T0}[j][J_0]-(-)^{J+T}\delta_{aa_h}\}\ , \tag{4.163}$$

with $a_h\leftrightarrow 1d_{5/2}$ and $a'=a$ restricted to lie below the Fermi surface (i.e., the closed $1d_{5/2}$ shell). The proton and neutron one-body density-matrix elements in Eq. (4.133) then become very simple:

$$\psi_J(a'a)_{m_t}=\delta_{a'a}\{\delta_{J0}[j][J_0]-(-)^J\tfrac{1}{2}(1+2m_t)\delta_{aa_h}\}\ , \tag{4.164}$$

that is, specifically the nonzero cases are

$$\psi_0(a^2)_{m_t}=\begin{cases}2\sqrt{3}, & a\leftrightarrow 1s_{1/2},\ m_t=\pm\frac{1}{2}\\ 2\sqrt{6}, & a\leftrightarrow 1p_{3/2},\ m_t=\pm\frac{1}{2}\\ 2\sqrt{3}, & a\leftrightarrow 1p_{1/2},\ m_t=\pm\frac{1}{2}\\ 5, & a\leftrightarrow 1d_{5/2},\ m_t=+\frac{1}{2}\\ 6, & a\leftrightarrow 1d_{5/2},\ m_t=-\frac{1}{2}\ ,\end{cases} \tag{4.165a}$$

$$\psi_{J\geq 1}(1d_{5/2}^2)_{m_t}=\begin{cases}-(-)^J, & m_t=+\frac{1}{2}\\ 0, & m_t=-\frac{1}{2}\ .\end{cases} \tag{4.165b}$$

Let us first compute the ground-state magnetic dipole moment using Eq. (4.134) with $B_1(2\frac{5}{2};2\frac{5}{2})=-6\sqrt{7/5}$ and $D_1^-(2\frac{5}{2};2\frac{5}{2})=\sqrt{14/5}$, obtained using Eqs. (4.120) and (4.121), respectively. We then find that $\mu=2+\mu_p$, which is the expected result, namely, the Schmidt limit. Next, to illustrate the use of the basic expressions for the form factors [Eqs. (4.129)—(4.132)] let us calculate the $C0$ contribution:

$$\rho_0(r)_{+1/2}=\sum_{a'a}A_0(l'j';lj)\psi_0(a'a)_{+1/2}\rho_{a'a}(r)_{+1/2}/[J_0] \tag{4.166}$$

using Eq. (4.129). The density-matrix elements are given above in Eq. (4.165a), and the coefficient A_0 was calculated in Eq. (4.119). So we have

$$\rho_0(r)_{+1/2}=\sum_a n_a^p\,|\,R_{nlj;+1/2}(r)\,|^2=\rho_p(r)\ , \tag{4.167}$$

where n_a^p is the number of protons in the shell labeled a (2 for $1s_{1/2}$, 4 for $1p_{3/2}$, 2 for $1p_{1/2}$, and 5 for $1d_{5/2}$), and $\rho_p(r)$ is the total nuclear charge density. Then Eq. (4.129) gives

$$\mathscr{F}_0(q)=\int_0^\infty r^2dr\,j_0(qr)\rho_p(r)\ , \tag{4.168}$$

as expected for the monopole charge form factor.

Similar results hold for the other form factors, although now only the $1d_{5/2}$ proton hole contributes [see Eq. (4.165b)]. We define

$$\rho(r)=|\,R_{1d_{5/2};+1/2}(r)\,|^2 \tag{4.169}$$

and then have

$$\rho_J(r)_{+1/2}=-\frac{1}{\sqrt{6}}A_J(2\tfrac{5}{2};2\tfrac{5}{2})\rho(r),\quad J=2,4 \tag{4.170a}$$

$$\alpha_J(r)_{+1/2}=-\frac{1}{\sqrt{6}}B_J(2\tfrac{5}{2};2\tfrac{5}{2})\rho(r),\quad J=1,3,5 \tag{4.170b}$$

$$\beta_J^+(r)_{+1/2}=-\frac{\sqrt{J}}{\sqrt{6}}\mu^pD_J^+(2\tfrac{5}{2};2\tfrac{5}{2})\rho(r),\quad J=1,3,5 \tag{4.170c}$$

$$\beta_J^-(r)_{+1/2}=\frac{\sqrt{J+1}}{\sqrt{6}}\mu^pD_J^-(2\tfrac{5}{2};2\tfrac{5}{2})\rho(r),\quad J=1,3,5\ . \tag{4.170d}$$

The coefficients A_J, B_J, and $D_J^\pm$ may be obtained from existing tables [Donnelly and Haxton (1980); in fact, this example was presented by Donnelly and Haxton (1980). The odd-J cases are given on pp. 8—9 of that reference, with one typographical error—$D_3^+(2\frac{5}{2};2\frac{5}{2})$ should have a minus sign]. Using the tables, we obtain for the even-J cases $A_2(2\frac{5}{2};2\frac{5}{2})=-4\sqrt{3/7}$ and $A_4(2\frac{5}{2};2\frac{5}{2})=6\sqrt{7}$. If we define

$$f_L(q)\equiv\int_0^\infty r^2dr\,j_L(qr)\rho(r)\ , \tag{4.171}$$

for $L=0,2,4$, then we find, using the above results,

$$\mathscr{F}_2(q)=2\sqrt{2/7}f_2(q)\ , \tag{4.172a}$$

$$\mathscr{F}_4(q)=\sqrt{6/7}f_4(q)\ , \tag{4.172b}$$

$$\mathscr{F}_1(q)=\sqrt{14/15}\left[\frac{q}{M_N}\right]\{[f_0(q)+f_2(q)]+\tfrac{1}{2}\mu^p[f_0(q)-\tfrac{2}{7}f_2(q)]\}\ , \tag{4.172c}$$

$$\mathscr{F}_3(q)=-\tfrac{3}{7}\sqrt{2/5}\left[\frac{q}{M_N}\right]\{[f_2(q)+f_4(q)]+4\mu^p[f_2(q)-\tfrac{1}{6}f_4(q)]\}\ , \tag{4.172d}$$

$$\mathscr{F}_5(q)=\sqrt{5/7}\left[\frac{q}{M_N}\right]\mu^pf_4(q)\ . \tag{4.172e}$$

Of course, with harmonic-oscillator wave functions, the form factors in Eq. (4.171) can be written in terms of simple functions, and the form factors calculated above involve simple polynomials in q^2 (Donnelly and Haxton, 1979). We note in passing that this example illustrates the absence of a convection-current contribution to the highest multipole with a stretched $J=l+\frac{1}{2}$ configura-

tion: only the magnetization current (which is proportional to μ^p) enters in $\mathscr{F}_5$.

D. Deformed nuclei ▲

The subject of electron scattering from deformed nuclei has been discussed in a series of papers (Moya de Guerra and Dieperink, 1978; Moya de Guerra and Kowalski, 1980; Moya de Guerra, 1980), and here we shall extract only the main ideas to illustrate what is seen in elastic magnetic scattering from such systems. The general structure of deformed nuclei is discussed in many places (see, for example, Nilsson, 1955; Bohr and Mottelson, 1975; de Shalit and Feshbach, 1974). In particular, a detailed treatment of the transverse form factors in the projected Hartree-Fock (HF) approach is presented in Moya de Guerra and Kowalski (1980). In fact, in that work it was seen that the gross behavior of the form factors is already largely accounted for by a simple approximation to the more involved HF formalism, namely by the Nilsson model (Nilsson, 1955). Thus in this subsection we shall restrict our attention to this special case, as it is clearer. Of course, in discussing comparisons with experiment in subsequent sections we shall give the projected Hartree-Fock results when available.

Let us begin by summarizing the basic formalism as it pertains to deformed nuclei and the Nilsson model in particular (Nilsson, 1955). We shall largely use the nomenclature of de Shalit and Feshbach (1974, Chap. VI), where there is a clear (and available) exposition of this formalism. The unified model begins by expanding the nuclear wave functions in a separable form,

$$\Psi(IKM)=\frac{[I]}{4\pi}[D^{I*}_{MK}(\theta_k)\chi_K(\mathbf{r}'_i) +(\hat{-})^{I-J}D^{I*}_{M,-K}(\theta_k)\chi_{-K}(\mathbf{r}'_i)] , \tag{4.173}$$

where we consider only $K>0$. The angular momentum quantum numbers in the problem are defined in Fig. 7. Here the total angular momentum $\mathbf{I}$ with projection M on the laboratory z axis $\mathbf{u}_z$ has been resolved into a collective angular momentum $\mathbf{R}$ and an internal angular momentum $\mathbf{J}$, with $\mathbf{I}=\mathbf{R}+\mathbf{J}$. The total angular momentum $\mathbf{I}$ has projection K along the body-fixed z axis $\mathbf{u}'_z$, and the internal angular momentum has projection Ω as shown in the figure. In fact, assuming that axial symmetry is retained all throughout the motion, we have $\Omega=K$. In Eq. (4.173) the rotation matrices depend on the angles θ_k, which determine the orientation of the body-fixed axes as a function of the particle coordinates $\mathbf{r}_i$. These functions

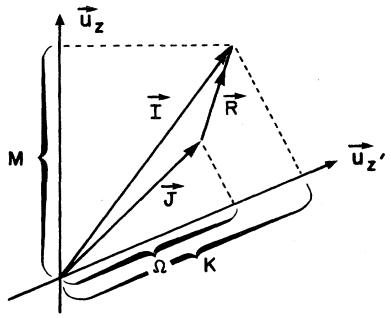

FIG. 7. Labeling of angular momenta used in discussing deformed nuclei. The z axis is in the laboratory frame and the z' axis in the body-fixed system.

contain the rotational content of the problem. The remaining factors in Eq. (4.173) involve the intrinsic wave functions χ with dependence only on coordinates $\mathbf{r}'_i$. These may be expanded in eigenfunctions of $\mathbf{J}^2$,

$$\chi_K(\mathbf{r}'_i)=\sum_{\mathscr{J}} a_{\mathscr{J}}\chi^{(\mathscr{J})}_K(\mathbf{r}'_i) , \tag{4.174}$$

where $\mathbf{J}^2\chi^{(\mathscr{J})}_K(\mathbf{r}'_i)=\mathscr{J}(\mathscr{J}+1)\chi^{(\mathscr{J})}_K(\mathbf{r}'_i)$. Furthermore, we follow de Shalit and Feshbach (1974) and introduce the notation

$$(\hat{-})^J\chi_{-K}(\mathbf{r}'_i)=\sum_{\mathscr{J}} a_{\mathscr{J}}(-)^{\mathscr{J}}\chi^{(\mathscr{J})}_{-K}(\mathbf{r}'_i) . \tag{4.175}$$

The occurrence of terms with K and $-K$ in the specific combination given in Eq. (4.173) is a consequence of the symmetry under a rotation by 180° about the y' direction, which must be obeyed for an axially symmetric nucleus as we assume here.

Let us next consider an irreducible tensor operator $\hat{T}_{JM_J}$ referred to the laboratory coordinate system so that it is related to irreducible tensor operators referred to the body-fixed system in the following way:

$$\hat{T}_{JM_J}(\mathbf{r}_i)=\sum_{M'_J} D^{J*}_{M_JM'_J}(\theta_k)\hat{T}_{JM'_J}(\mathbf{r}'_i) . \tag{4.176}$$

Inserting this between states of the form given in Eq. (4.173) and using the identity involving rotation matrices

$$\frac{1}{8\pi^2}\int d\Omega_k D^{I'}_{M'K'}(\theta_k)D^{J*}_{M_JM'_J}(\theta_k)D^{I*}_{MK}(\theta_k) =(-)^{M'-K'}\begin{bmatrix} I' & J & I \\ -M' & M_J & M\end{bmatrix}\begin{bmatrix} I' & J & I \\ -K' & M'_J & K\end{bmatrix} \tag{4.177}$$

yields the following basic equation for the reduced matrix elements:

$$\langle I'K'||\hat{T}_J||IK\rangle=(-)^{I'-K'}[I'][I]\sum_{M'_J}\left[\begin{bmatrix} I' & J & I \\ -K' & M'_J & K\end{bmatrix}\langle K'|T_{JM'_J}|K\rangle+\begin{bmatrix} I' & J & I \\ -K' & M'_J & -K\end{bmatrix}(-)^I\langle K'|T_{JM'_J}|-K\rangle\right] , \tag{4.178}$$

where

$$\langle K' \mid T_{JM'_J} \mid K \rangle = \int d\xi_\alpha \chi^\dagger_{K'}(\xi_\alpha) T_{JM'_J}(\xi_\alpha) \chi_K(\xi_\alpha) \ , \tag{4.179}$$

$$(-)^I \langle K' \mid T_{JM'_J} \mid -K \rangle = \int d\xi_\alpha \chi^\dagger_{K'}(\xi_\alpha) T_{JM'_J}(\xi_\alpha) \times (\hat{-})^{I-J} \chi_{-K}(\xi_\alpha)$$

and $\{\xi_\alpha\}$ stands for a set of $3A-3$ internal coordinates. Specifically, we shall be interested in the electromagnetic multipole operators and the calculation of their reduced matrix elements using Eq. (4.178).

Let us turn now from this general situation to the specific case of the Nilsson model. We assume that the intrinsic states have a single unpaired nucleon moving in a deformed potential plus an even-even core (thus we restrict our attention to odd-A nuclei here). The core may be treated in various ways, for example, as a rigid rotor or as irrotational fluid flow. Indeed, as may be seen in explicit model calculations (Moya de Guerra and Kowalski, 1980), these collective core contributions yield form factors which generally peak at low momentum transfer and then fall rapidly with increasing q. Thus, except in the low-q region, they may frequently be neglected with respect to the dominant contribution from the single unpaired nucleon. We shall do so in the rest of this section, although in any detailed comparison with experiment one should include the collective form factors as well.

The single unpaired nucleon is assumed to move in a potential of the form (Nilsson, 1955)

$$V = \tfrac{1}{2} M_N \omega_0^2 r^2 - M_N \omega_0^2 r^2 \delta \left[\frac{16\pi}{45} \right]^{1/2} Y^0_2(\theta,\phi) + C\mathbf{l}\cdot\mathbf{s} + D\mathbf{l}^2 \tag{4.180}$$

with Hamiltonian $H = -(\hbar^2/2M_N)\nabla^2 + V$. Here δ is a deformation parameter ($\delta > 0 \leftrightarrow$ prolate deformations, $\delta < 0 \leftrightarrow$ oblate deformations) and C and D are constants. The first two terms in this potential arise from assuming that we have an axially symmetric harmonic-oscillator potential with oscillator frequencies

$$\omega_z^2 = \omega_0^2(1 - \tfrac{4}{3}\delta) \ , \tag{4.181a}$$

$$\omega_x^2 = \omega_y^2 = \omega_0^2(1 - \tfrac{2}{3}\delta) \ , \tag{4.181b}$$

with

$$\omega_0(1 - \tfrac{4}{3}\delta^2 - \tfrac{16}{27}\delta^3)^{1/6} \equiv \omega_{00} = \text{const} \ . \tag{4.182}$$

The eigenstates of the Nilsson Hamiltonian with $C = D = 0$ may be labeled by the quantum numbers, $K^\pi[Nn_z\Lambda]$ where $N = n_x + n_y + n_z$ is the number of oscillator quanta, $n_z \leq N$ is that quantity for the z direction, and Λ is the z projection of the orbital angular momentum satisfying $|\Lambda| = N - n_z, N - n_z - 2, \ldots, 1$ or 0. In fact the parity π is given by $\pi = (-)^N$. The z projection of the spin must satisfy $\Sigma = K - \Lambda = \pm\frac{1}{2}$. For large deformations δ the terms $C\mathbf{l}\cdot\mathbf{s}$ and $D\mathbf{l}^2$ in Eq. (4.180) can be neglected, and so conventionally the actual eigenstates of the full Hamiltonian are labeled by the above set of "asymptotic" quantum numbers which are approached in that limit.

It is useful to expand the eigenfunctions of H in terms of spherical solutions (i.e., of H with $\delta = C = D = 0$) labeled $|Nl\Lambda\Sigma\rangle$ with $K = \Lambda + \Sigma$:

$$|NK\gamma\rangle = \sum_{l\Lambda} a^{NK\gamma}_{l\Lambda} \, |nl\Lambda\Sigma = K - \Lambda\rangle \ . \tag{4.183}$$

Here the principal quantum number N has been taken to be fixed, and the expansion coefficients are determined by diagonalizing the Hamiltonian H in the subspace with fixed N, K, and γ, the last corresponding to all other quantum numbers needed to characterize the state (for example, the asymptotic quantum numbers discussed above). We shall simplify the notation in the following and consider the set $\{NK\gamma\}$ to be given. For fixed ω_{00}, C, and D (or equivalently, fixed ω_{00}, $\kappa \equiv -C/2\hbar\omega_{00}$, and $\mu \equiv 2D/C$; see Nilsson, 1955), the energy eigenvalue corresponding to the state in Eq. (4.183) may be obtained as a function of δ. The expansion coefficients $a_{l\Lambda}$ have been tabulated[9] by Nilsson (1955), who expressed them in terms of μ, which is fixed for given N to reproduce the shell-model sequence of levels as well as possible in the spherical limit ($\delta = 0$), and in terms of $\eta \equiv (\delta/\kappa)(1 - \frac{4}{3}\delta^2 - \frac{16}{27}\delta^3)^{-1/6}$.

Finally, since we prefer to work with spherical states where orbital and spin angular momenta are coupled to a total j, $(l\tfrac{1}{2})j$, we write

$$|NK\gamma\rangle = \sum_{lj} \alpha_{lj} \, |N(l\tfrac{1}{2})j, m_j = K\rangle \ , \tag{4.184}$$

with

$$\alpha_{lj} = \sum_\Lambda \langle l\Lambda\tfrac{1}{2}\Sigma = K - \Lambda \mid (l\tfrac{1}{2})jK\rangle a_{l\Lambda} \tag{4.185a}$$

$$= \frac{1}{[l]} \times \begin{cases} \sqrt{l + 1/2 - K}\, a_{lK+1/2} + \sqrt{l + 1/2 + K}\, a_{lK-1/2} \\ \qquad \text{for } j = l + \tfrac{1}{2} \\ \sqrt{l + 1/2 + K}\, a_{lK+1/2} - \sqrt{l + 1/2 - K}\, a_{lK-1/2} \\ \qquad \text{for } j = l - \tfrac{1}{2} \ , \end{cases} \tag{4.185b}$$

where as above we suppress the labels $NK\gamma$ which are common to all of the a's or α's. In fact, for fixed N and j, only one value of l can occur, since the states have a definite parity, and so the sum over l can actually be omitted.

It is then straightforward to reexpress the reduced matrix elements in Eq. (4.178) for this single Nilsson orbit in a form which is closely allied to our discussions in the preceding formalism sections:

[9]Note that, in contrast to the $a_{l\Lambda}$ defined above, the numerical values given by Nilsson (1955) are not normalized. We use $\sum_{l\Lambda} a^2_{l\Lambda} = 1$, which implies that $\sum_{lj} \alpha^2_{lj} = 1$.

$$\langle NK\gamma;I'||\hat{T}_J(q)||NK\gamma;I\rangle = \sum_{a'a}\langle a'||T_J(q)||a\rangle\psi_J^{NK\gamma;I'I}(a'a)\ , \quad (4.186)$$

where now the one-body density-matrix elements are given by

$$\psi_J^{NK\gamma;I'I}(a'a)=\phi_J^{K;I'I}(j';j)\alpha_{l'j'}\alpha_{lj} \quad (4.187)$$

and where we have defined the following convenient function:

$$\phi_J^{K;I'I}(j';j)\equiv(-)^{I'-j'}[I'][I]\left[\begin{Bmatrix} I' & J & I \\ -K & 0 & K\end{Bmatrix}\begin{Bmatrix} j' & J & j \\ -K & 0 & K\end{Bmatrix}+(-)^{I-j}\begin{Bmatrix} I' & J & I \\ -K & 2K & -K\end{Bmatrix}\begin{Bmatrix} j' & J & j \\ -K & 2K & -K\end{Bmatrix}\right]. \quad (4.188)$$

Using properties of the 3-j symbols, it is easy to show that

$$\phi_J^{K;II'}(j;j')=(-)^{I'-I}(-)^{j'-j}\phi_J^{K;I'I}(j';j)\ . \quad (4.189)$$

Now, specifically for elastic electron scattering, we shall be interested in the case where the ground state begins a rotational band with $I'=I=K$, so that we have

$$\phi_J^K(j';j)\equiv\phi_J^{K;KK}(j';j)=(-)^{K-j'}[K]^2\left[\begin{Bmatrix} K & J & K \\ -K & 0 & K\end{Bmatrix}\begin{Bmatrix} j' & J & j \\ -K & 0 & K\end{Bmatrix}+(-)^{K-j}\begin{Bmatrix} K & J & K \\ -K & 2K & -K\end{Bmatrix}\begin{Bmatrix} j' & J & j \\ -K & 2K & -K\end{Bmatrix}\right]. \quad (4.190)$$

The density-matrix elements [the ψ's in Eq. (4.187)] are to be interpreted as proton or neutron densities, as discussed in Sec. IV.C. That is, we have elastic magnetic electron scattering form factors given by Eq. (4.130), where for the quantities $\psi_J(a'a)_{m_t}$ required in calculating the densities [Eqs. (4.131)] we use exactly our present ψ's with $m_t=+\frac{1}{2}$ only for an odd-proton deformed nucleus and $m_t=-\frac{1}{2}$ an odd-neutron case.

Furthermore, note that the second terms in Eqs. (4.188) and (4.190) vanish unless $J\geq 2K$. Generally one finds that the 3-j symbols occur in such a way that this second term is relatively large, whereas the first term may be quite small. Thus intermediate multipoles (such as $M3$ when $M1,M3,M5$ can occur) are generally suppressed with respect to the spherical single-particle form factors, while the $M1$ and the higher allowed multipoles having $J\geq K$ are not suppressed. We shall return to specific examples which illustrate this suppression in Sec. VI.D. Finally, we remark that these developments must in fact be modified somewhat for $K=\frac{1}{2}$, where decoupling parameters occur (Nilsson, 1955) and where the problem does not separate as easily into a collective core plus a valence nucleon contribution. We shall not consider the peculiarities of this $K=\frac{1}{2}$ case in the present review, as the published literature has not treated this special problem.

To conclude this section let us discuss this suppression in more general terms. Let us consider a given major shell (N fixed) and specifically take all Nilsson configurations which merge into a given spherical state (i.e., specific quantum numbers lj) in the $\delta=0$ limit. While we really cannot take $\delta=0$ in this model (since various couplings which have been neglected for finite δ would then be important), we can consider δ to be small, and so in Eq. (4.187) we have $\alpha_{l'j'}\approx\alpha_{lj}\approx 1$. Then we have, using Eqs. (4.186) and (4.187),

$$|\langle K;I'||\hat{T}_J(q)||K;I=K\rangle|^2 = |\langle lj||T_J(q)||lj\rangle|^2[\phi_J^{K;I'K}(j;j)]^2\ . \quad (4.191)$$

Let us now average over initial states and sum over final states in the following way. For final states we sum over the entire rotational bands built on each bandhead labeled K; that is, we have $\sum_{I'\geq K}$ for each K. In averaging over initial states we have a statistical factor $(2K+1)^{-1}$ and then must sum over K with a degeneracy factor $n_j:(1/n_j)\sum_{K>0}$. Here $n_j=j+\frac{1}{2}$ (i.e., there are $j+\frac{1}{2}$ positive K values for a given value of j). Performing these operations, we have

$$\overline{\sum_{if}}|\langle K;I'||\hat{T}_J(q)||K;I=K\rangle|^2 \equiv\frac{1}{2j+1}R_J(j)|\langle lj||T_J(q)||lj\rangle|^2\ , \quad (4.192)$$

where

$$R_J(j)=2\sum_{K>0}\frac{1}{2K+1}\left[\sum_{I'\geq K}[\phi_J^{K;I'K}(j;j)]^2\right] \quad (4.193a)$$

$$=2\sum_{K>0}\left[\begin{Bmatrix} j & j & J \\ K & -K & 0\end{Bmatrix}^2+\begin{Bmatrix} j & j & J \\ K & K & -2K\end{Bmatrix}^2\right] \quad (4.193b)$$

$$=\frac{1}{2J+1}+2\sum_{K>0}\begin{Bmatrix} j & j & J \\ K & K & -2K\end{Bmatrix}^2. \quad (4.193c)$$

For a spherical single-particle orbit labeled lj we would have

$$[R_J(j)]_{\text{spherical}} = \sum_{mm'} \begin{bmatrix} j & j & J \\ m & m' & -(m+m') \end{bmatrix}^2 = 1 \ , \tag{4.194}$$

and so the above expressions reflect the equivalent *total* single-particle strength in this simple deformed model. We have averaged over the different K states which merge into the same spherical limit and have summed over the entire rotational bands built on each K state, since these (in general inelastic transitions for $\delta \neq 0$) all become part of the spherical limit strength when $\delta \to 0$. In Fig. 8 we show the intensity reduction factor $R_J(j)$ for typical values of the quantum numbers J and j. For many cases the strength lies between about $\frac{1}{3}$ and $\frac{1}{2}$. This is to be contrasted with results for a given value of K and where we do not sum over the rotational band built on this bandhead. Then a given multipole may be very drastically reduced from the spherical single-particle estimate. For instance, we shall see in Sec. VI.D examples where specific multipoles may have strength reductions below 10^{-3}. The above exercise was performed to answer the question: Where does all the strength go? Clearly a lot of it goes into the inelastic excitations of the rotational band and into other states with different bandheads (different K values). Beyond this, the remaining reductions typically by 2 or 3 in strength, result from the limited number of magnetic quantum numbers which can be connected in the deformed case. The nature of the overlaps which occur when a deformed core is present allows only K to couple with $\pm K$ [as in Eq. (4.193b)], whereas the spherical case contains in general a wider selection [see Eq. (4.194)]. A special situation occurs when $j = \frac{1}{2}$, for then all magnetic substates can couple, and indeed the strength is unity (see Fig. 8).

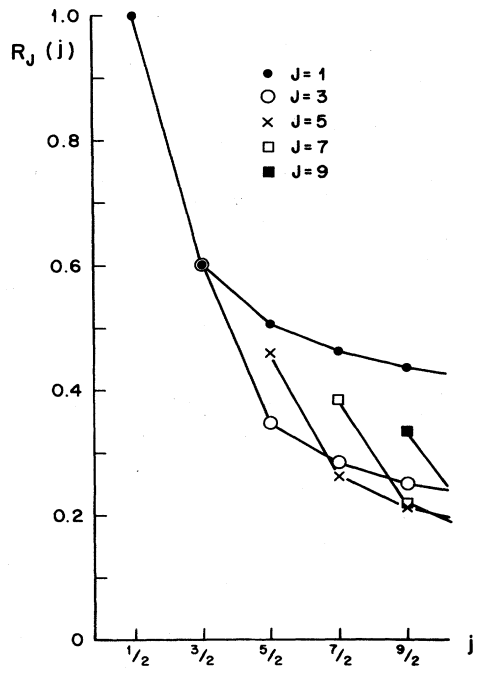

FIG. 8. The quantity $R_J(j)$ defined in Eq. (4.193) as a function of j for various multipolarities J.

E. Meson-exchange currents ▲

In this section we shall summarize some of the main features involved in discussing meson-exchange currents (MEC) for elastic magnetic electron scattering. The first attempts to include MEC effects in a realistic way were as corrections to one-body calculations of magnetic moments of nuclei (that is, the extreme long-wavelength limit of the elastic magnetic form factors). These calculations, as exemplified by the work of Villars (1947) and Miyazawa (1951), in general accounted for many of the existing discrepancies between experimentally measured values and previous one-body calculations, thus providing evidence for the presence of electromagnetic exchange currents. In more recent times MEC contributions to form factors have been explored over a wide range of momentum transfer.

The few-body nuclei in particular have been intensively studied, as they provide an ideal testing ground where nuclear dynamics and the nature of the electromagnetic responses come together in a reasonably controllable way. We shall return in Sec. VII to a discussion of the few-body ground states in more depth, including reference to current MEC calculations, and so at this point let us only note a few of the highlights of such studies. The $A=2$ system has been an important building block in discussions of such two-body effects as meson-exchange currents. For example, in considering np radiative capture, $n+p \to d+\gamma$, Riska and Brown (1972) found that inclusion of such effects led to a 10% increase in the cross section near threshold and brought the theoretical predictions into agreement with experiment. Important MEC effects can also be seen (Hockert *et al.*, 1973; see also Lock and Foldy, 1974,1975) in the electrodisintegration of the deuteron ($e+d \to e'+n+p$). These effects substantially change the shape of the differential cross section near threshold and account for as much as an order of magnitude increase at momentum transfers of $q \approx 650$ MeV/c (i.e., compared to simple impulse approximation calculations). This brings the theoretical calculation into rather good agreement with the experimental data. Meson-exchange-current effects in elastic electron scattering from the deuteron have also been studied (note that these are isoscalar currents and not the isovector ones we shall be focusing on for complex nuclei). We shall return in Sec. VII.A to the $A=2$ problem in more detail, and here only note a few of the published papers on this subject—Chemtob *et al.*, 1974; Fabian *et al.*, 1974; Jackson *et al.*, 1975; Gari *et al.*, 1976. In Sec. VII.A we shall also mention alternatives to these "standard" treatments of MEC, mainly through the use of relativistic two-nucleon wave functions.

The $A=3$ systems, ^{3}He and ^{3}H, have also received con-

siderable attention in studies of meson-exchange currents. Now both isoscalar and isovector contributions are present in elastic electron scattering. Since the nonrelativistic Schrödinger equation can be solved numerically with a high degree of accuracy using Faddeev or variational techniques, these nuclear ground states also provide special testing grounds for MEC studies. When high-q measurements on both ^{3}He and ^{3}H become available, it will be possible to separate the isoscalar and isovector contributions from one another. Predictions have been made for elastic magnetic electron scattering from both targets, and we shall return in Sec. VII.B to a more detailed discussion of the results of such calculations and comparisons with existing data.

For complex nuclei the problem is further complicated by uncertainties in the nuclear many-body wave functions. The general form of the lowest-order currents was discussed by Chemtob (1969), Chemtob and Lumbroso (1970), and Chemtob and Rho (1971), as it applies to complex nuclei. Building on this, calculations were performed using shell-model wave functions for a variety of nuclei (Dubach, 1975,1980; Dubach *et al.*, 1976), and we shall use these references as the basis for the rest of the discussion in this section. In addition to the work of Dubach and collaborators, the problem has also been considered by other authors (Suzuki, 1978; Mathiot and Desplanques, 1980; Suzuki *et al.*, 1981), and we shall quote their results when specific nuclei are discussed in Sec. VI.

A general approach to studies of meson-exchange currents was developed in early papers such as the work of Osborn and Foldy (1950) and modified and extended by Bosco and Piazza (1970), Stichel and Werner (1970), Lock *et al.* (1974), and Lock and Foldy (1975). Several recent papers provide useful discussions of the subject (Friar *et al.*, 1982; Friar, 1983; Riska, 1983). Let us begin by looking at the diagrams shown in Fig. 9, which are representative of typical meson-exchange-current contributions. Figure 9(a) shows a pion in flight between two nucleons, interacting through the electromagnetic field (i.e., in our case, with the virtual photon which is being exchanged with the electron, as in Fig. 5). Figure 9(b), on the other hand, has the photon interacting with a nucleon and producing an intermediate N or $\bar{N}$, which then exchanges the pion with another nucleon and goes to a final two-nucleon state. In the discussion to follow we shall see that our main interest is in the $\bar{N}$ intermediate state. Figure 9(c) is similar except that an intermediate nucleon resonance N^* is present. Important here is the inclusion of the $\Delta_{33}(1232)$. One common feature of Figs. 9(a)—9(c) is the exchange of a pion which will make these currents relatively long ranged, just as the one-pion-exchange part of the nuclear force provides a good representation of its long-range nature. In contrast, Figs. 9(d) and 9(e) have at least one heavier meson (e.g., ρ,ω) and so lead to shorter-ranged contributions to the overall meson-exchange current. The prevailing approach to this general problem of an infinite series of MEC diagrams has been assumed that these longest-ranged pieces are likely to be dominant

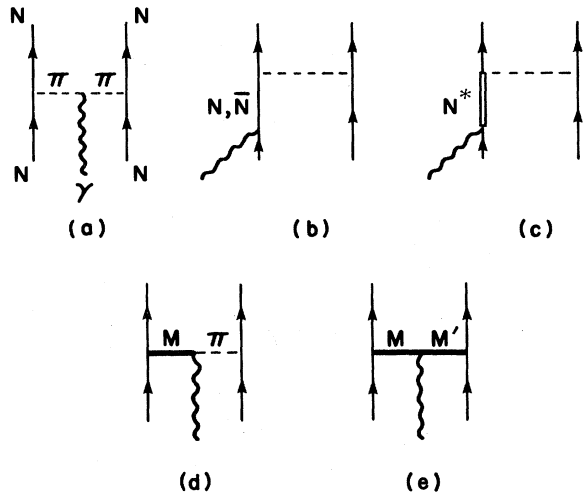

FIG. 9. General diagrammatic expansion including meson-exchange contributions. Here M,M' denote all exchanged mesons other than pions.

and that all shorter-ranged pieces will be suppressed by the repulsive short-range behavior of the NN interaction.

Alternatively, one might argue that the short-range nature of both the NN interaction and the MEC may be better described with quark-gluon degrees of freedom rather than the baryon-meson language we are using here. We shall not develop these parallel approaches further here, but instead follow the more conventional procedure. Thus we shall only consider contributions from pion-exchange MEC, although in discussing specific cases in the rest of the review we shall refer to work which goes beyond this limited scope whenever it is appropriate. Furthermore, we shall only consider the leading contributions in an expansion in powers of M_N^{-1}. As we shall see below, this leads us to conclude that the leading MEC contributions are (1) purely *isovector* and (2) purely *transverse* (i.e., with no charge contributions). Finally, we shall set up the problem in a form that is suited to discussions of complex nuclei, although the few-body systems are, of course, not excluded. As mentioned above, these latter systems are generally treated somewhat differently (and, in fact, the diagrams we are ignoring here are frequently included in contemporary calculations for the $A=2$ and $A=3$ nuclei).

Following Dubach (1975,1980; Dubach *et al.*, 1976), let us consider the currents corresponding to some of the Feynman diagrams in Fig. 9. We assume a pseudoscalar coupling of the pion to the nucleon and use the conventions of Schweber (1961) (in this subsection only). We begin with Fig. 9(a). Here a charged pion in flight between two nucleons undergoes an interaction with the virtual photon. We take the incoming nucleons to have four-momenta $(p_1)_\mu$ and $(p_2)_\mu$, the outgoing nucleus to have four-momenta $(p'_1)_\mu$ and $(p'_2)_\mu$, and the virtual photon as usual to bring in the four-momentum q_μ. Overall momentum conservation requires that $q_\mu=(p'_1+p'_2-p_1$

$-p_2)_\mu$. The fact that a charged pion must be exchanged forces the two-nucleon current to have a purely isovector isospin structure:

$$\tau_-^{(1)}\tau_+^{(2)}-\tau_+^{(1)}\tau_-^{(2)}=\frac{i}{2}(\boldsymbol{\tau}^{(1)}\times\boldsymbol{\tau}^{(2)})_3 , \tag{4.195}$$

where the labels (1) and (2) refer to the two nucleons. In momentum space this diagram then yields the current (we indicate by a 2 that this is a two-particle operator and in second quantization will yield a two-body operator)

$$J_\mu^{(2)}(p_1,p_1',p_2,p_2';q)_{\text{pionic}}=\frac{ieg^2}{(2\pi)^3}\frac{M_N^2}{(E_1E_1'E_2E_2')^{1/2}}(\boldsymbol{\tau}^{(1)}\times\boldsymbol{\tau}^{(2)})_3\delta(\mathbf{p}_1'+\mathbf{p}_2'-\mathbf{p}_1-\mathbf{p}_2-\mathbf{q})(p_1-p_1'+p_2'-p_2)_\mu$$
$$\times[(p_1'-p_1)^2-m_\pi^2+i\varepsilon]^{-1}[(p_2'-p_2)^2-m_\pi^2+i\varepsilon]^{-1}[\bar{U}(\mathbf{p}_1')\gamma_5U(\mathbf{p}_1)][\bar{U}(\mathbf{p}_2')\gamma_5U(\mathbf{p}_2)] , \tag{4.196}$$

where e is the proton charge, g is the pion-nucleon coupling strength [note also that $f^2=(gm_\pi/2M_N)^2/4\pi$], and where $E_1=(|\mathbf{p}_1|^2+M_N^2)^{1/2}$, etc. The two factors containing the pion mass m_π are propagators corresponding to the pion exchanged between nucleon 1 and the photon interaction vertex and between this vertex and nucleon 2. The final two factors contain the nucleon spinors U and $\bar{U}$ and involve γ_5 corresponding to the pseudoscalar coupling. The product of the two pion propagator factors may be rewritten (Dubach *et al.*, 1976) using the Feynman parametrization,

$$\int_{-1/2}^{+1/2}dv\{[\mathbf{p}_1-\mathbf{p}_1'+\tfrac{1}{2}\mathbf{q}(1-2v)]^2+L_\pi^2-i\varepsilon\}^{-2} , \tag{4.197}$$

where

$$L_\pi\equiv[m_\pi^2+\tfrac{1}{4}q^2(1-4v^2)]^{1/2} , \tag{4.198}$$

and where we take the lowest-order nonrelativistic reduction and neglect the nuclear recoil energy (i.e., take $q_0=0$). Doing this as well for the spinor matrix elements leads to the conclusion that, in this limit, the current depends only on $\mathbf{p}_1'-\mathbf{p}_1$ and $\mathbf{p}_2'-\mathbf{p}_2$ for fixed $\mathbf{q}$ and not on these independent momenta. Then, upon Fourier-transforming

$$J_\mu^{(2)}(\mathbf{x}_1,\mathbf{x}_1',\mathbf{x}_2,\mathbf{x}_2';\mathbf{q})_{\text{pionic}}=\frac{1}{(2\pi)^6}\int d\mathbf{p}_1d\mathbf{p}_1'd\mathbf{p}_2d\mathbf{p}_2'\exp[i(\mathbf{p}_1'\cdot\mathbf{x}_1'+\mathbf{p}_2'\cdot\mathbf{x}_2'-\mathbf{p}_1\cdot\mathbf{x}_1-\mathbf{p}_2\cdot\mathbf{x}_2)]J_\mu^{(2)}(\mathbf{p}_1,\mathbf{p}_1',\mathbf{p}_2,\mathbf{p}_2';\mathbf{q})_{\text{pionic}} , \tag{4.199}$$

we may define the coordinate space two-nucleon current corresponding to this "pionic" or "pion-in-flight" diagram by

$$J_\mu^{(2)}(\mathbf{x}_1,\mathbf{x}_1',\mathbf{x}_2,\mathbf{x}_2';\mathbf{q})_{\text{pionic}}=J_\mu^{(2)}(\mathbf{x}_1,\mathbf{x}_2;\mathbf{q})\delta(\mathbf{x}_1'-\mathbf{x}_1)\delta(\mathbf{x}_2'-\mathbf{x}_2) . \tag{4.200}$$

For the three-vector components ($\mu=1,2,3$) of this current (which we need for the magnetic multipole operators) we have

$$\mathbf{J}^{(2)}(\mathbf{x}_1,\mathbf{x}_2;\mathbf{q})_{\text{pionic}}=e(f/m_\pi)^2[\boldsymbol{\tau}^{(1)}\times\boldsymbol{\tau}^{(2)}]_3(\boldsymbol{\sigma}^{(1)}\cdot\boldsymbol{\nabla}^{(1)})(\boldsymbol{\sigma}^{(2)}\cdot\boldsymbol{\nabla}^{(2)})\int_{-1/2}^{+1/2}dv(i\mathbf{q}rv+\mathbf{x})\frac{e^{-x}}{x}e^{i\mathbf{q}\cdot(\mathbf{R}-v\mathbf{r})} , \tag{4.201}$$

where $\mathbf{r}=\mathbf{x}_1-\mathbf{x}_2$ and $\mathbf{R}=\frac{1}{2}(\mathbf{x}_1+\mathbf{x}_2)$ are the relative and center-of-mass coordinates for the nucleon pair, and where we define $\mathbf{x}=L_\pi\mathbf{r}$. Note that for the time component of this current ($\mu=0$), we have to lowest order

$$J_0^{(2)}(\mathbf{x}_1,\mathbf{x}_2;\mathbf{q})_{\text{pionic}}\approx 0 , \tag{4.202}$$

since by Eq. (4.196) it is proportional to $(p_1-p_1'+p_2'-p_2)_0\sim O(p^2/M_N)$ and so is of higher order in an expansion in powers of M_N^{-1}. Thus this meson-exchange current does not contribute to the Coulomb operator to the order we are considering.

Next let us consider Fig. 9(b), which has an intermediate nucleon or antinucleon between the photon-nucleon vertex and one of the pion-nucleon vertices. This contribution is expanded in Fig. 10 into a set of time-ordered

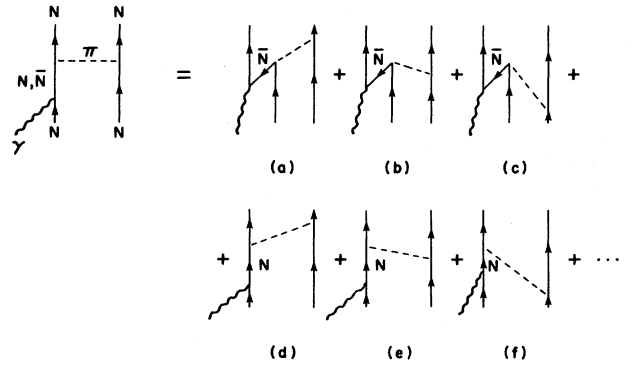

FIG. 10. Decomposition of Fig. 9(b) into time-ordered contributions.

diagrams (the downward-going solid line now represents an antinucleon $\bar{N}$). Figures 10(a)—10(c) are called "pair" diagrams, since the process here is one where the photon creates an $N\bar{N}$ pair, after which the $\bar{N}$ annihilates with another nucleon and creates an (exchange) pion. Such terms give rise to two-body currents and must be included, since they would not exist unless a pion were exchanged. Figures 10(d) and 10(e) are, on the other hand, not proper exchange contributions to the current. These may be cut to separate the one-body electromagnetic part from the simple nucleon binding via one-pion exchange, and this is part of the nuclear force which is handled differently (i.e., we actually use proton and neutron wave functions in a nucleus where NN interactions are incorporated by solving the many-body Schrödinger equation to some level of approximation). Finally, Fig. 10(f) shows a contribution stemming from the interaction with a nucleon that is at the same time exchanging a pion with another nucleon, the so-called "recoil" term. This term can be shown (Chemtob, 1969) to be down by a factor of m_π/M_N compared to the contributions from Figs. 10(a)—10(c); moreover, over much of the q range, this term is canceled by the wave-function renormalization graph. Thus, from all of these diagrams [all parts of Fig. 9(b)], we extract only the pair terms (of course the photon may attach to any of the four nucleon lines). To guarantee that only the $\bar{N}$ line occurs, we need to keep only the negative frequency part of the nucleon propagator and make the replacement (Chemtob and Lumbroso, 1970)

$$\frac{1}{\not{p}-M_N+i\varepsilon}\rightarrow\frac{1}{2E_p}\frac{\beta E_p+\boldsymbol{\gamma}\cdot\mathbf{p}-M_N}{p_0+E_p-i\varepsilon} \tag{4.203}$$

when applying the Feynman rules to these diagrams. The spinor matrix element for the particle labeled 1 then takes the form

$$-\frac{i}{2M_N}\bar{U}(\mathbf{p}_1')\gamma_\mu[\beta E_{p_1'-q}+\boldsymbol{\gamma}\cdot(\mathbf{p}_1'-\mathbf{q})-M_N]\gamma_5 U(\mathbf{p}_1)\ , \tag{4.204}$$

which reduces to

$$\begin{aligned}&\boldsymbol{\sigma}^{(1)}\quad(\mu=1,2,3)\ ,\\ &-\frac{1}{2M_N}\mathbf{q}\cdot\boldsymbol{\sigma}^{(1)}\quad(\mu=0)\ .\end{aligned} \tag{4.205}$$

Thus once again the meson-exchange current makes no contribution to the Coulomb operators in lowest order:

$$J_0^{(2)}(\mathbf{x}_1,\mathbf{x}_2;\mathbf{q})_{\text{pair}}\approx 0\ . \tag{4.206}$$

Upon taking the nonrelativistic limit of the spatial part of this current and neglecting q_0 as before (the details are given in Dubach *et al.*, 1976), and then performing the Fourier transform as above, we find for the pair currents

$$\mathbf{J}^{(2)}(\mathbf{x}_1,\mathbf{x}_2;\mathbf{q})_{\text{pair}}=-ef^2(\boldsymbol{\tau}^{(1)}\times\boldsymbol{\tau}^{(2)})_3[(\boldsymbol{\sigma}^{(1)}\cdot\mathbf{u}_r)\boldsymbol{\sigma}^{(2)}e^{i\mathbf{q}\cdot\mathbf{x}_2}+\boldsymbol{\sigma}^{(1)}(\boldsymbol{\sigma}^{(2)}\cdot\mathbf{u}_r)e^{i\mathbf{q}\cdot\mathbf{x}_1}](1+x_\pi)e^{-x_\pi}/x_\pi^2\ , \tag{4.207}$$

where $\mathbf{u}_r$ is a unit vector in the $\mathbf{r}$ direction and where $x_\pi=m_\pi r$. Note that once again the isospin dependence is contained in the factor $(\boldsymbol{\tau}^{(1)}\times\boldsymbol{\tau}^{(2)})_3$. When the two-body currents generated by taking the sum of these pionic and pair contributions are combined with the usual one-body electromagnetic current discussed above in Secs. IV.A—IV.D, we have a model for the total current to lowest nontrivial order in an expansion in powers of M_N^{-1}. It can be shown (Dubach *et al.*, 1976) that when the nuclear Hamiltonian is taken to be the sum of the one-body kinetic energy and a two-body potential energy which includes the one-pion exchange potential (OPEP),

$$\begin{aligned}V_{\text{OPEP}}=&-\frac{f^2}{m_\pi}(\boldsymbol{\tau}^{(1)}\cdot\boldsymbol{\tau}^{(2)})(\boldsymbol{\sigma}^{(1)}\cdot\boldsymbol{\nabla}^{(1)})\\ &\times(\boldsymbol{\sigma}^{(2)}\cdot\boldsymbol{\nabla}^{(2)})\frac{e^{-x_\pi}}{x_\pi}\end{aligned} \tag{4.208}$$

and any pieces due to the exchange of neutral mesons, then the principle of current conservation is satisfied.

Note that the currents described above [Eqs. (4.201) and (4.207)] have been obtained using point couplings for the NN vertices. In fact, vertex functions can be incorporated into the formalism to reflect the strong interaction dressings that occur (Arenhövel, 1979). This may be done in a variety of ways (Riska, 1980), but care must be taken to maintain the current conservation condition discussed above (Fabian and Arenhövel, 1976). Furthermore, different electromagnetic form factors may be used for the different particles (e.g., nucleons and pions as we have in the contributions discussed above), whereas in many calculations they are all taken to be equal to the single-nucleon electromagnetic form factor. If the former is done, then special provisions must be made to preserve gauge invariance (Friar, 1983).

Next let us turn to the nucleon resonance term [Fig. 9(c)]. For this we quote the results of Dubach (1980) and Chemtob and Rho (1971) without elaborating further on their derivation:[10]

[10]Note that the sign here is the opposite of that in Dubach (1980), where it must be remembered that we always have $\mathbf{q}$ entering the nuclear vertex. This difference in conventions on the direction of $\mathbf{q}$ led to the wrong sign in the above-quoted work (see Hicks, 1982).

$$\mathbf{J}^{(2)}(\mathbf{x}_1,\mathbf{x}_2,\mathbf{q})_{N^*}=i\frac{m_\pi^3}{12M_N}\mu^{(1)}(0)\left\{4h_2\left[(\mathbf{q}\times\mathbf{u}_r)\mathbf{u}_r\cdot(\tau_3^{(2)}\boldsymbol{\sigma}^{(2)}e^{i\mathbf{q}\cdot\mathbf{x}_1}+\tau_3^{(1)}\boldsymbol{\sigma}^{(1)}e^{i\mathbf{q}\cdot\mathbf{x}_2})\left[\frac{d}{dx_\pi}-\frac{1}{x_\pi}\right]\right.\right.$$
$$\left.+\mathbf{q}\times(\tau_3^{(2)}\boldsymbol{\sigma}^{(2)}e^{i\mathbf{q}\cdot\mathbf{x}_1}+\tau_3^{(1)}\boldsymbol{\sigma}^{(1)}e^{i\mathbf{q}\cdot\mathbf{x}_2})\frac{1}{x_\pi}\right]$$
$$-h_1(\boldsymbol{\tau}^{(1)}\times\boldsymbol{\tau}^{(2)})_3\mathbf{q}\times\left[(\boldsymbol{\sigma}^{(1)}\times\boldsymbol{\sigma}^{(2)})(e^{i\mathbf{q}\cdot\mathbf{x}_1}+e^{i\mathbf{q}\cdot\mathbf{x}_2})\frac{1}{x_\pi}\right.$$
$$+[(\boldsymbol{\sigma}^{(1)}\times\mathbf{u}_r)(\boldsymbol{\sigma}^{(2)}\cdot\mathbf{u}_r)e^{i\mathbf{q}\cdot\mathbf{x}_1}-(\boldsymbol{\sigma}^{(2)}\times\mathbf{u}_r)(\boldsymbol{\sigma}^{(1)}\cdot\mathbf{u}_r)e^{i\mathbf{q}\cdot\mathbf{x}_2}]$$
$$\left.\left.\times\left[\frac{d}{dx_\pi}-\frac{1}{x_\pi}\right]\right]\right\}\left[\frac{d}{dx_\pi}\frac{e^{-x_\pi}}{x_\pi}\right], \tag{4.209}$$

where $h_1=0.074m_\pi^{-3}$ and $h_2=0.0658m_\pi^{-3}$ are the couplings used by Chemtob and Rho (1971) to take into account both the Δ_{33} and Roper resonances. In fact, the values of $h_{1,2}$ are mainly given by the Δ_{33}. Note that now we have both charged pion exchange involving the factor $(\boldsymbol{\tau}^{(1)}\times\boldsymbol{\tau}^{(2)})_3$ and π^0 exchange involving the factors $\tau_3^{(1)}$ and $\tau_3^{(2)}$. Since this current may be shown to be divergence free by itself (Villars, 1947; Chemtob and Rho, 1971), it makes no contribution to the continuity equation discussed above. Once again the N^* MEC contributes nothing to the Coulomb operators to the order we are working:

$$J_0^{(2)}(\mathbf{x}_1,\mathbf{x}_2;\mathbf{q})_{N^*}\approx 0\ . \tag{4.210}$$

Then, neglecting contributions from heavier-meson exchanges [Figs. 9(d) and 9(e), for instance] and considering the present set of one-pion-exchange diagrams in lowest order only, we have as total MEC contributions

$$\mathbf{J}^{(2)}(\mathbf{x}_1,\mathbf{x}_2;\mathbf{q})=\mathbf{J}^{(2)}(\mathbf{x}_1,\mathbf{x}_2;\mathbf{q})_{\text{pionic+pair}+N^*}\ , \tag{4.211a}$$

$$J_0^{(2)}(\mathbf{x}_1,\mathbf{x}_2;\mathbf{q})\approx 0\ . \tag{4.211b}$$

This diagrammatic analysis of meson-exchange-current contributions may be pursued to include effects which go beyond the lowest order. For example, expansions to higher order in M_N^{-1} may be studied, relativistic effects may play a role, or heavy-meson exchanges may be incorporated into the formalism. For instance, as the momentum transfer is increased, shorter-range phenomena are expected to be of greater importance.

This is especially relevant for the few-body systems when the measurements extend to high q, and ρ-exchange diagrams for example have been considered in those cases (see Sec. VII). However, for complex nuclei, where the accessible range of momentum transfers is more limited, generally such extensions are not yet felt to be necessary.

To construct second-quantized operators, as in Eq. (4.89), we require two-particle reduced matrix elements of these currents. First, let us note the isospin dependence occurs in two (purely isovector, $T=1, M_T=0$) forms:

$$\mathscr{T}_{10}^{(12)}\equiv\frac{i}{2}(\boldsymbol{\tau}^{(1)}\times\boldsymbol{\tau}^{(2)})_3$$
$$=\tau_-^{(1)}\tau_+^{(2)}-\tau_+^{(1)}\tau_-^{(2)}\ ,$$
$$\mathscr{T}_{10}^{(n)}\equiv\tau_3^{(n)},\quad n=1,2\ . \tag{4.212}$$

Their reduced matrix elements are simply obtained:

$$\langle(\tfrac{1}{2}\tfrac{1}{2})\mathscr{T}'||\mathscr{T}_1^{(12)}||(\tfrac{1}{2}\tfrac{1}{2})\mathscr{T}\rangle=\sqrt{3}(\delta_{\mathscr{T}'0}\delta_{\mathscr{T}1}+\delta_{\mathscr{T}'1}\delta_{\mathscr{T}0})\ , \tag{4.213}$$
$$\langle(\tfrac{1}{2}\tfrac{1}{2})\mathscr{T}'||\mathscr{T}_1^{(n)}||(\tfrac{1}{2}\tfrac{1}{2})\mathscr{T}\rangle=\sqrt{3}[(-)^n(\delta_{\mathscr{T}'0}\delta_{\mathscr{T}1}-\delta_{\mathscr{T}'1}\delta_{\mathscr{T}0})+\sqrt{2}\delta_{\mathscr{T}'1}\delta_{\mathscr{T}1}]\ .$$

In dealing with the rest of the dependence in the operators we wish to make multipole projections in the usual way [Eq. (4.28)]. In fact, in the expressions for the meson-exchange currents above we have Fourier transformed from $\mathbf{x}$ dependence to $\mathbf{q}$ dependence and, after a little manipulation, we can write equivalently

$$T_{JM_J}^{(2)\text{mag}}(\mathbf{x}_1,\mathbf{x}_2;q)=\frac{1}{4\pi}(-i)^J\int d\Omega_q[Y_J(\Omega_q)\otimes J^{(2)}(\mathbf{x}_1,\mathbf{x}_2;\mathbf{q})]_J^{M_J}\ , \tag{4.214}$$

where $\mathbf{J}^{(2)}(\mathbf{x}_1,\mathbf{x}_2;\mathbf{q})$ is the sum of the MEC contributions discussed above (and is a rank one or three-vector operator) and where we have suppressed the isospin dependence for clarity. The two-particle matrix elements required in Eq. (4.89) may then be calculated. While this is straightforward in principle, it is in practice rather tedious, usually involving a Brody-Moshinsky (1960) transformation to the relative and center-of-mass coordinates of the pair of particles and requiring considerable nontrivial Clebsch-Gordanry (Dubach *et al.*, 1976; Dubach, 1980; for another approach see Suzuki and Hyuga, 1983). We shall not pursue these developments any further in the present review.

As in the treatment of one-body electromagnetic opera-

tors, the problem factors into one- and two-particle matrix elements, which we have now discussed, and one- and two-body density-matrix elements, which contain the detailed nuclear many-body problem input into the entire nuclear matrix elements. The one-body formalism proceeded from Eq. (4.86); now the two-body contributions are to be calculated using Eq. (4.92), with the two-body density-matrix elements defined in Eq. (4.93). Equivalently (and this is what was done, for example, by Dubach *et al.*, 1976), one may use coefficients of fractional parentage (de Shalit and Talmi, 1963). In fact it is necessary in general to consider operators with arbitrary ranks, which require an extension of the usual formalism as it applies to the special case of the two-body nuclear potential (Glaudemans *et al.*, 1964). Rather than discuss this approach further, let us conclude this section by considering the two-body density-matrix elements in one special case where the nuclear structure is very simple.

Let us return to a configuration which has one particle above a 0^+0 $N=Z$ closed shell $|\tilde{0}\rangle$, previously discussed within the context of one-body operators in Sec. IV.C [see Eq. (4.138a)]. Using this as the ground state and taking matrix elements as in Eq. (4.93), we find that

$$\Psi^{1p}_{J;1}((a'b')\mathscr{J}'\mathscr{T}';(ab)\mathscr{J}\mathscr{T})=\left[\delta_{\mathscr{T}'1}\delta_{\mathscr{T}1}-\frac{1}{\sqrt{2}}(\delta_{\mathscr{T}'0}\delta_{\mathscr{T}1}+\delta_{\mathscr{T}'1}\delta_{\mathscr{T}0})\right][\mathscr{J}'][\mathscr{J}]\sum_{a_x\le F}\begin{Bmatrix} j_p & j_p & J \\ \mathscr{J}' & \mathscr{J} & j_x \end{Bmatrix}$$

$$\times[\delta_{a'a_p}\delta_{b'a_x}-(-)^{\mathscr{J}'+\mathscr{T}'}(-)^{j_p-j_x}\delta_{a'a_x}\delta_{b'a_p}][\delta_{aa_x}\delta_{ba_p}-(-)^{\mathscr{J}+\mathscr{T}}(-)^{j_p-j_x}\delta_{aa_p}\delta_{ba_x}]\,, \quad (4.215)$$

where we are only interested in isovector operators and so have taken $T=1$, and where we consider only cases with $J=$odd. Clearly the single-particle labels (a', b', a, and b) are contracted together so that two become the quantum numbers of the valence particle a_p ($\varepsilon_a>\varepsilon_F$) and two become those of a core particle a_x ($\varepsilon_x\le\varepsilon_F$).

Now if this two-body density matrix is used with the two-particle matrix elements discussed above, we have two situations to discuss, $\pi^\pm$ exchange involving $\mathscr{J}^{(12)}_{10}$ and π^0 exchange involving $\mathscr{J}^{(n)}_{10}$, $n=1,2$ [see Eq. (4.212)]. This leads to (see also Dubach, 1980)

$$\langle 1p{:}J_0;T_0{::}\hat{T}^{(2)\text{mag}}_{J;1}(q){::}1p{:}J_0;T_0\rangle_{\pi^\pm\text{ exchange}}=-2\sqrt{6}\sum_{\mathscr{J}'\mathscr{J}}[\mathscr{J}'][\mathscr{J}]\sum_{a_x\le F}\begin{Bmatrix} j_p & j_p & J \\ \mathscr{J}' & \mathscr{J} & j_x \end{Bmatrix}\langle(j_pj_x)\mathscr{J}'||T^{(2)\text{mag}}_J(q)||(j_xj_p)\mathscr{J}\rangle\,, \quad (4.216)$$

$$\langle 1p{:}J_0;T_0{::}\hat{T}^{(2)\text{mag}}_{J;1}(q){::}1p{:}J_0;T_0\rangle_{\pi^0\text{ exchange}}$$

$$=-2\sqrt{6}(-)^n\sum_{\mathscr{J}'\mathscr{J}}(-)^{\mathscr{J}}[\mathscr{J}'][\mathscr{J}]\sum_{a_x\le F}(-)^{j_p-j_x}\begin{Bmatrix} j_p & j_p & J \\ \mathscr{J}' & \mathscr{J} & j_x \end{Bmatrix}\langle(j_pj_x)\mathscr{J}'||T^{(2)\text{mag}}_J(q)||(j_pj_x)\mathscr{J}\rangle\,,\ n=1,2\,. \quad (4.217)$$

Here $J_0=j_p$ and $T_0=\frac{1}{2}$ [we are using the ground state given in Eq. (4.138a)], and we have explicitly taken care of the isospin dependence in these matrix elements, leaving only matrix elements reduced in angular momentum. Note that only exchange terms can contribute in Eq. (4.216) and only direct terms in Eq. (4.217). In fact, looking even more closely at the isospin content in the problem, in the case of the $\pi^\pm$-exchange terms (the pionic, pair, and part of the N^* diagrams), if j_p refers to an odd valence proton, then the sum over a_x within the Fermi sea involves only neutrons and vice versa. In the case of the π^0-exchange terms (the rest of the N^* diagram), the sum extends over the entire Fermi sea in both cases.

V. ILLUSTRATIVE EXAMPLES

This section is of rather special character. It is intended to give a few examples of the physics accessible via magnetic electron scattering. This section is oriented towards the reader who is not interested in details, the smaller effects, or a quantitative comparison of theory and experiment. For a more thorough discussion, the interested reader is referred to Secs. VI and VII. Here, only a qualitative and superficial sketch of the physics of magnetic elastic form factors is given.

A. Configuration mixing

The first example we want to present concerns the magnetic form factor of ^{13}C. This nucleus has a spin of $\frac{1}{2}^-$, which makes the interpretation of magnetic form factors particularly straightforward. The only multipolarity that can contribute is $M1$. For most nuclei, with spin $J_0>\frac{1}{2}$, the multipoles $M1,M3,\ldots,2J_0$ contribute to the magnetic form factor. While charge and magnetic form factors can be separated via Rosenbluth plots, individual multipolarities cannot be separated experimentally unless polarization observables are measured (see Sec. VIII). An incoherent sum over different multipolarities containing different bits of physics obviously complicates

the interpretation.

For ^{13}C, the dominant configuration is that of a $1p_{1/2}$ neutron outside a closed ^{12}C core. However, this configuration has a spectroscopic factor of only 0.81 (Gubler *et al.*, 1977), and so other configurations cannot be neglected. The next dominant configuration involves an unpaired $p_{3/2}$ nucleon coupled to some excited state of the $A=12$ core. The shell-model calculation of Cohen and Kurath (1965) clearly shows the importance of this configuration.

For the qualitative discussion given here we shall restrict ourselves to configurations involving only unpaired $p_{1/2}$,$p_{3/2}$ nucleons, and we shall ignore the difference between protons and neutrons (for a detailed discussion see Sec. VI). In this case the magnetic form factor retains a very simple structure [see Eq. (4.130)],

$$F_{M1}(q) \sim \langle 1p \,|\, j_0(qr) - \alpha j_2(qr) \,|\, 1p \rangle \tag{5.1}$$

with

$$\langle \,|\, | \,\rangle = \int_0^\infty R^2(r) r^2 j_l(qr) dr \ . \tag{5.2}$$

Here $R(r)$ is the radial wave function, assumed to be identical for $p_{3/2}$ and $p_{1/2}$ nucleons. The coefficient α depends on the coupling scheme and the amount of configuration mixture in the ground-state wave function. Specifically, $\alpha=2$ for jj coupling, $\alpha=0.29$ for LS coupling, and $\alpha=1.18$ for the Cohen-Kurath wave function (Bernabeu and Ros, 1974; Lapikás *et al.*, 1975). An overall factor in front of the matrix element in Eq. (5.1) also depends on the coupling scheme. If this factor and $b_{\rm osc}$ are fine tuned to fit the low-q data, then one obtains the curves shown in Fig. 11 (Hicks *et al.*, 1982). It should be noted that the curves in Fig. 11 have been obtained with different values for the radial parameter (b or r_0) in order to reproduce the position of the diffraction minimum.

Ignoring for the moment the experimental data, we note that F_M is very sensitive to the single-particle configuration assumed. The form factors for the two extreme models differ by more than a factor of 10. This is to be contrasted with the charge form factor which, in the simple-minded model used here, would not depend at all on the configuration mixture; even for a more realistic model, $F_{\rm ch}$ would be quite insensitive to such nuclear structure effects.

The agreement between theoretical prediction and experiment in Fig. 11 is not good for $q>1$ fm^{-1}. This is due to the fact that, for such a weakly bound neutron, a harmonic-oscillator wave function is obviously too primitive. Using a more realistic radial wave function calculated in a Woods-Saxon potential well leads to a much larger F_M for $q>2$ fm^{-1} and allows a better, though not perfect, fit to the data (Fig. 11).

It is clear that the above interpretation of the data is deficient in several ways. In particular, the neglect of configurations other than $1p$ is doubtful. This neglect is probably responsible for the lack of fit for $q>2.5$ fm^{-1}. For the present purpose this does not change things in a decisive way. Figure 11 shows that F_{M1} strongly depends on the exact configuration of the unpaired nucleon. This results from the fact that magnetic form factors contain interference terms involving different components of the ground-state wave function. $M1$ transitions provide excellent observables for the study of spin-flip $j=1+\frac{1}{2} \leftrightarrow j=1-\frac{1}{2}$ transitions. Such interference terms are responsible for the high sensitivity of magnetic scattering, and have led us to think of magnetic form factors as configuration analyzers (Donnelly and Gökalp, 1981).

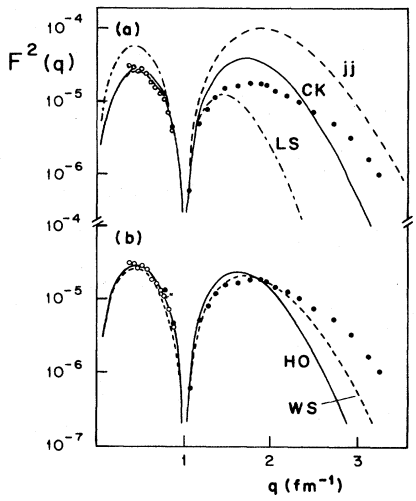

FIG. 11. Elastic magnetic electron scattering from ^{13}C. (a) Data for the $M1$ form factor $F_T^2 Z^2/4\pi$ of ^{13}C with predictions using harmonic-oscillator wave functions and different coupling schemes. (b) The effect of using a more realistic Woods-Saxon wave function (Hicks *et al.*, 1982).

B. Radial wave functions and high multipolarity

As a second example involving magnetic scattering we discuss nuclear moments of very high multipolarity. Here we try to go to the extreme opposite of the previous example and suppress the effect of configuration admixtures on $F(q)$ to the highest possible degree. If this is possible, then the momentum-transfer dependence of $F(q)$ can be exploited for a determination of the valence nucleon radial wave functions (Sick, 1980).

Having shown in the previous ^{13}C example the strong sensitivity of magnetic form factors to configuration mixing, we find that it is not immediately obvious how to eliminate this sensitivity. To understand how this can be done we shall consider a nucleus that has one unpaired particle (or hole) outside a closed shell. We assume that the j value of this nucleon ($j=l+\frac{1}{2}$) is the highest of all occupied shells, and that the ground-state spin J_0 is rather large ($\frac{7}{2},\frac{9}{2},\ldots$). For this particular case we can easily show that the form factor of the highest allowed multipolarity $\Lambda=2J_0$ has a strikingly different sensitivity from that discussed above (Donnelly and Walecka, 1973a).

The electromagnetic interaction being very weak, the electron interacts only with one nucleon at a time. Moreover, magnetic scattering of multipolarity $2J_0$ corresponds to a complete spin-flip of the nucleus. Consequently, this form factor cannot receive any contribution from shells with $j<J_0$. The nuclear ground state will contain, for example, $2p2h$ admixtures even for "closed-shell" nuclei. Most of these will concern states with $j<J_0$ (since J_0 is large) and will not contribute to multipolarity $2J_0$. Only those $2\hbar\omega$ excitations including states with $j\geq J_0$ will give a nonzero contribution to this form factor. A quantitative study of such excitations (Arita, 1977; Platchkov *et al.*, 1982) shows that for selected cases involving large multipolarity Λ their contribution is negligible at the present level of precision.

If $F_{M\Lambda}$ is indeed very insensitive to configuration admixtures, then the shape of $F(q)$ gives direct and precise information on the radial wave function of the valence nucleon. The equation

$$F_{M\Lambda}(q)=\text{const}\times\int R^2(r)j_{\Lambda-1}(qr)r^2dr \tag{5.3}$$

shows the direct relationship of $F_{M\Lambda}$ to $R^2(r)$. Equation (5.3) applies in particular near the main lobe of the $M\Lambda$ form factor, which results from the optimal overlap of the (surface) peak of $R^2(r)$ and the pronounced first maximum of $j_{\Lambda-1}(qr)$. A plot of $R^2(r)$ and $j_{\Lambda-1}(qr)$ for $\Lambda=9$ and two values of q is shown in Fig. 12 for a $1g_{9/2}$ neutron radial wave function. For $q\sim2.5$ fm^{-1} there is a strong constructive interference that is important in suppressing wave-function admixtures that show up mainly via the interference of smaller components responsible for diffraction minima and secondary maxima of F_M.

Magnetic form factors of very high multipolarity, $M7$,$M9$, are rather exotic subjects, and their geometric structure is less than obvious. For **J** aligned parallel to the z axis, the direction of the magnetization $\boldsymbol{\mu}(\mathbf{r})$ is parallel to the z axis. The radial dependence of the magnetization density is shown in Fig. 12. The azimuthal structure of $|\boldsymbol{\mu}(\mathbf{r})|=\mu(\mathbf{r})$ is determined by the corresponding spherical harmonic. We can represent this angular part by the length of the radius vector defining a closed surface. To avoid negative radii we shall take for values of $\mu(\mathbf{r})$ the difference between this radius and that of the unit sphere. The resulting surface (Sick, 1980) is shown in Fig. 13. It allows one to visualize the $M9$ magnetization density in the same way we usually employ to represent a quadrupole deformation by an ellipsoid.

Although these magnetic form factors of high multipolarity are somewhat exotic, they can actually be observed experimentally without too much difficulty (Li *et al.*, 1970). The main maximum of $F_{M\Lambda}$ occurs at large q (~3 fm^{-1}), where the charge form factor(s) and magnetic form factors of lower multipolarity have already become quite small. As an example, the $M7$ form factor of ^{51}V, a nucleus with an unpaired $f_{7/2}$ proton, can be observed even at $\theta=155°$, as shown by Fig. 14 (Platchkov *et al.*, 1982). The main peak of the $M7$ form factor stands out clearly and can be analyzed with little ambiguity.

From the $F_{M\Lambda}$ form factor, the rms radius of the corresponding radial wave function has been extracted with an accuracy of $\sim1\%$. The calculation of configuration mixing (Arita, 1977) shows that wave-function components with $j>J_0$ lead to changes of the extracted rms radius of $<1\%$. The meson-exchange-current contributions give a non-negligible effect that, expressed in terms of a change of rms, amounts to $\sim2\%$. Using modern calculations

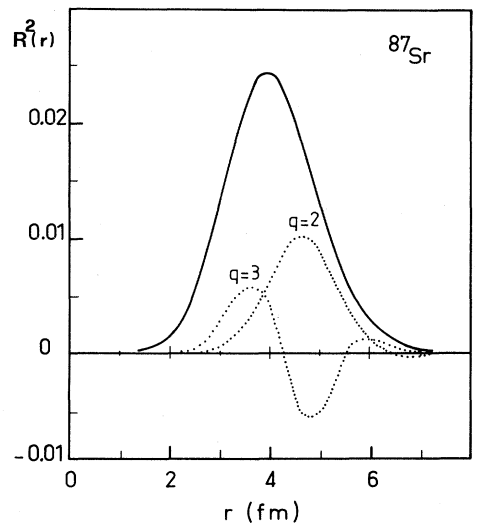

FIG. 12. $1g_{9/2}$ radial wave function squared of ^{87}Sr (solid curve) together with remainder of integrand [Eq. (5.3)] for two momentum transfers.

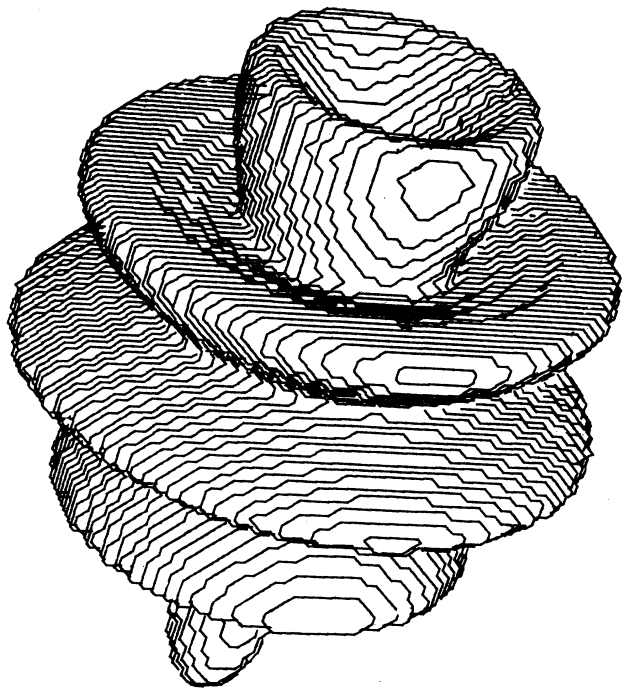

FIG. 13. Angular shape of the 2^9 pole (pentekosiadodekapole), magnetization density.

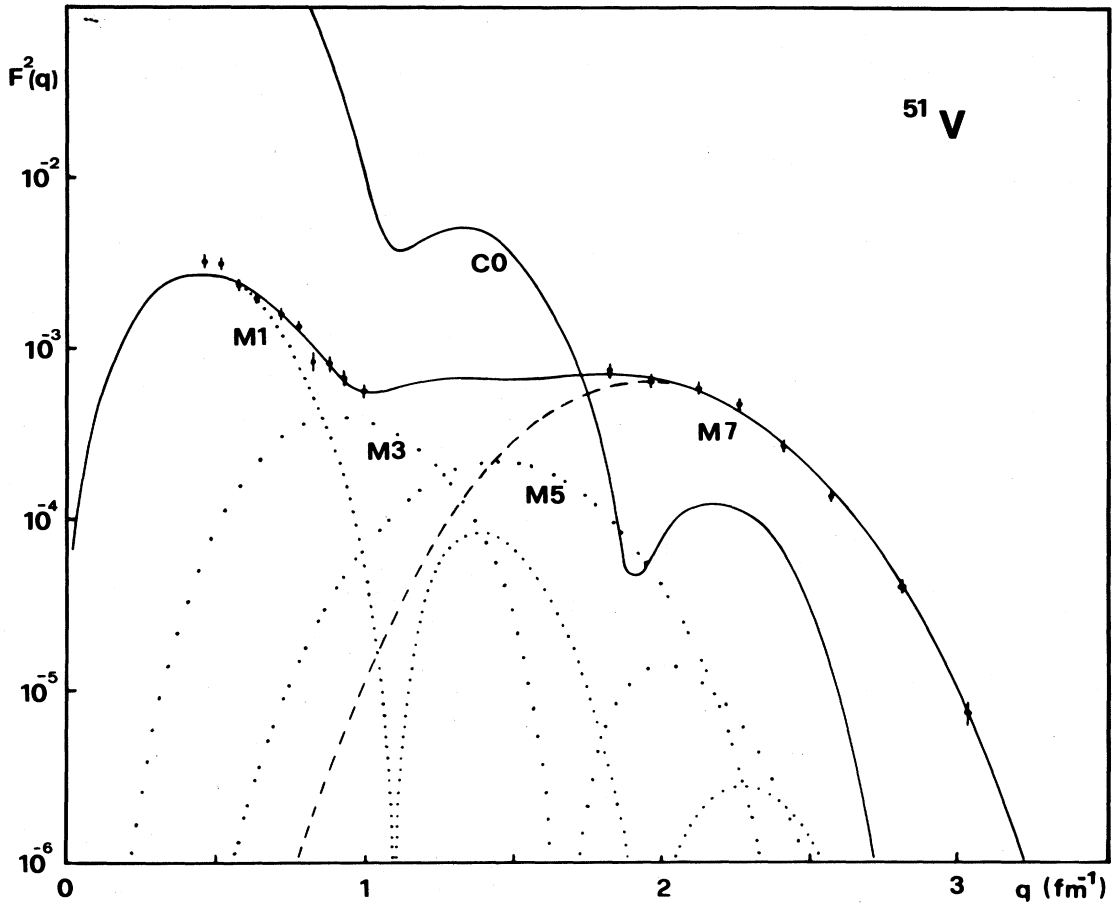

FIG. 14. The magnetic form factor $F_T^2 4\pi$ of ^{51}V (solid curve), together with the contribution of individual multipoles. The charge form factor contribution CO is given for a scattering angle of $\theta = 155°$.

(Mathiot and Desplanques, 1980), one can correct for this MEC contribution with an uncertainty of perhaps $\sim 1\%$ in the final rms radius. These numbers demonstrate that by appropriate choice of nucleus, multipolarity, and momentum transfer, the radial-wave-function sensitivity of magnetic scattering can be enhanced such that all other influences get reduced to manageable "corrections."

It is clear that such a precise measurement of the radial wave function $R(r)$ can be performed for a few special cases only. Even this limited information is most valuable, however. For unpaired neutrons, it provides the least ambiguous information on the neutron radial distribution (Sick *et al.*, 1977). For the interpretation of the many nuclear reactions that depend on a precise knowledge of $R(r)$—nucleon transfer reactions in particular—these cases can serve as valuable benchmarks (Dieperink and Sick, 1982).

C. Coupling to a deformed core

Our third example concerns the magnetic form factor of strongly deformed nuclei. With this case we want to illustrate that magnetic form factors not only provide information on the valence nucleon(s); they can also reveal very interesting properties of the core. On deformed nuclei, there is at present little work available from electron scattering. For charge scattering this is because of the extremely good energy resolution required to resolve levels at large q; only recently could the relative energy resolution be pushed down to a few times 10^{-5}, and a number of deformed nuclei be studied (Bertozzi, never to be published). For magnetic scattering, the smallness of the magnetic cross sections further complicates things. Investigations of deformed nuclei by magnetic electron scattering therefore at present are more characterized by promise than by achievements.

Two bits of physics are of particular interest. For even-even deformed nuclei, the magnetic form factor yields a measurement of the current distribution related to the collective rotation. A study of these current distributions is expected to allow much better insight into the way the deformed nuclei rotate. For odd-A nuclei the strong coupling of the unpaired nucleon to the deformed core is a subject of particular interest. For both problems, it is clear that the magnetic elastic form factor should not be considered in an isolated way, but combined with results on the magnetic form factors of the ground-state rotation-

al band; these form factors contain similar information. As in the case of charge form factors (Rad *et al.*, 1978), they can be expected to provide a powerful tool useful in disentangling the various charge and current distributions.

As an example, Fig. 15 shows the elastic magnetic form factor of ^{181}Ta, a nucleus with an unpaired $g_{7/2}$ proton. The magnetic form factors for two levels of the ground-state rotational band are given as well. The data in Fig. 15 (Rad *et al.*, 1980) are compared to predictions obtained from Hartree-Fock calculations (Moya de Guerra and Kowalski, 1980) performed using the pair-filling approximation. The result for the magnetic form factor of a $1g_{7/2}$ proton in the spherical shell model is indicated as well.

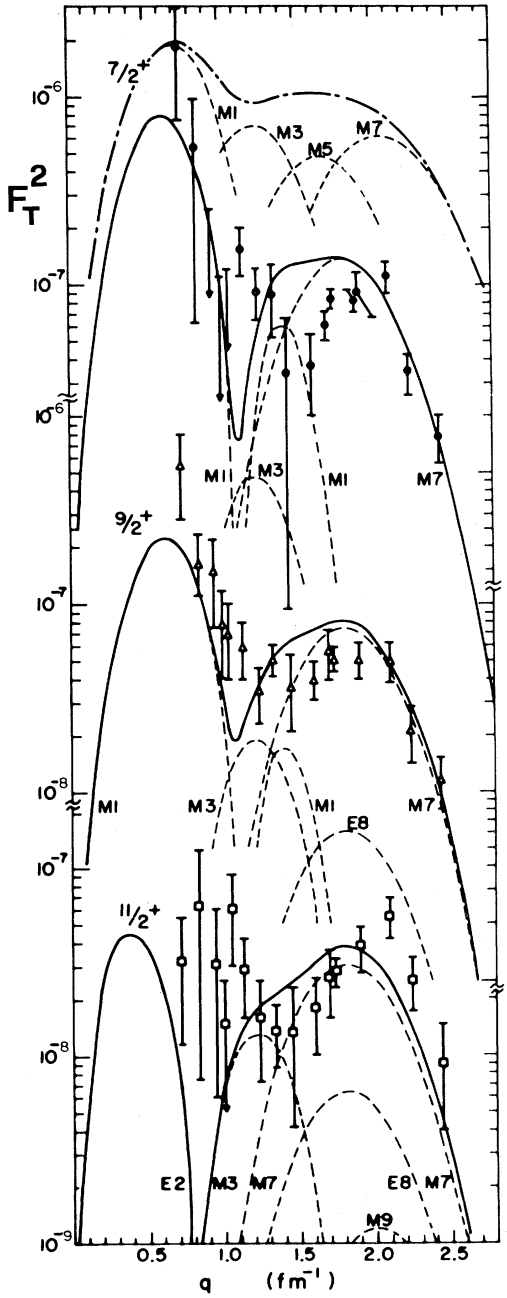

FIG. 15. Magnetic form factors for the ^{181}Ta ground-state rotational band. The solid curves are calculated using projected Hartree-Fock theory; the dotted-dashed curve corresponds to a $1g_{7/2}$ proton in a spherical harmonic-oscillator potential (Rad *et al.*, 1980).

Figure 15 shows that the coupling of the nucleon to the deformed core has a drastic effect on the magnetic form factor. For example, the highest multipolarity, $M7$, is changed by a factor of 4. This large change is due to the fact that some of the strength previously accounted for in the spherical limit has gone into inelastic scattering to states in the rotational band built on the deformed ground state. In addition, the very nature of the deformed states differs in a significant way from their spherical limit: states with different K appear as distinctly different configurations, only one of which approximates the specific deformed ground state. And yet several such states with different K all merge in the spherical limit. Indeed, each predicts drastically different relative strengths for the various magnetic multipoles. The large change of F_M between spherical and deformed calculations clearly indicates that F_M is a very sensitive tool for the study of particle-core coupling.

The calculation of $F_M(q)$ (Moya de Guerra and Kowalski, 1980) points out another interesting feature: The $M1$ form factor receives a large contribution from the convection current, which dominates over the intrinsic magnetization by a factor of 4. This reverses the usual relative contributions of convection current and intrinsic magnetization, and shows that the current distribution can indeed be measured once experiments of this type become feasible on a more routine basis. At the low momentum transfers, the collective contribution to $F_{M\Lambda}$ for inelastic scattering is also expected to show up in the transverse $E2$ form factor.

D. Meson-exchange currents

Our last example is intended to illustrate magnetic electron scattering from a very different viewpoint. This example deals with the sensitivity of magnetic form factors to the presence of meson-exchange currents (MEC) in nuclei. This topic has received increased attention recently, since it has become progressively clear that non-nucleonic degrees of freedom in nuclei are important for a quantitative understanding of nuclear properties.

The contribution of non-nucleonic nuclear constituents, such as π, Δ, etc., is in general hard to separate from the usual nucleonic effects. In particular, for processes involving strongly interacting probes (or reaction products), the uncertainties in multistep reaction mechanisms often cover up the effects of interest. For electron scattering, on the other hand, the reaction mechanism is sufficiently well understood to allow a search for more "exotic" effects. If, by appropriate choice of nucleus and type of form factor, the meson-exchange contribution can be

enhanced significantly over the (usually dominant) one-body contribution, then electron scattering can be the ideal tool for the study of MEC.

Magnetic electron scattering is particularly suitable for the study of MEC. The magnetization density of a nucleus receives a zeroth-order contribution from the currents connected, for example, to the presence of π, and so to the dominating one-pion-exchange nature of the NN force. Normally this contribution is of the order of, say, 10% of the magnetic moment. Such a contribution is very difficult to isolate in the presence of nuclear structure uncertainties such as configuration mixing, even for the case of near-magic nuclei. These difficulties do not occur for the $M1$ form factor of ^{3}He. At large momentum transfer, a cancellation reduces the one-body form factor by orders of magnitude. For such a case, the MEC effect dominates the total form factor and can be isolated.

The one-body (nucleon-only) magnetic form factor of ^{3}He can be calculated with reasonable confidence. The exact (though numerical) solutions of the Faddeev equations for a given nucleon-nucleon potential yield quite reliable results for the medium-range observables. The $M1$ magnetic form factor receives two contributions from the S-to-S state and the S-to-D state transitions. This latter contribution dominates F_{M1} at large q; in the charge form factor, in the absence of S-D interferences, the short-range S-S amplitude would dominate. All predictions for the ^{3}He one-body magnetic form factor yield a pronounced diffraction minimum at medium momentum transfer, $q \sim 2.5$ fm^{-1} (see Fig. 16).

The experimental data (Cavedon *et al.*, 1982) strongly deviate from these predictions. A diffraction minimum occurs only near $q = 3.5$ fm^{-1}, and the magnitude of the second maximum is 50 times lower than the one predicted by Faddeev calculations (Laverne and Gignoux, 1973).

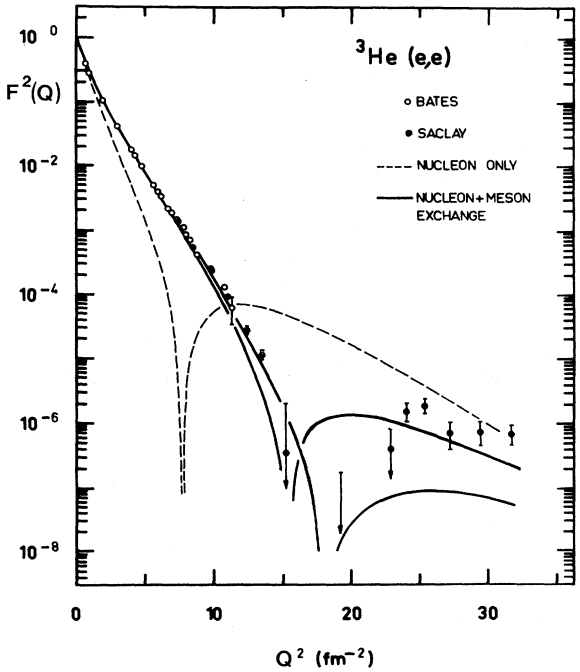

FIG. 16. Magnetic form factor $8\pi M_N^2 F_T^2/q^2\mu^2$ of ^{3}He. The dashed curve ignores non-nucleonic contributions; the two solid curves include meson-exchange effects.

To understand the experimental data, one must include the interaction of the electron with π or Δ in the nucleus. These MEC contributions are rather large for two reasons: (1) Very small values of the one-body magnetic form factor occur at large q, since the higher multipoles that usually cover up the small $M1$ contribution at large q are not allowed ($J_0^{\pi_0} = \frac{1}{2}^+$). (2) ^{3}He has an appreciable D-state component ($\sim 9\%$), which enhances the S-D interference that dominates in the resonance term.

The inclusion of MEC contributions (Riska, 1980) yields quite acceptable agreement with experiment. Figure 16 demonstrates that by suitable choice of q, J, and A magnetic scattering can be an excellent tool for isolating MEC contributions to a point where a quantitative study becomes possible.

VI. RESULTS FOR NUCLEI WITH $A > 4$ ▲

A. 1p-shell nuclei

In this section we describe what is known about elastic magnetic electron scattering from 1p-shell nuclei. All of the practical (i.e., stable) cases have been studied experimentally, and we catalog all known data here. For some of these nuclei a variety of nuclear models have been applied, and so we show how some of the theoretical calculations fare in comparisons with experimental data. In fact the 1p shell is somewhat special in this regard, since shell-model calculations (Cohen and Kurath, 1965) have been available for some time now. Allowing the 1p shell to be fully active does not lead to an overly large model space as it does for higher major shells (see below). Alternatively, other nuclear models (cluster model, Faddeev three-body model) can be applied in certain cases, and we refer to some of these where appropriate.

1. The nucleus ^{6}Li

We begin our discussion of the 1p shell with the first stable ground state beyond ^{4}He, namely, ^{6}Li. In fact it is not typical of what we shall be discussing in most of this review: it is an odd-odd nucleus, whereas the vast majority of cases we consider are odd-even or even-odd nuclei. Only four stable odd-odd nuclei exist, ^{2}H (discussed in Sec. VII.A) and ^{6}Li, ^{10}B, and ^{14}N (discussed in this section). The small number of density-matrix elements needed to describe ^{6}Li in the p-shell space then makes a phenomenological analysis of the data possible. As we saw in Sec. IV.E, the leading MEC effects are of an isovector nature, and consequently we do not expect meson-exchange currents to be important for elastic magnetic electron scattering from ^{6}Li (possibly) until very high momentum transfers are reached. Thus we shall ignore MEC effects for elastic scattering from ^{6}Li (and also ^{10}B

and ^{14}N) for the same reason, viz., $T_0=0$.

Let us begin by showing the data in Fig. 17. The earliest major measurements were taken at Stanford by Rand *et al.* (1966), using the 180° scattering system. A 0.259 g/cm^2 target of enriched ^{6}Li with a 0.7% ^{7}Li impurity was used in this experiment. At the energies considered (up to $\varepsilon=140$ MeV) there are large corrections from elastic charge scattering because of the small magnetic moment of ^{6}Li ($\mu=0.82$ n.m.), which yields a relatively small elastic magnetic form factor. Indeed, for energies above 120 MeV, the small impurities of ^{7}Li in fact dominate (the magnetic moment of ^{7}Li is large $\mu=3.26$ n.m.), resulting in large error bars for the higher momentum transfers explored. In this experiment momentum transfers $q=0.85$–1.39 fm^{-1} were covered. Somewhat later the low-q range ($q<0.9$ fm^{-1}) was studied at the (former) Institute voor Kernphysisch Onderzoek (IKO) by Lapikás (1978), also using a 180° scattering system. More recently Bergstrom *et al.* (1982) performed an experiment at Bates covering the range $q=0.8$–2.8 fm^{-1}, that is, extending over the diffraction minimum at $q=1.41$ fm^{-1} and spanning the second maximum (see Fig. 17). Again a 180° scattering system was employed (Peterson *et al.*, 1979) for some of the measurements, to suppress as much as possible the sizable Coulomb contributions found at energies below 200 MeV. At higher energies the Coulomb form factor decreases rapidly, allowing measurements to be made at scattering angles of 150°–160°, where targets could be oriented in the transmission mode to achieve optimum resolution and counting rates. For the data shown in Fig. 17 no corrections were made for Coulomb distortion effects.

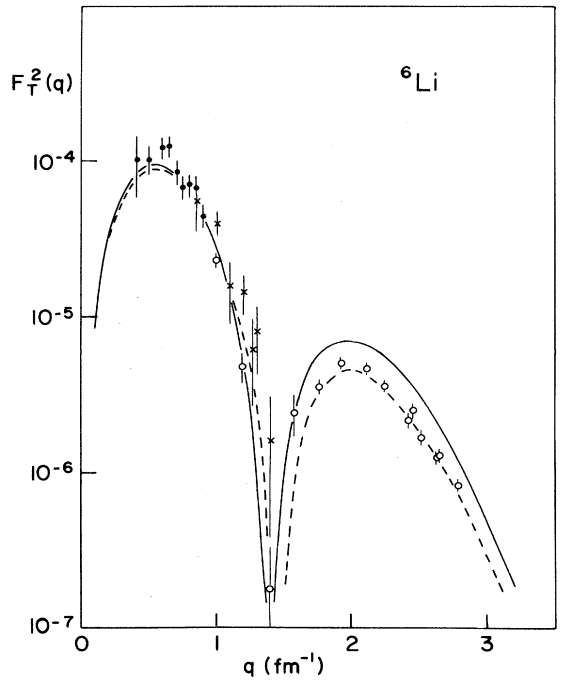

FIG. 17. The ^{6}Li data of Lapikás (1978) (solid circles), Rand *et al.* (1966) (crosses), and Bergstrom *et al.* (1982) (open circles), shown together with calculations (solid curve) using Cohen-Kurath (1965) (8-16)POT matrix elements and fitted Woods-Saxon radial wave functions ($r_0=1.52$ fm). The dashed curve is calculated using the same radial wave function and the phenomenological matrix elements of Donnelly and Walecka (1973b).

Let us now turn to a theoretical discussion and begin by describing the ground state of ^{6}Li in terms of two particles in the $1p$ shell, with a closed $1s$-shell core (^{4}He). Following Donnelly and Walecka (1973b), we use j-j coupling and write (see also Bergstrom *et al.*, 1982, for an L-S coupling description)

$$|1^+0\rangle = A\,|(p_{3/2})^2;1^+0\rangle + B\,|p_{3/2}p_{1/2};1^+0\rangle + C\,|(p_{1/2})^2;1^+0\rangle\ , \tag{6.1}$$

with the normalization condition

$$A^2+B^2+C^2=1\ . \tag{6.2}$$

Using the standard formalism discussed in Sec. IV [in particular, evaluating Eq. (4.87) with this ground state], we can show that the ground-state one-body density matrix has the form (see Donnelly and Peccei, 1979)

$$\begin{aligned}\psi_{0;0}((p_{3/2})^2)&=\sqrt{3/2}(A^2+\tfrac{1}{2}B^2)\ ,\\ \psi_{0;0}((p_{1/2})^2)&=\sqrt{3}(\tfrac{1}{2}B^2+C^2)\ ,\end{aligned} \tag{6.3a}$$

with $\psi_{0;0}((1s_{1/2})^2)=2\sqrt{3}$,

$$\begin{aligned}\psi_{1;0}((p_{3/2})^2)&=\frac{1}{\sqrt{5}}A^2+\frac{\sqrt{5}}{4}B^2\ ,\\ \psi_{1;0}((p_{1/2})^2)&=-\frac{1}{2\sqrt{2}}B^2+\sqrt{2}C^2\ ,\end{aligned} \tag{6.3b}$$

$$\begin{aligned}\psi_{1;0}(p_{3/2}p_{1/2})&=-\psi_{1;0}(p_{1/2}p_{3/2})\\ &=\frac{\sqrt{10}}{4}AB-\tfrac{1}{2}BC\ ,\\ \psi_{2;0}((p_{3/2})^2)&=-\frac{2\sqrt{3}}{5}A^2+\frac{\sqrt{3}}{4}B^2\ ,\\ \psi_{2;0}(p_{3/2}p_{1/2})&=-\psi_{2;0}(p_{1/2}p_{3/2})\\ &=-\frac{\sqrt{3}}{2\sqrt{10}}AB-\frac{\sqrt{3}}{2}BC\ .\end{aligned} \tag{6.3c}$$

Note that the special identities [Eqs. (4.128)] are automatically satisfied, as they should be. If we now use Eq. (4.134a) for the ground-state magnetic dipole moment, with Eq. (4.120) for B_1 and Eq. (4.121) for D_1^-, and with Eq. (4.133) for the density-matrix elements used in the expression for μ, we obtain

$$\mu=\tfrac{1}{3}\{[A^2+\tfrac{3}{4}B^2+2C^2+(\sqrt{5/2}A-C)B] +\mu^{(0)}(0)[A^2+\tfrac{3}{2}B^2-C^2-2(\sqrt{5/2}A-C)B]\}\ . \tag{6.4}$$

Using the experimental value of the magnetic moment, one then has a second relationship in addition to the normalization condition, Eq. (6.2), involving the amplitudes

A, B, and C. Furthermore, it is possible to write a similar expression for the ground-state quadrupole moment in this $1p$-shell model. This is obtained by taking the long-wavelength limit of the $C2$ form factor [see Eq. (4.54)]. We have for the quadrupole moment

$$Q_2' \equiv 2Q_2 = \frac{2}{5}\left[(\tfrac{2}{5}A^2 - \tfrac{1}{4}B^2)\langle r^2\rangle_{p_{3/2}p_{3/2}} + \left[\frac{1}{\sqrt{10}}A + C\right] B\langle r^2\rangle_{p_{3/2}p_{1/2}} \right], \quad (6.5)$$

where $\langle r^2\rangle_{p_{j'}p_j}$ is the mean-square radius computed using $1p_{j'}$ and $1p_j$ radial wave functions. Following Donnelly and Walecka (1973b), let us use harmonic-oscillator radial wave functions and then $\langle r^2\rangle_{p_{j'}p_j} = \frac{5}{2}b^2$, independent of j' and j, where b is the usual harmonic-oscillator parameter. Fits to $1p$-shell information for ^{6}Li yield a value $b = 2.03$ fm, and upon using the experimental value for this quadrupole moment, $Q_2' = -0.80 \pm 0.08$ mb (Ajzenberg-Selove and Lauritsen, 1974), we have a third independent relationship involving the amplitudes A, B, and C. Solving these three equations in three unknowns yields $A = 0.810$, $B = -0.581$, and $C = 0.084$ (Donnelly and Walecka, 1973b). Thus, by Eqs. (6.3), all of the ground-state density-matrix elements are known and, for a given set of radial wave functions, the complete $C0$, $M1$, and $C2$ elastic form factors may be calculated [i.e., using Eqs. (4.129)—(4.133)]. Before displaying the calculated $M1$ form factor together with the existing experimental data, let us collect together with the phenomenologically determined $J = 1$ density-matrix elements the results of $1p$-shell shell-model calculations (see Table I). Specifically, for the latter we consider Cohen and Kurath wave functions (Cohen and Kurath, 1965) and the resulting density matrices (Dubach, 1983). It is clear that, while qualitatively similar, in detail the results here show a spread in values. Of course, by construction, the phenomenological set of density-matrix elements yields the experimental dipole and quadrupole moments of the ground state, given that the $1p$-shell nuclear size is correctly represented by harmonic-oscillator wave functions having $b = 2.03$ fm. Other authors have followed similar approaches, and two bear mentioning at this point: (1) the phenomenological analysis of Bergstrom *et al.* (1975), which yields results in complete agreement with those above for the ground state, and (2) shell-model calculations of Vergados (1974), including core excitation, which span a range of amplitudes, but are generally rather similar to the results above.

In order to calculate form factors, we also need the $1p_{3/2}, 1p_{1/2}$ radial wave functions. For ^{6}Li as well as the other p-shell nuclei, these radial wave functions are calculated using Woods-Saxon potentials. Only when the separation energy is large, or the quality of the data rather poor, will we use harmonic-oscillator wave functions; in these cases, the difference between these wave functions has no effect on the comparison of experiment with theory.

The parameters of the Woods-Saxon potential are chosen in the following way: The radius parameter is fit to $F_T(q)$ and basically fixed by the high-q falloff of $F_T(q)$. The surface thickness, to which $F_T(q)$ is insensitive, is taken from fits of the charge scattering data, with densities calculated using Woods-Saxon potentials; this procedure is justified by the fact that density-dependent Hartree-Fock calculations give very similar surface thicknesses for the effective potentials seen by nucleons in different shells. The depth of the Woods-Saxon potential is fit to the experimental separation energy; this ensures that the large-radius behavior, which influences the low-q behavior of $F(q)$, is realistic. For the spin-orbit depth, we use a constant $V_{so} = 24$ MeV.

Figure 17 shows that the Cohen-Kurath matrix elements do quite well in explaining the experimental form factor. The phenomenological matrix elements, although fit to $q = 0$ properties only, give an excellent representation of the data.

Next let us consider the α-d cluster model as a basis for describing the ^{6}Li ground state. The phenomenological version (Kudeyarov *et al.*, 1971) was among the first antisymmetrized cluster models to be applied to descriptions of the electromagnetic form factors. Here antisymmetrization was shown to play a vital role. In a subsequent study (Bergstrom, 1979) applied to ^{6}Li, it was concluded that the longitudinal form factors of the ground and first excited states can be understood within the context of the basic phenomenological cluster model, but not the transverse form factors of other levels (notably the 3.56-MeV 0^+1 level, which has received considerable attention). Of particular interest to us here is the fact that this simple model was unsuccessful in describing the elastic magnetic form factor of ^{6}Li.

More recently the basic cluster model with spherical clusters has been extended to permit the deuteron to deform, or stretch, along a line connecting the cluster centers of mass (Bergstrom *et al.*, 1982). With this

TABLE I. $M1$ ground-state density matrix for ^{6}Li.

	Phenomenology[a]	Shell model[b,c] (6-16)2BME	(8-16)2BME	(8-16)POT
$\psi_{1;0}((p_{3/2})^2)$	0.482	0.519	0.518	0.518
$\psi_{1;0}((p_{1/2})^2)$	−0.109	−0.227	−0.225	−0.222
$2\psi_{1;0}(p_{3/2}p_{1/2})$	−0.696	−0.658	−0.620	−0.779

[a]Using $A = 0.810$, $B = -0.581$, and $C = 0.084$ (Donnelly and Walecka, 1973b).
[b]Cohen and Kurath, 1965.
[c]Dubach, 1983.

ad hoc modification Bergstrom and co-workers show that a consistent description of all of the available form factors (including the elastic $M1$ form factor) can be obtained. In particular, they take the ground state to be made up from Gaussian-shaped clusters multiplied by an s-wave relative-motion function (also of Gaussian form). The α cluster is characterized by range parameter α, whereas for the d cluster they take the basic Gaussian form with range parameter β and add a term which elongates the cluster along the direction $\mathbf{R}=\mathbf{R}_d-\mathbf{R}_\alpha$, where $\mathbf{R}_d$ and $\mathbf{R}_\alpha$ are the deuteron and alpha cluster centers, respectively. This elongation is characterized by the parameter $\Delta\beta$, where the limit $\Delta\beta=0$ corresponds to the usual (spherical) cluster model referred to above. Finally the relative-motion Gaussian (in R) is characterized by a range parameter γ. The parameter α was determined from the free ^{4}He radius ($\alpha=0.582$ fm^{-2}), and the other parameters, β, $\Delta\beta$ and γ, were constrained by fits to the ^{6}Li charge radius and to general features of the elastic form factors. They obtained values $\beta=0.29$ fm^{-2}, $\Delta\beta=0.099$ fm^{-2}, and $\gamma=0.24$ fm^{-2}. The resulting elastic magnetic form factor is displayed in Fig. 18. Clearly this is an excellent representation of the data. Bergstrom *et al.* (1982) note that, upon expanding in more shell-model-like language, this is reflected in different oscillator parameters for the $(1s)^4$ core and for each of the two $1p$ particles (differing by a factor which is proportional to $\Delta\beta$). In addition there is an effective harmonic-oscillator interaction potential characterized by $\frac{1}{4}(\alpha-3\gamma+2\beta)=0.11$ fm^{-2} (which of course vanishes in the independent-particle shell-model limit $\alpha=\beta=\gamma$).

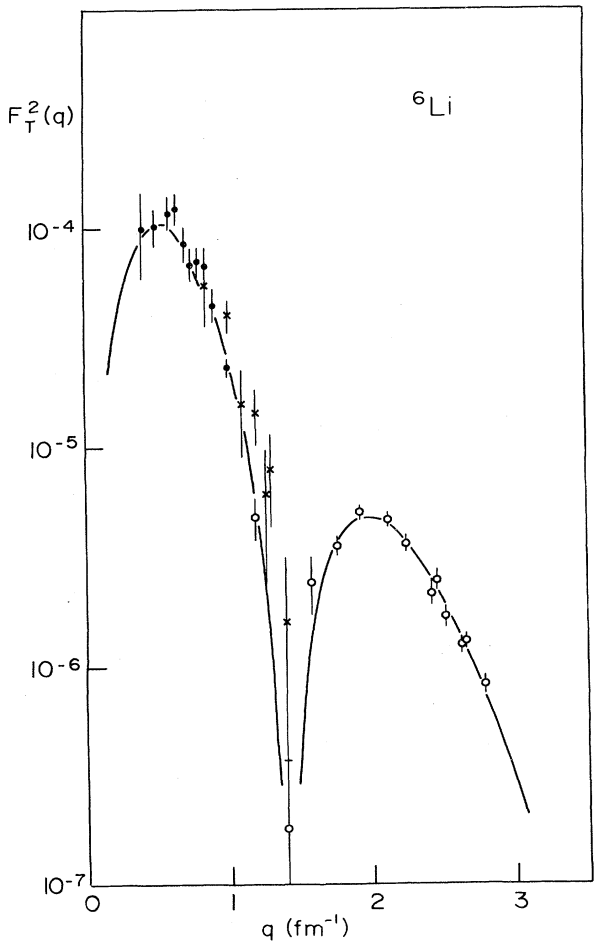

FIG. 18. The ^{6}Li data of Fig. 17, shown together with a fit obtained using a generalized cluster model (Bergstrom *et al.*, 1982).

In the same analysis described above (Bergstrom *et al.*, 1982) there is also a representation of the $M1$ data as a coordinate space density. Using Eqs. (4.28) and (4.29), we may write

$$\langle J_0;T_0::\hat{T}^{\rm mag}_{J;T}(q)::J_0;T_0\rangle \propto \int_0^\infty r^2dr\, j_J(qr)J_{JJ}^{(T)}(r)\ , \qquad (6.6)$$

where the angular integral in Eq. (4.28) has been absorbed into the definition of the current density $J_{JJ}^{(T)}(r)$, a function only of $r=|\mathbf{r}|$. It is perhaps worth noting at this point that, when the ground state has spin-$\frac{1}{2}$ or spin-1, the only allowed magnetic multipole is $M1$ and a model-independent analysis similar to the one used for ($C0$) elastic charge scattering can be attempted. The decomposition into convection and magnetization current contributions of course cannot be accomplished using only electron scattering information. The resulting $M1$ current density for elastic scattering from ^{6}Li is given by Bergstrom *et al.* (1982) and is seen to bear a striking resemblance to the (isovector) $M1$ transition current densities for the 3.56-MeV state of ^{6}Li (Bergstrom *et al.*, 1979) and for the 15.11-MeV state of ^{12}C (Deutschmann *et al.*, 1980).

Before leaving this discussion of the ground state of ^{6}Li, let us mention one further approach that has been taken. Lehman and Parke (1983) used a three-body (αNN) model which included $S_{1/2}$, $P_{1/2}$, and $P_{3/2}$ partial waves of the αN interaction and considered a $^3S_1$-$^3D_1$ NN interaction (leading to a 4% D-state component in the deuteron). The authors calculated the probabilities of the orbital components of the wave functions, the configuration-space single-particle orbital densities, and the configuration-space two-particle wave-function amplitudes in j-j coupling, with the nucleon coordinates referred to the α particle as the core. The results of this Faddeev calculation were compared with those from phenomenological or shell-model calculations of the type summarized above. The authors found that none of these have a distribution of orbital probabilities across shells that is like the distribution predicted in their three-body model. They found, for example, that the $p_{1/2}$ orbital lies outside the $p_{3/2}$ orbital, in contrast to pure harmonic-oscillator $1p$-shell wave functions, which are the same. As expected, the three-body orbital densities at large radial distances decay with exponential rather than Gaussian factors. However, the three-body model densities differ even from densities calculated using Woods-Saxon wave functions (which do fall off at large distances correctly). Furthermore, the authors note that allowing for core excitation in shell-model calculations (see, for example, Ver-

gados, 1974) tends to move the distribution of orbital probabilities towards the three-body values, but that this serves to emphasize that an apparent need for core excitation may actually indicate a need to move from "effective" two-body dynamics to three-body dynamics. Unfortunately no predictions for the elastic magnetic form factor are available. Hopefully this promising approach will be pursued and predictions will become available in the future.

2. The nucleus ^{7}Li

The low-q data for ^{7}Li have been measured by Van Niftrik *et al.* (1971) using the IKO 180° scattering system. The high-q data come from an experiment performed by Lichtenstadt *et al.* (1983) at the Bates accelerator. The data, shown in Fig. 19, are successful in defining the first maxima of the $M1$ and $M3$ form factors.

Predictions for the ^{7}Li form factor in terms of shell-model calculations (Van Niftrik *et al.*, 1971; Bernabeu and Ros, 1974; Lichtenstadt *et al.*, 1983) are quite sensitive to the coupling scheme employed. Cohen-Kurath-type wave functions explain the data well, as demonstrated by Lichtenstadt *et al.* (1983), who use the (8-16)POT matrix elements and harmonic-oscillator radial wave functions. The main difference from the data is an overall factor of 1.2 by which the calculation is high. In Fig. 19 we show a curve similar to that of Lichtenstadt *et al.* (1983); the same matrix elements, but a Woods-Saxon radial wave function, is employed here.

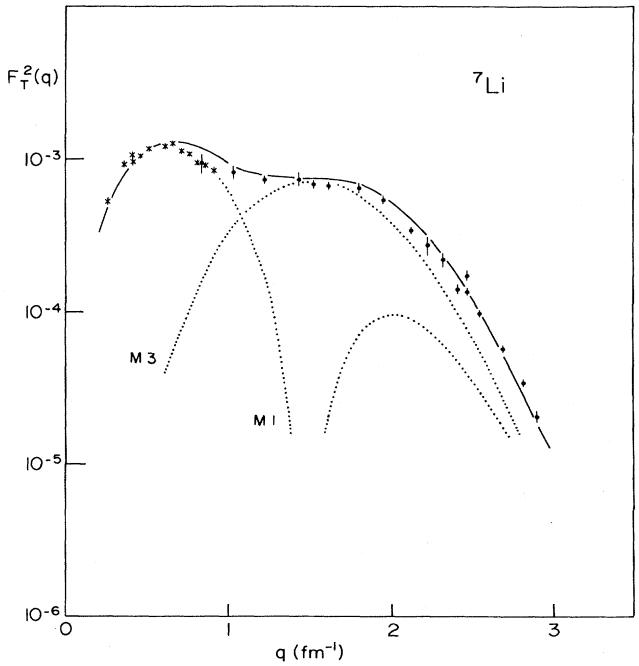

FIG. 19. The ^{7}Li data of Van Niftrik *et al.* (1971) (crosses) and Lichtenstadt *et al.* (1983) (solid circles), corrected for the MEC contribution obtained by Dubach (1983), and compared to a calculation that uses Cohen-Kurath (1965) (8-16)POT matrix elements and fitted Woods-Saxon radial wave functions. The dotted curves show the $M1$ and $M3$ contributions separately, while the solid curve shows the total.

For comparison with theory, the data shown in Fig. 19 have been corrected for the contributions of MEC as calculated by Dubach (1983). These MEC contributions turn out to be fairly small, however, and change F_T by only 7—15 % over most of the q region probed by experiment.

The $M3$ part of the data is explained very well. On the other hand, the main peak of the $M1$ is too large, while in the limit $q \to 0$, the magnetic form factor (moment) is predicted correctly ($\mu = 3.26$ vs 3.24 n.m.). These two observations cannot be reconciled by changing the $p^2_{1/2}$ or $p^2_{3/2}$ matrix elements; the corresponding magnetic form factors are too similar in shape. A change of the $p_{1/2}$-$p_{3/2}$ matrix element, or admixtures of other shells, is needed to change F_M ($q \cong 0.7$ fm^{-1}) without changing μ. Both can be expected to have a q dependence different from that of the p^2-diagonal terms; indeed, the $p_{1/2}$-$p_{3/2}$ contribution, for example, peaks at 1.5 fm^{-1} where the $p^2_{1/2}$ contribution has a zero.

The ^{7}Li form factor has also been studied by Kruger and Van Leuven (1969), who calculated the ^{7}Li ground-state wave function using the projected Hartree-Fock approach. These authors use an expansion in terms of oscillator wave functions up to the f/p shell, and a soft-core interaction proposed by Brink. In this calculation the energy of ^{7}Li is minimized by adjusting both the oscillator parameter and the occupation numbers. In the q region where $M1$ dominates, the results for F_M are similar to those shown in Fig. 19. In the region where $M3$ dominates, the calculation is successful in explaining the summed elastic plus inelastic (0.478 level) data measured by Rand *et al.* (1966); as compared to the elastic data shown in Fig. 19, the form factor obtained via the projected Hartree-Fock method falls off much too quickly, so as to be low by a factor of 3 at $q = 2.5$ fm^{-1}. This probably indicates that the $1p$ wave function obtained by the projected Hartree-Fock calculation has too large a radius.

3. The nuclei ^{9}Be, ^{10}B, ^{11}B

These nuclei near the middle of the p shell have received relatively little attention. Theoretical calculations are largely restricted to Cohen-Kurath-type wave functions, and the experimental data in most cases still have rather large uncertainties. Given this situation, we shall discuss these nuclei together.

Many of the data available are due to the pioneering experiment of Rand *et al.* (1966), an experiment that for the first time reached the region of transfer where a multipolarity larger than $M1$ dominates. Rand and collaborators used an early two-magnet, 180° system, together with the Stanford 1-GeV Mark III accelerator and 72″ spectrometer. Data were measured in the region $q = 0.7$—2.4 fm^{-1}, thereby covering the region where both $M1$ and $M3$ form factors peak. Less extensive, lower-q data were measured

by Goldemberg *et al.* (1965) using the Orsay accelerator. At very low $q \approx 0.3$–0.9 fm^{-1}, most of the data have been obtained at the Amsterdam IKO machine, using the three-magnet 180° system (Lapikás *et al.*, 1975; Lapikás, 1978). These data, together with some isolated points from other experiments (Goldemberg and Torizuka, 1963; Vanpraet and Kossanyi-Demay, 1965), are displayed in Figs. 20–22.

Most of the early experiments on p-shell nuclei were interpreted using a phenomenological model derived from shell-model calculations. Assuming that the active nucleons are restricted to the $1p$ shell, and ignoring the difference between neutron and proton radial wave functions, one finds that the form factor [Eq. (4.129)] is given by a simple expression, since all the radial dependences factorize into two terms,

$$F_T(q) = f_{\text{c.m.}}(q) f_N(q) \left[\alpha \int R^2(r) j_0(qr) r^2 dr + \beta \int R^2(r) j_2(qr) r^2 dr \right] . \quad (6.7)$$

Here, $f_{\text{c.m.}}$ represents the center-of-mass correction (Tassie and Barker, 1958), f_N the single-nucleon form factor [see Eq. (4.102), for instance], and α,β are constants that depend on the particular coupling scheme used (Griffy and Yu, 1965). These constants are combinations of the $T=0,1$ $p_{3/2}/p_{1/2}$-space density-matrix elements used in Eq. (4.131) and are obtained by ignoring the difference between $p_{1/2}$ and $p_{3/2}$ wave functions.

Much of the database on magnetic form factors has been interpreted using the above equation together with harmonic-oscillator radial wave functions; in this case the above integrals can be performed analytically (Griffy and Yu, 1965). The quantities b (the oscillator parameter), α, and β in this case are the ones used to parametrize the data. A recent systematic analysis of this type, done by replacing the harmonic-oscillator by Woods-Saxon radial wave functions of the dominant valence shell, has been performed by Lapikás (1978).

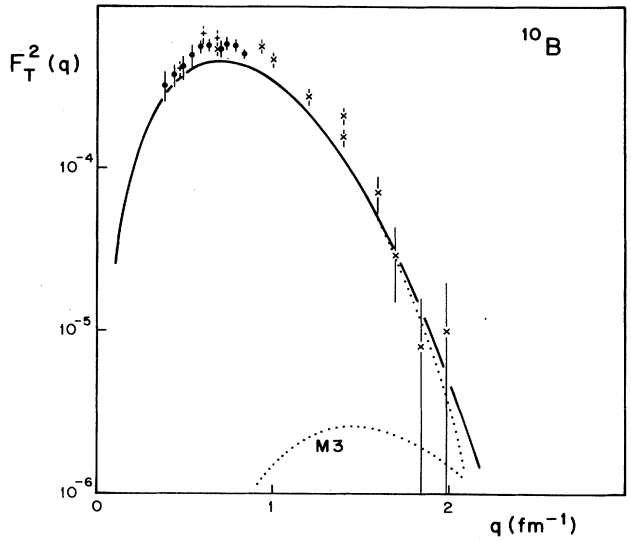

FIG. 21. The ^{10}B data of Lapikás (1978) (solid circles) and Rand *et al.* (1966) (crosses), shown together with a calculation that uses p-shell matrix elements of Van Hees and Glaudemans (1984) and fitted Woods-Saxon radial wave functions ($r_0 = 1.10$ fm). The dotted curves show the $M1$ and $M3$ contributions separately, while the solid curve shows the total. The other data shown are referred to in Table III.

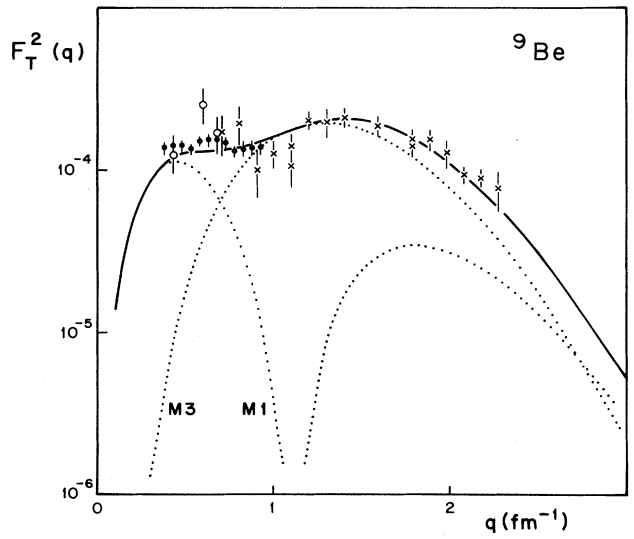

FIG. 20. The ^{9}Be data of Lapikás *et al.* (1975) (solid circles) and Rand *et al.* (1966) (crosses), compared to a calculation that uses Cohen-Kurath (1965) (8-16)POT matrix elements and fitted Woods-Saxon radial wave functions ($r_0 = 1.0$ fm). The dotted curves show the $M1$ and $M3$ contributions separately, while the solid curve shows the total. The other data shown are referred to in Table III.

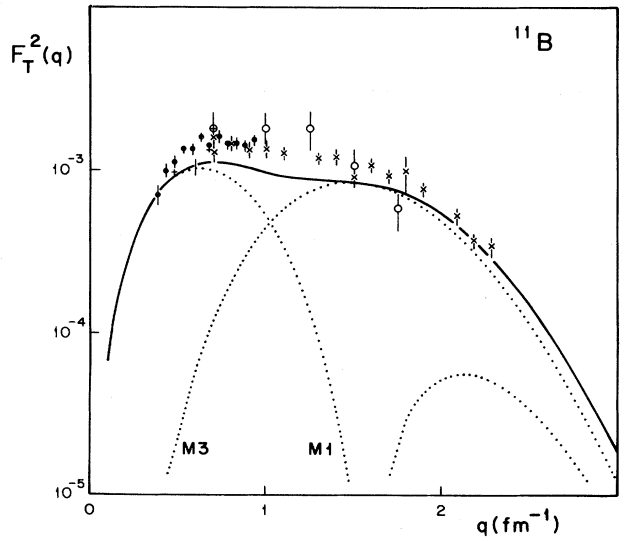

FIG. 22. The ^{11}B data of Lapikás (1978) (solid circles), Goldemberg *et al.* (1965) (open circles), and Rand *et al.* (1966) (crosses), compared to a calculation using Cohen-Kurath (1965) (8-16)POT matrix elements and fitted Woods-Saxon radial wave functions ($r_0 = 1.20$ fm). The other data shown are referred to in Table III.

On a microscopic level, the shell model provides a deeper understanding of $F_T(q)$. In particular, the many-body wave functions obtained by Cohen and Kurath (1965) have been employed extensively. These calculations again use as an active model space the $1p_{1/2}$,$1p_{3/2}$ shells, treating the $1s$ shell as closed and ignoring $\geq 2\hbar\omega$ admixtures involving higher shells (most calculations neglect $1\hbar\omega$ excitations as well, but these are of no importance for magnetic elastic scattering, as they are of the wrong parity). These intermediate coupling calculations of the type pioneered by Cohen and Kurath start from two-body matrix elements fitted to reproduce the energy-level systematics of $1p$-shell nuclei. Calculations within this framework, mostly using harmonic-oscillator radial wave functions, have been published by Kabachnik and Grishanova (1966), Bernabeu and Ros (1974), Lapikás *et al.* (1975), and Dubach *et al.* (1976). Below we concentrate on a discussion of analyses where more realistic, Woods-Saxon wave functions are used. Once one of the $1p_{1/2}$,$1p_{3/2}$ subshell contributions no longer dominates $F_T(q)$, differences in the shape of $R(r)$ due to different binding energies become important, and show up in F_T mainly through the $p_{1/2}$-$p_{3/2}$ mixed terms.

For light nuclei, a number of calculations of a different type are available as well. The Nilsson model, often with admixtures of $\geq 2\hbar\omega$ shells included, has been employed by Vinciguerra and Stovall (1969), and Slight *et al.* (1973), and projected Hartree-Fock calculations (Bouten *et al.*, 1969) have been used to study nuclei with $A=7-11$. These calculations, however, have been applied mostly to charge scattering, which is less sensitive to details of the ground-state configuration than is magnetic scattering (Bernabeu and Ros, 1974).

In Figs. 20—22 we show the results of calculations done using Woods-Saxon radial wave functions and density-matrix elements obtained from Cohen-Kurath-type shell-model wave functions. The density-matrix elements have been calculated by Dubach (1983) or by Van Hees and Glaudemans (1984). Dubach uses the (8-16)POT two-body matrix elements ($0\hbar\omega$) of Cohen and Kurath in his calculation. Van Hees and Glaudemans perform a shell-model calculation in the $0\hbar\omega$ and $1\hbar\omega$ harmonic-oscillator space, using interaction matrix elements which satisfy translational invariance. The two-body matrix elements of Van Hees, also fitted to energy levels of nuclei $A=8-16$, are, roughly speaking, between the phenomenological ones of Cohen and Kurath and the more microscopic ones which result when the Sussex interaction is used. Differences between the two sets of density-matrix elements lead to minor differences in F_T, unless otherwise noted. The radial wave functions are calculated using standard parameters, with the size parameter r_0 fit to the magnetic scattering data at large q.

On the whole, agreement with experiment is quite reasonable, although many smaller discrepancies appear. For ^{9}Be, agreement is found only when a rather small radius parameter ($r_0=1.0$ fm) is used, while for the other nuclei the r_0 values are more in line with what is known from charge scattering. This peculiarity of ^{9}Be, partly linked to the small neutron separation energy (1.7 MeV), is discussed below. For all nuclei, the radial wave functions are not well fixed by the data; the dynamical range over which F_T^2 is measured is too small, and $F_T(q)$ as a function of q has too little structure.

In all cases, the calculations have a tendency to underestimate the value of F_{M1} in the $M1$ peak, even though the magnetic moments [$F_{M1}(q\rightarrow 0)$] are reproduced quite well. This points to the presence of MEC or contributions of configuration admixtures involving shells other than $1p$. When only $1p$ contributions are present, and particularly in situations where one of the subshells dominates, the q dependence of F_T is difficult to change effectively, even when allowing for large changes of the matrix elements.

We note that the nucleus ^{9}Be is unusual in that it has a low neutron separation energy. In this case large differences occur between the radial wave functions found when using harmonic-oscillator or Woods-Saxon potentials. Normally, the difference between these two types of radial wave functions shows up mainly in the falloff of $F_T(q)$ at large q. For very small separation energies, a large effect also is visible in the maxima of the $M1$,$M3$ form factors, where F_T^2 is 1.5—2 times lower for Woods-Saxon radial wave functions. Woods-Saxon wave functions $R^2_{1p}(r)$ have a peak that is more pointed and is lower in amplitude, and have a larger tail at large radius. This leads to the reduction of the amplitude of the first maximum of F_T^2, together with an increase of the second maximum of F_{M1}^2. The difference between the $1p_{1/2}$,$1p_{3/2}$ and neutron-proton radial wave functions also affects the mixed $p_{1/2}$-$p_{3/2}$ and $T=1$ terms and affects the form factor in those cases where the ground-state configuration is far from an extreme single-particle model configuration.

For the case of ^{9}Be, a study of the magnetic form factor in terms of an alternative theoretical approach, that of the projected Hartree-Fock calculation, has been published. Bouten *et al.* (1969) use harmonic-oscillator wave functions and a basis extending through the f/p shell. In this large model space one can expect to account more successfully for those features of p-shell nuclei that are reminiscent of well-deformed systems. Bouten *et al.* (1969) have applied their projected Hartree-Fock calculations to both charge and magnetic form factors, and find, with no free parameters, good agreement with the data. As compared to the shell-model calculations shown in Fig. 20, the major difference appears to be a value of F_T near the maximum of F_{M3} which is somewhat higher.

It is perhaps worthwhile to point out one peculiarity of the magnetic form factor of ^{10}B. This nucleus has a ground state with $J_0^{\pi_0}T_0=3^+0$, thus allowing a maximal magnetic multipolarity of $M5$. Shell-model calculations restricted to the $1p$ shell, on the other hand, give at maximum an $M3$ contribution. Moreover, the $M3$ density-matrix elements predicted for ^{10}B are quite small; the dominant wave-function configuration, with an unpaired proton and neutron aligned and all other nucleons paired off, does not give a diagonal contribution to $M3$. Thus,

despite the large spin, the magnetic form factor of ^{10}B is dominated by $M1$. The $M3$ peak that dominates the form factors of ^{9}Be and ^{11}B at medium q is barely visible for ^{10}B.

A study of ^{10}B at somewhat higher q can be expected to show the $M3$ contribution. This would allow a very useful test of the wave functions employed here; F^2_{M3} as predicted by the calculation of Van Hees is more than a factor of 2 lower than the prediction of Dubach. It would be of particular interest to push the measurements to even higher q, $q\sim 2$–2.5 fm^{-1}, where an eventual $M5$ form factor would peak. Such an $M5$ contribution could be a signature for d- or higher-shell admixtures, and is perhaps easier to interpret than the coherent admixtures occurring in F_{M1} and F_{M3}. The isoscalar nature of ^{10}B can be hoped to make MEC contributions sufficiently small so as not to introduce too much uncertainty at large q, and thus allow the identification of F_{M5}.

4. The nucleus ^{13}C

Magnetic scattering from ^{13}C has received considerable attention both experimentally and theoretically. This interest is related mainly to its spin-$\frac{1}{2}$ nature, which makes the interpretation of F_M particularly straightforward; only one multipolarity ($M1$) is present. The data at low q ($q \lesssim 0.8$ fm^{-1}) come from an experiment of Lapikás *et al.* (1975) performed using the 180° scattering system of the IKO accelerator. An experiment performed at Stanford to measure the charge form factor (Heisenberg *et al.*, 1970) produced a few points near $q=2$ fm^{-1}, where the magnetic contribution showed up in the very deep minimum of $F_{ch}(q)$. An extensive coverage of the higher-q region is provided by the recent experiment of Hicks *et al.* (1982a), who used the Bates 180° scattering system. The experimental data, shown in Fig. 23, exhibit a pronounced diffraction feature, characterized by a second maximum as high as the first one, with a rather slow falloff of F_{M1} at large q.

An interpretation of F_M naturally starts from the extreme single-particle model, which assumes ^{13}C to have a pure $1p_{1/2}$ neutron configuration outside a closed $1p_{3/2}$ shell. The form factor calculated using this assumption fails to explain the data (see Fig. 11); the amplitude of the second maximum of F_T in particular is far too large. More realistic wave functions (Mosconi and Ricci, 1974; Cheon, 1983) allow a much improved fit. The result of a calculation done using the $p_{3/2}$,$p_{1/2}$ space and density-matrix elements calculated by Dubach (1983) with Cohen-Kurath (8–16)POT matrix elements, is shown in Fig. 23. The matrix elements obtained by Van Hees and Glaudemans (1984) give a very similar result.

The effects of additional configuration mixing have been explored by Suzuki *et al.* (1981a,1981b). Starting from Cohen-Kurath wave functions and harmonic-oscillator radial wave functions, Suzuki *et al.* added core-polarization terms calculated in first-order perturbation theory, taking into account excitations up to $12\hbar\omega$.

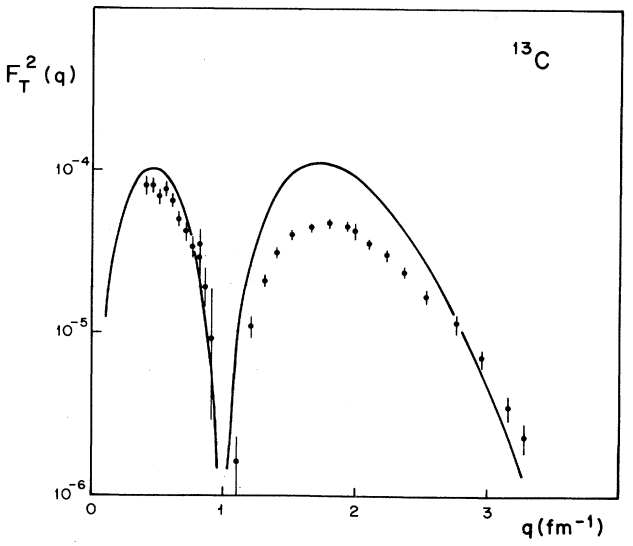

FIG. 23. The ^{13}C data of Lapikás *et al.* (1975) and Hicks *et al.* (1982) shown together with a calculation that uses p-shell matrix elements of Van Hees and Glaudemans (1984) and fitted Woods-Saxon radial wave functions ($r_0=1.14$ fm).

As residual interactions, Suzuki *et al.* (1981a,1981b) used both phenomenological forces (with a Rosenfeld mixture for the exchange terms) and a set of the Michigan State three-range interactions. They found that core polarization improved the agreement with the data by further reducing the amplitude of F_M in the second maximum, and that the diffraction minimum was shifted to larger q. The reduction of F_M in the maximum was attributed mainly to the effects of the tensor interaction. The best fit obtained by Suzuki *et al.* (1981a,1981b) by variation of the residual force parameters still does not satisfactorily reproduce the data. In particular, at large q F_M falls off more quickly than the experimental data.

Attempts to explain F_M in terms of delta-hole admixtures in the framework of Landau-Migdal theory have been described by Delorme *et al.* (1981). These authors achieve a rather good description of the data, at the expense of introducing a Landau-Migdal parameter $g'=0.44$ having a very small value. At the large q of interest, the use of δ interactions leads to further uncertainties.

An attempt to understand the ^{13}C form factor within a different framework has been described by Lin (1983).[11] Recognizing that there exists ample evidence that ^{12}C is deformed, Lin treats ^{13}C in terms of the Nilsson model in order to study the collective aspects of core polarization, aspects that might be difficult to account for by a shell-model calculation. This Nilsson calculation includes $\Delta N=2$ admixtures and uses harmonic oscillators to

[11]Note that the published version of this work (Lin and Zamick, 1981) contains errors (Zamick, 1983) which were corrected by Lin (1983).

describe the radial structure. Furthermore, the Nilsson model is generalized to allow the deformation to depend on the relative orientation of the nuclear spin and the core symmetry axis, a feature that qualitatively has proven to be very helpful (Zamick, 1978) in explaining the $M3$ suppression in, for example, ^{17}O (see next section).

The calculations of Lin show that the $\Delta N=2$ mixing is beneficial in explaining $F_M(q)$; it reduces F_T^2 in the second maximum by $\sim 30\%$. The generalization introduced, which basically allows core neutrons and protons to have different deformations, also helps to improve agreement with experiment, although the effect on the ^{13}C form factor is not large. Lin also calculates the rotational-current contribution of the core; as pointed out in Sec. IV.D for the special case $K=\frac{1}{2}$ this core contribution cannot be ignored. The quantitative contribution of this core term is found to degrade agreement with experiment, since F_T^2 in the first diffraction maximum is increased by a factor of ~ 1.8.

On the whole, the description of ^{13}C in terms of the Nilsson model is no more successful than the one in terms of the shell model. It does, however, allow some additional insights into the mechanisms that are possibly important for a more quantitative understanding of F_T.

The comparison of experiment and the various theoretical calculations discussed above shows a systematic discrepancy. The amplitude predicted for the second maximum of F_T^2 is too high, and the form factor falls off too rapidly at large q. From such a discrepancy one could hope to learn additional physics, and below we describe some attempts to uncover its origin. For such a detailed study of F_{M1} at large q, ^{13}C turns out to be particularly favorable. The one-body contribution stays large up to high q, in which case the MEC contributions, which become progressively more uncertain as q increases, produce a small change of F_T.

The approach taken to interpret magnetic form factors for ^{13}C (and for other nuclei in general) is the following: Using Woods-Saxon radial wave functions $R(r)$ with parameters largely fixed by charge electron scattering, and using shell-model ($0\hbar\omega$) density-matrix elements ψ, one fits the data, allowing for small changes in ψ or in R. Given the systematic discrepancy with experiment that appears for ^{13}C, we have explored an extended space of quantities that possibly can be "freely" adjusted to reproduce the data. Some of the parameters explored can be taken as sufficiently poorly fixed by our theoretical understanding to be varied at will; others are strongly constrained by other data, or prejudice, and their variation should be taken as a test that serves to find out whether magnetic scattering is sensitive to this particular ingredient.

When exploring the degrees of freedom of interest for ^{13}C we have constrained the density-matrix elements and radial wave functions by a number of observables beyond F_T. A sum rule involving $M1$ diagonal matrix elements [Eq. (4.128c)] has to be fulfilled to guarantee that the spin projection of ^{13}C is $\frac{1}{2}$. The beta-decay rate $^{13}\mathrm{N}\rightarrow{}^{13}\mathrm{C}$ is well known, and fixes [Eq. (4.137)] a combination of matrix elements. The asymptotic normalization of the $1p_{1/2}$ neutron radial wave function is well known from sub-Coulomb transfer reactions (Gubler *et al.*, 1977) and fixes a combination of $p_{1/2}$ diagonal matrix elements and the radial-wave-function radius. The asymptotic normalization of the $p_{1/2}$ proton is determined by an interpretation of $p+{}^{12}$C scattering in terms of forward dispersion relations (Meyer and Plattner, 1977), although with an error bar that is not very constraining when fitting F_T.

We do not intend to give here a complete account of the possibilities explored, and only list some of the conclusions reached. The parameters explored cover the values of $1p$ density-matrix elements, possible $2\hbar\omega$ admixtures of higher shells, and the effects of the shape of the radial wave functions involving harmonic-oscillator, Woods-Saxon, and double Woods-Saxon potentials. The conclusions to be discussed below are valid for data both corrected and not corrected for the MEC contribution, calculated by Dubach (Hicks, 1982a; Dubach, 1983).

The density-matrix elements used in the interpretation of p-shell magnetic form factors come largely from Cohen-Kurath-type wave functions. The space of these calculations is restricted to the $1p_{1/2}$ and $1p_{3/2}$ shells. The calculations of Dubach (1983), Bakkum and Glaudemans (1982), and Van Hees (1982) give density-matrix elements that are reasonably close together. Allowing for a free variation of all six density-matrix elements leads to considerable improvement of the fit, although the falloff of F_T^2 at large q cannot be reproduced (see also Hicks, 1982). However, some of the matrix elements are very far from the shell-model predictions, and probably are not very realistic. Fitting the data with constraints that keep the density-matrix elements reasonably close to the shell-model predictions shows that the $1p_{1/2}^2 T=1$ density-matrix element is the main one that needs to be changed to improve the fit to data. The value of 0.55—0.65 found is significantly smaller than the one predicted, 0.75—0.85. This is found systematically in the fits described below, and is required in order to decrease the value of F_T^2 in the second maximum down to the observed value.

The difference between harmonic-oscillator (HO) and Woods-Saxon radial wave functions is appreciable, since the $1p_{1/2}$ separation energy is rather small ($\varepsilon_{\mathrm{SE}}=4.9$ MeV). The lack of a large-radius tail for R_{HO} can be expected to have a significant effect; indeed the use of a more realistic Woods-Saxon radial wave function does improve the fit to the data by reducing the value of $F(q)$ in the second maximum. On the other hand, the exact shape of the tail of $R(r)$ is of less importance. Using a separation energy changed by ± 2 MeV, a typical inherent uncertainty due to differences between separation energy and energy eigenvalue, does not change the fit significantly.

More drastic variations of the shape of $R(r)$, obtained by large changes of the potential radius parameter, could yield a further improvement of the fit. Reducing the r_0 parameter from the standard value of $r_0=1.20$ fm to 0.9 fm allows one to improve significantly the agreement with experiment at large q. This change results in a dis-

placement of the peak of $R^2(r)$ to smaller radius, together with a narrowing of the peak. However, such a large change of r_0 is not very reasonable, and is assumed to mock up some other deficiency in the analysis.

We also have explored the effect of using potentials with shapes different from the standard Woods-Saxon form. Both microscopic optical potentials and intermediate-energy proton-nucleus scattering motivate the use of double Woods-Saxon potentials (Von Geramb, 1983). Parameter sets for double Woods-Saxon potentials that allow a good fit of F_T^2 can be found. The changes of $R(r)$ which result show the same features as discussed above, moving the peak of $R(r)$ to smaller r and sharpening it as required to fit the data. However, the shapes of the effective potentials found have little to do with the shapes expected from a microscopic calculation (Von Geramb, 1983) for the low energies of interest here.

Given the lack of success in finding plausible changes of $R(r)$, an enlargement of the shell-model space seems imperative. In order to affect F_M, admixtures of $\geq 2\hbar\omega$ need to be considered. Shell-model calculations in such a large space are still at the limit of what is feasible, and the first systematic calculations are at present underway (Dubach and Haxton, 1982; Glaudemans, 1983).

In order to find out which matrix elements could be important, we have fitted the data with combinations of $2\hbar\omega$ density-matrix elements involving the $1s$, $2s$, $1d$, and $2p$ shells. In order not to allow undue freedom, the $1p$-shell density-matrix elements have been included as data, with an "error bar" of ± 0.05, and the Woods-Saxon potential well has been constrained to have a reasonable radius ($r_0 = 1.2 \pm 0.1$ fm). From a rather systematic exploration of $2\hbar\omega$ contributions we conclude that the most likely admixture is the one involving the $(2p)^2$ configuration; with a reasonably small $\psi = 0.04$, the data can be fitted over the entire range of q. Admixtures of other shells ($2s, 1d$), as well as $1p$-$2p$ transitions (see also Hicks, 1982), are insufficient to explain the data, and require large ψ's for a moderate improvement of the fit.

The effect of $(2p)^2$ admixtures is the same as described above when discussing changes of R_{1p}. The $M1$ form factor receives its main contributions from an integral over the incoherent sum of $1p$ and $2p$ radial wave functions squared [Eq. (4.130)], and the $2p$ contribution leads to a shift and narrowing of the peak of the integrand, as described above for $R(r)^2_{1p}$.

One might speculate that the $(2p)^2$ term could be related to the deformation of the ^{12}C core, a model in which a $(2p)^2$ term appears in a natural way. The calculation of Lin (1983), however, gives $(2p)$ matrix elements much smaller than those found above. At present, therefore, the ^{13}C magnetic form factor is not satisfactorily understood, despite a rather extensive exploration of different possible causes.

5. The nucleus ^{14}N

For this nucleus, much of the data presently available comes from a very recent experiment performed at the Bates accelerator (Huffman *et al.*, 1984). Little theoretical study has been devoted to F_T, although we note that a phenomenological analysis which parallels the one discussed within the context of ^{6}Li [Eqs. (6.1)—(6.5)] can be performed. In the case of ^{14}N we have two holes in a closed-shell ^{16}O, rather than two particles above ^{4}He as we had there. For completeness, we show instead in Fig. 24 the data together with results obtained using Cohen-Kurath (8-16)POT density-matrix elements (Dubach, 1983) and Woods-Saxon radial wave functions.

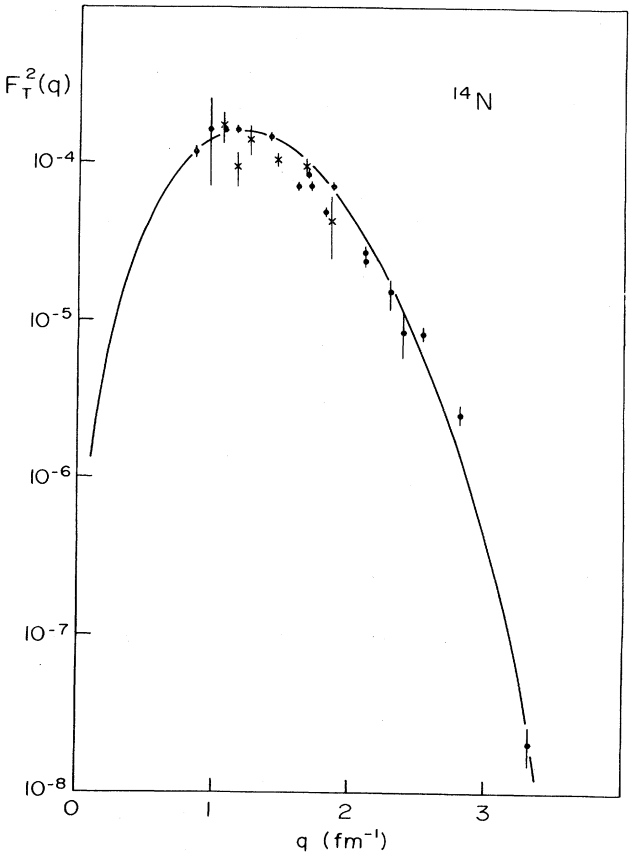

FIG. 24. The ^{14}N data of Rand *et al.* (1966) (crosses) and Huffman *et al.* (1984) (solid circles) compared to a calculation that uses Cohen-Kurath (1965) (8-16)POT matrix elements and fitted Woods-Saxon radial wave functions ($r_0 = 1.27$ fm).

6. The nucleus ^{15}N

In the extreme single-particle model, ^{15}N is described by a pure $1p_{1/2}$ proton hole in a closed-shell ^{16}O, and, as for the ^{13}C case, has a single magnetic multipole ($M1$). Deviations from this configuration that are of interest for studies of F_T involve excitations of $\geq 2\hbar\omega$. For the exploration of such admixtures, ^{15}N is a particularly interesting case.

An experiment on ^{15}N has been performed recently by Singhal *et al.* (1983), using the Bates 180° scattering system. With a gaseous ^{15}N target of thickness 20—100 mg/cm^2, data were taken in the q range 0.8—3.2 fm^{-1}.

The PWBA form factors are shown in Fig. 25.

The dashed curve in Fig. 25 shows the prediction (Singhal *et al.*, 1983) for a pure $(1p_{1/2})^{-1}$ state and a harmonic-oscillator wave function (a Woods-Saxon wave function yields a small reduction of F_M in the maximum, but no major improvement of the fit). The solid curve, which includes the contribution of MEC as calculated by Dubach, shows a more pronounced disagreement with the data; F_T in the maximum is too high, and falls off too quickly at large q. Results leading to the same conclusions have been given by Suzuki *et al.* (1981).

To improve agreement with experiment, Singhal *et al.* have done a shell-model calculation that involves $2\hbar\omega$ excitations to the $(2s,1d)$ and $(2p,1f)$ shells. In this calculation, the $1p$ matrix elements of Cohen and Kurath, the $(1p)^{-1}(2s,1d)$ matrix elements of Millener and Kurath (1975), and the $(2s,1d)$ matrix elements of Kuo (1967) have been used. This calculation predicts a significant depletion of the single-hole configuration by $\sim 40\%$. The agreement with experiment is improved (Fig. 25) in the maximum of F_T, while the form factor at large q still falls off too quickly.

The core-polarization calculation of Suzuki *et al.* (1981a) investigates a different aspect of configuration mixing, i.e., the effects of higher-lying shells. This calculation treats the core polarization in first-order perturbation theory (see Fig. 26) and employs residual interactions with both central and tensor components. It shows that the ^{15}N form factor is sensitive to the tensor component, which reduces $F_T(q)$ in the maximum as desired (Fig. 27). The full calculations differ from experiment in the same way as discussed above for Fig. 25.

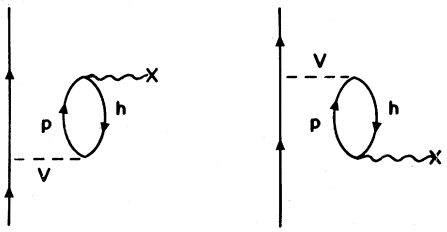

FIG. 26. Typical core-polarization diagrams.

The comparison of experiment and data shows the same features as discussed in detail for ^{13}C. F_T in the maximum is too large, and falls too quickly at large q. As for ^{13}C, there is at present no satisfactory explanation; attempts to explain these failures by including admixtures of $\geq 2\hbar\omega$ configurations (see also Singhal *et al.*, 1983) leads to amplitudes of admixtures larger than can easily be accepted. A detailed theoretical study of such excitations is needed, since at present our expectations for the amplitudes of such wave-function admixtures are not on a very firm basis.

In order to resolve the difficulties at large q, a more de-

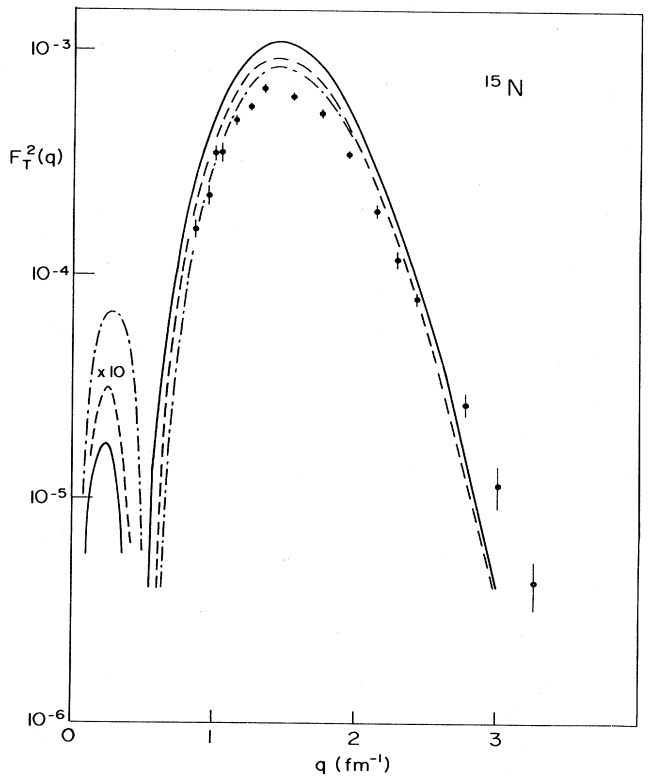

FIG. 25. The ^{15}N data and calculations using harmonic-oscillator radial wave functions: pure $p_{1/2}$ hole state (dashed curve), with MEC added (solid curve), and with excitation to s/d and f/p shells allowed for in addition (dotted-dashed curve) (Singhal *et al.*, 1983).

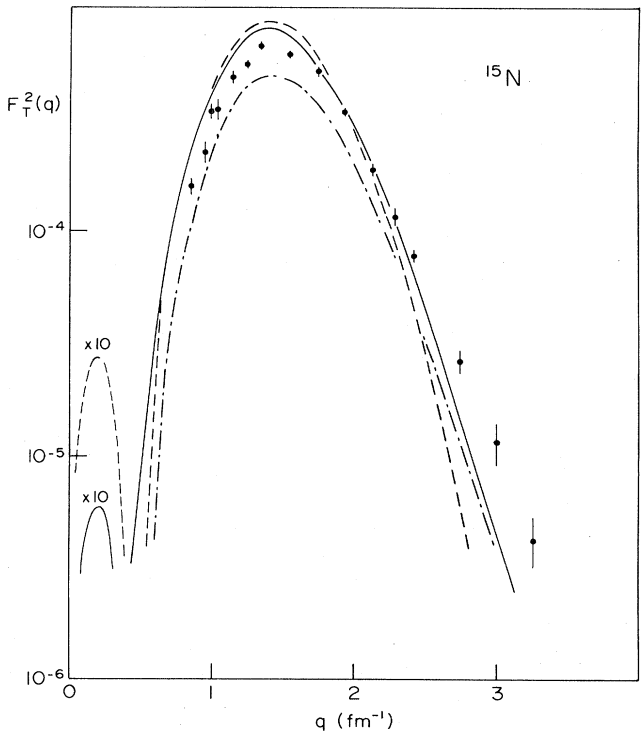

FIG. 27. The ^{15}N data of Singhal *et al.* (1983), shown together with calculations of Suzuki: pure $p_{1/2}$ hole state (dashed curve), with core polarization added (dotted-dashed curve), and with MEC in addition (solid curve) (Suzuki *et al.*, 1981).

tailed study of the tensor correlations in the nucleonic ground-state wave function will be needed. One of the most important results that has emerged from the investigations of the deuteron electrodisintegration at threshold (Bernheim *et al.*, 1972; Hockert *et al.*, 1973) is the importance of the tensor correlation (i.e., the deuteron D state) in calculating the effects of MEC. It is therefore questionable whether realistic estimates for exchange currents can be obtained with overly simplified shell-model wave functions. The importance of the tensor correlations is very well illustrated by the work of Mathiot and Desplanques (1980) for $2p$-$1f$ shell nuclei and the case of the magnetic form factor of ^{3}He (Sec. VII.B).

B. $2s/1d$-shell nuclei

In this section we describe what is known experimentally about the magnetic form factors of nuclei with $17 \leq A \leq 39$ and what has been learned from the comparison of experiment and theory, and give some predictions for those cases where data are likely to be taken and physical effects of special interest might show up. Partly the results described are taken from the literature; to a large extent, however, they have been calculated for the present review in order to allow a reasonably systematic comparison of experiment and shell-model calculations.

The s/d shell is a very nice region for nuclear structure investigations by magnetic electron scattering. In the same shell one goes from nuclei which are well described by the single-particle shell model to cases exhibiting features of deformed nuclei. This allows one to study how the "core" contributes to the magnetic properties, whereas the transition nuclei allow one to understand better the nuclei where the extremes are realized. In addition, the s/d shell exhibits a wide variety of features, since two subshells of very different radial wave functions $R(r)$ contribute. The magnetic form factor being, basically, the Fourier transform of $R(r)$, this leads to quite different patterns for $F(q)$, allowing one to disentangle the different pieces of the physics involved more effectively.

Several shell-model calculations for s/d-shell nuclei are available. These calculations differ by the completeness of the shell-model space, the mass dependence of the parameters involved, and the way the two-body matrix elements have been fit to experimental data. In this section we shall refer most often to calculations performed by Brown, Chung, Wildenthal, and their collaborators at Michigan State University (Wildenthal and Chung, 1979; Brown *et al.*, 1980; Wildenthal, 1984), calculations that are perhaps the most extensive available.

The calculation of Wildenthal (1984) assumes ^{16}O to be an inert core, and uses the full $1d_{5/2}, 2s_{1/2}, 1d_{3/2}$ space for the valence nucleons; excitations to the $1f_{7/2}$ shell and beyond are ignored. The Hamiltonian used contains one- and two-body terms. The two-body matrix elements have been obtained by starting from those calculated using the Hamada-Johnston nucleon-nucleon interaction. These matrix elements then have been adjusted empirically to fit experimental binding energies. Unlike earlier calculations that used different matrix elements for the upper and lower parts of the s/d shell, the most recent calculation (Wildenthal, 1984) incorporates a simple mass dependence $A^{-0.3}$ for the matrix elements.

The results of previous calculations have been compared in detail to dipole moments (Wildenthal and Chung, 1979), multipole moments (Brown *et al.*, 1980), and some magnetic form factors (Singhal *et al.*, 1982). Here we compare systematically to magnetic form factors, and do not discuss moments for $J>1$. The experimental values for these moments, determined from phenomenological fits using form factors with a q dependence obtained from the extreme single-particle model are quite uncertain due to model-dependent extrapolations to $q=0$; moreover, with increasing multipole order they depend increasingly on the tails of the radial wave functions used.

In many of the previous studies, effective g factors and charges were employed (see, for example, Wildenthal and Chung, 1979; Singhal *et al.*, 1982). For the magnetic properties, the effective g factors brought little improvement, however. In the present calculations we use free g factors throughout. For integral properties ($q=0$), effective g factors perhaps represent a sensible attempt to account for deficiencies of the wave functions resulting from truncations of the space. At momentum transfers $q\neq 0$, we see no reason why this should be the case. The q dependence of form factors resulting from configuration admixtures is very different for a different major shell, and cannot in general be absorbed as a q-independent scaling.

When comparing experimental form factors and shell-model calculations, we take the following approach: the single-particle matrix elements are taken from theory; the radial wave functions, which are not fixed by theory, are fit to experiment. The basic set of equations used for these calculations comprises Eqs. (4.130)—(4.133). Nucleon finite-size effects (4.102) and corrections for center-of-mass movement (Tassie and Barker, 1958) have been accounted for. As radial wave functions we take harmonic-oscillator or Woods-Saxon wave functions, the latter if the quality of the experimental data warrants the use of a more realistic radial dependence.

The parameters of the Woods-Saxon potential are chosen in the following way: The radius parameter is fit to $F_T(q)$ and is basically fixed by the highest multipole form factor. The surface thickness, to which present data on $F_T(q)$ are insensitive, is taken from fits of the charge scattering data employing densities calculated using Woods-Saxon potentials; this procedure is justified by the fact that density-dependent Hartree-Fock calculations give very similar surface thicknesses for the effective potentials seen by nucleons in different shells. The depth of the Woods-Saxon potential is fit to the experimental separation energy; this ensures that the large-radius behavior, which influences the low-q behavior of $F(q)$, is realistic. For the spin-orbit depth, we use a constant $V_{so}=24$ MeV [in the notation of Gubler *et al.* (1977)].

1. The nucleus ^{17}O

The first s/d-shell nucleus we want to discuss is ^{17}O. Starting from the shell model, we expect ^{17}O to be a rather clean case of a single $d_{5/2}$ neutron outside a closed ^{16}O core. This simple picture is confirmed by the spectrum of excited states and the spectroscopic factors determined from one-nucleon transfer reactions. The magnetic moment ($\mu=-1.894$ n.m.) is also very close to the Schmidt value ($\mu=-1.913$ n.m.). We can therefore consider ^{17}O as a good test case for the interpretation of magnetic scattering in terms of simple models.

An experiment on magnetic electron scattering from ^{17}O has been performed at the Bates accelerator by Hynes *et al.* (1979). The data were taken using targets of BeO enriched to 20—85 % in ^{17}O with target foils of thickness 20—40 mg/cm^2. The magnetic cross sections were measured at 160° and at 180°, using the Bates 180° scattering facility (Peterson *et al.*, 1979). The charge scattering contributions (Miska *et al.*, 1979) were measured at forward scattering angles, and subtracted. The magnetic cross sections, taken at energies between 60 and 300 MeV, cover a momentum transfer range $q=0.6$—2.7 fm^{-1}.

The cross sections have been converted to PWBA form factors using a DWBA calculation (Hicks, 1982). The resulting form factors are shown in Fig. 28. They mainly cover the q region where the first maxima of the $M3$ and $M5$ form factors are expected to dominate. Little is known experimentally about the $M1$ form factor that is expected to peak near 0.4 fm^{-1}. [Of course, the $q=0$ behavior provided by the magnetic moment is accurately known. Since $F_T(0)=0$, this information does not show in the figures, but is always taken into account in the fits or the discussion of theoretical results.]

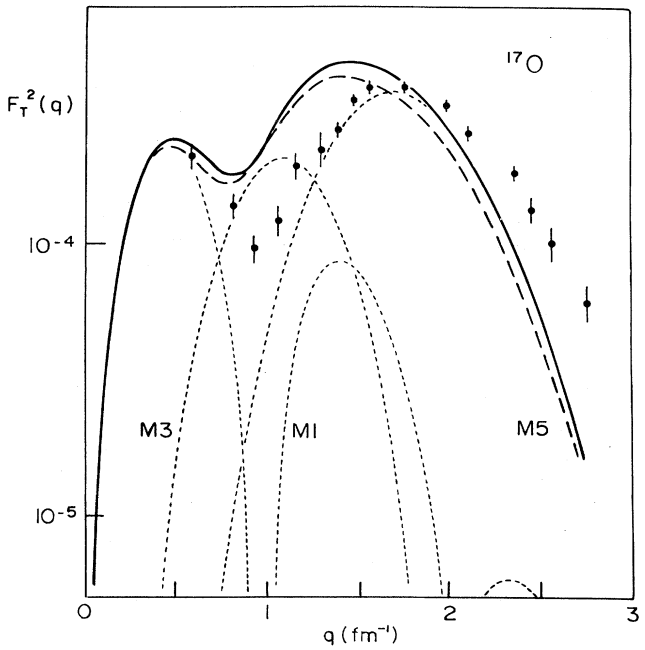

FIG. 28. The ^{17}O data of Hynes *et al.* (1979) compared to prediction of the extreme single-particle model calculated using a harmonic-oscillator wave function (solid curve). The long-dashed curve is calculated using a Woods-Saxon radial wave function.

In Fig. 28 the data are compared to a prediction of $F(q)$ obtained by Hynes *et al.* (1979). These authors use a harmonic-oscillator radial wave function ($b_{osc}=1.80$ fm) and a pure $1d_{5/2}$ neutron configuration ($\psi_{5;0}=\psi_{5;1}=1$). Also shown is a calculation using a Woods-Saxon radial wave function with parameters determined by $A=15,17$ energy levels, and ^{16}O charge scattering. One observes a pronounced disagreement between prediction and experiment.

The results of several theoretical studies are important for an understanding of the ^{17}O magnetic form factor. Suzuki (1978) and Arima *et al.* (1978) have investigated the role of configuration mixing and meson-exchange currents (MEC). They show that MEC, dominated by the pair contribution, change $F_T(q)$ by a non-negligible amount at large momentum transfer. They also show that the $M1$ and particularly the $M5$ form factors are little changed by configuration mixing in the q region of interest. Zamick (1978) and Bohannon *et al.* (1980) point out that the $M3$ operator is very similar to an $E2\times M1$ operator. This leads to a pronounced influence of $E2$ core excitations on the $M3$ form factor; in particular, a general decrease of $M3$ strength is expected near the first lobe of the $M3$ form factor. Vary *et al.* (1980) have performed a self-consistent Brueckner calculation for ^{17}O. They show that the $1d_{5/2}$ radial wave function is peaked at a smaller radius than the $R(r)$ calculated from a Woods-Saxon potential fit to the ^{16}O charge density. We shall discuss these calculations in more detail below, and show how they lead to an understanding of the transverse form factor.

The interpretation of Hynes *et al.* shown in Fig. 28 does not include two important pieces of physics mentioned in the preceding paragraph. The radial extent of $R(r)$ is smaller than that deduced via Woods-Saxon potentials fit to (basically) the $1p$-shell orbit. This observation has previously been made in the study of magnetic form factors of high multipolarity $M7,M9$ (Platchkov *et al.*, 1982), and is discussed in more detail in Sec. VI.C. The second physical effect not accounted for in Fig. 28 concerns the expected reduction of the $M3$ contribution. From the comparison shown in Fig. 28 it is clear that these two effects will reduce the discrepancy with experiment. A smaller radial extension of $R(r)$ will move the maxima of individual multipole form factors F_{MJ} to larger momentum transfer; this will lead to a better fit for $q>1.5$ fm^{-1}. A reduction of the $M3$ contribution will lead to a better reproduction of the data for $0.8<q<1.4$ fm^{-1}.

A phenomenological analysis of the ^{17}O data that allows for these two effects has been presented by Burzynski *et al.* (1983). Given the small sensitivity to configuration mixing, the $M5$ form factor is parametrized as the Fourier transform of a radial wave function calculated in a Woods-Saxon potential well. This $M5$ form factor is

multiplied with a factor α_5 close to one that accounts for an eventual depletion of $M5$ strength due to partial occupation of this shell. Given the comparatively minor effect of configuration mixing near 0.5 fm^{-1} and the very limited amount of data concerning $M1$, the $M1$ form factor is parametrized in a similar way. The q dependence of the $M3$ contribution is strongly dependent on configuration mixing. If the $M3$ contribution is parametrized similarly, then no significance can be attributed to the resulting parameters other than the demonstration that a small value of α_3 indeed shows that the $M3$ contribution is strongly reduced relative to the single-particle prediction, and barely visible in the data.

Figure 29 shows again the ^{17}O data. There the form factors (converted to PWBA) have been corrected for the MEC contribution as calculated by Suzuki (1978) and Arima *et al.* (1978). The data have been fit using a Woods-Saxon radial wave function with radius parameter $r_0=1.232$ fm. The surface thickness $a=0.6$ fm is taken from a fit of the ^{16}O charge form factor using a density computed in a Woods-Saxon well (Poth *et al.*, 1978). The spin-orbit depth is 24 MeV. The value of the parameter, $\alpha_5=0.94\pm0.09$, indicates that the $d_{5/2}$ contribution is quite close to that predicted by the extreme single-particle model ($\alpha_5=1$), as does $\alpha_1=0.99$. The small value of $\alpha_3=0.67$ clearly shows the mixing with core-excited states. The fit of the data is excellent, with a χ^2 of 0.7 per degree of freedom.

This fit yields two results that are independent of the complications brought on by configuration mixing and that can be interpreted in a quantitative way; the parameter α_5 and the shape of $R(r)$ are derived from the fit to the $M5$-dominated part of the magnetic form factor. The radial wave function, together with α_5, determines the asymptotic normalization $\bar{C}^2$ of the $1d_{5/2}$ wave function, defined for large r by

$$\Psi(r)=Y_2^m(\Omega_r)N\kappa h_2(i\kappa r),\quad \bar{C}^2=SN^2/2\kappa\ , \tag{6.8}$$

where S is the spectroscopic factor, h_2 the Hankel function, and $i\kappa$ the wave number of the bound state. This same quantity is measured by transfer reactions. Transfer reactions involving projectiles of energies below the Coulomb barrier (Franey *et al.*, 1979; Burzynski *et al.*, 1983) in particular yield a value of N insensitive to uncertainties of the reaction mechanism. The values of $\bar{C}^2=0.79\pm0.05$ obtained agree perfectly well with the value of 0.82 ± 0.08 derived from magnetic electron scattering. Phrasing this comparison differently, one can say that the asymptotic normalization determined from transfer reactions, together with the knowledge on the shape of $R(r)$ furnished by electron scattering, determines the spectroscopic factor $S=1.03\pm0.07$ of the $1d_{5/2}$ neutron configuration. [Note that in the standard convention used in transfer reactions the ^{17}O spectroscopic factor has a maximum possible value of $(A/A-1)^2=1.13$; for a detailed discussion of center-of-mass effects, see Dieperink and Sick (1981) and Clement (1973).] To the extent that no other $1d_{5/2}$ strength is observed in transfer reactions (Mairle *et al.*, 1978), the parameter α_5 (plus a correction due to c.m. movement; Dieperink and Sick, 1981) directly gives this spectroscopic factor $S=1.06\pm0.10$, again in perfect agreement with transfer reactions. Given the strong dependence on $R(r)$ of S values derived from transfer reactions—as discussed in Sec. VI.C, S changes typically by 10% for a 1% change of the orbit rms radius—this agreement constitutes a significant check on the $R(r)$ deduced from magnetic electron scattering.

The value of the spectroscopic factor, $S=1.05$, is unusually high and indicates that the $1d_{5/2}$ configuration is a quite pure one.

How, then, can we understand the small value of α_3 that demonstrates a large effect of configuration mixing? The reduction of $M3$ strength in general has qualitatively been explained by Zamick (1978) and Bohannon *et al.* (1980), using a simplified model. With a zero-range interaction, a valence neutron will only interact with core neutrons of opposite spin, due to the Pauli principle. Accordingly, the valence neutron will deform those core nucleons only. This introduces a correlation between valence nucleon spin and core neutron quadrupole deformation. Such a correlation has a pronounced effect on the $M3$ moment, since the $M3$ operator is basically a quadrupole operator coupled with the magnetic dipole operator to $J=3$; the term involving the orbital angular momentum is often smaller. Using qualitative estimates, Zamick shows that a reduction of the $M3$ moment by a factor 0.35—0.5 can be expected for ^{17}O. Bohannon *et al.* (1980) have investigated this point in more detail by performing a deformed Hartree-Fock calculation for ^{17}O. Using a simplified Skyrme interaction, they confirm that spin-up and spin-down core nucleons have different de-

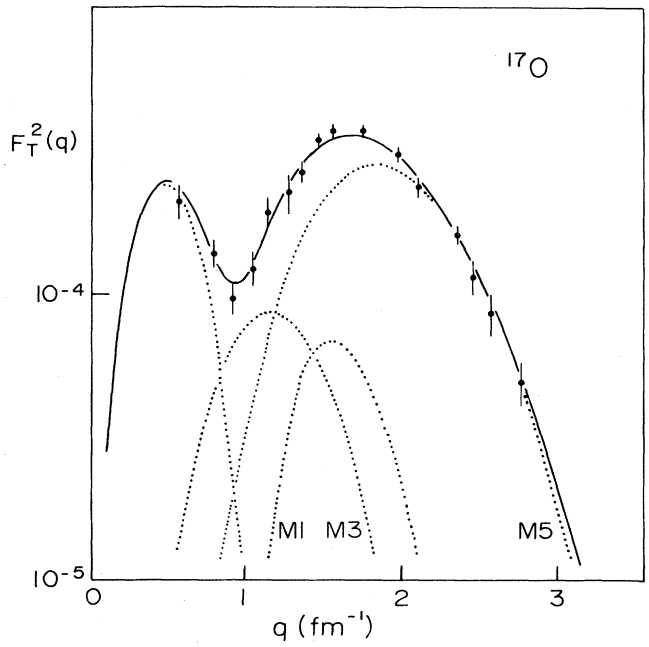

FIG. 29. The ^{17}O data of Hynes *et al.* (1979), corrected for the contribution of MEC, compared to the fit of Burzynski *et al.* (1983), calculated using a Woods-Saxon radial wave function.

formations. For ^{17}O, the reduction of the $M3$ moment and the $M3$ form factor in its main lobe ($q \sim 1.1$ fm^{-1}) amounts to a factor of approximately 2, with little change of the $M1$ or $M5$.

The shell-model calculations of Suzuki (1978) and Arima *et al.* (1978) confirm the above result. Using a large space ($6\hbar\omega$) and harmonic-oscillator radial wave functions, these authors calculate core polarization in first-order perturbation theory, using two phenomenological finite-range residual interactions with a Rosenfeld mixture. These calculations show that the core polarization for a single nucleon outside a closed L-S shell is rapidly decreasing with increasing multipolarity. The direct term, which decreases with increasing J, at high J largely cancels the exchange term. Given the fact that, in the long-wavelength limit, the first-order core polarization vanishes for $M1$, the largest effect occurs for $M3$, which consequently changes markedly in size and q dependence. These calculations show again that the core acts in a diamagnetic way such that the $M3$ form factor $F_{M3}(q)$ is reduced by a factor of 2 in its main lobe.

The calculation of Suzuki also gives the effect of configuration mixing on the $M5$ form factor. The only possible changes result from admixtures of shells with $j \geq \frac{5}{2}$, which are not very large. The numerical calculation gives an increase of $F(q)$ for momentum transfers beyond the principal peak at $q \sim 2$ fm^{-1}. If the resulting $F(q)$ is interpreted in terms of a pure $1d_{5/2}$ configuration, the radius of the resulting orbit becomes 0.6% too small. This change of 0.6% may be taken as a typical systematical uncertainty of any interpretation of F_{M5} that neglects configuration mixing.

A quantitative study of the $d_{5/2}$ radial wave function in ^{17}O has been performed by Vary *et al.* (1980) and Coon *et al.* (1982). These authors perform a renormalized Brueckner calculation for the $A=16$ core and use the self-consistent core results as input for the $A=17$ effective interaction. Using a large harmonic-oscillator space ($11\hbar\omega$) as a basis, they determine the wave function starting from the Reid soft-core nucleon-nucleon interaction. Due to the large basis size, the resulting $d_{5/2}$ radial wave function assumes a shape quite close to the one calculated in a Woods-Saxon potential, with a tail that is correct out to $r \sim 8$ fm. The $d_{5/2}$ state is underbound, its energy being -2.97 rather than -4.11 MeV. The ^{16}O core has a radius that agrees closely with that determined from charge electron scattering (2.72 fm).

The radial wave function calculated by Vary *et al.* is compared in Fig. 30 to one determined via magnetic electron scattering. A straightforward comparison actually would be somewhat misleading, since the separation energy of Vary *et al.* is low; for a loosely bound nucleon this leads to a significant shift of strength into the large-radius tail. We therefore show in Fig. 30 the $R(r)$ calculated using the Woods-Saxon geometry derived from magnetic (e,e'), but with a depth slightly decreased to produce a separation energy identical to that of the Brueckner calculation. The resulting radial wave function agrees closely with that predicted by Vary *et al.* To within 1% the peak of $R(r)$, the quantity mainly measured by (e,e'), occurs at the same radius.

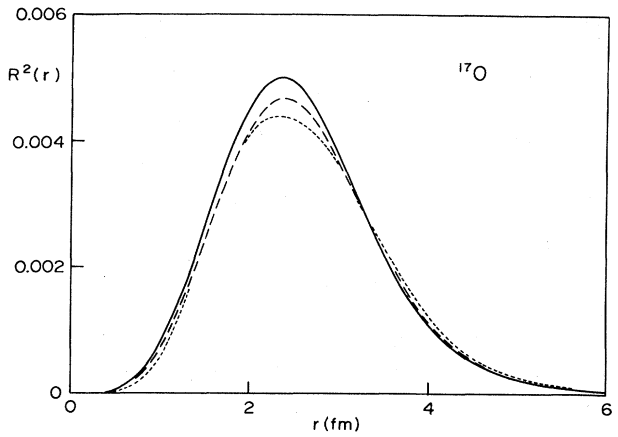

FIG. 30. The $1d_{5/2}$ radial wave function of Burzynski *et al.* (1983), adjusted to yield the separation energy of Vary *et al.* (1980), is shown as a solid curve. The Brueckner calculation of Vary *et al.* (1980) is shown as a dashed curve, the wave function obtained from the fit to the ^{16}O charge density as a dotted curve.

Figure 30 shows that an $R(r)$ calculated self-consistently in a mean field produced by a core of the correct size closely agrees with experiment. The fact that the radial wave function is peaked at a radius smaller than that predicted by a Woods-Saxon potential fixed (basically) by the $1p$ wave function (Fig. 30) thus is reasonably well understood.

We have also compared the radial wave function determined by electron scattering to that calculated by Campi (1982) in the framework of density-dependent Hartree-Fock theory. The main peak of $R^2(r)$ in this theory occurs at a radius 3.3% larger than that given by experiment.

To summarize the ^{17}O case, we can comment on the two outstanding features visible in Fig. 28. The shape of $R(r)$ connected to the displacement of the $M5$ peak is quite well understood. The reduction of the $M3$ form factor is qualitatively understood by different theoretical approaches, but a quantitative explanation of the exact amount of configuration mixing is not yet available.

2. The nucleus ^{23}Na

The next s/d-shell nucleus we want to discuss is ^{23}Na. For this nucleus a very small amount of experimental data is available. We show the calculated form factors, since they exhibit some unusual features.

The nucleus ^{23}Na has a ground-state spin of $\frac{3}{2}^+$, so naively a $1d_{3/2}$ odd-proton configuration might be assigned. Spectroscopic factors, however, do not confirm this assignment, and the experimental magnetic dipole moment $\mu = 2.218$ n.m. is far from the Schmidt value 0.126 n.m. Shell-model calculations clearly show that the main contributing configurations involve the proton $d_{5/2}$ shell.

In Fig. 31 we show the experimental form factors obtained by Torizuka (Goldemberg and Torizuka, 1963; Singhal *et al.*, 1982). The curves shown are calculated using the shell-model wave functions of Brown and Wildenthal (1982); the difference between these curves and the results of Wildenthal and Chung (1979) is very small. Given the very limited amount of data, the harmonic oscillator with $b=1.69$ fm was chosen for the radial dependence of $R(r)$.

Figure 31 shows the individual contributions of magnetization, proton convection current, and neutron magnetization. [Note that we present $F^2(q)$ for the individual, coherent contributions.] The nucleus ^{23}Na is unusual since, contrary to the normal case, the convection current provides a large contribution. It accounts for $\sim 40\%$ of the magnetic moment and the $M1$ form factor as a whole. Only at large q does the magnetization contribution start to dominate, as it does for the entire $M3$ form factor. The neutron contribution to F^2 is a very minor one.

Figure 32 shows the contributions of different shells to F_T^2. The effect of the $d_{5/2}^2$ piece is large. The main difference between $d_{5/2}^2$ and the full form factor results from the $d_{3/2}$-$d_{5/2}$ interference term. This emphasizes that $d_{5/2}$ is indeed the dominant shell; if $d_{3/2}$ were the major component, F_{M1}^2 at low q would be 10 times smaller, and F_{M3}^2 at large q 10 times larger. Figure 32 also shows that the $2s_{1/2}$ shell is of minor importance; only at large $q>2$ fm^{-1} does the $d_{3/2}$-$s_{1/2}$ interference term start to show up.

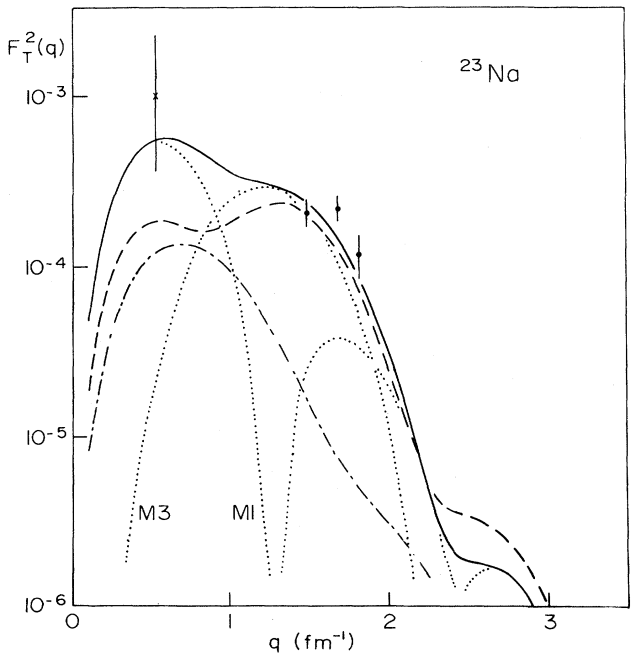

FIG. 31. Shell-model prediction for ^{23}Na calculated using density-matrix elements of Brown and Wildenthal (1982) and oscillator radial wave functions (solid curve). The contributions of proton magnetization (dashed curve) and convection current (dotted-dashed curve) are shown. The effect of neutron magnetization is too small to appear.

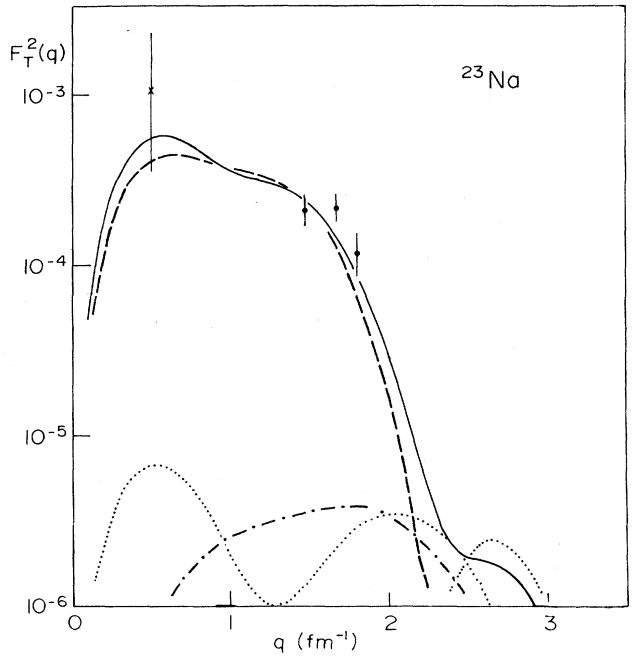

FIG. 32. The full shell-model result of Fig. 31 (solid curve), compared to the contribution of individual matrix elements: $1d_{3/2}^2$ (dotted-dashed curve), $2s_{1/2}^2$ (dotted curve), $1d_{5/2}^2$ (dashed curve).

3. The nucleus ^{25}Mg

The nucleus ^{25}Mg has received considerable attention both experimentally and theoretically. Experiments have been performed at the (former) Instituut voor Kernphysisch Onderzoek (IKO) in Amsterdam (Euteneuer *et al.*, 1977) at the Bates accelerator (Euteneuer *et al.*, 1977), and more recently at Bates again (York and Peterson, 1979). While the latter Bates data ($q=0.9$–2.2 fm^{-1}) and the IKO data were taken at a scattering angle $\theta=180°$, the earlier Bates data were obtained at $\theta=160°$. The resulting cross sections have been converted to PWBA form factors using DWBA codes. These form factors, with error bars that include the statistical and systematical errors, are shown in Fig. 33.

At low transfer, the data cover the region where the $M1$ form factor is expected to peak. Uncertainties are large, due to the large correction required to subtract the charge contribution to the measured cross section. At $q\sim 1.5$ fm^{-1} the $M3$ form factor is expected to peak. In this region the data from the $\theta=160°$ and 180° Bates experiments disagree somewhat. We shall see later that the 180° data are much closer to anything that can be explained using reasonable wave functions. We estimate these data to be more reliable than the 160° cross sections. The latter required large corrections for the charge contributions, amounting to 84% at the lowest q of 1.44 fm^{-1}; such large corrections are subject to systematic experimental uncertainties unless the technique of normalization relative to a very similar nucleus, ^{24}Mg, for instance, is used.

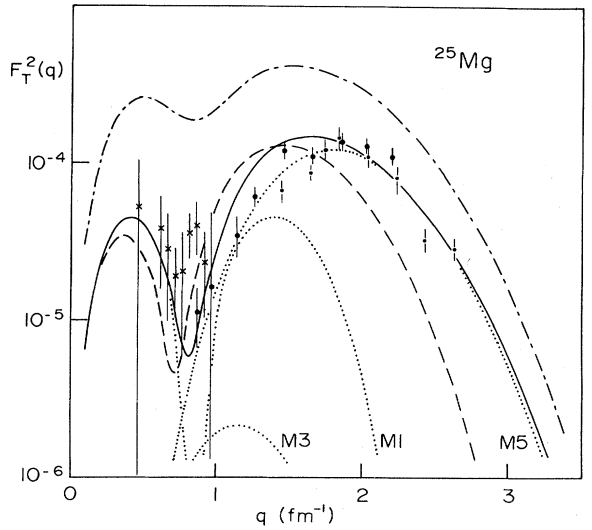

FIG. 33. The ^{25}Mg data of York and Peterson (1979) (large circles) and Euteneuer *et al.* (1977) (crosses), taken at 180°. The points (dotted curve) of Euteneuer *et al.* (1977) were taken at 160°. The solid curve uses the matrix elements of Brown and Wildenthal (1982) and a fitted Woods-Saxon radial wave function. The dotted-dashed curve uses the same $R(r)$, but the extreme single-particle model. The dashed curve is calculated using the Woods-Saxon potential determined from charge scattering [Li *et al.* (1974)].

^{25}Mg is an interesting case for the study of magnetic form factors: the unpaired $1d_{5/2}$ neutron is coupled to a core that is far from inert or spherical. In the shell model, ^{24}Mg is a nucleus near the middle of the s/d shell, with a rather complicated structure. In the language of the collective models, ^{24}Mg has a considerable deformation. Either fact is expected to influence the magnetic properties appreciably. In order to demonstrate this point, we show in Fig. 33 the form factor calculated in the extreme single-particle model, with a pure $(1d_{5/2})^{-1}$ configuration. The magnetic dipole moment is off by more than a factor of 2, and a similar or larger factor in $F(q)$ occurs for the $M5$ and $M3$ multipoles.

Euteneuer *et al.* (1977) have shown that the magnetic form factor is explained quite well once the shell-model calculation of Chung (1976; Wildenthal and Chung, 1979) is utilized. In Fig. 33 we show a similar calculation performed using the more recent s/d-shell matrix elements of Brown and Wildenthal (1982). This calculation explains quite well the magnetic dipole moment ($\mu=0.90$ n.m., $\mu_{\rm exp}=0.85$ n.m.) and the first maximum of the $M1$ form factor. It predicts a very large reduction of F_{M3}^2 by a factor ~ 100, in agreement with the data, and a reduction by a factor of ~ 4 for F_{M5}^2. According to this calculation, the main contribution to F_T comes from $d_{5/2}$ neutrons; the protons give a small contribution of similar q dependence. The main change of the q dependence relative to the extreme single-particle model prediction results from the convection-current contribution to $M1$, which is quite important for $q<1.5$ fm^{-1} (Singhal *et al.*, 1982). The form factor of Fig. 33 is quite similar to the one obtained using the matrix elements of Chung (1976); the main difference occurs for $M3$, which is a factor of 2 smaller for Brown and Wildenthal (1982). Given the very small contribution of $M3$ and the error bars of the data in the relevant q region, it is not yet possible to check upon this difference.

We note from Fig. 33 that the agreement with experiment in the region 1.0—1.5 fm^{-1} is not very good, even if we ignore the 160° data (see above). Apparently, the contribution to $F_T(q)$ of the second lobe of F_{M1} is too large. This second maximum results mainly from an interference term involving the $d_{5/2}$ neutron magnetization and the proton convection current, which gives a significant contribution for $q<1$ fm^{-1} and accounts for a -45% contribution to the magnetic dipole moment.

The form factors shown in Fig. 33 are calculated using wave functions calculated in a Woods-Saxon potential. The surface thickness, $a=0.72$ fm, is taken from a fit of the charge form factor of ^{24}Mg, using a Woods-Saxon density (Li *et al.*, 1974). The value of the parameter a is larger than usual, since the deformation of ^{24}Mg in a spherical calculation is mocked up by a larger effective surface thickness. This large value of a accounts in part for the small $r_0=1.06$ fm used to fit $F_M(q)$. Singhal *et al.* (1982), who fit F_M using the s/d-matrix elements of Whitehead *et al.* (1977), have also observed that the $d_{5/2}$ orbit size required to fit F_M is smaller than the one derived from charge scattering. In order to obtain agreement with $F_M(q)$, the rms radius of the $d_{5/2}$ orbit (which dominates F_M as discussed above) has to be $\sim 10\%$ smaller than that derived from $F_{\rm ch}(q)$. This point is exemplified by the curve in Fig. 33 calculated using the matrix elements of Brown and Wildenthal (1982) and the Woods-Saxon parameters of Li *et al.* (1974) ($r_0=1.35$ fm). The smaller radius of $R(r)$ improves both the agreement at large q for F_{M5} and the agreement for the $M1$ peak near 0.5 fm^{-1}.

We note that when using the matrix elements of Brown and Wildenthal (1982) and harmonic-oscillator radial wave functions, one can obtain a fit to the data of similar quality. The resulting oscillator parameter, $b=1.73$ fm, yields an orbit radius 3% smaller than the Woods-Saxon wave function. This shows the need to supplement, via the separation energy, information on the large-radius behavior of $R(r)$ if the low-q data are not precise enough to fix its shape.

In connection with the use of F_T data of high multipolarity to determine $R(r)$ (Sec. VI.C), we may mention here one test performed using the theoretical ^{25}Mg form factors. When determining phenomenological radial wave functions from F_T, one usually neglects the contributions of configuration mixing. Using the magnetic form factor calculated with the matrix elements of Brown and Wildenthal (1982) (Fig. 33) as "data," we have determined the $R(r)$ obtained when ignoring all configuration mixing in the analysis, as was done, for example, for $A=17,49,51,87,93$. The resulting $R(r)$ has a radius that differs from the starting value by $\sim 1\%$. This difference is quite small despite the fact that ^{25}Mg is very far from

the configuration of a single particle or hole outside an inert core. This test establishes the negligible role of configuration mixing due to multipoles $J<2J_0$ assumed in the single-particle–single-hole cases.

For ^{25}Mg, the magnetic data have been interpreted in an alternative way. Moya de Guerra and Dieperink (1978) and Moya de Guerra and Kowalski (1980) have calculated form factors of odd-even axially symmetric deformed nuclei using the projected Hartree-Fock approach. They also give the expressions for magnetic form factors using the Nilsson model and deformed harmonic-oscillator wave functions. This work shows that in general the elastic magnetic form factors of intermediate multipolarity $1<J<2J_0$ are strongly quenched as compared to the spherical single-particle values. The formalism is discussed in more detail in Secs. IV.D and VI.D, where the appearance of large reduction factors is explained as well. The predictions of Moya de Guerra and Dieperink (1978), obtained using the rotational model, are shown in Fig. 34. For the $M5$ multipole, a q-independent quenching of $F(q)$ by a factor of 0.55 relative to the single-particle prediction is found; this factor is independent of the deformation as well, and results from the fragmentation of a given shell-model orbital into several Nilsson orbitals. For $M3$, a quenching factor of ~ 0.12 in F_{M3} is obtained; the collective contribution reduces F_{M3} further, but is generally small. For $M1$, the overall reduction in amplitude is significantly modified by the collective contribution of the $A=24$ core. This term, calculated using a spherical ^{16}O and eight nucleons in the [220] $\frac{1}{2}^+$ and [211] $\frac{3}{2}^+$ Nilsson orbitals, shifts the first minimum of F_{M1} from $q=0.95$ to 0.75 fm^{-1}. The resulting form factor F_T agrees quite well with experiment; the difference present at large q results from an oscillator parameter which is too large.

For comparison, we have repeated in Fig. 34 the shell-model results, calculated this time using the same harmonic-oscillator parameter ($b=1.83$ fm) as used by Moya de Guerra and Dieperink (1978). Figure 34 shows that, despite apparently very different physics input, the collective and shell models give a similar prediction for $F_T(q)$. In particular, the strong quenchings of the $M3$ and $M5$ multipoles closely agree. Moreover, the shift of the first zero of $F_M(q)$ due to the collective contribution of the $d_{5/2}$ protons is quite similar. This convergence of different theoretical approaches is quite satisfying.

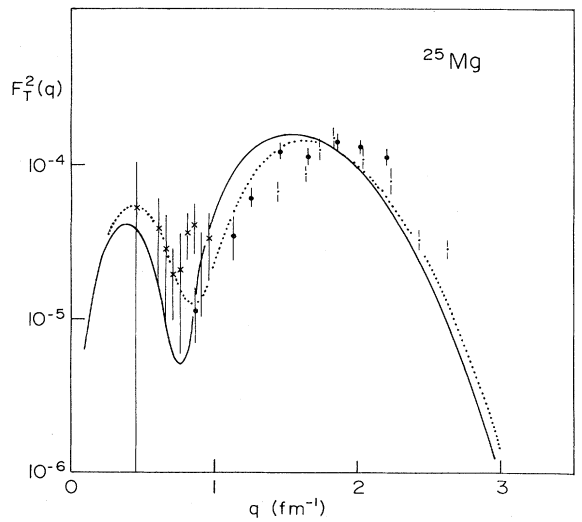

FIG. 34. The shell-model prediction (solid curve), compared to the results of Moya de Guerra and Dieperink (1978) obtained using the Nilsson model (dotted curve). The data are identified in Fig. 33.

4. The nucleus ^{27}Al

The next s/d-shell nucleus we shall briefly discuss is ^{27}Al; in the extreme single-particle model ^{27}Al has a proton hole in the closed $1d_{5/2}$ subshell.

Experimental form factors have been measured at forward and backward angles and energies up to 500 MeV by Li *et al.* (1970,1974). The magnetic data were taken at a "normal" scattering angle of 145°, using the Stanford HEPL accelerator. They cover a q range of 1.5–2.5 fm^{-1}, where the $M5$ form factor dominates. The data at low momentum transfer were measured by Lapikás *et al.* (1973), using the IKO 180° scattering system. The resulting cross sections cover the $M1$ region 0.3–1 fm^{-1}. Some data points near the expected maximum of the $M3$ form factor have been obtained by Macauley *et al.* (1977), using the Glasgow accelerator. Recently, an experiment covering a large region of q was performed at Bates ($q=0.8$–2.9 fm^{-1}), at scattering angles $\theta=160°$–$180°$ (Hicks *et al.*, 1983). The resulting cross sections, converted to PWBA form factors using a DWBA calculation, are displayed in Fig. 35.

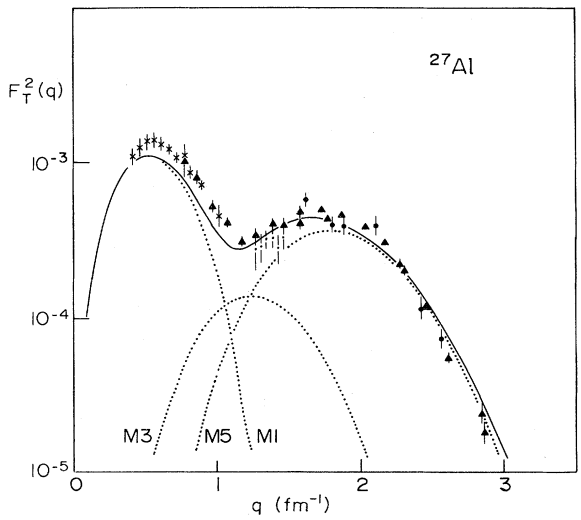

FIG. 35. The ^{27}Al data measured by Lapikás *et al.* (1973) (crosses), Macauley *et al.* (1977) (dots), Li *et al.* (1970) (solid points), and Hicks *et al.* (1983) (triangles), compared to the shell-model prediction calculated using the Brown and Wildenthal (1982) matrix elements and a Woods-Saxon radial wave function.

A comparison of a shell-model calculation with the experimental data has been performed by Lapikás *et al.* (1973), with the wave function calculated by Wildenthal and McGrory using a modified surface-delta residual interaction; quantitatively quite good agreement was obtained. The same is true for the prediction obtained by Singhal *et al.* (1982), who used the matrix elements of Whitehead *et al.* (1977), obtained by using the effective interaction of Wildenthal and Chung (1979). In Fig. 35 we show the most recent calculation, using the matrix elements of Brown and Wildenthal (1982). Again quite good agreement with the data is found. The form factor shown in Fig. 35 is calculated using a Woods-Saxon radial wave function ($r_0=1.12$ fm, $a=0.72$ fm) with parameters determined as discussed for ^{25}Mg.

For all three shell-model calculations the $M1$ contribution is somewhat too small. The reduction by nearly a factor of 2 in F_M^2 relative to the extreme single-particle model is too large. The magnetic moment, on the other hand, is well explained by the shell-model calculation ($\mu_{\rm exp}=3.67$ n.m., $\mu_{\rm SM}=3.58$ n.m.). The $M3$ contribution near the $M3$ maximum is roughly correct in all calculations and about five times smaller than the extreme single-particle value. The $M5$ form factor, which is reduced very little, agrees reasonably well with experiment for all calculations.

A closer study of the theoretical form factors reveals that the neutron contribution to F_M is negligible. The $M1$ form factor at low q receives a large convection-current contribution, which accounts for 50% of the magnetic dipole moment. $M3$ and $M5$ depend nearly exclusively on the proton intrinsic magnetization. The $d_{5/2}^2$ term dominates the entire form factor. The only other matrix element of importance is the $1d_{5/2}$-$2s_{1/2}$ $M3$ contribution. This matrix element is responsible for the large suppression of $M3$, and reduces F_{M3}^2 near the maximum by a factor of 2. The contribution of other matrix elements, given in the work of Singhal *et al.* (1982), is very small.

Given the dominating role of one shell and one type of nucleon, the magnetic form factor of ^{27}Al is a good case for the determination of the $d_{5/2}$ radial wave function using the $M5$ form factor. A purely phenomenological fit of data available before 1983 shows that the quality of the data was marginal; the uncertainty of the resulting radius amounted to several percent. The $M5$ form factor was measured over too small a q range (or, more precisely, the dynamic range in F_{M5}^2 was too small). In this case the $M5$ form factor could not be separated well enough from the $M3$ contribution, the shape and overall amplitude of which is subject to large uncertainties due to configuration mixing. The recent data taken at Bates up to 2.9 fm^{-1} (Hicks *et al.*, 1983) have greatly improved this situation. The rms radius of the $1d_{5/2}$ orbit is now well determined (3.26 ± 0.04 fm) and insensitive to variations of quantities (F_{M3}) that are quite uncertain. Both this orbit radius and the r_0 obtained when using shell-model single-particle matrix elements show that the radial wave function required to get a fit has a radius significantly smaller than the one implied by the charge form factor, 3.55 fm (Li *et al.*, 1974).

5. The nuclei ^{29}Si, ^{31}P

The nuclei ^{29}Si and ^{31}P are very interesting cases for the study of magnetic form factors. For a ground-state spin of $\frac{1}{2}$, only the multipolarity $M1$ will contribute over the whole q range. In this case, the $M1$ form factor can be treated in the same way as the Coulomb monopole $C0$ charge form factor; a Fourier transform of F_{M1} yields the magnetization density in radial space.

In the extreme single-particle model the structure of these nuclei corresponds to an unpaired $2s_{1/2}$ neutron or proton, respectively. The Fourier transform of a $2s$ radial wave function should lead to a very distinctive pattern due to the node present in $R(r)$. Given this particular pattern, configurations involving shells with nodeless radial wave functions, $1d_{5/2}$ and $1d_{3/2}$ in particular, should stand out clearly. Due to the distinct shape of the $2s$ radial wave function, we might hope that the interpretation of the ^{29}Si and ^{31}P form factors actually could be easier than for the analogous ^{13}C case.

Before we compare experimental results and theory, we briefly discuss different predictions for the magnetic form factor of ^{29}Si; this allows us to illustrate the role of $d_{5/2}$-$d_{3/2}$ spin-flip transitions and the differences among some of the most recent shell-model calculations (see also Brown *et al.*, 1983).

The solid curve shown in Fig. 36 represents the predictions for $F_T(q)$ obtained using a harmonic-oscillator wave function ($b=1.69$ fm) and the matrix elements of Brown

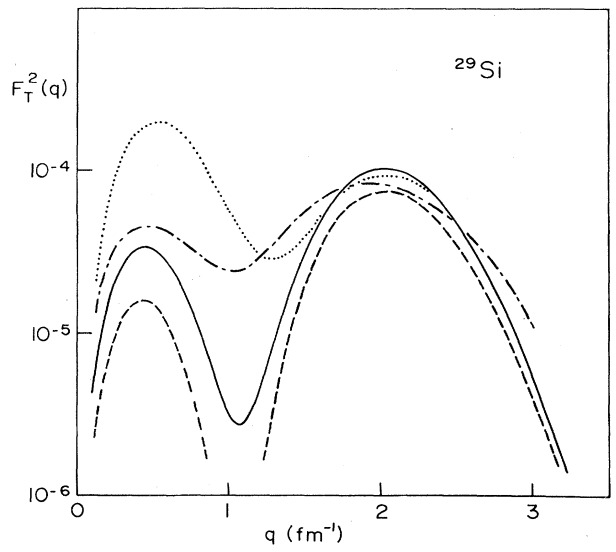

FIG. 36. Elastic magnetic electron scattering from ^{29}Si. The solid curve is calculated using the ^{29}Si matrix elements of Brown and Wildenthal (1982); the dotted curve represents the $2s_{1/2}^2$ contributions alone. The dashed curve uses the matrix elements of Wildenthal and Chung (1979), the dotted dashed curve uses the matrix elements of Whitehead *et al.* (1977).

and Wildenthal (1982). The dashed curve was calculated using the matrix elements of Wildenthal and Chung (1979). The dashed-dotted curve, taken from Singhal *et al.* (1982), was obtained using the matrix elements of Whitehead *et al.* (1977) and an almost identical ($b=1.70$ fm) harmonic-oscillator wave function. Very pronounced differences occur at low q, in the region of the first maximum and minimum of F^2_{M1}.

The work of Singhal *et al.* (1982) shows that the region $q<1.5$ fm^{-1} is strongly influenced by configuration admixtures, while for $q>1.5$ fm^{-1} the form factor is dominated by the $2s_{1/2}$ shell. This is emphasized by the dotted curve in Fig. 36, which represents the $2s^2_{1/2}$ contribution alone. This dominance of $2s^2$ at large q results from the high-frequency Fourier component introduced by the node in the $2s$ radial wave function.

The main difference between the $2s$ contribution and the full calculation results from the presence of the $d_{5/2}$-$d_{3/2}$ matrix element, which interferes destructively with the $2s^2$ term. The $d_{5/2}$-$d_{3/2}$ matrix element is smallest in the calculation of Whitehead *et al.* (1977) due to the fact that in this calculation the full s/d space was not allowed for; the number of holes in the $d_{5/2}$ shell was restricted to ≤ 2. The difference between the two calculations performed by the Michigan State University group is mainly due to an increase in the $2s^2$ term in Brown and Wildenthal (1982). This increase results from a continuous mass dependence of the two-body matrix elements through the s/d shell that replaced the previous discontinuous change at $A=28$.

The large effect of the $d_{5/2}$-$d_{3/2}$ interference on magnetic moments (Wildenthal and Chung, 1979) and $M1$ form factors is clearly demonstrated by Fig. 36. The importance of this spin-flip term is similar for the other s/d nuclei and plays a major role in the understanding of other $M1$ form factors, such as the one in the ^{13}C case.

A calculation using a Woods-Saxon radial wave function also shows that the shape of the first maximum and minimum of F_M is quite sensitive to the $R(r)$ used. This is to be expected once two amplitudes interfere significantly. Under these circumstances, the effects of configuration mixing and the shape of $R(r)$ will be difficult to disentangle unless independent experimental information (spectroscopic factors, etc.) is included.

An experiment on ^{29}Si and ^{31}P has recently been performed by Miessen (1982). Using the Bates and Mainz accelerators, he measured both charge and magnetic form factors, the latter at scattering angles $\theta=160°$–$180°$. The resulting form factors, which cover the q region 1–2.8 fm^{-1}, are shown in Figs. 37 and 38.

The solid curves shown in Figs. 37 and 38 are obtained using the matrix elements of Brown and Wildenthal (1982) together with Woods-Saxon radial wave functions. The radius parameter ($r_0=1.27$ fm) has been fitted to the data; the surface thickness ($a=0.72$ fm) has been taken from a Woods-Saxon fit to the charge density (Li *et al.*, 1974). For ^{31}P, this calculation reproduces rather well the experimental data, except for the lowest q point. The minimum near 1.2 fm^{-1}, which is influenced considerably

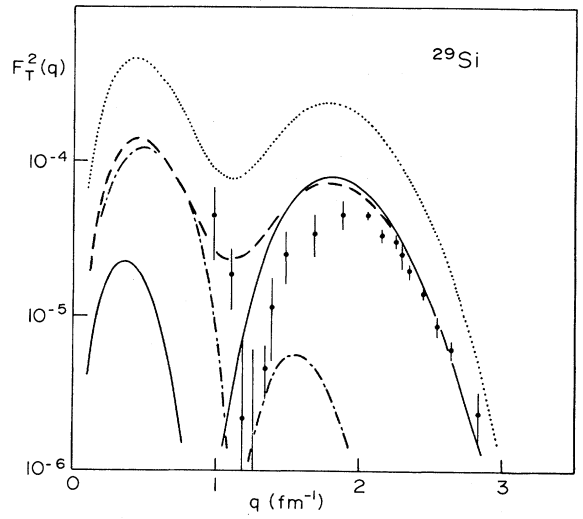

FIG. 37. The ^{29}Si data of Miessen *et al.* (1982) compared to a calculation based on the Brown and Wildenthal (1982) matrix elements and Woods-Saxon radial wave functions. The dashed and dotted-dashed curves give the $2s^2$ and $d_{5/2}$-$d_{3/2}$ contributions, respectively. The dotted curve gives the extreme single-particle model prediction.

by the interference of the s^2 and the $d_{5/2}$-$d_{3/2}$ terms, is quite well predicted. The magnetic moment ($\mu_{exp}=1.13$ n.m., $\mu_{calc}=1.02$ n.m.) is well accounted for also.

For ^{29}Si, the agreement between experiment and shell-model calculations is not as good. The amplitude of the second diffraction maximum—mainly due to the $(2s_{1/2})^2$ term—is too large. Figure 37 also shows a calculation for a pure $2s_{1/2}$ particle, with spectroscopic factor 1. Given

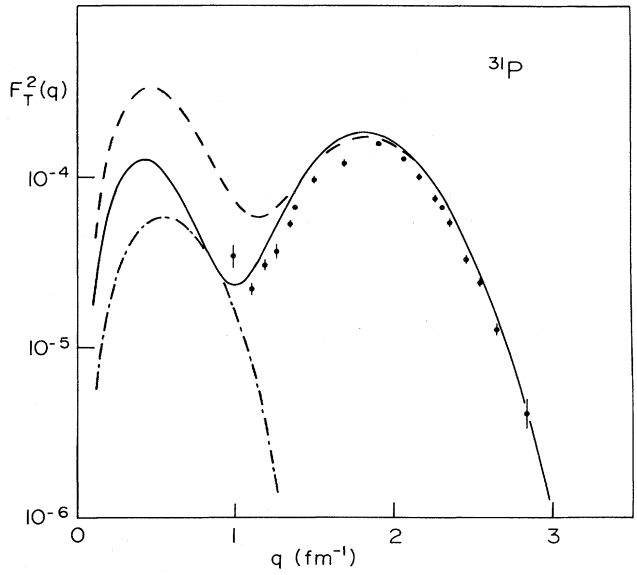

FIG. 38. The ^{31}P data of Miessen *et al.* (1982) compared to a calculation based on the Brown and Wildenthal (1982) matrix elements and Woods-Saxon radial wave functions. The dashed and dotted-dashed curves give the $2s^2$- and $1d$-shell contributions, respectively.

the large reduction in the amplitude of the peak predicted by the shell-model calculation, we may conclude that a moderate further reduction of the $2s$ occupation could lead to agreement with experiment in the range 1.5—3 fm^{-1}; the d-shell amplitudes contribute very little in this region. The amplitude of the first peak predicted by the shell-model calculation seems too small, although the agreement with experiment at $q=0$ ($\mu_{exp}=-0.56$ n.m., $\mu_{calc}=-0.50$ n.m.) is quite good. Better data for $q<1.2$ fm^{-1} would be very interesting, and would allow one to detect the large quenching due to d-shell contributions predicted for $q<1$ fm^{-1}.

We should add here one comment concerning the sign of $F_T(q)$. The various figures always give curves for F_T^2; features loosely referred to as "diffraction minima" in individual multipole contributions MJ usually correspond to a sign change in F_{MJ}. For ^{29}Si and ^{31}P, this is not the case. Both $M1$ form factors exhibit near $q\sim1$ fm^{-1} a true minimum *without* sign change. The ^{29}Si (^{31}P) form factor remains negative (positive) all the way up to 3.4 fm^{-1}. As pointed out by Sick (1974), the Fourier transform of a $2s$ radial wave function leads to a true minimum, and the admixtures due to d-shell contributions to F_{M1} do not change this. These two maxima for F_T result from the overlap of the first lobe of $\sin(qr)$ with the two peaks of $R^2(r)$.

This absence of a sign change of F_T has important consequences for phenomenological analyses in terms of magnetization densities (Miessen, 1982) in cases where the experimental data are not extensive enough to determine the sign of $F(q)$ via continuity starting at $q=0$.

6. The nucleus ^{39}K

For ^{39}K the extreme single-particle model predicts a $1d_{3/2}$ proton-hole structure. The same configuration is assumed in shell-model calculations that do not allow for excitation outside the s/d shell. From experimental spectroscopic factors we know that $Z=20$ in general, and ^{40}Ca in particular, are not actually a good shell closure. Accordingly, the $(1d_{3/2})^{-1}$ configuration is not expected to explain the magnetic form factor. The nucleus ^{39}K should be a particularly favorable place to study admixtures of configurations from the next-higher f/p shell.

Two sets of data are available for electron scattering. At IKO, De Jager has measured cross sections at 180° scattering angle in the q range 0.7—1 fm^{-1} (see Lapikás, 1978); the data measured at Bates (Lapikás, 1979) cover the range 1.4—2.5 fm^{-1} (Fig. 39).

The experimental form factor of ^{39}K is rather far from a $d_{3/2}^{-1}$ configuration; the $M1$ form factor is reduced by a factor of ~0.8 in F^2 relative to the extreme single-particle value, the $M3$ form factor by a factor of ~5. In the absence of theoretical form factors, the data have been fitted using a phenomenological parametrization (Lapikás, 1978) similar to the one described for ^{17}O. The $M1$ data and the magnetic dipole moment can be fit simultaneously only if a multipole-dependent effective g factor is allowed for. This clearly shows that pure $(d_{3/2})^{-1}$ form factors, even with phenomenological reduction factors, do not allow one to describe properly the physics contained in the data.

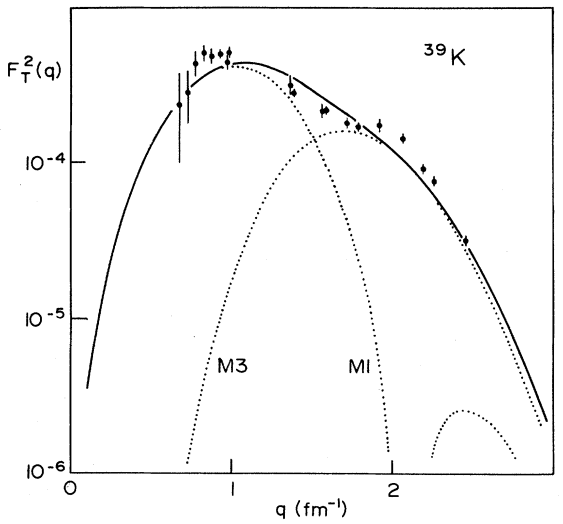

FIG. 39. The ^{39}K data of De Jager *et al.* (1979) compared to a phenomenological fit made using $d_{3/2}^2$ and $f_{7/2}^2$ matrix elements and a harmonic-oscillator radial wave function.

Several theoretical calculations have dealt with the open-shell nature of ^{39}K. Zucker (1971) and Poves *et al.* (1977) performed shell-model calculations in the $d_{3/2}$-$f_{7/2}$ space. They found an appreciable occupation of the $f_{7/2}$ shell, which according to Poves *et al.* (1977) amounted to occupation numbers $n_\pi(f_{7/2})=0.31$, $n_\nu(f_{7/2})=0.54$, and $n_\pi(d_{3/2})=2.69$. While $d_{3/2}$-$f_{7/2}$ matrix elements give no contribution to the magnetic elastic form factors (due to parity conservation), the $(f_{7/2})^2$ terms could lead to an appreciable influence.

In order to see whether such an $f_{7/2}$ admixture could explain the magnetic form factor, we have made a fit to the data using phenomenological matrix elements. In addition to the $M1$ and $M3$ $(d_{3/2})^2$ matrix elements, we have allowed for an $M1$ $(f_{7/2})^2$ contribution; the $M3$ $(f_{7/2})^2$ contribution turns out to be rather poorly determined and brings with it little improvement of the fit. In order to constrain the fit as much as possible, we allowed only for contributions of protons. Given the limited amount of data, a harmonic-oscillator wave function ($b=1.80$ fm) was employed.

The resulting fit of MJ form factor data and magnetic moment is quite good, as shown in Fig. 39. The $(T=0)d_{3/2}^2$ matrix elements have values that reflect the reduction relative to the extreme single-particle model, 0.77 and 0.55 for $M1$ and $M3$, respectively. The $f_{7/2}^2$ matrix element, which is very important in fitting the full $M1$ region, turns out to be reasonably small, 0.069. The goodness of the fit and the smallness of the $f_{7/2}$ contribution could make this a plausible parametrization of the data. However, the $f_{7/2}^2$ matrix element found is much larger than that resulting from the above-mentioned

shell-model calculation of Poves (1982), who obtains $M1$ matrix elements of 0.002 (0.008) for $T=0$ ($T=1$), respectively.

A detailed study of magnetic scattering from ^{39}K has recently been performed by Suzuki (1978,1983), who studied both the effects of core polarization and meson-exchange currents. In this calculation, the single-particle wave functions were calculated using Woods-Saxon wells. The core-polarization effects were estimated using first-order perturbation theory and the Green's-function method. This allows one to perform a calculation without explicitly restricting the configuration space. As a residual interaction, the Michigan three-range interaction is used.

The results of this calculation are shown in Fig. 40. Comparison of the dashed curve and the dotted curve shows the effect of configuration mixing. The largest part of this core-polarization effect is actually due to the tensor part of the interaction. This study reveals an interesting difference between nuclei of jackknifed ($j=l-\frac{1}{2}$) or stretched ($j=l+\frac{1}{2}$) valence nucleon configurations. For the former, the magnetic form factor is dominated by the $(\sigma Y_{J+1})_J$ term, which has a destructive interference with the $(\sigma Y_{J-1})_J$ amplitude. As this amplitude is increased by the tensor part of the residual interaction, an overall decrease of F_M results. For the stretched configuration, the dominant term contributing to F_M is $(\sigma Y_{J-1})_J$. In this case the central and tensor terms cancel to some degree, and lead to an overall increase of F_M.

The contribution of MEC is also calculated by Suzuki: the pair current is found to increase the form factor, while the pionic currents and the isobar diagram lead to a smaller reduction. The isobar diagram is particularly effective in the $M3$ form factor, in accordance with experience in other nuclei. The total effect of meson-exchange currents plus core polarization is shown in Fig. 40 as a solid line.

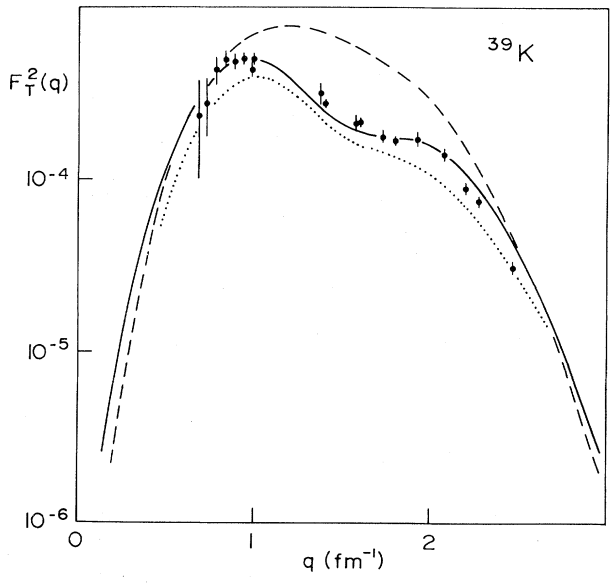

FIG. 40. Elastic magnetic electron scattering from ^{39}K. The dashed curve represents the single-particle result of Suzuki (1978,1983); the dotted curve includes core polarization; the solid curve includes MEC in addition.

The calculation of Suzuki shows that for MEC, as well, the jackknifed case differs considerably from the stretched configurations mainly studied in the past. For $j=l-\frac{1}{2}$, MEC play a role at a relatively smaller momentum transfer. They lead, for example, to a change of the magnetic moment of $\Delta\mu_{\rm MEC}=0.26$ n.m.; given the small one-body magnetic moment (0.13 n.m.), the MEC effect at very low q turns out to be quite large.

7. Other s/d-shell nuclei

Above, we have presented a detailed discussion of those s/d-shell nuclei that hold special interest due to the availability of experimental data or of theoretical calculations. A number of other nuclei—^{19}F, ^{33}S, ^{35}Cl, ^{37}Cl—remain to be investigated in more detail. For completeness we present in Fig. 41 a set of predictions, all calculated using harmonic-oscillator wave functions and the matrix elements of Brown, Chung, and Wildenthal (1980).

We do not intend to discuss these predictions in detail, but we point out a few peculiarities. The ^{19}F nucleus is another case where only $M1$ contributes, and it is again the s^2 matrix element that dominates at large q. In contrast to the case of ^{29}Si and ^{31}P, however, the d-shell terms interfere constructively and greatly increase the amplitude of the first lobe of F_T. Again, the total form factor shows a true diffraction minimum, without sign change.

For ^{33}S, both $M1$ and $M3$ give a sign change near 0.9 fm^{-1}, with a resulting near-zero in F_T^2. The pure $(d_{3/2})^2$ $M1$ contribution in the first diffraction lobe is larger by a factor of 2; the reduction to the low F_{M1}^2 results mainly from the $d_{5/2}$-$d_{3/2}$ interference term. The individual $M3$ contributions at low q largely interfere anyway; the structure of F_{M3} resulting from this interference should serve as a warning against attempts to deduce $M3$ moments by extrapolating phenomenological fits (done in the region 1—3 fm^{-1}, where F_{M3} can be measured) to zero momentum transfer (Lapikás, 1979).

C. $2p/1f$- and $1g$-shell nuclei

As compared to the p and s/d shells, the region of $A>40$ is poorly explored by magnetic electron scattering. This is mainly because of increasing difficulties in performing experiments as the separation of the magnetic contribution for large Z becomes harder due to the Z^2 dependence of the charge contribution. In this situation, one depends on the availability of 180° scattering systems, of which there are few, and one has to deal with experiments that are considerably more time consuming.

The complexity of the form factors, largely due to the higher number of multipolarities contributing, also makes more difficult the interpretation of experimental data.

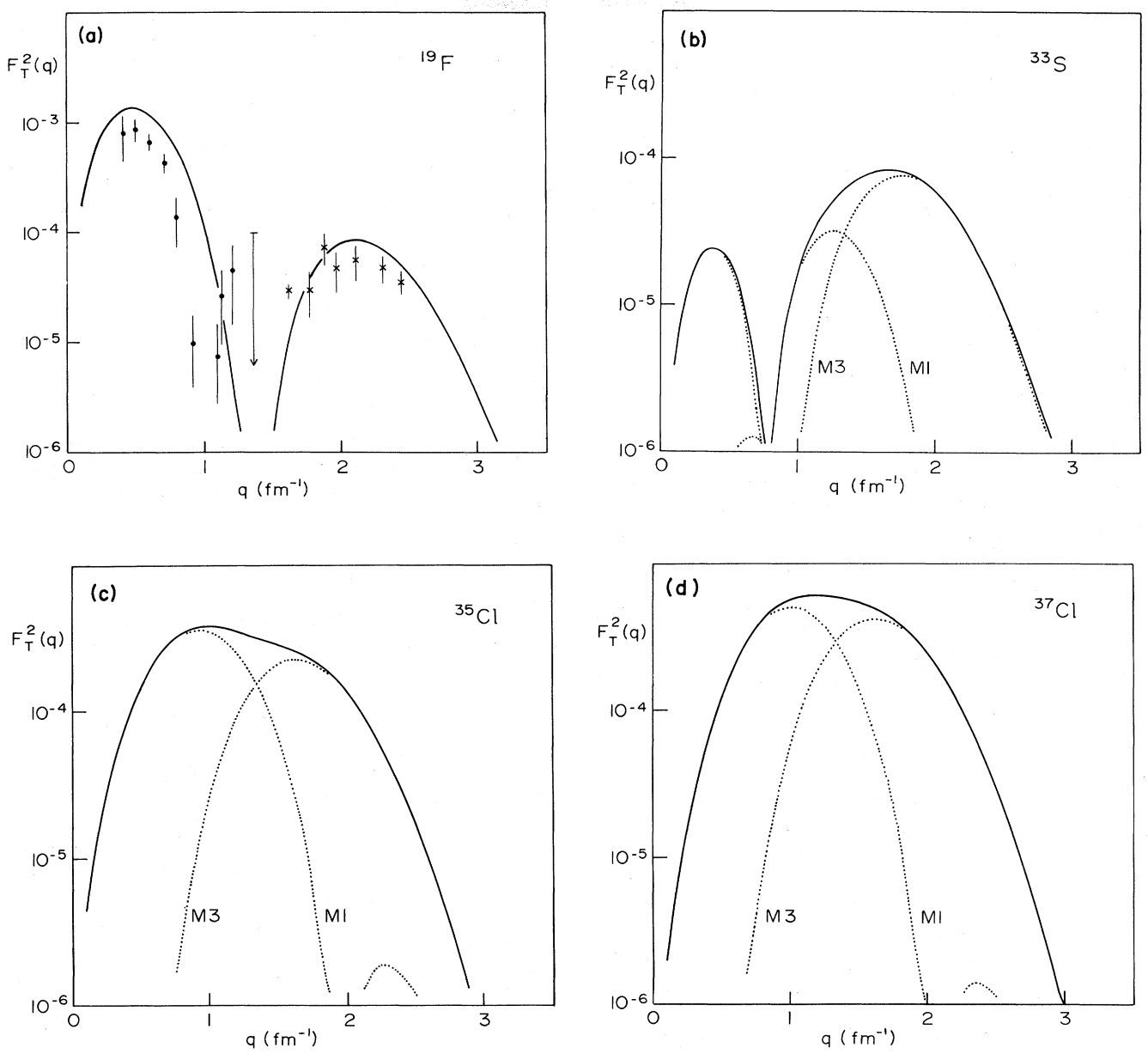

FIG. 41. Form factors for (a) ^{19}F, (b) ^{33}S, (c) ^{35}Cl, and (d) ^{37}Cl, calculated using harmonic-oscillator wave functions and the s/d-shell density-matrix elements of Brown, Chung, and Wildenthal (1980). The ^{19}F data are from Williamson *et al.* (1983) and Donné *et al.* (1983).

For the heavier nuclei, phenomenological fits become less suitable for an understanding of the data, and increasingly one depends on a comparison with shell-model calculations. Systematic calculations, like those discussed in the preceding section on s/d-shell nuclei, are not very abundant, and are rarely quoted in terms of one-body density-matrix elements. It would actually be very desirable to present these calculations in such terms, as described for example in Sec. IV.B. Thereby, in a few numbers, the one-body matrix elements for a rather complicated ground-state wave function could be represented; these numbers form an ideal interface between theory and experiments sensitive to such observables.

Given the scarcity of systematic work, we shall not attempt to present an exhaustive discussion of the experiments and calculations performed. Section VI.F contains a list of references on experiments. For a comparison of theoretical calculations and measured form factors see, for example, Suzuki *et al.* (1979), Donnelly and Gökalp (1981), Arita *et al.* (1981), and Selig *et al.* (1982).

The main body of this section will concentrate on one special aspect of the results obtained: the use of magnetization densities of high multipolarity for the determination of valence nucleon radial wave functions (Donnelly

and Walecka, 1973a; Sick, 1980; Platchkov *et al.*, 1982). This topic has been covered in a fairly systematic manner for both theory and experiment. The interpretation of the high-multipolarity form factors is straightforward enough to be carried out even in the absence of shell-model calculations; much of the physics contained in the data can be extracted by a phenomenological analysis, without undue recourse to phenomenological concepts.

The plan of this section is to develop the basic idea starting from the formal properties of magnetic form factors, as presented in Sec. IV, to discuss corrections that apply to these simple-minded ideas, and to describe the extraction of orbit sizes from $F_M(q)$.

1. Radial wave functions and high multipolarity

In the following, we first consider nuclei having a particularly simple structure. We assume that the magnetization density for a nucleus having a spin J_0 is entirely given by one shell containing the unpaired valence nucleon of spin $j=J_0$. Nucleons in all other shells are assumed to be paired off. We select cases where this unpaired nucleon has the highest spin j of all occupied orbits, and we restrict ourselves to cases of stretched configuration $j=l+\frac{1}{2}$. For such nuclei, we study magnetic form factors of the highest possible multipolarity $\Lambda=2j$. For this particular case, the description of magnetic scattering simplifies considerably (Donnelly and Walecka, 1973a).

According to Eqs. (4.115) and (4.131), the term involving $\beta_J^+ j_{J+1}(qr)$ vanishes, since the selection rules for D^+ require $J\leq 2l-1$. The term proportional to $\alpha_J j_J(qr)$, the contribution of the convection current, vanishes as well, since the selection rules for B impose $J\leq 2l-1$. These selection rules basically express the fact that for multipolarity $\Lambda=2J_0$ both the nuclear spin and the valence nucleon j have to undergo a complete flip. The spin-flip contribution is given by the term proportional to $\beta_J^- j_{J-1}(qr)$. Consequently, the magnetic form factor of multipolarity $J=\Lambda$ is given by [Eq. (4.130)]

$$\sqrt{\Lambda+1}/\sqrt{4\pi}\sum_{aa'}\int R_a(r)R_{a'}(r)j_{\Lambda-1}(qr)D_\Lambda^-(lj;l'j') \times\mu_n\psi_\Lambda(aa')_{-1/2}r^2dr \qquad (6.9)$$

for neutrons, and the same with $\mu_n(\psi_J)_{-1/2}$ replaced by $\mu_p(\psi_J)_{+1/2}$ for protons.

Exploiting now the condition that j be the highest of all occupied shells, we reduce the sum over a,a' in Eq. (6.9) to one single term for $a=a'=j$. All other terms drop out due to the triangle condition $\Delta(J-1,l,l')$ for D_J^-. We thus obtain the very simple result

$$F_{M\Lambda}(q)=\sqrt{\Lambda+1}/\sqrt{4\pi}D_\Lambda^-(lj;lj)\psi_J\mu_n \times\int R^2(r)j_{\Lambda-1}(qr)r^2dr\ . \qquad (6.10)$$

The $M\Lambda$ form factor is given by the Fourier transform of the valence nucleon radial wave function, in striking similarity to elastic charge $C0$ scattering. The only difference appears in $j_{\Lambda-1}$ rather than j_0, and the numerical constant D_Λ^-.

The remarkable features of Eq. (6.10) result from the terms that are absent: The convection current for protons does not contribute. This is due to the fact that scattering from the convection current, together with nucleon spin-flip, is a two-step process negligible for a weakly interacting probe. Configuration mixing involving all shells with $j'<J_0$ does not appear either. Since the electron interacts with only one nucleon at a time, a shell with $j'<J$ cannot contribute to multipolarity $2J_0=\Lambda$ (this is true as long as we neglect MEC). To the extent that the assumptions leading to Eq. (6.10) are realistic, a measurement of $F_{M\Lambda}$ allows a determination of the valence shell radial wave function, independent of the complications usually prominent in the interpretation of magnetic form factors.

Equation (6.10) is most attractive for another reason: it applies to both protons and neutrons (Donnelly and Walecka, 1973a; Sick *et al.*, 1977). Unlike charge electron scattering, which is basically blind to neutrons, $M\Lambda$ magnetic scattering places both types of nucleons on an equal footing. The reduction in cross section occurring for neutrons, a factor $(\mu_n/\mu_p)^2$ resulting from the smaller intrinsic magnetic moment of neutrons, is quite acceptable.

The extreme case discussed above immediately raises a number of questions. (1) Experimentally, only the incoherent sum of multipole contributions F_{MJ}^2 can be determined (unless we observe ground-state nuclear-spin observables; see Sec. VIII). Can the $M\Lambda$ multipole be isolated from the other multipoles over a large enough q range to make Eq. (6.10) interesting? (2) Configuration mixing involving shells with $j'>J_0$ may be small; to what degree can one extract quantitative information when entirely neglecting their contribution? (3) The impulse approximation used to derive Eq. (6.10) is modified by the contributions of meson-exchange currents; to what degree do these MEC quantitatively modify the results? These questions are discussed in turn below.

a. Separation of multipolarity $\Lambda=2J_0$

The first question to be discussed is the extent to which the $M\Lambda$ contribution can be measured and isolated. For most odd-A nuclei, the ground-state J_0 does not correspond to the highest j of all (normally) occupied shells. For the heavier nuclei in particular, the shells of large j are filled pairwise, and the odd nucleon regularly occupies a state of low j. For $A\leq 120$, however, there are a number of nuclei where the ground-state J_0 value of $\frac{5}{2}$, $\frac{7}{2}$, or $\frac{9}{2}$ conforms with the conditions mentioned above. In these cases the $M5$–$M9$ form factors can be obtained, in principle.

For these high multipolarities, the separation of the $M\Lambda$ multipole actually becomes reasonably easy. The radial wave functions for large l (large j) exhibit a well-

defined peak at the nuclear surface. The $M\Lambda$ form factor consequently shows a pronounced peak at a momentum transfer where the maximum of $R^2(r)$ coincides with the maximum of the first lobe of $j_{\Lambda-1}(qr)$ [Eq. (6.10)], which occurs near $qr \approx 1.1\Lambda$ for large Λ. The highest allowed multipolarity Λ thus will lead to a form-factor maximum at a q higher than for all lower multipolarities. This peak occurs at a momentum transfer where the usually dominating charge form-factor contribution, which peaks at $q=0$, has fallen off by many orders of magnitude. As was shown in Fig. 14, the $M7$ contribution indeed dominates over a fairly large q region. This allows one to perform experiments at $\theta < 180°$; with targets in transmission geometry, this greatly facilitates data taking at large q and low cross sections.

The separation of the $M\Lambda$ contribution from the magnetic multipoles $J < \Lambda$ is possible in a rather limited region of q only, near the maximum of $F_{M\Lambda}$. At larger transfer, after $F_{M\Lambda}$ has fallen off by 2—3 orders of magnitude, the $M\Lambda$ form factor usually reaches a diffraction minimum. In this region, secondary maxima of the $F_{MJ<\Lambda}$ form factors are likely to become important again. At lower q, the $\Lambda-2$ form factor is *a priori* quite large and quickly dominates F_T, in the extreme single-particle model at least. In practice, the $\Lambda-2$ form factors are systematically quenched by factors 2—10. In this case, the $M\Lambda$ term sticks out over a considerable q range.

Since $F_{M\Lambda}$ can only be isolated over a limited region of q, Eq. (6.10) cannot be inverted to give $R(r)$ as the Fourier transform of $F_{M\Lambda}$. Consequently, only specific aspects of $R(r)$ can be determined experimentally. $R^2(r)$ is measured reasonably well in the region where $R^2(r)$ is larger than $\sim 10\%$ of its maximum value (see Fig. 12). The small-radius behavior could be measured only if $M\Lambda$ could be isolated at large q; for wave functions with large orbital angular momentum l, however, this small-r behavior is of little interest. For large radii, the low-q shape of $F_{M\Lambda}$ is of importance, but not accessible experimentally. For an interpretation of $F(q)$ in terms of $R(r)$ this lack of information has to be made up for by model assumptions or independent experimental evidence. Fortunately, for radial wave functions of individual shells, the large-r behavior is well known and largely constrained by the separation energy. This compares favorably to the situation encountered for charge scattering, where the large-r shape, resulting from the sum of many different shells, is much more difficult to predict on general grounds (Sick, 1982).

The influence of multipoles of order $J < \Lambda$ has been investigated by Donnelly and Gökalp (1981). These authors allow a free variation of matrix elements involving $1p$-$2h$ admixtures to the one-hole states of interest. They show that multipoles $J < \Lambda$ can lead to appreciable changes of F_T in the q region where $M\Lambda$ is expected to dominate. In particular, the secondary maxima of $F_{M\Lambda-2}$ can modify the form factor in the q region used for the determination of valence nucleon radial wave functions. Donnelly and Gökalp (1981) also point out that a few experimental points in the q region, where $F_{M\Lambda-2}$ peaks, are very effective in constraining the amount of configuration mixing admissible.

In order to determine quantitatively the influence of such admixtures for specific nuclei, one needs shell-model calculations for the single-particle matrix elements. Here we cite two cases where such calculations have been performed. For s/d-shell nuclei (Sec. VI.B) we have available a rather complete set of wave-function calculations. The form factors calculated from these matrix elements using a given $R(r)$ can be interpreted in terms of radial wave functions by ignoring the configuration admixtures that were used to calculate $F(q)$. The resulting change in $R(r)$, needed to simulate this neglect of configuration mixing, then yields a good estimate for the uncertainties introduced by this procedure. One of these tests was described in Sec. VI.B for ^{25}Mg, a nucleus that obviously is very far from the assumptions made above; ^{25}Mg is located in the middle of the s/d shell, and is quite deformed. The rms radius of the $1d_{5/2}$ orbit, extracted from a calculated form factor by ignoring the configuration admixtures as given by the wave functions of Wildenthal *et al.*, differs by 1% from the one injected into the full calculation. This leads us to expect that the neglect of configuration admixtures of multipolarity $J < \Lambda$, for reasonably pure single-particle cases, will introduce uncertainties of much less than 1% in the radii extracted.

For the nuclei $A=49,51,87,93$, discussed below, Suzuki (1978) and Suzuki *et al.* (1979) have performed shell-model calculations using a large harmonic-oscillator space ($\sim 14\hbar\omega$) and different schematic, finite-range residual interactions, both central and tensor. Qualitatively, these calculations correctly reproduce the reduction of the $\Lambda-2$ multipole strength, which shows that the amount of configuration mixing is of the right size. Using Suzuki's form factors as "data" for the determination of $R(r)$, again ignoring configuration mixing, one can make yet another test of the importance of these admixtures. Again, the effect on the extracted rms radius is significantly less than 1%.

b. Wave-function admixtures with $j' > J_0$

The second question raised above concerns the influence of configuration admixtures with $j' > J_0$. Due to conservation of parity, $\geq 2\hbar\omega$ excitations with $j' > J_0$ are required in order to change the $M\Lambda$ form factor in a way not accounted for by Eq. (6.10). Even for nuclei exhibiting relatively pure single-particle or single-hole states, such $2\hbar\omega$ excitations will in general be present. The large radial overlap of shells with low orbital angular momentum l will, however, favor states with l lower than is required to change $F_{M\Lambda}$. In addition, np-nh excitations involving paired-off nucleons are not effective in changing magnetic observables.

For a quantitative estimate, we again refer to the calculations of Suzuki (1978) and Suzuki *et al.* (1979). Using a $\leq 14\hbar\omega$ space and realistical finite-range residual interac-

tions, Suzuki allows for contributions of $j' > J_0$ shells. From his calculated form factors one can deduce that the neglect of admixtures with $j' > J_0$ in the interpretation of the $A=49,51,87,93$ form factors leads to an error in the rms radius extracted of $\sim 0.5\%$

Larger effects have been obtained by Desplanques and Mathiot (1982), who use a residual force that, besides π and ρ exchange, contains a δ-force term proportional to a phenomenological parameter g'. Such a parametrization has been used recently in many cases to simulate the effects of residual interactions at low momentum transfer. At large q, $q \sim 3$ fm^{-1}, the use of a δ term can be expected to produce unrealistic effects, however. This is shown by the slow convergence of $F(q)$ (requiring $35\hbar\omega$ for $q=3$ fm^{-1}); much faster convergence ($\sim 8\hbar\omega$) and smaller effects on $F(q)$ are obtained if a finite-range force is employed (Suzuki, 1978). The same tendency is also shown by Suzuki (1980), who compared the core-polarization effects in magnetic scattering calculated with zero-range and with finite-range interactions; much smaller effects are found with the latter. The large renormalization of $F(q)$, by a factor of 0.3—0.5, needed by Desplanques and Mathiot (1982) to get the calculated form factor into agreement with experiment, also indicates that the results obtained using this $g'\delta$ term are unrealistic at large q.

c. Contribution of exchange currents

The third complication that interferes with the conceptually simple interpretation of $F_{M\Lambda}$ via Eq. (6.10) relates to the presence of meson-exchange currents. Processes where the virtual photon couples to a pion or an $N\bar{N}$ pair are of some importance for magnetic properties in general; unlike in charge form factors, MEC give a first-order effect in F_M. Already the magnetic dipole moment receives a 5—10% contribution of MEC. At large q, a larger influence of MEC can be expected, since MEC processes allow one to split the momentum transfer and distribute it to two nucleons. The larger nuclear form factor at $\sim q/2$ compensates to some extent for the smaller probability resulting from the two-body nature of the MEC process.

On the whole, MEC contributions fall with increasing q only somewhat less quickly than the one-body form factor [Eq. (6.10)]. As described in Sec. VII, an important effect of MEC can be expected only if the one-body form factor becomes very small, due, for example, to the appearance of a diffraction minimum. This is not the case near the maxima of the $M\Lambda$ form factors of interest here. As a consequence, MEC effects on $M\Lambda$ form factors are comparatively small. They still require careful discussion, since one aims at a determination of accurate valence nucleon radial wave functions.

For a detailed discussion of MEC we refer the reader to Sec. IV.E. Here, we mention only those points specific to form factors of high multipole order. We have to discuss some of those points separately because the history of calculations on the quantitative effect of MEC on $M\Lambda$ form factors has been somewhat confusing.

Some of the early calculations were performed using an incorrect sign for the Δ-resonance term (Dubach, 1980) or by omitting it entirely (Suzuki, 1978). This led to an overestimation of the MEC contribution. In a number of calculations, the important S-D transitions were not accounted for; according to Mathiot and Desplanques (1981), this led to an underestimation of the MEC contribution. Many of the calculations (Suzuki, 1978; Dubach, 1980) ignored the effect of the πNN vertex form factor. Experimentally (Bongardt *et al.*, 1974), these vertex form factors fall about as quickly with q as the nucleon form factor, an observation in agreement with the naive expectation that assigns similar form factors to systems $(\pi, N, \Delta, \ldots)$ of similar size. Allowing for realistic vertex form factors reduces the MEC contributions considerably. For computational reasons, many of the MEC calculations are performed using harmonic-oscillator wave functions. If the resulting $F_{\rm MEC}$ is added to a one-body contribution [Eq. (6.10)] computed using a radial wave function with a different overall size (oscillator parameter), a potentially incorrect picture will result. Beyond the maximum of $F_{M\Lambda}$ the ratio of MEC to one-body form factors at large q may depend significantly on the relative falloff due to different radial wave functions.

The approach taken by Platchkov *et al.* (1982) to obtaining a realistic estimate of the MEC effect tries to avoid these problems. MEC form factors not including $F_{\pi NN}$ have been multiplied with a factor $F^2_{\pi NN}(q/2)$. From a calculation performed using a given type of radial wave function, only the relative effect of MEC is extracted. This is done by fitting the calculated one-body or one-body—plus—two-body form factors with radial wave functions in order to determine the relative change of the orbit radius due to MEC.

The overall effect of MEC on the radius of the valence orbit, as extracted from $M\Lambda$ form factors, is given by Platchkov *et al.* (1982). Ignoring the MEC contribution would yield rms radii $\sim 1.5\%$ too small. Given the present state of the art of MEC calculations, a fairly large error bar, $\pm 50\%$, say, should be attributed to this correction.

If we compare MEC with the other effects that complicate an interpretation of $F_{M\Lambda}$ in terms of Eq. (6.10), we see that the MEC yield the largest correction. At the present level of experimental accuracy, one needs to take the MEC effect into account, while the uncertainties due to configuration mixing can be absorbed into the overall error bar. A more firmly based calculation of MEC effects on $M\Lambda$ form factors is therefore desirable.

2. Experimental results

Experiments to date on scattering from high-multipole-order moments have produced data for $M7$ and $M9$ moments and $A=49,51,59,87,93,115$. For a number of cases, the conditions discussed above apply; in those cases, the data can be used to determine the valence nu-

cleon radial wave functions.

^{49}Ti is a nucleus with a neutron hole in the closed $f_{7/2}$ shell, ^{51}V has three $f_{7/2}$ protons and a closed neutron shell, ^{87}Sr has a hole in the closed $g_{9/2}$ neutron shell, while ^{93}Nb has a single unpaired $g_{9/2}$ proton. As indicated by transfer reactions, magnetic scattering (see below), and the calculations of configuration mixing (Suzuki, 1978) mentioned above, these nuclei have reasonably pure single-particle configurations that allow an application of Eq. (6.10) to the $M\Lambda$ form factor. ^{59}Co, on the other hand, is quite deformed, and a quantitative interpretation of F_{M7} cannot be attempted in terms of Eq. (6.10). For ^{115}In, only preliminary data (Lapikás, 1979) are available at the present time.

The cross sections for the highest multipole $M\Lambda$ have all been measured at Saclay, where a systematic investigation of high-Λ scattering has been pursued (De Witt Huberts *et al.*, 1976; Sick *et al.*, 1977; Platchkov *et al.*, 1979,1982). The (mainly) magnetic cross sections were measured at energies of 100—350 MeV and at a scattering angle of $\theta=155°$. Using targets of thickness ~ 100 mg/cm^2 and electron intensities up to 30 μA, cross sections were measured at Saclay down to a level of 2×10^{-37} cm^2/sr. The (mainly) charge contribution was measured at 500-MeV electron energy and forward angles, and subtracted. To reduce the influence of systematic errors in the charge contribution subtraction, neighboring spin-zero isotopes in general were measured simultaneously at both forward and backward angles.

The data, converted to PWBA form factors, are displayed in Figs. 42—46. Cross sections for the region where the lower multipoles dominate are available only

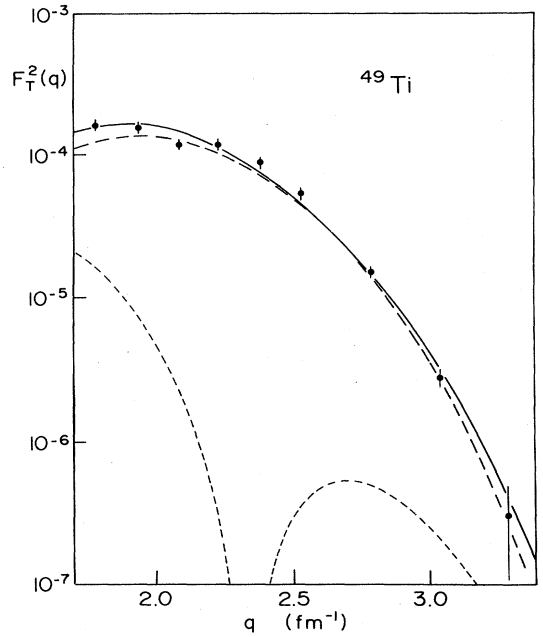

FIG. 42. The ^{49}Ti data of Platchkov *et al.* (1982) shown together with a fit calculated using a Woods-Saxon radial wave function; the dashed curves represent the $M5$ and $M7$ contributions.

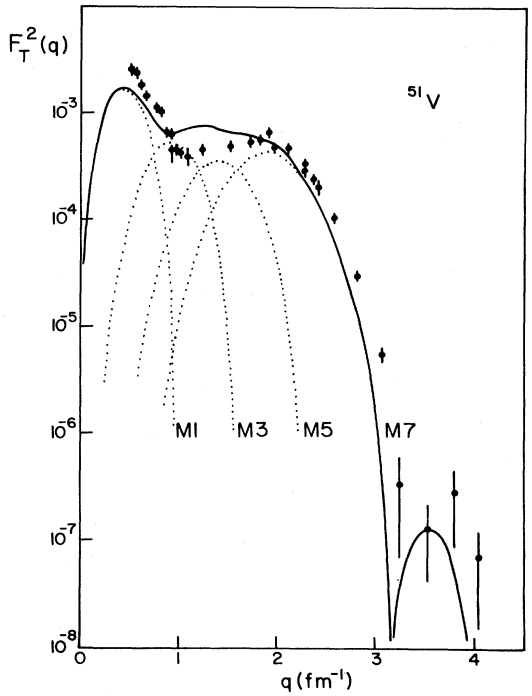

FIG. 43. The ^{51}V data of De Vries *et al.* (1978), Arita *et al.* (1981), and Platchkov *et al.* (1982,1983) compared to the density-dependent Hartree-Fock-Bogoliubov prediction of Dechargé and Gogny (1980) (secondary maxima of $F_{M\lambda}$ have been suppressed).

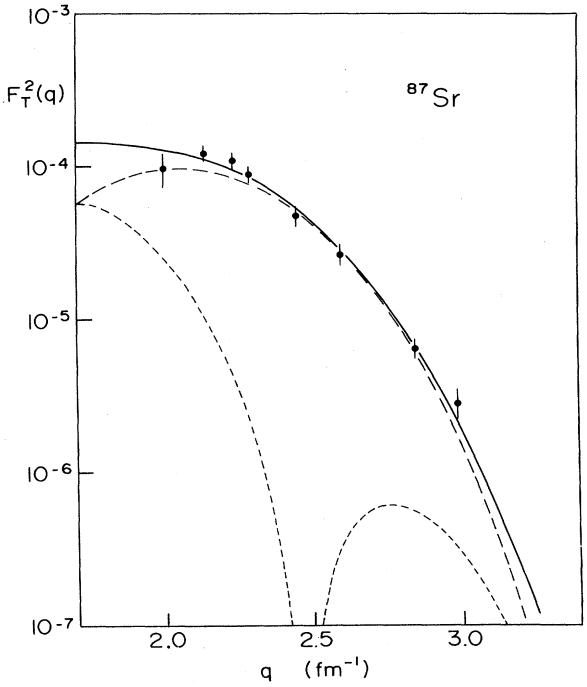

FIG. 44. The ^{87}Sr data of Platchkov *et al.* (1982) shown together with a fit calculated using a Woods-Saxon radial wave function; the dashed curves represent the $M7$ and $M9$ contributions.

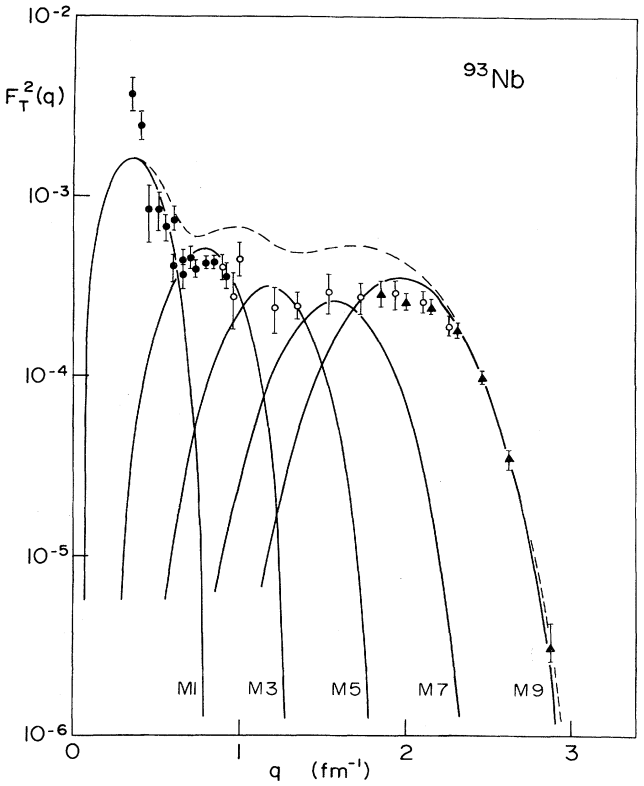

FIG. 45. The ^{93}Nb data of Box (1976) (solid circles), York and Peterson (1979) (open circles), and Platchkov *et al.* (1982) (triangles) compared to the density-dependent Hartree-Fock-Bogoliubov prediction of Dechargé and Gogny (1980) (secondary maxima of $F_{M\lambda}$ have been suppressed).

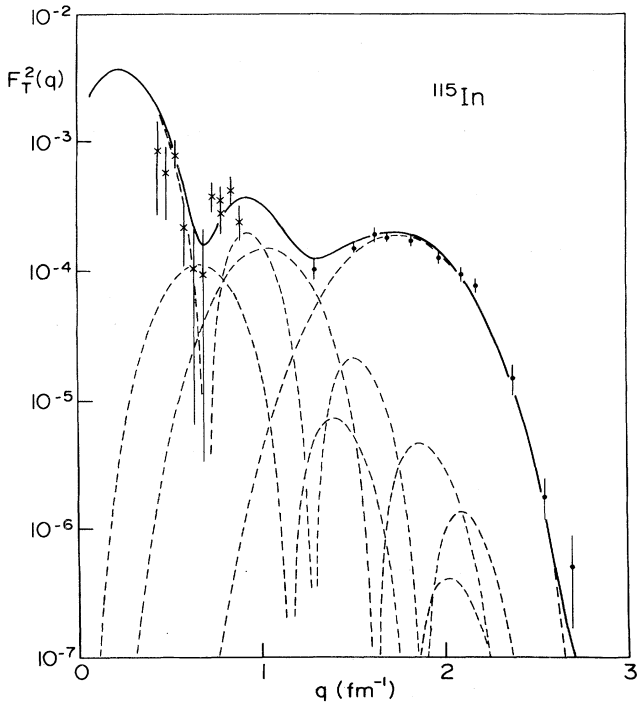

FIG. 46. The ^{115}In data of Box *et al.* (1976) (crosses) and De Jager *et al.* (1979) (solid circles) compared to a fit calculated using a Woods-Saxon radial wave function.

for some cases. These cross sections have been measured using the Bates 180° scattering system; the very-low-q data covering the $M1$ region have been measured at IKO (De Vries *et al.*, 1970; Box, 1976; York and Peterson, 1979; Arita *et al.*, 1981).

These experimental form factors have been interpreted in terms of the radial wave function of the valence shell by parametrizing $F_{M\Lambda}$ according to Eq. (6.10). A Woods-Saxon radial wave function is used to calculate the radial integral. The overall factor $\alpha_\Lambda=(\psi_\Lambda)^2_{\pm 1/2}$ accounts for the depletion of the $1f_{7/2}$ ($1g_{9/2}$) strength due to admixtures with $j<\frac{7}{2}$ ($\frac{9}{2}$). The main information extracted, the localization of the peak of $R^2(r)$, is fixed by the $F_{M\Lambda}$ data at and beyond the maximum. The region where $F_{M\Lambda}$ falls by the first factor of 10, say, basically fixes the radial scale.

For the lower multipoles, $J<\Lambda$, Eq. (6.10) is not appropriate; configuration mixing is expected to influence strongly the shape of F_{MJ}. Near the first maximum of $F_{M\Lambda-2}$, and for data of limited accuracy, a fit using the equivalent of Eq. (6.10) for $J=\Lambda-2$ can be tried. Little significance can be attributed to the parameters resulting for $J=\Lambda-2$. The smallness of $\alpha_{\Lambda-2}$ often found does qualitatively indicate, however, that the $\Lambda-2$ form factor is systematically quenched due to configuration mixing.

As radial wave functions entering Eq. (6.10), those calculated in local Woods-Saxon wells have been used. The fit to $F_{M\Lambda}$ in this case determines the radius of the potential well. The surface thickness, which is poorly constrained by the $F_{M\Lambda}$ data available at present, has been set to a standard value, $a=0.65$ fm, determined by fitting charge form factors by densities computed from Woods-Saxon wells. This procedure is suggested by self-consistent Hartree-Fock calculations, which give for different shells practically the same surface thickness of the effective potential (Negele, 1970). An important feature of interpretations using Woods-Saxon wave functions is their use of the experimentally known separation energy to fix the large-radius behavior of $R(r)$. This tail of $R(r)$, which is not measured by magnetic scattering due to the lack of low-q $M\Lambda$ data, is strongly constrained by the separation energy.

Fits to the experimental form factors using the above approach have been described in detail by Platchkov *et al.* (1982). Some results are shown in Figs. 42—45, and some numerical results are given in Table II. These fits show that $(\psi_\Lambda)_{\pm 1/2}$, the $M\Lambda$ "quenching factor," is reasonably close to one, as it should be for a single-particle state of reasonable purity. The accuracy of the rms radii of $R(r)$ quoted in Table II is of the order of 1—1.5 %.

It is clear that the experimental data do not directly determine these rms radii. $F_{M\Lambda}$ basically fixes the location of the peak in r space of $R^2(r)$. Model assumptions (a Woods-Saxon shape) and other experimental information (the separation energy, mainly) yield the ingredients needed to proceed to the rms radius. Because rms radii

TABLE II. Theoretical and experimental point nucleon valence rms radii expressed in fm.

Nucleus	Orbit	DME[a]	DDHF[b]	DDHFB[c]	Expt.
^{49}Ti	$1f^n_{7/2}$	4.210	4.124	4.068	4.042(56)
^{51}V	$1f^p_{7/2}$	4.246	4.140	4.107	4.063(53)
^{87}Sr	$1g^n_{9/2}$	4.946	4.880	4.732	4.823(76)
^{93}Nb	$1g^p_{9/2}$	5.047	4.954	4.931	4.946(64)
^{49}Ti/^{51}V	$f^n_{7/2}/f^p_{7/2}$				0.980(10)
^{87}Sr/^{93}Nb	$g^n_{9/2}/g^p_{9/2}$				0.968(10)

[a]DME, density-matrix expansion (Negele and Vautherin, 1972).
[b]DDHF, density-dependent Hartree-Fock (Campi and Sprung, 1972).
[c]DDHFB, density-dependent Hartree-Fock-Bogoliubov (Dechargé and Gogny, 1980).

provide a convenient way to discuss the results, a brief consideration of the ambiguities inherent in the deduction of rms radii is in order.

While $F(q)$ fixes the main peak of $R(r)$, the detailed shape is influenced by the shape of $V(r)$. This influence is rather indirect, though, and makes $R(r)$ much less model dependent than, for example, the charge density used to fit charge scattering. The radial wave function $R(r)$ is a solution of the Schrödinger equation; this suppresses many unphysical features introduced by the somewhat arbitrary shape of the potential $V(r)$. The most important property of $V(r)$ turns out to be the surface thickness a. A typical uncertainty of ± 0.05 fm in the choice of a leads to an uncertainty of the rms radii already included in the error bars quoted in Table II. Another effect of importance concerns the nonlocality of $V(r)$. From the interpretation of transfer reactions, we know that the relation between $R(r)$ near the nuclear surface and $R(r)$ in the tail region can depend strongly on the nonlocality of the effective potential assumed. This is true in particular for wave functions with nodes. For magnetic electron scattering and the nodeless $R(r)$ of interest, the contribution to the rms radius of the tail of $R(r)$ is rather small. In contrast to transfer reactions, electron scattering measures $R(r)$ in the region where it is large; an "extrapolation" depending on model assumptions is needed only for the region where $R(r)$ is small. Passing from a nonlocal to a local potential changes rms radii for a fixed large-r tail by ~ 0.02 fm (Chapman *et al.*, 1976). For the interpretation of $F_{M\Lambda}$ this translates into an entirely negligible uncertainty in rms radii. Ambiguities in the choice of the separation energy, due to admixtures of core-excited states, also present no problem, due to the small contribution of the tail region to $r_{\rm rms}$. Given the unimportance of these effects, it seems reasonable indeed to condense the information provided by magnetic electron scattering into one single number, $r_{\rm rms}$, and hereby facilitate comparison with theory.

A quantity of particular interest, the difference between the radii of neutron and proton orbits, actually can be obtained with model assumptions considerably weaker than those discussed above (Sick *et al.*, 1977). According to Hartree-Fock calculations, the wave functions of protons and neutrons in the same shell and for neighboring nuclei are very similar in shape. These wave functions differ mainly by a change of a few percent in radial scale. If $R(r)$ differs in radial scale only, by a factor $\beta \approx 1$, then the form factors differ by a factor β^{-1} in q scale only. A comparison of the experimental $M\Lambda$ form factors for pairs of neighboring nuclei with an odd proton/neutron then allows a precise determination of the relative proton/neutron orbit size, largely independent of model assumptions on $R(r)$.

Such a direct neutron/proton comparison has been performed for the pairs ^{49}Ti/^{51}V and ^{87}Sr/^{93}Nb. The resulting ratios β have been corrected for very small differences due to the neutron/proton difference of the large-radius tails, to which $F_{M\Lambda}$ is not very sensitive. In addition, these ratios have been corrected for the residual difference of MEC effects; these MEC corrections again are very small, since the MEC contributions largely cancel in the ratio analysis. The resulting ratios of neutron to proton orbit sizes are quoted in Table II.

3. Comparison with theory

A detailed comparison of the radii determined by magnetic scattering and those predicted by Hartree-Fock calculations has been undertaken by Platchkov *et al.* (1982). These authors employ three different mean-field calculations that use effective, density-dependent nucleon-nucleon interactions. The calculation of Campi and Sprung (1972), denoted in Table II as DDHF, uses the Sprung and Banerjee (1971) effective interaction and treats the open-shell nature of the nuclei of interest, using the filling approximation and the BCS equations. The calculation of Negele and Vautherin (1972), abbreviated as DME, uses the density-matrix expansion, a simplified version of the full DDHF calculation previously performed by Negele (1970). Dechargé and Gogny (1980) perform a Hartree-Fock-Bogoliubov calculation (DDHFB), which treats the pairing in a self-consistent way, using the same finite-range effective force.

The first two calculations use effective interactions derived via Brueckner G-matrix calculations from the Reid soft-core nucleon-nucleon interaction. The third calculation (DDHFB) uses a purely phenomenological effective interaction of finite range. In all cases, certain parameters of the effective force have been adjusted to fit specific nuclear properties. In particular, the charge radii and binding energies of selected (magic) nuclei have been used

to adjust parameters. Accordingly, the total proton densities are very well reproduced by these HF calculations; the total charge rms radii agree with experiment to better than 1%. Table II compares these HF calculations and experiment for the valence-orbit radii of f- and g-shell nuclei.

From Table II we can observe two trends. First, the valence-orbit radii predicted by HF theory are systematically too large by a few percent. Second, the ratio of neutron to proton radii predicted by HF theory is too large by 1–2 %. We shall discuss this latter observation first.

The ratio of n and p orbit radii as predicted by HF calculations actually is quite close to experiment; the size of the neutron orbits relative to that for proton orbits is too large by only 1–2 %. The $F_{M\Lambda}$ data thus constitute a very significant test of the predictions of the HF approach. Given the small systematic uncertainty in the ratio of neutron to proton orbit size, magnetic scattering provides us with the most discriminating test of Hartree-Fock neutron wave functions available at present. Of course, this test concerns the valence neutron shell only, and not the entire neutron density radius generally discussed. We note, however, that both ^{49}Ti and ^{87}Sr are single-hole nuclei for which the valence shell measured by (e,e') contributes $\sim 30\%$ of the total neutron rms radius. This shell entirely dominates $\rho_n(r)$ at those radii where strongly interacting (absorbed) probes are sensitive to $\rho_n(r)$ (Platchkov *et al.*, 1982).

The second point that emerges from Table II concerns the absolute value of the valence-orbit radii. Here the experimental values are systematically smaller than those predicted by HF calculations. This difference is largest for the density-matrix expansion calculation and light nuclei, and smallest for DDHFB and heavy nuclei. Such a systematic deviation, which occurs for both neutrons and protons, calls for an explanation. One might have expected the proton radii to agree with experiment, given the fact that the parameters of the HF theories have been adjusted to fit experimental total proton radii.

A number of calculations relating to this point are available, and basically concern the energy dependence of the nucleon effective mass. In a shell-model calculation such as the Hartree-Fock, nucleons move in an average field that, to first approximation, turns out to be state independent. In real nuclei, individual single-particle states are not pure, but couple mainly to collective states of the core. It was shown by Bertsch and Kuo (1968) that this coupling is responsible for the fact that near the Fermi level the nucleon effective mass m^* is larger than far from it. Near the Fermi level $m^*/m \approx 1$, while $m^*/m \approx 0.7$ elsewhere. This change of m^* leads to a compression of the single-particle spectrum near the Fermi edge (Brown *et al.*, 1963) and to an appreciable depletion of single-particle spectroscopic factors; both consequences are in agreement with experiment. The decrease of the valence-orbit rms radius due to this variation of m^* was pointed out by Zamick (1979). Estimates obtained by various authors (Zamick, 1979; Lejeune and Mahaux, 1979; Castel and Goeke, 1979; Lejeune, 1980; Ma and Wambach, 1983) indicate that this effect is of the right size, amounting to a few percent of the valence-orbit radius. This particle-core coupling thus can be taken as the main explanation of the differences in valence-orbit radii obtained from Hartree-Fock theory and magnetic electron scattering.

4. Other aspects

The above discussion of a selected aspect of the interpretation of $F_{M\Lambda}$ of some f/g-shell nuclei presents only one particular facet of the general problem. We have chosen to discuss it in detail since reasonably systematic work is available. Obviously, a number of other nuclei, the sensitivity of $F_T(q)$ in other q regions to different physics questions, etc., have been investigated both experimentally and theoretically. Form factors at low q have been used to determine radii of magnetization densities (De Vries *et al.*, 1970; De Vries, 1973; Box, 1976; Selig *et al.*, 1982); data at intermediate q have been studied in connection with configuration mixing (York and Peterson, 1979; De Jager *et al.*, 1979; Donnelly and Gökalp, 1981). Deformed nuclei have been investigated (De Vries *et al.*, 1970; Platchkov *et al.*, 1982) in order to study the coupling of valence nucleons and core, a topic discussed in the next section. Here, we cite only one additional example for a form factor of large multipolarity. Figure 46 shows the data of De Jager *et al.* (1979) for the magnetic form factor of ^{115}In. The detailed analysis of these data will allow one to follow the change of $g_{9/2}$ proton radii through the g shell; the value of $r_{\rm rms}$ for the fit shown (with no corrections for MEC) is 5.54 fm.

D. Deformed nuclei

In this section we deal with magnetic scattering from deformed nuclei. The focus of the discussion is on the region of well-deformed nuclei, $120 < A < 200$. In addition, we also come back to some of the lighter nuclei, $A = 24,59$, for which an understanding in terms of the Nilsson model is desirable. The discussion in this section also serves to illustrate some aspects of the formalism developed in Sec. IV.D.

We start by studying a simple case, ^{25}Mg, a nucleus for which data and interpretation in terms of the shell model are already given in Sec. VI.B. ^{25}Mg has $J_0^{\pi_0} = \frac{5}{2}^+$, $T_0 = -M_{T_0} = \frac{1}{2}$. Treating this as a pure single-neutron Nilsson state labeled $K^\pi[Nn_z\Lambda] = \frac{5}{2}^+[202]$, we have as the only nonzero expansion coefficients in Eqs. (4.183) and (4.184) the terms $a_{22} = 1$ and, by Eq. (4.185b), $\alpha_{25/2} = 1$. Thus $I' = I = K = j' = j = \frac{5}{2}$, and so we have from Eq. (4.190)

$$\phi_J^{5/2}(\tfrac{5}{2};\tfrac{5}{2}) = 6\left[\begin{pmatrix} \frac{5}{2} & J & \frac{5}{2} \\ -\frac{5}{2} & 0 & \frac{5}{2} \end{pmatrix}^2 + \begin{pmatrix} \frac{5}{2} & J & \frac{5}{2} \\ -\frac{5}{2} & 5 & -\frac{5}{2} \end{pmatrix}^2\right]. \tag{6.11}$$

Of the three cases that can occur in elastic magnetic electron scattering ($J=1,3,5$), only for the highest multipole, $M5$, can the second term here contribute. We have explicitly [cf. Eq. (4.133)]

$$\phi_J^{5/2}(\tfrac{5}{2};\tfrac{5}{2})=\psi_J(1d_{5/2}^2)_{m_t=-1/2}$$
$$=\begin{cases}\frac{5}{7}=0.71, & J=1\\ \frac{5}{42}=0.12, & J=3\\ \frac{23}{42}=0.55, & J=5\ .\end{cases} \tag{6.12}$$

Thus we immediately see a strong suppression of the $M3$ compared to its single-particle spherical value (where the ψ's are all unity). The form factors are obtained in the usual way, employing Eq. (4.130) [with no $\alpha_J(r)$ densities, since this is an odd-neutron case]. The densities $\beta_J^{\pm}(r)$ presented at the end of Sec. IV.C in discussing the case of ^{27}Al may be used, necessitating only the change $\mu^p\to\mu^n$ in Eqs. (4.170c) and (4.170d). In Fig. 47 we show the results of such a calculation. Clearly the Nilsson model does much better than the pure $1d_{5/2}$ neutron configuration in yielding reasonably good agreement with the data, which, together with the shell-model predictions, were discussed in Sec. VI.B. In fact the $M1$ contribution at low q should not be taken too seriously since, in addition to the pure odd-neutron contributions shown here, there must also be a core contribution, as discussed by Moya de Guerra and Dieperink (1978).

Another example of a deformed lighter nucleus is ^{59}Co, a nucleus that has been studied in several experiments. An experiment performed by De Vries *et al.* (1970) using the IKO 180° scattering system produced data in the q range 0.4–0.9 fm^{-1}; an experiment performed at Saclay by Platchkov *et al.* (1982) at scattering angles up to 155° measured data in the range 1.8–3.1 fm^{-1}. While the former experiment essentially covers the region where the $M1$ form factor dominates, the latter measures mainly the $M7$ form factor. Data for the intermediate q region, the one where the largest effects due to deformation can be expected, unfortunately are not yet available. The form factors are shown in Fig. 48.

In the extreme spherical shell model ^{59}Co, with $J_0^{\pi_0}=\frac{7}{2}^-$, would be approximated by a single $1f_{7/2}$ hole in ^{60}Ni, treated as a closed-shell nucleus. Let us instead treat it as having a single unpaired proton in the Nilsson orbit labeled $\frac{7}{2}^-[303]$. As above, the only nonzero expansion coefficients are $a_{33}=1$ and hence $\alpha_{3\,7/2}=1$. Then for this configuration having $I'=I=K=j'=j=\frac{7}{2}$ we obtain for Eq. (4.190) [cf. Eq. (4.133)]

$$\phi_J^{7/2}(\tfrac{7}{2};\tfrac{7}{2})=\psi_J(1f_{7/2}^2)_{m_t=+1/2}$$
$$=\begin{cases}\frac{7}{9}=0.78, & J=1\\ \frac{7}{33}=0.21, & J=3\\ \frac{7}{429}=0.016, & J=5\\ \frac{3433}{6435}=0.53, & J=7\ .\end{cases} \tag{6.13}$$

Again the suppression of the intermediate multipoles with respect to the spherical single-particle limit, where the ψ's are of unit strength, is evident. As usual, once these density-matrix elements are multiplied into the appropriate single-particle ($1f_{1/2}$) form factors, we obtain the $\mathcal{F}_J(q)$'s using Eq. (4.130). The results are shown in Fig. 48 together with the data. In fact the $M5$ contribution is so much suppressed here that it does not appear in the figure at all. Once again the $M1$ contribution at low q

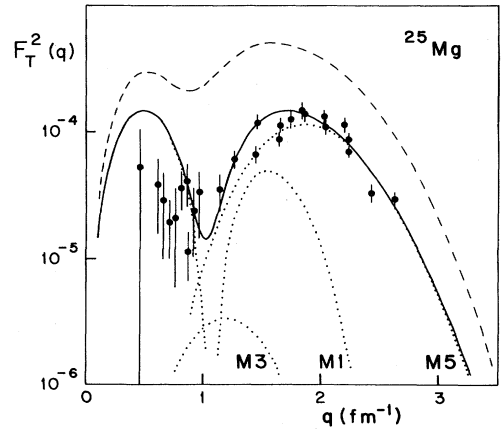

FIG. 47. The ^{25}Mg magnetic form factor for the extreme single-particle model (dashed curve) and the Nilsson model (solid and dotted curves), all calculated using harmonic-oscillator radial wave functions ($b=1.63$ fm).

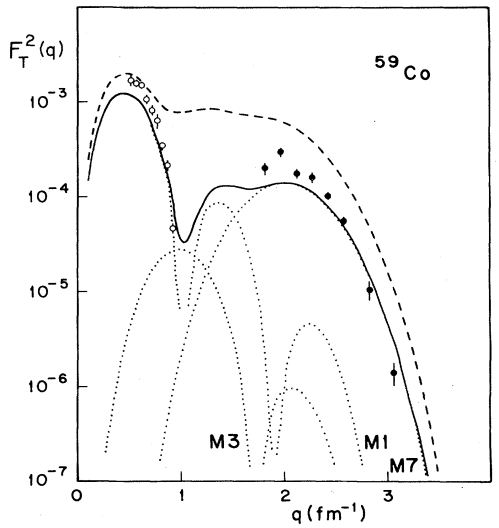

FIG. 48. The ^{59}Co data of De Vries *et al.* (1970) (open circles) and Platchkov *et al.* (1982) (solid circles) shown together with predictions from the extreme single-particle model (dashed curve) and the Nilsson model (solid and dotted curves). Both are calculated using Woods-Saxon radial wave functions ($r_0=1.11$ fm, $a=0.65$ fm).

should not be taken too seriously, as it lacks the core contribution.

Let us investigate such "stretched" Nilsson cases a little more fully. They all have contributions only from a single expansion coefficient $a_{l\Lambda}$ (and hence α_{lj}) of unit strength, and involve the geometric factor ϕ in Eq. (4.190) with $j'=j=K=K_M$, where K_M is the maximum value that can occur within a given major shell. Substituting for the 3-j symbols we obtain

$$[\phi_J^K(j';j)]_{j'=j=K=K_M}=\frac{(2K_M)!(2K_M+1)!}{(2K_M-J)!(2K_M+1+J)!}+\delta_{J,2K_M}\left[\frac{2K_M+1}{4K_M+1}\right]. \quad (6.14)$$

For $J=1$, the first term gives $K_M/(K_M+1)$. For $J=J_{\max}=2K_M$, the first term gives $(2K_M)!(2K_M+1)!/(4K_M+1)!$ which, for K_M large, is very small. On the other hand, the second term also contributes for this highest multipole and gives $(2K_M+1)/(4K_M+1)$, which is always greater than $\frac{1}{2}$, even for very large K_M. For $K=J_{\max}-2$, the next-to-highest multipole, the first term is again small for large K_M, and yet now the second term cannot contribute, and so clearly the overall density-matrix element is suppressed with respect to unity (the spherical single-particle value).

Next, let us turn to a case which is not of the simple stretched nature discussed above, and consider ^{181}Ta. This nucleus has $J_0^{\pi_0}=\frac{7}{2}^+$, which might be interpreted in the spherical limit as a $g_{7/2}$ proton configuration. For such a "jackknifed" configuration, we may expect a more complicated pattern for $F_T(q)$, given the interference terms between several shells that now can occur even for the highest multipole.

Following Moya de Guerra and Dieperink (1978), let us represent the ground state as a $\frac{7}{2}^+[404]$ configuration and fix the deformation parameter at $\delta=0.3$. Then in Eq. (4.183) we have two expansion coefficients, $a_{44}=0.976$ and $a_{43}=-0.218$, or equivalently, using Eq. (4.185b), $\alpha_{47/2}=0.993$ and $\alpha_{49/2}=0.120$. Using Eq. (4.187) with these α's and with the ϕ's calculated from Eq. (4.190), we obtain

$$\psi_J(a'a)=\begin{cases}0.767, & J=1,\ a'=1g_{7/2},\ a=1g_{7/2}\\ 0.209, & J=3\\ 0.016, & J=5\\ 0.526, & J=7\\ 0.044, & J=1,\ a'=1g_{9/2},\ a=1g_{7/2}\\ 0.032, & J=3\\ 0.005, & J=5\\ -0.042, & J=7\\ 0.008, & J=1,\ a'=1g_{9/2},\ a=1g_{9/2}\\ -0.001, & J=3\\ -0.001, & J=5\\ -0.005, & J=7\,,\end{cases} \quad (6.15)$$

where by Eq. (4.189) and $a'=1g_{7/2}$, $a=1g_{9/2}$ cases have the opposite signs from the $a'=1g_{9/2}$, $a=1g_{7/2}$ cases given here. Thus we see that the main effect here is to reduce the strengths of the $(1g_{7/2})^2$ multipole matrix elements from their spherical limit values (where the ψ's are unity), with only very small admixtures of $1g_{9/2}1g_{7/2}$ or $(1g_{9/2})^2$ contributions. Specifically, these contributions to the elastic magnetic electron scattering cross section are reduced approximately by $(0.767)^2=0.588$ for the $M1$, 0.044 for the $M3$, 2.6×10^{-4} for the $M5$, and 0.277 for the $M7$. Clearly the intermediate multipoles show the characteristic drastic suppression discussed above.

In Fig. 49 we show the resulting form factors (Moya de Guerra and Dieperink, 1978), together with the experimental data. An experiment on ^{181}Ta has been performed by Rad *et al.* (1980) using the Bates 180° system and a high-resolution spectrometer. The data, shown in Fig. 49, cover the region 0.7—2.5 fm^{-1}. The lower limit in q was imposed by the subtraction of large Coulomb scattering contributions that occur even at $\theta=180°$, due to finite angular resolution and multiple scattering and taking into account the finite mass of the electron. For ^{181}Ta, these Coulomb contributions at low q were obtained by interpolation between cross sections of neighboring even-even W isotopes.

Naturally, in the developments presented here, we have taken a somewhat pedagogical approach in stressing the simple Nilsson model. Of course, more sophisticated treatments of deformed nuclei exist, and we wish to direct the reader to some of the published literature which focuses specifically on the subject of electron scattering from deformed nuclei. Notably the work of Moya de Guerra and collaborators (Moya de Guerra and Dieperink, 1978; Moya de Guerra and Kowalski, 1979,1980; Moya de Guerra, 1980) provides a foundation for such

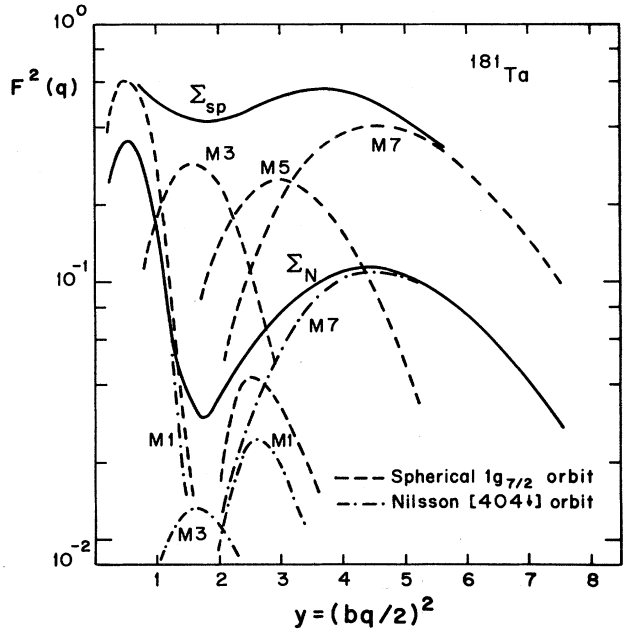

FIG. 49. Form factor of ^{181}Ta (arbitrary normalization) in the extreme single-particle model and the Nilsson model (Moya de Guerra and Dieperink, 1978).

discussions. The projected Hartree-Fock approach, in particular, provides a plausible first step for investigating the properties of the first few states in the ground-state rotation band, including the elastic electron scattering form factors. Although in this case projection after variation does not usually lead to the correct inertial parameters (Peierls and Yoccoz, 1957; Peierls and Thouless, 1962; Villars and Schmeing-Rogerson, 1971) and its description of rotational properties is open to question, Moya de Guerra and Kowalski (1979) have shown that it does lead to collective gyromagnetic ratios in good agreement with experiment. One might therefore expect that it would give a reasonable description of the collective current distributions. To first order in $\langle J_1^2 \rangle^{-1}$ the projected Hartree-Fock approach leads to a decomposition of the transverse form factors in terms of single-particle and collective form factors, as discussed by Moya de Guerra and Kowalski (1980) (the $K=\frac{1}{2}$ case is a special one which must be handled somewhat differently). The results presented in that reference used intrinsic wave functions Φ_K determined using Negele's DME effective interaction (Negele and Rinker, 1977). This required a generalization of the formalism to permit odd-A nuclei to be studied. In particular (Moya de Guerra and Kowalski, 1979,1980), the pair filling approximation of Flocard *et al.* (1973) was adopted.

Here we shall not go into any detailed discussion of the formal aspects of projected Hartree-Fock calculations, but rather shall extract from the work of Moya de Guerra and Kowalski (1980) some of the results for the case of ^{181}Ta. Other targets of interest in studying elastic magnetic electron scattering were also considered there (namely, ^{159}Tb and ^{165}Ho); however, we show results only for the one case where experimental data exist. In Fig. 50 the projected Hartree-Fock results for the single-particle form factors are compared to the Nilsson calculations discussed above. Generally speaking, we see that the simple Nilsson model does very well in reproducing the behavior seen for the much more involved projected Hartree-Fock calculations [and, of course, as we saw before (Fig. 49), both differ significantly from the extreme spherical predictions]. The differences between the projected Hartree-Fock and Nilsson results seen in Fig. 50 are due to the fact that the projected Hartree-Fock single-particle wave function contains many small admixtures of higher N shells. As a consequence, the strengths of the $M1$ and $M7$ peaks are slightly reduced, and the latter is shifted to lower momentum transfer. In Fig. 50, (dot-dashed curve), we also show the collective form factor (multiplied by 10) calculated by Moya de Guerra and Kowalski (1980). This collective contribution is clearly only important at rather low momentum transfer. It added coherently in that region to increase the first peak of the $M1$ from 8.4×10^{-7} to 9.1×10^{-7} (see Fig. 50). Finally, in Fig. 51 we show the data of Rad *et al.* (1980) and comparisons with the form factors calculated by the projected Hartree-Fock method.

E. Nuclei in the lead region

The next group of nuclei we want to discuss is that of the odd-A nuclei around ^{208}Pb, in particular ^{205}Tl, ^{207}Pb, and ^{209}Bi. The theoretical study of nuclei near ^{208}Pb has received considerable attention due to the doubly magic nature of ^{208}Pb. With this magic nature of ^{208}Pb we might hope that an interpretation of magnetic scattering data in terms of single-particle (hole) states would be particularly applicable. As we shall show below, the magnetic form factors demonstrate that the structure of those nuclei is more complicated. Core polarization must be understood if the magnetic form factors are to be

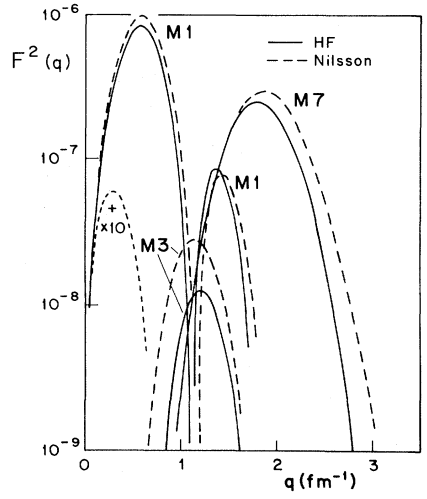

FIG. 50. Single-particle contributions from the projected Hartree-Fock calculation of Moya de Guerra and Kowalski (1980) (solid curve) and the Nilsson model (long-dashed curve). The short-dashed curve gives the collective core contribution multiplied by ten.

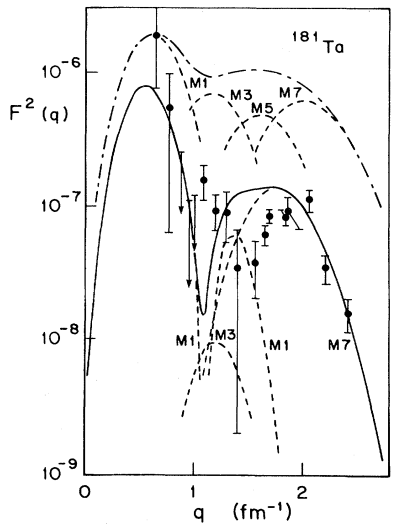

FIG. 51. The ^{181}Ta data of Rad *et al.* (1980) compared to predictions of the extreme single-particle model (dotted-dashed curve, $b_{H0}=2.0$ fm) and Hartree-Fock theory of Moya de Guerra and Kowalski (1980) (solid curve).

described quantitatively.

The Pb region offers two types of extreme situations for magnetic scattering: ^{205}Tl and ^{207}Pb have, as the dominant wave-function component, a $3s_{1/2}$ proton hole and a $3p_{1/2}$ neutron hole, respectively. In these two cases, the only multipolarity is $M1$. Given the pronounced structures in the radial wave functions $R(r)$, each having two nodes and three maxima, a very structured form factor can be expected. This has two consequences. First, the form factor at large q is quite sensitive to the inner part of the wave function; the main Fourier component of $R^2(r)$ shows up only at fairly large q, 2 fm^{-1} (Cavedon *et al.*, 1983). Second, the form factor becomes quite sensitive to MEC contributions; their effect on the $M1$ form factor at large q is not covered up by higher multipole contributions.

The nucleus ^{209}Bi, on the other side, has a $1g_{9/2}$ unpaired proton. Multipolarities $M1$ through $M9$ contribute, and lead to a form factor similar in appearance to the ones described for f/g-shell nuclei. The major difference between these nuclei and those in the f/g shell comes from the fact that ^{209}Bi has a jackknifed configuration. In this case, configuration mixing can be expected to influence even the highest multipolarity in a major way.

The first case we should like to discuss concerns ^{207}Pb. Data are available from an experiment of Papanicolas (1979) aimed mainly at inelastic scattering (Papanicolas *et al.*, 1980). Using the Bates accelerator, Papanicolas *et al.* have measured cross sections at scattering angles of 90° and 160°, and a variety of beam energies. Elastic magnetic form factors were determined in the q range 1.5—2.6 fm^{-1}. At smaller momentum transfers, the separation of magnetic and dominating charge scattering was no longer possible. The resulting data are shown in Fig. 52.

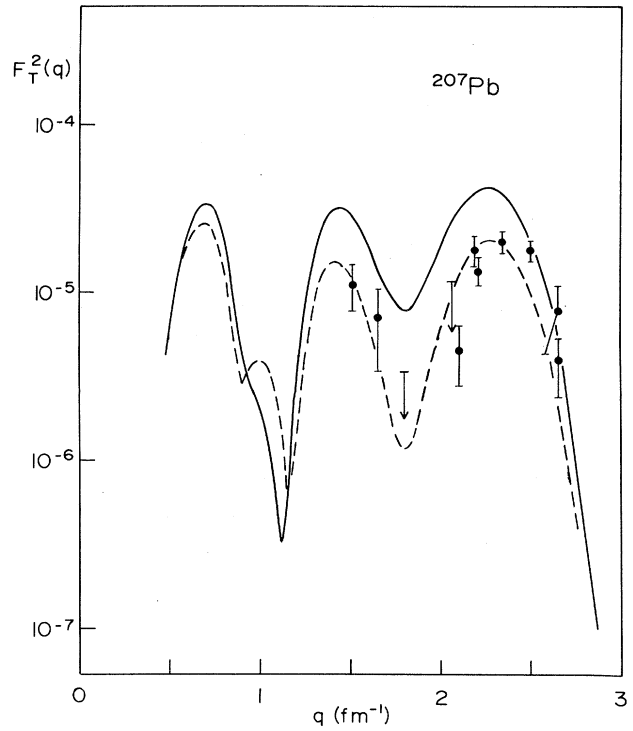

FIG. 52. The ^{207}Pb data of Papanicolas (1979), together with the predictions of Hamamoto *et al.* (1980) for the single-particle model without (solid curve) and with (dashed curve) core polarization.

The solid curve in Fig. 52 gives the prediction of the extreme single-particle model, obtained by Hamamoto *et al.* (1980) using a Woods-Saxon radial wave function. This form factor shows a pronounced dependence on momentum transfer, displaying four minima and maxima before the principal maximum at $q \simeq 2.3$ fm^{-1} is reached. This structure is due partly to the presence of three nodes and three maxima in the $3p$ radial wave function. The overlap of $R^2(r)$ with the dominant j_2 term [Eq. (4.130)] accounts for the maxima at 0.5, 1.3, and 2.3 fm^{-1}, and yields a form factor with minima without sign changes. The additional contribution due to the j_0 term gives further structure that shows up predominantly at low q ($q < 1.3$ fm^{-1}).

Comparison with the data shows that the extreme single-particle model overestimates the amplitude of the main peak of $F_M(q)$ near 2.3 fm^{-1}. In order to understand this difference, we must consider core polarization effects and the contribution of MEC. Several calculations (Sagawa, 1980; Hamamoto *et al.*, 1980; Suzuki *et al.*, 1982; Suzuki and Hyuga, 1983) are available, and are discussed in turn below.

Hamamoto *et al.* (1980) calculate the effects of first-order core polarization resulting from admixtures of one-particle—one-hole states to the dominant one-hole configuration. This calculation is performed using a δ force as a residual interaction. Only the direct matrix elements are included, while exchange terms are neglected. The parameters of the δ force are estimated by fitting energy shifts of high-spin particle-hole states in ^{208}Pb, and by a derivation from the nucleon-nucleon scattering amplitude via the T-matrix approximation.

The main goal of the calculation of Hamamoto *et al.* (1980) was to explain the strong reduction of the observed strength for high-spin (12^-,14^-) particle-hole states in ^{208}Pb (Papanicolas *et al.*, 1980). The magnetic form factor predicted for the ^{207}Pb ground state, calculated in DWBA, is shown in Fig. 52 as a dashed line. For $q > 1.3$ fm^{-1} the form factor gets more or less uniformly reduced by a factor of 2; for smaller q, a small reduction with a more complicated q dependence is found. In the limit $q \to 0$, this calculation does not change the magnetic moment and predicts the Schmidt value (0.64 n.m.) rather than the experimental one (0.59 n.m.). This calculation of Hamamoto *et al.* appears to explain the experimental data quite well.

Suzuki and Oka (1980), on the other hand, have performed similar calculations and studied the effects of finite-range interactions and exchange contributions. They find that the results strongly depend on both the range of the interaction and the exchange nature of the force. A δ interaction moves the strength to a very high

excitation energy ($>5\hbar\omega$), a feature not observed with finite-range interactions. At nonzero momentum transfer, δ interactions (the use of which have become popular with the application of Landau-Migdal theory) may be expected to give unreliable results.

In the calculation of Sagawa (1980), a different mechanism for core polarization is investigated. The coupling of the unpaired particle (hole) to the core vibrations is a mechanism known to influence static magnetic properties. The collective vibrations are calculated by Sagawa, using the random-phase-approximation, including $0\hbar\omega$ and $2\hbar\omega$ one-particle—one-hole states. The main configurations found to contribute to magnetic scattering are the $\pi h_{11/2}^{-1}$-$h_{9/2}$ and $\nu i_{13/2}^{-1}$-$i_{11/2}$ states, which occur around 7-MeV excitation energy in ^{208}Pb. The peaks of the radial wave functions of these orbits occur at large radii, 6—8 fm. Accordingly, they affect the magnetic form factor mainly at low q. Other configurations that turn out to influence the magnetic properties are high-lying 1^+ states. Their transition density again has little structure as compared to the $3p$ single-particle wave function, and their effect on the $M1$ form factor for $q>1$ fm^{-1} is small.

The main change of $F(q)$ in the region where data are available ($q>1.5$ fm^{-1}) is predicted by Sagawa to result from MEC. The contribution of the pair and pionic current diagrams is found to increase the form factor systematically for $q>1$ fm^{-1}. Consequently, the total form factor is predicted to be, for $q>1$ fm^{-1}, about twice as large as the single-particle form factor given in Fig. 52. This enhancement of F_{M1} is clearly in contradiction to the experimental results. The contribution of MEC as calculated by Suzuki and Hyuga (1983; see below) is much smaller.

From the calculation of Sagawa we can learn that the coupling of the single hole to collective excitations of the ^{208}Pb core leads to a core contribution that mainly affects the form factor at low q. We also can expect (Krewald and Speth, 1980) that this coupling should lead to a spreading of single-particle strength over several levels, so as to yield an overall reduction of single-particle $M1$ strength seen in the ^{207}Pb ground state. A decrease of the $3p_{1/2}$ spectroscopic factor similar to that observed in charge scattering for the $3s_{1/2}$ proton hole in Pb (Cavedon *et al.*, 1983) can be expected.

The effects of core polarization and meson-exchange currents on the magnetic form factor of ^{207}Pb have been studied in detail by Suzuki *et al.* (1982) and Suzuki and Hyuga (1983). The core polarization is calculated in first order using a finite-range residual interaction, the three-range Yukawa interaction of Bertsch *et al.* (1977). This interaction includes tensor components and has parameters fitted to the Reid G-matrix and Elliott matrix elements. The exchange contributions, which are important at large q (Suzuki *et al.*, 1982), are included. In the calculation of Suzuki *et al.* (1982) the magnetic scattering from the unperturbed single-particle (hole) configuration receives a first-order contribution that sums over all possible intermediate particle-hole states of the configuration space used. The matrix elements are partly calculated in radial space using Green's-function techniques in order to avoid restrictions of the configuration space size. The radial wave functions employed both for single-particle predictions and for configuration mixing are calculated using Woods-Saxon potentials.

Also included in the calculation of Suzuki and Hyuga (1983) are the effects of meson-exchange currents. The contributions of the pionic current and pair and isobar diagrams are calculated, and the effects of both π and ρ exchange are accounted for.

The results for the ^{207}Pb magnetic form factor are shown in Fig. 53. As compared to the single-particle prediction (dashed curve), the form factor is strongly changed by configuration mixing. Much of this change results from the tensor component of the residual interaction. The core polarization influences the entire q range; the magnetic moment is reduced from the single-particle value (0.64 n.m.) to 0.47 n.m., as compared to the experimental value of 0.59 n.m.

The effect of adding the meson-exchange currents is shown by the solid curve in Fig. 53. While the pair and pionic currents largely cancel the pionic Δ piece, thus leading to a small overall reduction of F_M, the addition of the ρ term leads to an overall enhancement of F_T for $q>0.5$ fm^{-1}. This is shown by the solid line in Fig. 53. At very low q, the MEC lead to enhancements or reductions of F_T according to the changing sign of the one-

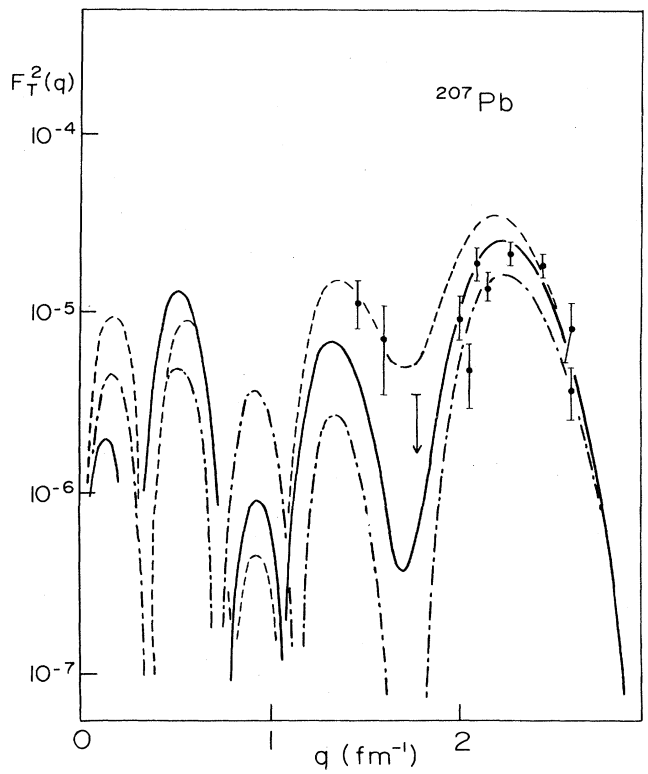

FIG. 53. The ^{207}Pb data of Papanicolas (1979), together with predictions of Suzuki and Hyuga (1983): single-particle model (dashed curve), with core polarization included (dotted-dashed curve), and with MEC in addition (solid curve).

body form factor.

The full form factor calculated by Suzuki *et al.* fits the data quite well in the main diffraction lobe near 2.3 fm^{-1}. The amplitude of the maximum near 1.5 fm^{-1}, strongly reduced by configuration mixing, turns out to be too low. The pronounced changes of $F_T(q)$ due to both configuration mixing and MEC at lower q await confirmation by an experiment which, via 180° scattering, can push the data to lower momentum transfer.

The nucleus ^{205}Tl has two features that make its form factor quite similar to that for ^{207}Pb. Due to the ground-state spin of 1/2, again only an $M1$ contribution to the magnetic form factor occurs. The $3s_{1/2}$ radial wave function (the dominant ground-state configuration is $\pi 3s_{1/2}^{-1}\nu 3p_{1/2}^{-2}$) again has pronounced radial structure, with three maxima and two zeros; this leads to a very structured form factor. The magnetic form factor will, however, be somewhat simpler than that of ^{207}Pb. The dominant wave-function component does not contribute to the convection current, and the term containing $j_{J+1}(qr)$ in Eq. (4.130) does not occur. Accordingly, in the extreme single-particle model, the magnetic form factor of ^{205}Tl is simply the Fourier transform of $R(r)$.

Predictions for the magnetic form factor have been obtained by Suzuki and Hyuga (1983) in the same way as described above for ^{207}Pb. The result is shown in Fig. 54. The single-particle prediction (dashed) shows the three maxima expected from the three maxima of $R(r)$, with no sign change of F_T in the minima. The core polarization reduces F_T in a very pronounced way for momentum transfer $q<2$ fm^{-1}. This reduction is much more dramatic than for ^{207}Tl, a more ideal (but unstable) single-hole nucleus. The $\nu 3p_{3/2}^{-1}3p_{1/2}(1^+)$ excitation possible in ^{205}Tl leads to a strong interference at medium momentum transfer. The effect of MEC, on the other hand, turns out to be much smaller.

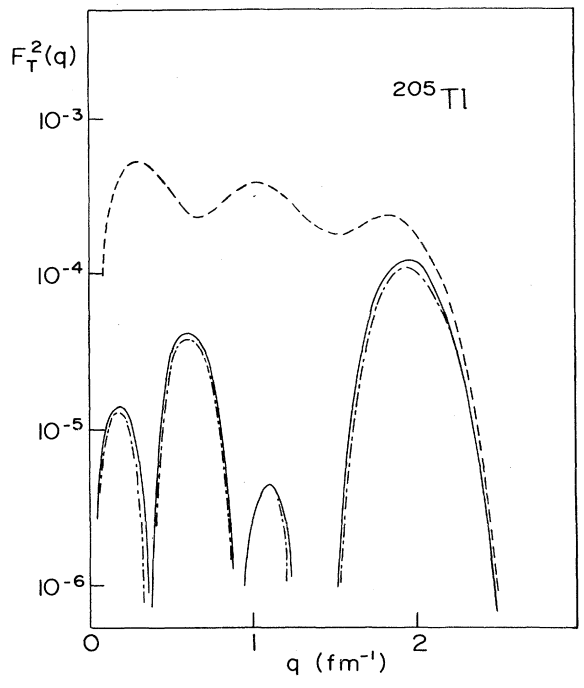

FIG. 54. Predictions for ^{205}Tl of Suzuki and Hyuga (1983) for the single-particle model (dashed curve), with core polarization included (dotted-dashed curve), and with MEC in addition (solid curve).

Figure 54 demonstrates that the magnetic form factors of low multipolarity are particularly sensitive to configuration mixing, an observation repeatedly made when discussing p- and s/d-shell nuclei. The effect on F_T from configuration mixing is much larger than the equivalent effect in charge scattering. There, the radial wave function, as extracted from the difference between the cross sections of ^{205}Tl and ^{206}Pb, is much less affected (Cavedon *et al.*, 1982).

The calculation of Hamamoto (quoted in Cardman *et al.*, 1983) shows a reduction of F_T that is much less structured than the prediction of Suzuki and Hyuga (1983). Basically, Hamamoto's calculation yields a form factor that, relative to the single-particle prediction, is reduced more or less uniformly by a factor of 0.6. This reduction is reminiscent of the reduction in the $3s$ occupation number found by charge scattering (Cavedon *et al.*, 1983). An experiment by Cardman *et al.* (1983) that should allow one to decide between the various predictions for F_T is currently in progress at the Bates accelerator.

The last nucleus of the Pb region we discuss is ^{209}Bi. Due to its large ground-state spin, $J_0=\frac{9}{2}$, the magnetic form factor is very different from those of ^{207}Pb, ^{205}Ti, and resembles those encountered for the f/g-shell nuclei (Sec. VI.C). This resemblance is a superficial one, though. ^{209}Bi has an unpaired $h_{9/2}$ proton with a jackknifed configuration, and both proton and neutron shells with $j>\frac{9}{2}$ are occupied. For these reasons (discussed in detail in Sec. VI.C), the magnetic form factor of ^{209}Bi must be expected to be more complicated and to exhibit a high sensitivity to configuration mixing.

Several experiments, compiled in Fig. 55 have been performed, all in the region $q=1.9$–2.7 fm^{-1}, where a separation of magnetic scattering from charge scattering is possible at angles away from 180°. As pointed out in Sec. II, ^{209}Bi was the first nucleus for which a large multipolarity form factor was observed (Li *et al.*, 1970). In an experiment designed to investigate charge scattering and performed at Stanford at 250 MeV, the contribution of the $M9$ form factor showed up at an angle $\theta\simeq 120°$ (Sick, 1973); this was a surprising result, which showed that what were then regarded to be exotic multipolarities $>M3$ were observable. The experiment performed by Moreira *et al.* (1976), using the Tohuku accelerator, produced data in the region 1.9–2.3 fm^{-1}; the difficulties encountered in subtracting the charge contribution show up in the fluctuations of the form factors. The most extensive experiment was performed at Saclay by Platchkov *et al.* (1982) at energies from 170 to 300 MeV and a scattering angle of 155°. The data from this experiment, converted to PWBA form factors and plotted as a function of effective momentum transfer, are also shown in

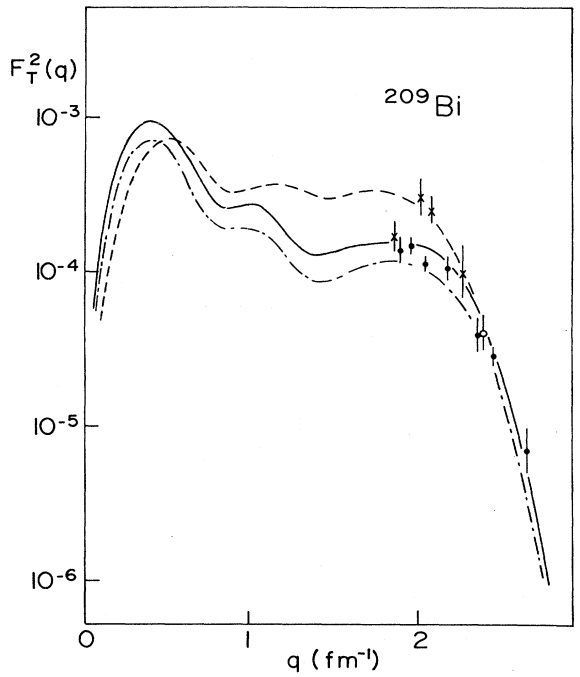

FIG. 55. Data for ^{209}Bi of Platchkov *et al.* (1982) (solid dots), Li *et al.* (1970), (open circle), and Moreira *et al.* (1976) (crosses). The predictions of Suzuki and Hyuga (1983) are shown for the single-particle model (dashed curve), with core polarization included (dotted-dashed curve), and with MEC in addition (solid curve).

Fig. 55. While they define quite well the $M9$ form factor, little is known experimentally about the lower multipolarities.

Calculations concerning ^{209}Bi have been performed by Moreira *et al.* (1976), who estimated the effects of first-order core polarization using schematic finite-range residual forces. This calculation showed that, depending on the exchange character of the force employed, appreciable reductions of F_T^2 at large q could be expected.

The most complete calculation of the effects of configuration mixing and MEC is that of Suzuki *et al.* (1982) and Suzuki and Hyuga (1983), described in more detail above when discussing ^{207}Pb. This calculation shows that, for a realistic residual interaction, core polarization significantly enhances (reduces) the low (high) multipole form factors. At very low q, the form factor is enhanced, so that the single-particle magnetic moment of 2.63 n.m. gets increased to 3.73 n.m., which agrees with experiment ($\mu=4.12$ n.m.) once the MEC contribution of ~ 0.4 n.m. (Arima and Hyuga, 1979), is added. For the high multipoles, on the other hand, central and tensor components contribute coherently to reduce F_M^2 by a factor 2—3. This is related to the jackknifed configuration for which the high-J form factors are dominated by the $(\sigma Y_{J+1})_J$ terms [see Eq. (4.112)]. The core-polarization effect is mainly determined by the $(\sigma Y_{J-1})_J$ term which, greatly enhanced by the tensor force, interferes destructively, and reduces F_T at large q.

Suzuki *et al.* also observe that the shapes of individual multipoles change appreciably as (tensor) configuration mixing is turned on. In particular, the peak of the highest multipole $M9$ gets shifted by 2—3% in momentum transfer, a feature absent for the stretched high-J cases discussed in Sec. VI.C.

Meson-exchange currents, as calculated by Suzuki and Hyuga (1983), lead to an increase of F_T over the entire region of q. This calculation shows that the isobar current contribution is particularly important in those q regions where configuration mixing is effective. The Δ effect calculated by Suzuki and Hyuga (1983) is largest for the higher multipolarities, and suggests that this might be a better case to test their relevance than the $M1$ form factors employed for this purpose up until now.

Calculated form factors and experiment are compared in Fig. 55. The large effect of configuration mixing is exhibited by the difference between the dashed and dashed-dotted curves. The solid curve, which includes MEC as well, explains the (rather limited) experimental data quite well.

The theoretical calculations for nuclei $A>4$ discussed in this section all treat the nucleus as a system of nonrelativistic nucleons and use the Schrödinger equation to describe the purely nucleonic wave function. Relativistic quantum field theories for nuclei recently have been developed (Miller, 1974; Walecka, 1974; Brockmann and Weise, 1977; Horowitz and Serot, 1983). In these calculations mesonic degrees of freedom are included explicitly, since the theory contains baryon, scalar and vector meson fields. Nucleons are described by the Dirac equation, thereby assuring a more correct treatment of relativistic aspects. Fits to nuclear matter properties yield the strength of the coupling constants required. These relativistic calculations have been shown to yield a good description of nuclear ground states and have been found to improve greatly our understanding of spin observables in proton-nucleus scattering. One such calculation (Serot, 1981) has been applied to a spin observable of interest for this review, the ^{209}Bi magnetic form factor, and is discussed below.

Serot uses the self-consistent relativistic Hartree approach to describe the core ^{208}Pb. The resulting depth of the scalar and vector potentials is of the order of half the nucleon mass; this implies that the binding effects are large and that relativistic effects cannot be calculated using the usual nonrelativistic reduction plus an eventual v/c expansion. The calculation shows that the large component of the Dirac wave function is quite similar to the corresponding Schrödinger wave function. The main difference from the nonrelativistic calculation results from the small component; according to the calculation of Shepard *et al.* (1984), the small component is about a factor of 1.7 larger than the one calculated from the large component using the usual free-space relation between small and large components.

This enhancement of the small component is of importance for the magnetic form factor, which contains a cross term between small and large components. This is

the case in particular for the Δ_J term [Eq. (4.110d)], which contains the convection-current contribution to F_T.

In the calculation for ^{209}Bi, Serot uses a simple model for the nuclear structure, a $1h_{9/2}$ proton coupled to a closed ^{208}Pb core. Both the nonrelativistic and relativistic approaches are used to calculate F_T. The results show that, over most of the q range, 0—3 fm^{-1}, the Dirac form factor F_T^2 is a factor of 2 larger than the nonrelativistic result. This increase is largely due to the fact that in the relativistic calculation the velocities are larger, because of the lower effective mass $m^* \simeq M_N - U_S$ resulting from the large depth of the scalar potential $U_S \simeq 450$ MeV.

At present, a comparison of this calculation with experiment is not yet conclusive, given the simple model used for the ^{209}Bi nuclear structure. The reduction in $F_T(q)$ expected from core polarization (see Fig. 55) should be calculated first. The calculation of Serot does show, however, that magnetic form factors are very sensitive to differences between relativistic and nonrelativistic descriptions of the nucleus. A more extensive comparison with magnetic form factors, elastic or inelastic (Shepard *et al.*, 1984), holds promise for investigating the consequences of strong scalar and vector nucleon-nucleus potentials, and the validity of the Dirac approach.

F. Compilation of experimental data

In the preceding sections, the experimental data for a number of selected nuclei have been presented. Many cases were not discussed, for lack of space and because data and/or theory are not very extensive. In Table III we give a more complete account of the experimental data presently available. Data for $A=1$, not listed here, have been compiled by De Jager *et al.* (1974).

VII. FEW-BODY NUCLEI

This section on $A=2,3$ nuclei is of a somewhat special character. The emphasis of the discussion is not, as in Secs. VI.A—VI.E, on nuclear structure. Rather, questions concerning the fundamental understanding of the simplest systems in terms of their constituents and interactions are discussed. Internal degrees of freedom of the nucleonic constituents also play a much more important role. Due to the (relative) simplicity of the systems under consideration, the $A=2,3$ nuclei can serve as examples for a number of ideas which are most useful within the more general context of our study of electron-nucleus scattering.

This section is split into two subsections, on the deuteron and on the $A=3$ nuclei. In connection with our understanding of meson-exchange currents, another observable for the deuteron, electrodisintegration at threshold, provides relevant information. For a detailed discussion of this process, the reader is referred to Bernheim *et al.* (1981), Arenhövel and Leidemann (1983), and Mathiot (1983). A topic that repeatedly will come up without receiving due attention, the properties of the nucleon magnetic form factors, is discussed in detail in Gourdin (1974).

A. The deuteron

The deuteron form factors have been studied extensively over the past 20 years. This continuing interest stems from a combination of reasons. (1) For a given nucleon-nucleon interaction, the wave function and one-body form factor can be predicted accurately; experimental data allow one to check the calculations, in particular the predictions concerning the short-range behavior of the wave function's observables at large q. (2) The loosely bound deuteron, for certain types of experiments, can serve as a neutron target; the electromagnetic neutron form factors, needed for an understanding of both the neutron and the form factors for heavier nuclei, can be measured. (3) For a simple system like the deuteron, the purely nucleonic aspects of the wave function are reasonably well understood; non-nucleonic degrees of freedom, MEC in particular, then can be isolated.

The many kinds of physics input cited above indicate that the individual pieces might be hard to sort out (Lomon, 1980). It can be done if the proper observables, F_{C0}, F_{C2}, F_{M1}, tensor polarization, and inclusive scattering cross section, are studied together. The different sensitivities to the various ingredients allow us to separate them. If the complementarity of observables until now has been exploited in part only, then that is mainly because some of the important observables, such as the tensor polarization or quadrupole form factor at large q, have not yet been measured because of accelerator limitations in energy and duty cycle (see also Sec. VIII). In the following, we shall limit the discussion to the observable of interest for this review, the magnetic form factor.

A variety of experimental techniques have been devised to measure the deuteron magnetic form factor. Besides the conventional single-arm scattering at large scattering angle (Friedman *et al.*, 1960; Goldemberg and Schaerf, 1964; Grossetête *et al.*, 1966; Rand *et al.*, 1967; Ganichot *et al.*, 1972; Simon *et al.*, 1981; Bernheim *et al.*, 1981; Cavedon *et al.*, 1984), the recoil deuterons have been detected at 0° (Benaksas *et al.*, 1964,1966), and the electron and deuteron have been measured in coincidence (Buchanan and Yearian, 1965; Martin *et al.*, 1977). The latter techniques profit from the absence of particle-stable excited states of the deuteron; in this case an experiment with very bad energy resolution still allows one to identify the elastic scattering properly. Data taken with the recoil detected at 0° exploit the increase in effective solid angle occurring under this kinematical regime. A coincidence measurement allows one to reduce the background drastically, without loss in count rate, owing to the fixed angular correlation between electron and deuteron.

The experimental data in general are expressed in terms of the structure functions $A(q), B(q)$,

$$\frac{d\sigma}{d\Omega} = \sigma_M f_{\rm rec}^{-1} [A(Q) + \tan^2(\theta/2) B(Q)] \,. \tag{7.1}$$

For reasons of experimental feasibility more than physical significance, the terms are separated in a way different from the usual split into electric and magnetic contribu-

TABLE III. Experimental data on elastic magnetic electron scattering.

Nucleus	Spin	q range (fm^{-1})	θ range (deg)	Main λ	Reference
^{2}H	1^+	1.5–2.2	→145	$M1$	Friedman *et al.*, 1960
			180	$M1$	Benaksas *et al.*, 1966
		0.5–0.7	180	$M1$	Goldemberg and Schaerf, 1964
		2.4–3.5	→145	$M1$	Buchanan and Yearian, 1965
		1.1–1.4	→145	$M1$	Grossetête *et al.*, 1966
		1.7–2.2	180	$M1$	Benaksas *et al.*, 1966
		2.2–3.2	180	$M1$	Rand *et al.*, 1967
		0.7–2.4	180	$M1$	Ganichot *et al.*, 1972
		5.0	→82	$M1$	Martin *et al.*, 1977
		0.5	180	$M1$	Jones *et al.*, 1980
		1.2–2	→157	$M1$	Simon *et al.*, 1981
		2.4–4.2	155	$M1$	Bernheim *et al.*, 1981
		2.7–5.3	155	$M1$	Auffert *et al.*, 1984
^{3}H	$\frac{1}{2}^+$	1.0–2.8	→135	$M1$	Collard *et al.*, 1965
^{3}He	$\frac{1}{2}^+$	1.0–2.8	→135	$M1$	Collard *et al.*, 1965
		1.3–4.0	→135	$M1$	McCarthy *et al.*, 1970
		3.0–3.9		$M1$	Bernheim *et al.*, 1972
		0.6	180	$M1$	Jones *et al.*, 1979
		2.7–5.6	155	$M1$	Cavedon *et al.*, 1982a
		0.9–3.4	160	$M1$	Dunn *et al.*, 1983
^{6}Li	1^+	0.4	180	$M1$	Peterson, 1962
		0.4	180	$M1$	Goldemberg and Torizuka, 1963
		0.8–1.4	180	$M1$	Rand *et al.*, 1966
		0.5–0.9	180	$M1$	Lapikás, 1978
		0.8–2.8	150–180	$M1$	Bergstrom *et al.*, 1982
^{7}Li	$\frac{3}{2}^-$	0.4	180	$M1$	Peterson, 1962
		0.4	180	$M1$	Goldemberg and Torizuka, 1963
		0.7–2.0	180	$M1,M3$	Rand *et al.*, 1966
		0.3–0.9	180	$M1$	Van Niftrik *et al.*, 1971a
		0.8–2.9	150–180	$M1,M3$	Lichtenstadt *et al.*, 1983
^{9}Be	$\frac{3}{2}^-$	0.4	180	$M1$	Goldemberg *et al.*, 1965
		0.4–0.7	180	$M1$	Vanpraet and Kossanyi-Demay, 1965
		0.7–2.5	180	$M1,M3$	Rand *et al.*, 1966
		0.3–0.9	180	$M1,M3$	Lapikás *et al.*, 1975
^{10}B	3^+	0.4	180	$M1$	Goldemberg and Torizuka, 1963
		0.7–1.7	180	$M1,M3$	Goldemberg *et al.*, 1965
		0.5–0.7	180	$M1$	Vanpraet and Kossanyi-Demay, 1965
		0.7–2.0	180	$M1,M3$	Rand *et al.*, 1966
		0.3–0.9	180	$M1$	Lapikás, 1978
^{11}B	$\frac{3}{2}^-$	0.4	180	$M1$	Goldemberg and Torizuka, 1963
		0.7–1.7	180	$M1,M3$	Goldemberg *et al.*, 1965
		0.5–0.7	180	$M1$	Vanpraet and Kossanyi-Demay, 1965
		0.7–2.3	180	$M1,M3$	Rand *et al.*, 1966
		0.3–0.9	180	$M1$	Lapikás, 1978

TABLE III. (*Continued*).

Nucleus	Spin	q range (fm^{-1})	θ range (deg)	Main λ	Reference
^{13}C	$\frac{1}{2}^-$	1.8–2.1	50–100	$M1$	Heisenberg *et al.*, 1970
		0.4–0.8	180	$M1$	Lapikás *et al.*, 1975
		0.8–3.3	180	$M1$	Hicks *et al.*, 1982a
^{14}N	1^+	0.4	180	$M1$	Goldemberg and Torizuka, 1963
		1.0–1.8	180	$M1$	Rand *et al.*, 1966
		1.7	50–90	$M1$	Dally *et al.*, 1970
		0.8–3.3		$M1$	Huffman *et al.*, 1984
^{15}N	$\frac{1}{2}^-$	1.7	50–90	$M1$	Dally *et al.*, 1970
		0.7–3.2	180	$M1$	Singhal *et al.*, 1983
^{17}O	$\frac{5}{2}^+$	0.5–2.7	180	$M1$–$M5$	Hynes *et al.*, 1979
^{19}F	$\frac{1}{2}^+$	0.4	180	$M1$	Goldemberg and Torizuka, 1963
		1.6–2.4	45–90	$M1$	Williamson *et al.*, 1983
		0.4–2.8	154–180	$M1$	Donné *et al.*, 1983
^{23}Na	$\frac{3}{2}^+$	0.4	180	$M1$	Goldemberg and Torizuka, 1963
		1.4–1.8	180	$M3$	Torizuka, 1977
^{25}Mg	$\frac{5}{2}^+$	0.4–2.6	160–180	$M1,M5$	Euteneuer *et al.*, 1977
		0.9–2.2	180	$M3,M5$	York and Peterson, 1979
^{27}Al	$\frac{5}{2}^+$	0.4	180	$M1$	Goldemberg and Torizuka, 1963
		1.5	180		Stovall *et al.*, 1967
		1.5–2.5	80–140	$M3,M5$	Li *et al.*, 1970
		0.4–1.0	180	$M1,M3$	Lapikás *et al.*, 1973
		1.2–1.5	180	$M3,M5$	Macauley *et al.*, 1977
		0.8–2.9		$M3,M5$	Hicks *et al.*, 1983
^{29}Si	$\frac{1}{2}^+$	1.0–2.8	156–180	$M1$	Miessen, 1982
^{31}P	$\frac{1}{2}^+$	0.4	180	$M1$	Goldemberg and Torizuka, 1963
		1.0–2.8	156–180	$M1$	Miessen, 1982
^{39}K	$\frac{3}{2}^+$	0.4	180	$M1$	Goldemberg and Torizuka, 1963
		2.0		$M3$	Likhachev *et al.*, 1975
		0.7–2.4	180	$M1,M3$	De Jager *et al.*, 1979
^{45}Sc	$\frac{7}{2}^-$	0.4–0.9	180	$M1,M3$	De Vries *et al.*, 1970
^{49}Ti	$\frac{7}{2}^-$	1.9–2.0	150	$M7$	Likhachev *et al.*, 1976
		1.8–3.3	155	$M5,M7$	Platchkov *et al.*, 1982
		0.7–1.4	180	$M1$–$M5$	Selig,1984

TABLE III. (*Continued*).

Nucleus	Spin	q range (fm^{-1})	θ range (deg)	Main λ	Reference
^{51}V	$\frac{7}{2}^-$	0.4–0.9	180	$M1,M3$	De Vries *et al.*, 1970
		1.5	90	$M5$	Peterson *et al.*, 1973
		1.2–2.4	155	$M5,M7$	Nascimento *et al.*, 1974
		1.8–3.1	155	$M5,M7$	Platchkov *et al.*, 1982
		0.9–2.4	180	$M3$–$M7$	Arita *et al.*, 1981
		3.3–4.0	155	$M5,M7$	Platchkov *et al.*, 1983
^{55}Mn	$\frac{5}{2}^-$	0.4–0.9	180	$M1$	De Vries, 1973
^{59}Co	$\frac{7}{2}^-$	0.4–0.9	180	$M1,M3$	De Vries *et al.*, 1970
		1.8		$M7$	Likhachev *et al.*, 1975b
		1.8–3.1	155	$M5,M7$	Platchkov *et al.*, 1982
^{63}Cu	$\frac{3}{2}^-$	2.1–2.4		$M7$	Schwentker, 1977
		0.4–0.9	180	$M1,M3$	Selig *et al.*, 1982
^{65}Cu	$\frac{3}{2}^-$	2.1–2.4		$M7$	Schwentker, 1977
		0.4–0.9	180	$M1,M3$	Selig *et al.*, 1982
^{87}Sr	$\frac{9}{2}^+$	2.0–3.0	155	$M7,M9$	Platchkov *et al.*, 1982
^{93}Nb	$\frac{9}{2}^+$	0.5–1.1	180	$M1,M3$	Box, 1976
		1.7–2.5	155	$M7,M9$	De Witt Huberts *et al.*, 1976
		0.9–2.3	180	$M3$–$M9$	York and Peterson, 1979
		1.8–2.9	155	$M7,M9$	Platchkov *et al.*, 1982
^{115}In	$\frac{9}{2}^+$	0.4–0.9	180	$M1,M3$	Box, 1976
		1.3–2.7	180	$M5,M7$	De Jager *et al.*, 1979
^{181}Ta	$\frac{7}{2}^+$	0.7–2.5	180	$M1$–$M7$	Rad *et al.*, 1980
^{207}Pb	$\frac{1}{2}^+$	1.5–2.6	180	$M1$	Papanicolas, 1979
^{209}Bi	$\frac{9}{2}^-$	2.3	122	$M9$	Li *et al.*, 1970
		1.9–2.3	155	$M7,M9$	Moreira *et al.*, 1976
		1.9–2.7	155	$M7,M9$	Platchkov *et al.*, 1982

tions [cf. Eq. (4.18)]. For a nucleus as light as the deuteron it is worthwhile to emphasize that Q^2 represents the four-momentum transfer squared $q^2-\omega^2$ with $Q\equiv(Q^2)^{1/2}\geq 0$.

A compilation of the available experimental data is given in Fig. 56. The data at low and medium q come mainly from the experiments of Buchanan and Yearian (1965), Rand *et al.* (1967), and Simon *et al.* (1981), while many of the higher-q results come from unpublished work done in connection with electrodisintegration (Bernheim, 1981) and an experiment (Auffret *et al.*, 1984) currently underway at Saclay.

In order to understand the ingredients that go into the magnetic form factor, we first study the impulse approximation contribution (Gourdin, 1963) given by

$$B(Q)=\tfrac{16}{3}\eta(1+\eta)G_M^2(Q) \tag{7.2}$$

with

$$\eta=Q^2/4M_d^2 \tag{7.3}$$

and $G_M(0)=\mu$, where G_M is given in terms of the electric and magnetic nucleon form factor $G_{Ep},G_{En},G_{Mp},G_{Mn}$,

$$G_M(Q)=[G_{Mp}(Q)+G_{Mn}(Q)]C_S(Q)+\tfrac{1}{2}[G_{Ep}(Q)+G_{En}(Q)]C_L(Q) \tag{7.4}$$

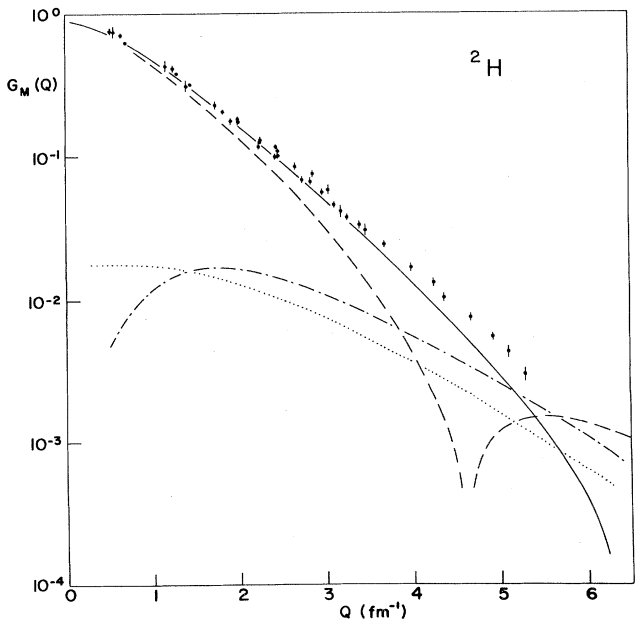

FIG. 56. The data (see Table III) for the deuteron magnetic form factor $G_M(Q)$, compared to the one-body calculation of Mathelitsch and Zingl (1978) done for the Paris NN interaction and dipole nucleon form factors. The S^2 (dashed curve), D^2 (dotted curve), and S-D contributions (dotted-dashed curve) are shown separately.

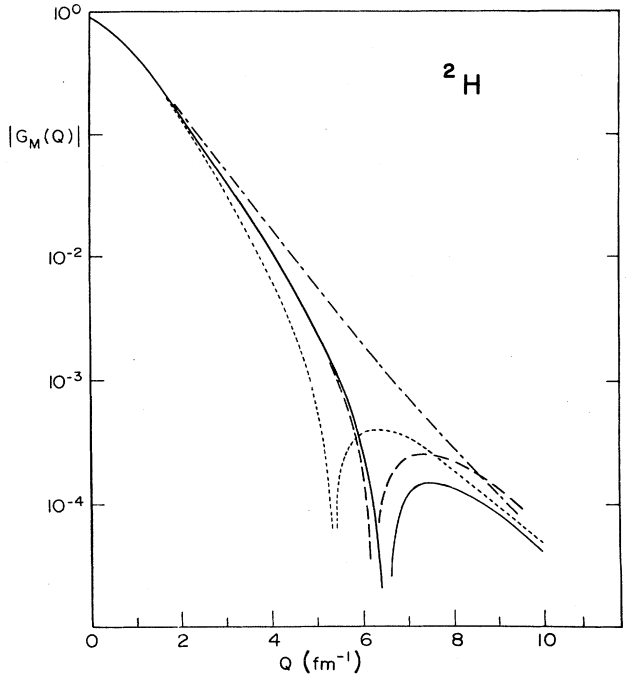

FIG. 57. Deuteron magnetic form factor of Mathelitsch and Zingl (1978) for different nucleon-nucleon potentials: Paris (dotted-dashed curve), Reid soft-core (solid curve), Reid hard-core (dashed-curve), and Bonn (dotted curve).

and integrals over the deuteron S- and D-state wave functions u and w,

$$C_S(Q)=\int (u^2-w^2/2)j_0(Qr/2)dr + \int (uw/\sqrt{2}+w^2/2)j_2(Qr/2)dr\ , \quad (7.5)$$

$$C_L(Q)=\int 3w^2/2[\,j_0(Qr/2)+j_2(Qr/2)]dr\ . \quad (7.6)$$

Here, the indices L and S refer to orbital and spin contributions to the magnetic dipole density. In Fig. 56 we show the magnetic form factor broken down into the different contributions from the S and D states and the S-D transition. The curve in Fig. 56, calculated using the integrals of Mathelitsch and Zingl (1978, and private communication) for the Paris potential, shows that at low Q the form factor is entirely dominated by the intrinsic magnetization piece due to the S state. In the region 4—6 fm^{-1}, most nucleon-nucleon potentials produce a diffraction zero in the S-state contribution. In this region the D state amplitudes will thus dominate, mainly through the S-D interference term. This latter contribution affects the magnetic form factor in a very pronounced way, and its influence leads to a characteristic difference in the "charge" structure function $A(Q)$. In $B(Q)$ there is an interference that decreases $B(Q)$ for $Q>5.5$ fm^{-1}; for $A(Q)$ the D-state contribution occurs mainly through incoherent terms that increase $A(Q)$ throughout. A comparison of A and B in the region 4—7 fm^{-1} thus should be very instructive for a separation of the D-state contribution to the deuteron form factors.

Figure 57, taken from the work of Mathelitsch and Zingl (1978), shows the sensitivity of $B(Q)$ to different NN potentials. Changes in the S- and D-state wave functions show up in a very pronounced way at large Q. The form factor shows a diffraction structure mainly influenced by the repulsive core of V_{NN} at short range—the more strongly repulsive the potential, the lower the momentum transfer of the minimum of the S-state form factor. The S-D interference amplifies these differences, to the point where, for example, the earlier version of the Paris potential (Lacombe *et al.*, 1975) used by Mathelitsch and Zingl (1983) displays no minimum in $B(Q)$, while the more recent version used to calculate the results in Fig. 57 does have a minimum at $Q\simeq 6$ fm^{-1}. While some of this sensitivity to V_{NN} is reduced by the non-impulse-approximation contributions (see below), much of it remains (isoscalar MEC are small) and can serve as a sensitive test of the deuteron wave function.

In order to calculate $B(Q)$, one has to know the nucleon electromagnetic form factors. The deuteron magnetic form factor depends mainly on the isoscalar nucleon form factor $G_{Mp}+G_{Mn}$ (Rand *et al.*, 1973). This combination is actually a difference of two comparable numbers ($G_{Mn}<0$), and therefore sensitive to experimental errors. On the other hand, G_{Mn} can be determined from quasielastic e-d scattering, and the interpretation of these e-d data is largely independent of the deuteron wave function assumed. As a consequence, $G_{Mn}+G_{Mp}$ is known with a reasonable accuracy and a small systematic error. Among the popular nucleon form-factor models (Gourdin, 1974), the dipole form factor and the param-

etrization of Iachello *et al.* (1973) reproduce the data rather well for $Q<5$ fm^{-1}. The fits of Blatnik and Zovko (1974) and Höhler *et al.* (1976) for the specific quantity of interest, G_{Ms} ($q<5$ fm^{-1}), are systematically larger than the data. When discussing only those parametrizations that correctly fit G_{Ms} for $Q<5$ fm^{-1}, an error of $\sim 10\%$ for $B(Q)$ results from the uncertainty in the nucleon form-factor input.

As compared to the "electric" form factor $A(Q)$, $B(Q)$ has the advantage that the neutron electric form factor plays a minor role. The intrinsic magnetization terms dominate, and the convection current [terms proportional to $G_{Ep}+G_{En}$ in Eq. (7.4)] only gradually increase with Q, and reach a total of 30% at the highest Q where data are available. A realistic assessment of the error of G_{En} of $\pm 50\%$ leads to a negligible uncertainty, $\pm 5\%$, in B (5 fm^{-1}).

At the large momentum transfer achievable experimentally for light nuclei, non-nucleonic degrees of freedom are expected to play an important role. Historically, both the charge and magnetic form factors have been taken as test cases for non-nucleonic contributions and have provided a continuing impetus to developments in the theory of meson-exchange currents (Chemtob, 1971; Chemtob *et al.*, 1974). Many of the more exotic exchange effects (Adler and Drell, 1964; Blankenbecler and Gunion, 1971) were investigated for the deuteron before the calculations centered on the diagrams considered to be important today. It now has become clear that the MEC contributions are not of dominating importance for the deuteron form factor; the deuteron being an isoscalar object, MEC in general are small. Despite this fact a study of MEC in the deuteron is of great interest. The simplicity of the two-nucleon system allows alternative theoretical approaches to be explored, which can be used to check the standard MEC calculations.

The standard approach used to calculate MEC is described in detail in Sec. IV.E. For the deuteron, the important diagram at low Q is the one for the pair current, while at higher Q the $\pi\rho\gamma$ current dominates. The pionic current, a contribution that is usually important at low Q, is absent due to G parity. The Δ contribution, although at present still of somewhat uncertain magnitude, also plays a role at low Q.

The calculation of Fabian, Arenhövel, and Miller (1974) includes the diagrams of the pair current and one-boson exchange. In order to describe these currents in a way consistent with the calculation of the nucleonic wave function, Fabian, Arenhövel, and Miller (1974) use the one-boson exchange (OBE) potential of Bryan and Scott. Strong-vertex form factors and the effect of $\Delta\Delta$ components (see below) are included. The calculation of Jackson, Lande, and Riska (1975), done for the Reid soft-core NN potential, includes pair, recoil, and wave-function renormalization diagrams. The calculation of Gari, Hyuga, and Sommer (1976), performed for a modified Reid soft-core potential, includes the same diagrams and allows in addition for the exchange of heavier mesons (ρ,ω), which become more important at large momentum transfer. In addition, Gari, Hyuga, and Sommer (1976) calculate the $\pi\rho\gamma$ contribution to $B(Q)$ (these calculations use a ρ width of 112 MeV, while more recent data suggest $\Gamma_\rho \simeq 150$MeV); the importance of this term already at medium q was first pointed out by Adler and Drell (1964).

Both the calculations of Fabian, Arenhövel, and Miller (1974) and of Gari, Hyuga, and Sommer (1976) include the presence of $\Delta\Delta$ components in the deuteron ground state (Weber and Arenhövel, 1978). While the earlier calculations (Fabian, Arenhövel, and Miller, 1974) treat the $\Delta\Delta$ perturbatively, the later ones (Arenhövel, 1975; Gari, Hyuga, and Sommer, 1976) describe the $\Delta\Delta$ by a coupled-channel approach. The $\Delta\Delta$ probability predicted by different calculations varies somewhat, $P_{\Delta\Delta}=0.5$–1.5%, and depends on the strong-vertex form factors chosen. As Gari, Hyuga, and Sommer (1976) point out, the $\Delta\Delta$ component in addition depends on the inclusion of short-range exchange processes; for example, ω exchange is omitted by Gari, Hyuga, and Sommer (1976), since it would lead to "unphysically large" $\Delta\Delta$ probabilities. Given the range of variation of $P_{\Delta\Delta}$, the $\Delta\Delta$ effect predicted for $B(Q)$ strongly depends on the specific calculation under discussion. For Gari, Hyuga, and Sommer (1976), the $\Delta\Delta$ component increases B (4 fm^{-1}), by 7×10^{-6}; for Fabian, Arenhövel, and Miller (1974), the $\Delta\Delta$ effect amounts to an increase of 4.8×10^{-5}. Much of this difference is due to the fact that Gari, Hyuga, and Sommer (1976) use the same isoscalar magnetic moment for the nucleon and Δ, while Fabian, Arenhövel, and Miller (1974) use a three times larger Δ isoscalar moment, as given by the quark model (Arenhövel, 1983).

In Fig. 58 we compare the calculations discussed above to the experimental data. In order to present sets of curves that are reasonably comparable, we have selected individual contributions from the calculations cited, and partly supplemented them by MEC terms provided by other calculations. In particular, for the calculation of Fabian, Arenhövel, and Miller (1974), we have added the $\pi\rho\gamma$ contribution as calculated by Gari, Hyuga, and Sommer (1976). For Jackson *et al.* (1975), we have done the same, and we have omitted the recoil and wave-function renormalization contributions. These latter terms are of relativistic order in Q^2/M_N^2, and the calculation of Jackson *et al.* (1975) neglects some of the terms of this order. For Gari, Hyuga, and Sommer (1976), we include their full MEC calculation. For all references, we omit the $\Delta\Delta$ contribution, although it could be quite important; as discussed above, this contribution is poorly determined at the present time.

Figure 58 shows that the differences predicted for $B(Q)$ are quite appreciable at large Q. The calculation of Fabian *et al.* (1974) gives the largest value for $B(Q)$, a consequence of the use of the Bryan-Scott (BS) potential. At $Q=5$ fm^{-1}, the impulse approximation contribution using the BS potential exceeds that for the Reid soft-core potential by a factor of 2. Comparison of calculation and experiment shows that the impulse approximation result, calculated with the Reid soft-core potential, is somewhat

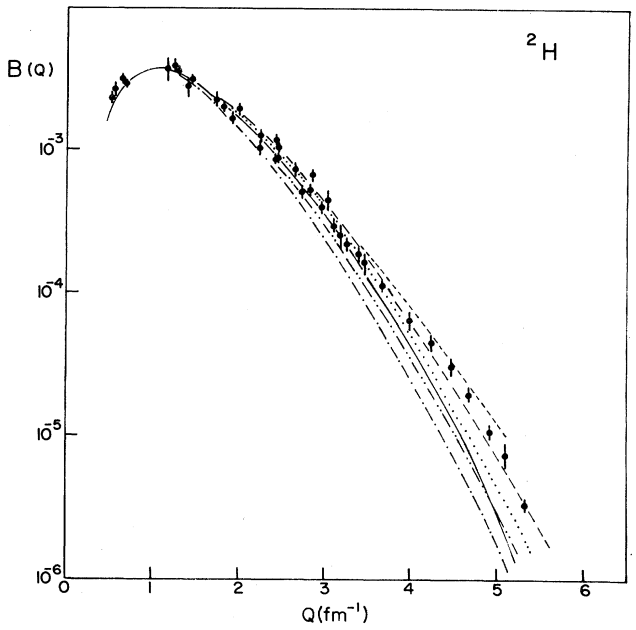

FIG. 58. Deuteron structure function $B(Q)$ with different theoretical predictions. Impulse approximation: Mathelitsch and Zingl (1978) (solid curve). Full calculations including MEC: Fabian *et al.* (1974) (short-dashed curve), Jackson *et al.* (1975) (long-dashed curve), Gari *et al.* (1976) (dotted curve). Relativistic calculations: Arnold *et al.* (1980) (dotted-dashed curve), and Zuilhof and Tjon (1980) (dash—double-dotted curve).

low at large Q. Adding the MEC (but not the $\Delta\Delta$) leads to good agreement for the calculation of Gari and Hyuga (1976a; Gari *et al.*, 1976). The result of Jackson *et al.* (1975) is somewhat high, presumably because they have not included strong-vertex form factors which cut down MEC at large Q.

The calculations summarized above obtain the deuteron wave function from a solution of the (nonrelativistic) Schrödinger equation for a given NN potential. Meson-exchange diagrams, which partly account for relativistic effects, are added to order Q^2/M_N^2. The pair diagram in particular corresponds to a perturbative inclusion of the $\overline{N}$ component of the two-body wave function. An alternative theoretical approach (Buck and Gross, 1979; Arnold *et al.*, 1980; Zuilhof and Tjon, 1980) is to solve the relativistic Bethe-Salpeter equation for a given NN interaction. In this case the relativistic aspects are included to all orders in Q/M_N. Such a relativistic calculation can be expected to be equivalent to a nonrelativistic calculation supplemented by the antinucleon diagram (pair term) plus the usual electromagnetic relativistic corrections discussed by Friar (1973) and Licht and Pagnamenta (1970). As shown by Gross (1978), these approaches are indeed formally equivalent to first order in Q^2/M_N^2.

For the deuteron, with its smoothly falling magnetic form factor, the electromagnetic relativistic corrections actually are very small; the use of $\tilde{G}_e$ and the argument shift, where the form factor is evaluated at a shifted effective momentum transfer (Friar, 1973), nearly cancel. Consequently, the relativistic calculations should give the same result as the nonrelativistic impulse approximation plus the pair contribution.

Two relativistic calculations for $B(Q)$ are available at present. Arnold *et al.* (1980) calculate form factors starting from the wave function of Buck and Gross (1979), who use a quasipotential model which approximates the Bethe-Salpeter equation by a three-dimensional relativistic wave equation. Buck and Gross (1979) calculate the deuteron wave function for several one-boson exchange potentials, and assume that one of the nucleons is off-shell. Zuilhof and Tjon (1980,1981) solve the Bethe-Salpeter equation in the ladder approximation, using again OBE potentials. Both calculations thus include the physics described in nonrelativistic calculations by the pair diagram. In order to get curves that are comparable to each other, we have added the $\pi\rho\gamma$ contribution of Gari *et al.* (1976). The resulting predictions for $B(Q)$ are shown in Fig. 58. Both relativistic calculations are lower than the experimental data.

Clearly, Fig. 58 shows a disturbing result, the nonrelativistic calculations give a $B(Q)$ systematically larger than the impulse approximation result, while the relativistic calculations give a smaller form factor. Two supposedly equivalent approaches give qualitatively different answers. This difference could perhaps be attributed to the treatment of MEC to order Q^2/M_N^2 only; at $Q=5$ fm^{-1} this could lead to problems (the typical expansion parameter is $Q^2/4M_N^2$). The calculation of Cheon (1981) indeed points out that relativistic effects lead to a decrease of the pair contribution at large Q. In addition, Zuilhof and Tjon (1981) point out that in pseudoscalar πN coupling the two-pion exchange current gives a contribution comparable in size to the pair current, but opposite in sign. This could explain why the pair contribution leads to too large a $B(Q)$.

Given this comparison, one may wonder whether the standard MEC calculations (Sec. IV.E) overestimate the relativistic effects. It seems most desirable to make a more detailed study of the theoretical approaches alluded to above, in order to take care of this worrying contradiction. Comparison with experiment at the present time cannot determine which of the approaches is more correct; depending on the size of the $\Delta\Delta$ contribution, either could be in agreement with the data.

B. The $A=3$ systems

The $A=3$ system is distinguished by a number of unique properties. The nucleonic wave function can be calculated "exactly" for a given nucleon-nucleon potential. By Faddeev or variational techniques, the (nonrelativistic) Schrödinger equation can be solved numerically with a fair degree of accuracy. Calculations using different techniques and truncation schemes are in reasonable agreement, so the nucleonic part of the wave function, and certainly the long- and medium-range properties, are under control. The presence of three nucleons in a (mainly) relative S state leads to a large density (in con-

trast to the loosely bound deuteron) that makes the $A=3$ systems interesting for study of short-range phenomena. The investigation of isovector meson-exchange currents then promises to be a fruitful subject, particularly if observables receiving a large MEC contribution such as magnetic form factors are studied. The existence of a pair of (almost) stable mirror nuclei, ^{3}H and ^{3}He, is unique; once sufficient data for ^{3}H become available, the separation of form factors into their isospin components promises to be very instructive.

There is a large body of literature on the three-body problem. Much of the work related to electron scattering deals with the charge form factor. Here, we shall concentrate on those aspects accessible via magnetic scattering. We shall mainly discuss ^{3}He, for which more accurate and much more extensive data are available. A discussion of ^{3}H will become more fruitful once the experiments on ^{3}H magnetic form factors, at present in progress at the Bates and Saclay accelerators, are carried out. Theoretical calculations concerning differences between ^{3}H and ^{3}He can be found in Villars (1947), Schiff (1964), Gibson (1965), Kloet and Tjon (1971), Harper *et al.* (1972), Barroso and Hadjimichael (1975), Bornais (1981), and Hajduk *et al.* (1983).

The pioneering experiment on both helium and tritium was performed by Collard and collaborators (1965) at Stanford. Using sealed gas targets, cylinders 20 cm long filled to a pressure of 230 atm, this group measured cross sections between 100 and 680 MeV energy and 40°—135° scattering angle. From these data the magnetic form factors in the Q range 1—2.8 fm^{-1} were extracted. The magnetic form factors obtained showed an exponentially falling tendency as a function of Q^2, similar to what was found for the charge form factors (see Fig. 59). The data were extended to higher momentum transfer by McCarthy *et al.* (1970), who used a liquid-^{3}He target 2 cm long, cooled to 1.8 K. Data were taken at energies 200—750 MeV, and $\theta=30°-145°$. The main emphasis of this experiment was the charge form factor (McCarthy *et al.*, 1977); the resulting $F_{\rm ch}(Q)$ showed the diffraction feature that has received so much attention since. For magnetic scattering, the experiment produced form factors (other than upper limits) up to $Q=3.5$ fm^{-1}. Within the error bars, F_M continued to fall smoothly, in agreement with theoretical predictions (ignoring S-D interferences and MEC) of the time. The subsequent impulse approximation predictions including the S-D term produced a diffraction minimum not present in the data.

The next major experiment devoted to magnetic scattering was that of Cavedon *et al.* (1982), performed at Saclay. Using a gas target with 12-atm pressure cooled to liquid-hydrogen temperature (22 K), the experimentors were able to increase substantially the product of target density times maximum electron current (40 μA). With the gas-cell windows not visible to the spectrometer, the measurements could be pushed to very small cross section, 2×10^{-38} cm^2/sr. With the maximum accelerator energy of 700 MeV and $\theta=155°$, a momentum transfer of $Q=5.6$ fm^{-1} was reached. This experiment discovered

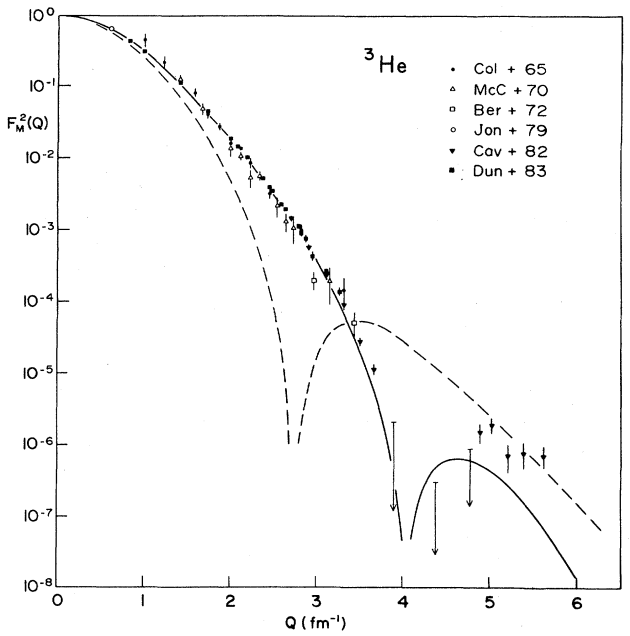

FIG. 59. The ^{3}He data (with reasonably small error bars), compared to the prediction of Maize and Kim (1983) for impulse approximation (dashed curve) and impulse approximation plus MEC (solid curve). See Table III for a listing of the data.

the diffraction feature predicted by the theory that includes MEC.

The experiment of Dunn *et al.* (1983) was performed at the Bates accelerator. Using a ^{3}He gas target, 15-atm pressure, and 80-K temperature, measurements were carried out at energies from 60 to 350 MeV and $\theta=60°-160°$. This experiment greatly increased the accuracy of data in the Q range 0.8—3.4 fm^{-1}. The form factors measured in these experiments, together with isolated points produced by others (Bernheim *et al.*, 1972; Jones *et al.*, 1979) are shown in Fig. 59. The data are plotted in terms of the form factor traditionally used for $M1$, $F^2=F_T^2\times 8\pi M_N^2/q^2\mu^2$ [with $F(0)=1$]. In order not to clutter the picture, we have omitted data points that have rather large error bars. In the following figures, we shall show only the most recent data sets, the ones measured at Bates and Saclay.

One feature of the data perhaps needs explaining: the diffraction minimum, in the region $Q=4-4.5$ fm^{-1}, is poorly defined. In this region, the charge form factor (McCarthy *et al.*, 1970) has its diffraction maximum; experiments carried out at $\theta\neq180°$ (imperative in order to eliminate the large contribution of quasielastic electron-window scattering) will thus mainly measure $F_{\rm ch}$ and produce large error bars for F_M.

The theoretical interpretation of the $A=3$ form factors has received extensive attention, starting with the first experiment (Schiff *et al.*, 1963; Schiff, 1964). While the emphasis initially was put on phenomenological analyses, more and more calculations using sophisticated wave functions were published (Sarker, 1964; Gibson, 1965; Tjon *et al.*, 1970; Malfliet and Tjon, 1971; Yang and

Jackson, 1971; Hennel and Delves, 1971). Much of this work, however, ignored the fact that, besides the diagonal contributions of S and D states (the only ones to occur in charge scattering), the magnetic form factor also receives a contribution from the S-D interference term. The presence of this contribution was already realized in some of the earliest work (Schiff, 1964; Gibson, 1965), where the close connection of the interference term to MEC was alluded to as well. In most of the subsequent work this term was omitted, and only the calculation of Brandenburg *et al.* (1974) showed its numerical importance and the striking change of F_M this S-D interference produces.

The presence of this S-D term gives F_M a character quite different from that seen in F_{ch}. The latter at large Q is dominated by the short-range properties of the S-state wave function, which are still rather uncertain. The magnetic form factor is given at large Q by the S-D term, which is dominated by the better known medium-range properties.

Today, a number of calculations for the three-body magnetic form factor are available. Figures 59—61 show some of the results. The prediction of Maize and Kim (1983) is obtained using the wave function of Brandenburg *et al.* (1974), and that in turn is obtained by solving the Faddeev equation in momentum space for the Reid soft-core potential. The form factor of Strueve *et al.* (1983) is calculated from a solution of the Faddeev equations for the nucleon-delta coupled-channel system and the Reid soft-core or Paris NN interaction. Torre *et al.* (1981) solve the Faddeev equations in configuration space for the de Tourreil—Sprung super soft-core (SSC) interaction. The impulse approximation results for the calculations shown in Figs. 59 and 61 agree quite closely. Some dependence on the nucleon-nucleon interaction used emerges: the Reid soft-core potential, for example, gives a value of F^2 in the maximum, which is $\sim 30\%$ larger than for the Paris potential.

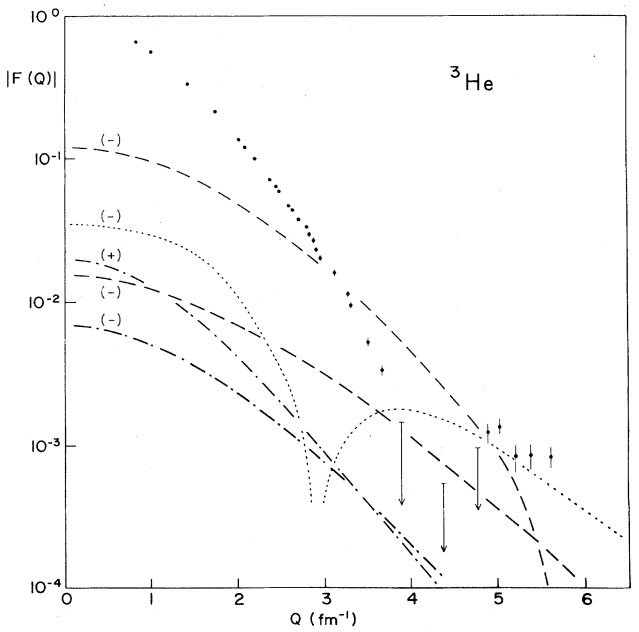

FIG. 60. Meson-exchange current contributions to ^{3}He form factor calculated by Strueve *et al.* (1983): pionic pair (dashed, upper curve), pionic current (dashed, lower curve), ρ pair current (dotted-dashed curves), and full Δ contribution (dotted curve).

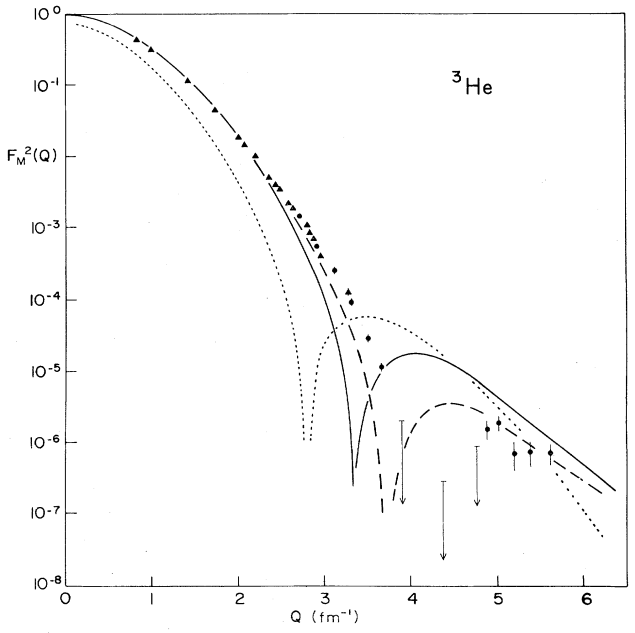

FIG. 61. ^{3}He data of Cavedon *et al.* (1982) and Dunn *et al.* (1983) compared to predictions of Strueve *et al.* (1983) obtained using G_E (solid curve), F_1 (dashed curve), and without MEC (dotted curve).

The importance of meson-exchange currents for the magnetic properties of ^{3}He has been known since the early calculation of Villars (1947), who found that the isovector magnetic moment receives $\sim 15\%$ contribution from MEC. Much of the development of MEC theory (Chemtob and Rho, 1971) actually is linked to this question of the $A=3$ magnetic moments (Kuroboshi and Hara, 1958; Rho, 1970; Horikawa *et al.*, 1972; Hadjimichael *et al.*, 1972; Ichimura *et al.*, 1972; Gerstenberger and Nogami, 1972; Green and Schucan, 1972). Using a realistic wave function, obtained from a Faddeev calculation, Harper *et al.* (1972) found that the discrepancy between the nucleon-only prediction and experimental magnetic moments could be quantitatively understood. Harper *et al.* (1972) showed, in particular, that the S-D matrix elements were important for MEC as well, especially for diagrams involving the delta.

The magnetic form factor at large Q was calculated by Kloet and Tjon (1971) using Faddeev wave functions. Although still done without the S-D term, this calculation pointed out the increasing importance of MEC at large Q. Subsequent calculations (Hadjimichael and Barroso, 1973; Barroso and Hadjimichael, 1975) involving additional refinements, were mostly carried out using more phenomenological wave functions.

A systematic investigation of the role played by dif-

ferent ingredients entering the calculation of MEC contributions has been performed by Riska (1980). For this work a phenomenological Irving wave function was used; in order to assess properly the sensitivity to short-range MEC, a wave function with a sensible short-range behavior was selected. Riska found that the total form factor is not very sensitive to the D-state probability; the S-D impulse approximation contribution and the MEC effect largely cancel [in analogy with deuteron electrodisintegration at threshold (Hockert *et al.*, 1973)]. The total ρ-exchange contribution shifts the diffraction minimum only by ~ 0.2 fm^{-1}, although individual pieces involving the ρ have a large effect. Interestingly, for ^{3}He the ρ contribution goes in the same direction as the pion exchange effects; ordinarily, the ρ has the effect of cutting down the π contribution at large q. The strong vertex form factors turn out to be quite important, even though only monopole form factors with large cutoff masses were employed. When passing from a cutoff mass $\Lambda = 1200$ MeV to $\Lambda = 2000$ MeV the diffraction minimum shifts by 0.5 fm^{-1}; more realistic (smaller) Λ's would lead to larger changes.

The contribution of diagrams involving the Δ can be included in the standard perturbation way (see Sec. IV.E). In the case of ^{3}He, the wave function is still simple enough to make a coupled-channel calculation for nucleon and Δ components feasible. This has been done by Strueve *et al.* (1983), who calculate the N,Δ wave functions by solving the coupled Faddeev equations in momentum space. The total Δ effect, the sum due to polarization of the nucleonic wave function plus diagonal and nondiagonal Δ pieces, differs considerably from the perturbative calculations. In particular, the Δ effect at large momentum transfer, $Q > 5$ fm^{-1}, becomes the dominant MEC contribution.

In order to show the relative size of the different MEC pieces discussed above, Fig. 60 gives the individual contributions to $F_M(q)$ as calculated by Strueve *et al.* (1983). The data are displayed only in order to indicate where the relative MEC contributions are large. Recent work has shown that current conservation plays an important role in the calculation of MEC. The electromagnetic form factors appearing in the one-body and two-body pieces have to be the same if current conservation is to be respected. Given the fact that the electric form factors G_E are used in the one-body form factors, G_E (rather than F_1) should be used in the MEC calculation as well. It has been pointed out by Strueve *et al* (1983) and Maize and Kim (1983) that this has important consequences for the calculation of the ^{3}He form factor at large q; this is demonstrated by Fig. 61. It is important to respect current conservation, since this very law was the major reason for introducing MEC in the first place.

The importance of using G_E rather than F_1 points out that relativistic corrections to the standard MEC operators are non-negligible. Mathiot and Riska (1983) recently derived these for one particular case, the pair diagram for deuteron electrodisintegration. They showed that for this particular case, the relativistic corrections produce an additional term of the same size as the difference of F_1 and G_E; this term goes in the same direction (Maize and Kim, 1984) as the replacement of F_1 by G_E, and makes agreement with experiment even worse (see below). As already remarked in the section on the deuteron, the relativistic effects in MEC need further study. Relativistic effects in the wave function clearly must also be understood to the same order in Q/M_N.

In Figs. 59 and 61 we show the predictions of two recent calculations for F_M, those of Maize and Kim (1983) and Strueve *et al.* (1983). The former use the Faddeev wave function of Brandenburg *et al.* (1974), calculated for the Reid soft-core NN interaction. Strueve *et al.* (1983) solve the coupled N/Δ Faddeev equations for the Paris potential. Both use G_E for the calculation of MEC, but the curves obtained by Maize and Kim do not include strong-vertex form factors that would cut down the MEC contribution at large momentum transfer (see Maize and Kim, 1983). Additional calculations, using F_1 rather than G_E, can be found in Hadjimichael *et al.* (1983). In view of the ambiguities still present in the treatment of MEC—particularly as concerns relativistic effects and uncertainty in strong-vertex form factors—the agreement between prediction and experiment, while qualitatively satisfactory, is not quantitatively as good as one could hope for. Given the very large effect of MEC on the ^{3}He magnetic form factor, further study of this observable should help to eliminate some of the questions that are still open.

To conclude this section, we should like to point out a few topics that will become important in the future. The first is the measurement of data for ^{3}H at high momentum transfer. We have not discussed ^{3}H above, since the existing set of data is very limited; it will be most important to change this, and to explore the features predicted by theoretical calculations concerning the difference between ^{3}H and ^{3}He. A determination of both form factors would allow a separation into isoscalar and isovector contributions. The isovector form factor would allow us to study in a very clean way the dominating MEC diagrams. The isoscalar form factor would represent an ideal complement to that for the deuteron; the higher densities present in $A = 3$ would allow the study of short-range exchange phenomena hardly accessible in the deuteron.

An extension of the data for $B(Q)$ to higher momentum transfer also is of high priority. The $B(Q)$ is predicted (Gari *et al.*, 1976) to flatten out at large Q, as a consequence of the S-state diffraction maximum and the contribution of the $\pi\rho\gamma$ exchange term. The cross sections predicted are large enough to be measured once high-intensity electron beams of energy > 700 MeV are available. The features offered by the use of electron and recoil nucleus polarization (see Sec. VIII) are most promising; amplitudes that are generally difficult to isolate can be measured as interference terms. Experiments exploiting these ideas can be performed once CW beams of appropriate energy, as planned for the CEBAF facility and others, become a reality. Once this high-Q region becomes accessible, then a topic not touched upon in this review—the role of quark degrees of freedom—will re-

ceive a great deal of attention. For light nuclei and large Q, this topic is certainly very relevant. The currents observed in magnetic electron scattering can be expected to depend sensitively on the submesonic degrees of freedom; for instance, even in the absence of believable theoretical predictions, an extrapolation from what we already know about the important role played by MEC suggests that the results observed under these conditions will be sensitive probes at the microscopic level. This topic will be a major frontier of, among other fields of study, magnetic electron scattering.

VIII. POLARIZATION IN ELASTIC ELECTRON SCATTERING ▲

In this section we discuss the special problem of elastic scattering from nuclei, with nucleus and/or electron polarized. This topic has received little attention in the past (Weigert and Rose, 1964; Gourdin and Piketty, 1964; Schildknecht, 1965; Arnold *et al.*, 1981). Only two experiments for $A > 1$, electron scattering from a polarized holmium target (Uhrhane *et al.*, 1971; Ravenhall and Mercer, 1976), and elastic scattering from the deuteron with a measurement of the recoil deuteron vector polarization (Prepost *et al.*, 1968), have been published. Here, we include a discussion of polarization, since progress in experimental techniques will make feasible the use of polarization in electron-nucleus scattering. The additional information accessible via polarization observables renders this new tool most valuable, and justifies a large effort in this direction.

In analogy with hadron-nucleus scattering, one might expect the "obvious" polarization experiment to be the one in which polarized electrons are scattered off an unpolarized target, in order to measure the analyzing power. Experimentally, this is the easiest observable to measure, given the fact that intense sources of polarized electrons today are available (Prescott *et al.*, 1978). Unfortunately, for single-arm scattering, this type of experiment does not produce any new information. At the energies of interest for nuclear physics, electrons are ultrarelativistic ($\varepsilon,\varepsilon' \gg m_e$), the electron helicity is conserved, and the scattering cross section is independent of electron orientation (provided we take parity conservation for granted). New information is obtained only once target or recoil nucleus polarization observables are measured. Then incoherent mixtures of form factors can be separated, and small form factors can be measured through their interferences with large ones.

Two developments in experimental techniques point to an increase in the importance of polarization in the future: (1) The construction of CW facilities with high beam intensity makes coincidence experiments orders of magnitude easier than in the past; experiments involving the analysis of the recoil nucleus polarization then become feasible. (2) The construction of stretcher rings will allow experiments using internal targets in the form of polarized atomic beams; the high intensity of internal electron beams produces luminosities that approach those needed to do electron scattering experiments over extended ranges of momentum transfer.

A. Formalism

The formalism and calculations summarized here are taken from a more general treatment of the problem (Donnelly, 1983; Donnelly and Raskin, 1984), in which both elastic and inelastic electron scattering involving discrete nuclear states were discussed. Here, we allow for two situations for the electron spin: (1) where the electrons are unpolarized and (2) where the incident electron beam is assumed to be longitudinally polarized. We discuss only the extreme relativistic limit ($\varepsilon,\varepsilon' \gg m_e$), and so the incident electrons are assumed to have specific helicities $h = \pm 1$. The helicities of the scattered electrons are summed over. The more general situation of arbitrary initial and/or final electron polarizations is discussed by Donnelly and Raskin (1984). For the nuclear spin we also allow for two cases: (1) initial nucleus polarized and recoil nucleus spins summed over, and (2) initial nucleus unpolarized, recoil nucleus spin orientation measured.

The electron scattering cross section may be written

$$\left[\frac{d\sigma}{d\Omega}\right]_{fi}^{h} = \Sigma_{fi} + h\Delta_{fi} , \tag{8.1}$$

where fi refers to a transition from the initial state labeled i to a final state labeled f. Here, Σ_{fi} is the electron-spin-averaged cross section

$$\Sigma_{fi} = \frac{1}{2}\left[\left[\frac{d\sigma}{d\Omega}\right]_{fi}^{+1} + \left[\frac{d\sigma}{d\Omega}\right]_{fi}^{-1}\right] , \tag{8.2}$$

and Δ_{fi} is the electron polarization cross section

$$\Delta_{fi} = \frac{1}{2}\left[\left[\frac{d\sigma}{d\Omega}\right]_{fi}^{+1} - \left[\frac{d\sigma}{d\Omega}\right]_{fi}^{-1}\right] . \tag{8.3}$$

In the single-photon exchange or first Born approximation it may be shown that the cross sections take on the forms (Donnelly, 1983; Donnelly and Raskin, 1984)

$$\Sigma_{fi} = \sigma_M f_{\rm rec}^{-1}(v_L R_{fi}^{L} + v_T R_{fi}^{T} + v_{TT} R_{fi}^{TT} + v_{TL} R_{fi}^{TL}) , \tag{8.4}$$

$$\Delta_{fi} = \sigma_M f_{\rm rec}^{-1}(v'_T R_{fi}^{T'} + v'_{TL} R_{fi}^{TL'}) . \tag{8.5}$$

The six electron kinematic factors are given by

$$v_L = (Q^2/q^2)^2 , \tag{8.6}$$

$$\begin{cases} v_T = \frac{1}{2}(Q^2/q^2) + \tan^2\dfrac{\theta}{2} , \\ v'_T = \left[(Q^2/q^2) + \tan^2\dfrac{\theta}{2}\right]^{1/2} \tan\dfrac{\theta}{2} , \\ v_{TT} = -\frac{1}{2}(Q^2/q^2) , \end{cases} \tag{8.7}$$

$$\begin{cases} v_{TL} = -\frac{1}{\sqrt{2}}(Q^2/q^2)\left[(Q^2/q^2)+\tan^2\frac{\theta}{2}\right]^{1/2} , \\ v'_{TL} = -\frac{1}{\sqrt{2}}(Q^2/q^2)\tan\frac{\theta}{2} . \end{cases} \tag{8.8}$$

The first two are the usual factors occurring in the Rosenbluth formula; v_{TT} and v_{TL} also occur in studying coincidence reactions [$(e,e'x)$; see, for example, Donnelly, 1983, Sec. 6]; v'_T and v'_{TL} are peculiar to polarized electron scattering.

Typically for elastic electron scattering at high momentum transfer, $Q^2/q^2 \approx 1$ and so, even at rather high energies and forward electron scattering angles, v_L, v_T, v_{TT}, and v_{TL} are all of order unity. On the other hand, if θ is very small (and ε very large so that q is fixed), then v'_T and v'_{TL} will be suppressed by the multiplying factor $\tan(\theta/2)$ [see Eqs. (8.7) and (8.8)], and so the overall effect of Δ_{fi} will be diminished.

The nuclear structure physics is then contained in the remaining nuclear response functions defined by

$$\begin{aligned} R_{fi}^{L} &\equiv |\rho(\mathbf{q})_{fi}|^2 , \\ R_{fi}^{T} &= |J(\mathbf{q};+1)_{fi}|^2 + |J(\mathbf{q};-1)_{fi}|^2 , \\ R_{fi}^{TT} &\equiv 2\,\mathrm{Re}[J(\mathbf{q};+1)^*_{fi}J(\mathbf{q};-1)_{fi}] , \\ R_{fi}^{TL} &\equiv -2\,\mathrm{Re}\{\rho(\mathbf{q})^*_{fi}[J(\mathbf{q};+1)_{fi} - J(\mathbf{q};-1)_{fi}]\} , \\ R_{fi}^{T'} &\equiv |J(\mathbf{q};+1)_{fi}|^2 - |J(\mathbf{q};-1)|^2 , \\ R_{fi}^{TL'} &= -2\,\mathrm{Re}\{\rho(\mathbf{q})^*_{fi}[J(\mathbf{q};+1)_{fi} + J(\mathbf{q};-1)_{fi}]\} . \end{aligned} \tag{8.9}$$

Here J^μ is the Fourier transform of the nuclear electromagnetic four-vector current density for the transition $i \to f$, and we employ spherical vector projections labeled ± 1, defined in the standard way [see Donnelly (1983), Sec. 5, for details]. Throughout we employ the coordinate system shown in Fig. 62, where the z axis is along $\mathbf{q}$ and the electron scattering occurs in the xz plane. Conservation of the nuclear electromagnetic current has been used in obtaining the above results. Thus far we have not invoked any detailed knowledge of the nuclear states involved, but we shall in the following.

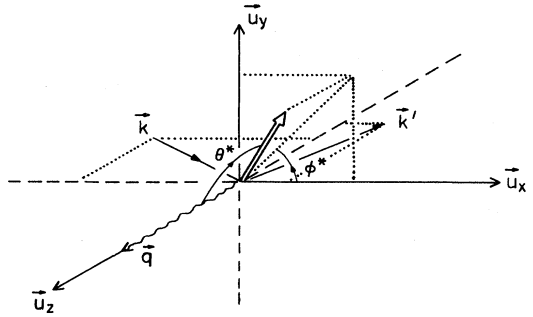

FIG. 62. Orientation of the nuclear polarization axis and definition of the electron scattering coordinate system. The incident electron of momentum $\mathbf{k}$ and scattered electron of momentum $\mathbf{k}'$ define the xz scattering plane with momentum transfer $\mathbf{q}$ in the z direction and with $\mathbf{u}_q = \mathbf{k}\times\mathbf{k}'/|\mathbf{k}\times\mathbf{k}'|$ as a unit vector normal to the scattering plane.

Now let us focus on elastic electron scattering in which $J_i = J_f \equiv J_0$ and $\pi_i = \pi_f = \pi_0$. Furthermore, let us assume that the initial state is polarized (i.e., the nuclear target is polarized whether or not the electron is polarized). In other words, the target is prepared with its magnetic substates labeled M_{J_0} populated in a nonuniform manner with probabilities $p_{(i)}(M_{J_0})$. An unpolarized target then has $p_{(i)}(M_{J_0}) = (2J_0+1)^{-1}$. In fact, because it is more convenient in what follows to work with spherical tensors, we define the Fano tensors by

$$f^{(i)}_{\mathscr{J}} \equiv \sum_{M_{J_0}} (-)^{J_0 - M_{J_0}} \langle J_0 M_{J_0} J_0 - M_{J_0} | (J_0 J_0) \mathscr{J} 0 \rangle \times p_{(i)}(M_{J_0}) . \tag{8.10}$$

In particular, $f^{(i)}_0 = 1/(2J_0+1)^{1/2}$, regardless of the detailed population of the magnetic substates. Frequently we shall be interested in the situation where $p_{(i)}(M_{J_0} = +J_0) = 1$ and all other probabilities equal 0 (100% polarization), in which case

$$f^{(i)}_{\mathscr{J}} = \frac{(2J_0)!\sqrt{2\mathscr{J}+1}}{[(2J_0+1+\mathscr{J})!(2J_0-\mathscr{J})!]^{1/2}} . \tag{8.11}$$

We may now make use of multipole expansions of the nuclear current matrix elements involving the basic multipole operators (see Sec. IV),

$$\begin{aligned} \hat{M}^{\mathrm{Coul}}_{JM_J}(q) &\equiv \int d\mathbf{x}\, M_J^{M_J}(q\mathbf{x})\hat{\rho}(\mathbf{x}) , \\ \hat{T}^{\mathrm{mag}}_{JM_J}(q) &\equiv \int d\mathbf{x}\, \mathbf{M}_{JJ}^{M_J}(q\mathbf{x})\cdot\hat{\mathbf{J}}(\mathbf{x}) , \end{aligned} \tag{8.12}$$

defined in the standard way. However, in contrast to the situation in which no nuclear polarizations are involved, here, where the initial nuclear polarization is specified, the developments are considerably more complicated [a full treatment of this problem, including situations when initial nuclear polarization, final nuclear (recoil) polarization, or both are specified, is given by Donnelly and Raskin (1984)].

Now it may be shown for the case of a polarized target with no final nuclear polarization measured (indicated by fi) that

$$\begin{aligned} R^L_{fi} &= 4\pi \sum_{\substack{\mathscr{J}\geq 0 \\ \text{even}}} f^{(i)}_{\mathscr{J}} P_{\mathscr{J}}(\cos\theta^*) W^L_{\mathscr{J}}(q)_{fi} , \\ R^T_{fi} &= 4\pi \sum_{\substack{\mathscr{J}\geq 0 \\ \text{even}}} f^{(i)}_{\mathscr{J}} P_{\mathscr{J}}(\cos\theta^*) W^T_{\mathscr{J}}(q)_{fi} , \\ R^{TT}_{fi} &= 4\pi \sum_{\substack{\mathscr{J}\geq 2 \\ \text{even}}} f^{(i)}_{\mathscr{J}} P^2_{\mathscr{J}}(\cos\theta^*)\cos 2\phi^* W^{TT}_{\mathscr{J}}(q)_{fi} , \\ R^{TL}_{fi} &= 4\pi \sum_{\substack{\mathscr{J}\geq 2 \\ \text{even}}} f^{(i)}_{\mathscr{J}} P^1_{\mathscr{J}}(\cos\theta^*)\cos\phi^* W^{TL}_{\mathscr{J}}(q)_{fi} , \end{aligned} \tag{8.13}$$

where only tensors of even rank occur in the terms which contribute to Σ_{fi}, and

$$R_{fi}^{T'}=4\pi\sum_{\substack{\mathscr{J}\geq 1\\ \text{odd}}} f_{\mathscr{J}}^{(i)}P_{\mathscr{J}}(\cos\theta^*)W_{\mathscr{J}}^{T'}(q)_{fi}\ ,$$

$$R_{fi}^{TI'}=4\pi\sum_{\substack{\mathscr{J}\geq 1\\ \text{odd}}} f_{\mathscr{J}}^{(i)}P_{\mathscr{J}}^{1}(\cos\theta^*)\cos\phi^*W_{\mathscr{J}}^{TL'}(q)_{fi}\ , \tag{8.14}$$

where only odd-rank tensors contribute to Δ_{fi}. The angles (θ^*,ϕ^*) refer to the axis along which the target M-state populations have been specified, so that, for example, the f's in Eq. (8.11) are to be used if the target is polarized with $M_{J_0}=+J_0$ in the direction (θ^*,ϕ^*). These angles are given with respect to the momentum transfer direction **q** (see Fig. 62).

The W's now contain the nuclear structure information in the form of bilinear products of the ground-state Coulomb and magnetic multipole matrix elements. Thus W^L contains only Coulomb matrix elements together with the interferences between CJ and CJ' multipoles; W^T, W^{TT}, and $W^{T'}$ contain only magnetic multipoles with MJ/MJ' interferences in general; finally W^{TL} and $W^{TL'}$ contain Coulomb-magnetic interferences, CJ/MJ'. In all cases only interfering multipoles satisfying $|J'-J|\leq\mathscr{J}\leq J'+J$ are permitted. Furthermore, $0\leq\mathscr{J}\leq 2J_0$ for this case of polarized targets.

To display the complete (θ^*,ϕ^*) dependence of the cross sections and to separate this dependence from their (q,θ) behavior, it is useful to rewrite Eqs. (8.4) and (8.5) in the form

$$\Sigma_{fi}\equiv\Sigma_0\left[1+\sum_{\substack{\mathscr{J}\geq 2\\ \text{even}}}\left[P_{\mathscr{J}}(\cos\theta^*)R_{\mathscr{J}}^{0}(q,\theta)_{fi}+P_{\mathscr{J}}^{1}(\cos\theta^*)\cos\phi^*R_{\mathscr{J}}^{1}(q,\theta)_{fi}+P_{\mathscr{J}}^{2}(\cos\theta^*)\cos 2\phi^*R_{\mathscr{J}}^{2}(q,\theta)_{fi}\right]\right]\ , \tag{8.15}$$

$$\Delta_{fi}\equiv\Sigma_0\left[\sum_{\substack{\mathscr{J}\geq 1\\ \text{odd}}}\left[P_{\mathscr{J}}(\cos\theta^*)R_{\mathscr{J}}^{0}(q,\theta)_{fi}+P_{\mathscr{J}}^{1}(\cos\theta^*)\cos\phi^*R_{\mathscr{J}}^{1}(q,\theta)_{fi}\right]\right]\ , \tag{8.16}$$

where

$$\Sigma_0\equiv\left[\frac{d\sigma}{d\Omega}\right]^{\text{unpolarized}}=4\pi\sigma_M f_{\text{rec}}^{-1}F^2(q,\theta)\ , \tag{8.17}$$

with

$$F^2(q,\theta)=f_0^{(i)}[v_L W_0^L(q)_{fi}+v_T W_0^T(q)_{fi}]$$
$$=v_L F_L^2(q)+v_T F_T^2(q)\ , \tag{8.18}$$

the usual unpolarized (e,e') elastic form factor with its longitudinal and transverse pieces, F_L^2 and F_T^2, respectively. The quantities $R_{\mathscr{J}}^{\mathscr{M}}(q,\theta)_{fi}$, the tensor polarizations, are then given by, for $\mathscr{J}$ even,

$$R_{\mathscr{J}}^{0}(q,\theta)_{fi}=f_{\mathscr{J}}^{(i)}[v_L W_{\mathscr{J}}^{L}(q)_{fi}+v_T W_{\mathscr{J}}^{T}(q)_{fi}]/F^2(q,\theta)\ ,$$
$$R_{\mathscr{J}}^{1}(q,\theta)_{fi}=f_{\mathscr{J}}^{(i)}v_{TL}W_{\mathscr{J}}^{TL}(q)_{fi}/F^2(q,\theta)\ , \tag{8.19a}$$
$$R_{\mathscr{J}}^{2}(q,\theta)_{fi}=f_{\mathscr{J}}^{(i)}v_{TT}W_{\mathscr{J}}^{TT}(q)_{fi}/F^2(q,\theta)\ ,$$

and for $\mathscr{J}$ odd,

$$R_{\mathscr{J}}^{0}(q,\theta)_{fi}=f_{\mathscr{J}}^{(i)}v_T' W_{\mathscr{J}}^{T'}(q)_{fi}/F^2(q,\theta)\ ,$$
$$R_{\mathscr{J}}^{1}(q,\theta)_{fi}=f_{\mathscr{J}}^{(i)}v_{TL}' W_{\mathscr{J}}^{TL'}(q)_{fi}/F^2(q,\theta)\ . \tag{8.19b}$$

The above equations apply for the case where the target is polarized and the recoil nucleus polarization summed over. A second case of interest is that in which the target is unpolarized but the recoil nucleus polarization measured. This case, denoted by $f\hat{i}$, is very closely related to that discussed above, and simple relationships exist between the response functions in the two cases (elastic electron scattering):

$$R_{f\hat{i}}^{K}=\pm R_{fi}^{K}\ , \tag{8.20}$$

with similar relationships for the W's [see Eqs. (8.13) and (8.14)], where the plus sign occurs for $K=L$, T, TT, and TL' and the minus sign for $K=TL$ and T'. Thus all of the above analysis applies (up to a sign) whenever either initial or final nuclear polarizations are specified. In the situation when the final-state recoil polarization is measured, it is convenient to express the cross section in terms of analyzing powers and polarization tensors. The latter are given in terms of the quantities discussed in the present work by

$$t_{\mathscr{J}\mathscr{M}}(J_0)=\frac{(-)^{\mathscr{M}}R_{\mathscr{J}}^{\mathscr{M}}(q,\theta)_{f\hat{i}}}{[J_0]f_{\mathscr{J}}^{(f)}}\times\begin{cases}1, & \mathscr{M}=0,\ 0\leq\mathscr{J}\leq 2J_0\\ \frac{1}{2}\sqrt{\mathscr{J}(\mathscr{J}+1)}, & \mathscr{M}=1,\ 1\leq\mathscr{J}\leq 2J_0\\ \frac{1}{2}\sqrt{(\mathscr{J}-1)\mathscr{J}(\mathscr{J}+1)(\mathscr{J}+2)}, & \mathscr{M}=2,\ 2\leq\mathscr{J}\leq 2J_0\ .\end{cases} \tag{8.21}$$

We shall return to an example where these are used (viz., the deuteron) a little later.

If both initial and final nucleus polarizations are specified then the analysis is somewhat more complicated [see Donnelly and Raskin (1984)]. Perhaps the most obvious case of interest of this last type would be a vector-polarized deuterium target with the vector polarization of the recoiling deuterons in elastic scattering measured to obtain information that presently can only be accessed by use of a tensor-polarized target or measurement of a recoil tensor polarization.

Let us now return to explicit expressions for the reduced response functions $W^K_{\mathscr{J}}(q)_{fi}$, $K=L$, T, TT, TL, T', and TL'. Let us define the elastic form factors by

$$F_J(q)\equiv\frac{1}{[J_0]}\times\begin{cases}\langle J_0||\hat{M}^{\rm Coul}_J(q)||J_0\rangle, & J=\text{even}\\ \langle J_0||i\hat{T}^{\rm mag}_J(q)||J_0\rangle, & J=\text{odd}\ .\end{cases}\tag{8.22}$$

This agrees with the usage in Sec. IV, but additionally yields real quantities (once time-reversal invariance is invoked) and constitutes a specific choice of sign convention. Then we may write

$$W^K_{\mathscr{J}}(q)_{fi}=\sum_{J'J}A^K_{J'J;\mathscr{J}}(J_0)F_{J'}(q)F_J(q)\ ,\tag{8.23}$$

where, of course, only the appropriate even- or odd-J multipole form factors occur:

$K=L$: $J'=$even, $J=$even

$K=T,TT,T'$: $J'=$odd, $J=$odd

$K=TL,TL'$: $J'=$even, $J=$odd .

The expansion coefficients may be expressed in the form (Donnelly and Raskin, 1984)

$$A^K_{J'J;\mathscr{J}}(J_0)=X_{J'J\mathscr{J}}(J_0)\times\begin{cases}\alpha_{J'J;\mathscr{J}}, & K=L\\ \beta^0_{J'J;\mathscr{J}}, & K=T,T'\\ \dfrac{2\sqrt{2}}{\sqrt{\mathscr{J}(\mathscr{J}+1)}}\beta^1_{J'J;\mathscr{J}}, & K=TL,TL'\\ \dfrac{1}{\sqrt{(\mathscr{J}-1)\mathscr{J}(\mathscr{J}+1)(\mathscr{J}+2)}}\beta^2_{J'J;\mathscr{J}}, & K=TT\ ,\end{cases}\tag{8.24}$$

where we have defined functions

$$X_{J'J\mathscr{J}}(J_0)\equiv(-)^{2J_0}[J_0]^2[J'][J][\mathscr{J}]\times\begin{Bmatrix}J' & J & \mathscr{J}\\ J_0 & J_0 & J_0\end{Bmatrix},\tag{8.25}$$

$$\alpha_{J'J;\mathscr{J}}\equiv(-)^{(1/2)(J'+J)}\begin{bmatrix}J & J' & \mathscr{J}\\ 0 & 0 & 0\end{bmatrix},\tag{8.26}$$

and

$$\beta^{\mathscr{M}}_{J'J;\mathscr{J}}\equiv(-)^{(1/2)(J'+J-\mathscr{M})}\begin{bmatrix}J & J' & \mathscr{J}\\ 1 & \mathscr{M}-1 & -\mathscr{M}\end{bmatrix},$$
$$\mathscr{M}=0,1,2 \text{ and } \mathscr{J}\geq\mathscr{M} \text{ only}\ .\tag{8.27}$$

From these definitions we see that X coefficients are completely symmetrical under permutations of J', J, and $\mathscr{J}$, and that $\alpha_{J'J;\mathscr{J}}$, $\beta^0_{J'J;\mathscr{J}}$, and $\beta^2_{J'J;\mathscr{J}}$ are symmetrical under interchange of J' and J (since only $J'=$odd, $J=$odd, $\mathscr{J}=$even enters for the TT term where $\mathscr{M}=2$). Thus the summation in Eq. (8.23) may be written

$$\sum_{J'J}(\ )=\sum_{J'=J}(\ )+2\sum_{J'<J}(\ )\tag{8.28}$$

for the L, T, TT, and T' cases.

B. Specific examples

Let us now turn from the general to the specific and look at a few examples.

(i) $J_0=0$

We recover only the usual unpolarized cross section

$$\Sigma_{fi}=\Sigma_0,\quad \Delta_{fi}=0\ .\tag{8.29}$$

(ii) $J_0=\frac{1}{2}$

Only $C0$ and $M1$ multipoles, respectively, can occur:

$$F_L(q)\equiv\frac{1}{\sqrt{2}}\langle\tfrac{1}{2}||\hat{M}^{\rm Coul}_0(q)||\tfrac{1}{2}\rangle\ ,\tag{8.30}$$

$$F_T(q)\equiv\frac{1}{\sqrt{2}}\langle\tfrac{1}{2}||i\hat{T}^{\rm mag}_1(q)||\tfrac{1}{2}\rangle\ .\tag{8.31}$$

Then we have, using Eq. (8.11),

$$f^{(i)}_0=f^{(i)}_1=\frac{1}{\sqrt{2}}$$

[we assume $p_{(i)}(M_{J_0}=+J_0)=1$]. In this case we find

$$\Sigma_{fi}=\Sigma_0\ ,$$
$$\Delta_{fi}=\Sigma_0[\cos\theta^*R^0_1(q,\theta)_{fi}+\sin\theta^*\cos\phi^*R^1_1(q,\theta)_{fi}]\ .\tag{8.32}$$

Using expressions (8.23)—(8.32), we obtain

$$\Delta_{fi}=-\Sigma_0[\cos\theta^*v'_T(F^2_T(q))+\sin\theta^*\cos\phi^*v'_{TL}(2F_L(q)F_T(q))]F^{-2}(q,\theta)\ .\tag{8.33}$$

With a polarized target and yet no electron polarization, one does not learn anything beyond the usual unpo-

larized (e,e') cross section. In cases where $|F_L(q)| \ll |F_T(q)|$ or $|F_L(q)| \gg |F_T(q)|$ the small form factor is hard to separate from the large one by using the usual Rosenbluth separation method [i.e., varying v_T for fixed q to separate $F_L^2(q)$ and $F_T^2(q)$ in Eq. (8.18)], as they occur as their squares. On the other hand, for polarized targets and polarized electrons, one may determine Δ_{fi}, which involves the interference $F_L(q)F_T(q)$ and hence is a much more sensitive probe of the small piece. A specific example is provided by the proton itself, where at high q $F_T(q)$ dominates over $F_L(q)$ (see Arnold *et al.*, 1981, for more discussion on this point).

We also note that if the target is aligned [i.e., $p_{(i)}(+M_{J_0})=p_{(i)}(-M_{J_0})$], then $f_{\mathscr{J}}^{(i)}=0$ for odd $\mathscr{J}$ and so the corresponding R's are zero [see Eqs. (8.19b)] and $\Delta_{fi}=0$. This is a general statement, true for arbitrary J_0 and not just $J_0=\frac{1}{2}$ as above. Of course, the situation considered in Eq. (8.11) is not an aligned one, and so the odd Fano tensors do not vanish.

(iii) $J_0=1$

The possible multipoles are now $C0$, $M1$, and $C2$, respectively,

$$F_0(q)\equiv\frac{1}{\sqrt{3}}\langle 1||\hat{M}_0^{\text{Coul}}(q)||1\rangle ,$$
$$F_1(q)\equiv\frac{1}{\sqrt{3}}\langle 1||i\hat{T}_1^{\text{mag}}(q)||1\rangle , \tag{8.34}$$
$$F_2(q)\equiv\frac{1}{\sqrt{3}}\langle 1||\hat{M}_2^{\text{Coul}}(q)||1\rangle ,$$

and we have for the unpolarized cross section,

$$\Sigma_0=4\pi\sigma_M f_{\text{rec}}^{-1}[v_L F_L^2(q)+v_T F_T^2(q)]$$

with

$$F_L^2(q)=F_0^2(q)+F_2^2(q) ,$$
$$F_T^2(q)=F_1^2(q) ,$$

and

$$F^2(q,\theta)=v_L F_L^2(q)+v_T F_T^2(q) . \tag{8.35}$$

Thus, with unpolarized scattering, only the sum of the squares of the $C0$ and $C2$ contributions may be determined, not the $C0$ and $C2$ pieces separately. With polarized targets, however, we have

$$\Sigma_{fi}=\Sigma_0\{1+[P_2(\cos\theta^*)R_2^0(q,\theta)_{fi}+P_2^1(\cos\theta^*)\cos\phi^* R_2^1(q,\theta)_{fi}+P_2^2(\cos\theta^*)\cos 2\phi^* R_2^2(q,\theta)_{fi}]\} , \tag{8.36}$$
$$\Delta_{fi}=\Sigma_0[P_1(\cos\theta^*)R_1^0(q,\theta)_{fi}+P_1^1(\cos\theta^*)\cos\phi^* R_1^1(q,\theta)_{fi}] , \tag{8.37}$$

where, again using Eq. (8.11) in which $f_1^{(i)}=1/\sqrt{2}$ and $f_2^{(i)}=1/\sqrt{6}$,

$$R_2^0(q,\theta)_{fi}=-\left\{v_L\left[\sqrt{2}F_2\left[F_0+\frac{1}{2\sqrt{2}}F_2\right]\right]+v_T[\tfrac{1}{4}F_1^2]\right\}\Big/F^2(q,\theta) ,$$
$$R_2^1(q,\theta)_{fi}=v_{TL}\left[\frac{\sqrt{3}}{2}F_1F_2\right]\Big/F^2(q,\theta) ,$$
$$R_2^2(q,\theta)_{fi}=v_{TT}[\tfrac{1}{8}F_1^2]/F^2(q,\theta) , \tag{8.38}$$
$$R_1^0(q,\theta)_{fi}=-v_T'[\tfrac{3}{4}F_1^2]/F^2(q,\theta) ,$$
$$R_1^1(q,\theta)_{fi}=-v_{TL}'\left[\sqrt{6}F_1\left[F_0+\frac{1}{2\sqrt{2}}F_2\right]\right]\Big/F^2(q,\theta) .$$

Thus, for example, a measurement of R_2^0, either as here with polarized targets or by measuring the recoil polarization, together with the unpolarized longitudinal and transverse form factors, allows us to determine the $C0$ and $C2$ contributions separately. Note that these tensor moments may be separated by using the (θ^*,ϕ^*) dependence above. In particular, Σ_{fi} and Δ_{fi} may be separated using the dependence on the electron helicity $h=\pm 1$. Then R_1^0 and R_1^1 may be separated using either the θ^* dependence or the ϕ^* dependence or both. Likewise R_2^0, R_2^1, and R_2^2 may be separated from each other and from the unpolarized cross section.

For completeness, let us use Eq. (8.20) to convert these expressions to the forms appropriate for measurements of the recoil polarization (R_2^1 and R_1^0 change sign) and use Eq. (8.21) to obtain the polarization tensors for spin 1:

$$\begin{aligned} t_{00}(1)&=R_0^0=1 ,\\ t_{10}(1)&=\sqrt{2/3}R_1^0 ,\\ t_{11}(1)&=-\sqrt{1/3}R_1^1 ,\\ t_{20}(1)&=\sqrt{2}R_2^0 ,\\ t_{21}(1)&=-\sqrt{3}R_2^1 ,\\ t_{22}(1)&=2\sqrt{3}R_2^2 . \end{aligned} \tag{8.39}$$

Upon employing the following relationships between the F's as used here and the G's as used elsewhere,

$$\sqrt{4\pi}F_0=(1+\eta)G_c ,$$
$$\sqrt{4\pi}F_1=-\frac{2}{\sqrt{3}}\sqrt{\eta(1+\eta)}G_M , \tag{8.40}$$
$$\sqrt{4\pi}F_2=\frac{2\sqrt{2}}{3}\eta(1+\eta)G_Q ,$$

where $\eta\equiv(Q/4M_N)^2$, we obtain the usual expressions for the polarization tensors as applied to the case of elastic scattering from deuterium.[12]

[12]Note that the sign of t_{20} is reversed in Arnold *et al.* (1981), $t_{20}=+p_{zz}/\sqrt{2}$, and that the expression for t_{21} in Haftel *et al.* (1980) should be multiplied by $\sqrt{2/3}$. Both sets of authors use capital letters for the tensor polarization, whereas the Madison convention advocates the use of lower-case t's.

Let us briefly discuss the experimental situation for elastic scattering from the deuteron. Via Rosenbluth plots, the magnetic form factor F_{M1}^2 has been separated from the charge form factors $F_{C0}^2+F_{C2}^2$ (see Sec. VII.A). The $C0$ and $C2$ contributions, at large transfer, have not been separated. These two form factors contain very different pieces of physics, which one would like very much to measure individually.

The monopole form factor is expected to exhibit a diffraction minimum near $q\sim 4$–4.5 fm^{-1}, and a maximum at somewhat higher transfer (5–6 fm^{-1}). This diffraction feature is very sensitive to the short-range properties of the S-state wave function, a property well known from the $A=3,4$ charge form factors. The wave function at short range, in turn, is sensitive to the short-range S-wave N-N interaction and internal nucleon degrees of freedom. The quadrupole form factor at large q depends on the short-range properties of the D-state wave function, particularly in the region of the expected minimum ($q\sim 8$–11 fm^{-1}) and following maximum. In contrast to the long- and medium-range properties, these short-range properties are poorly known and represent the major gap in our understanding of the D-state wave function.

The existing measurements on $A(q)$ do not allow one to separate these two ingredients. The quadrupole form factor obscures the diffraction minimum of F_{C0}^2 completely. The diffraction maximum of F_{C0}^2 complicates the interpretation of $A(q)$ at large q in terms of the dominating contribution of F_{C2}^2. Measuring one of the tensor polarization observables mentioned above would allow one to separate the two ingredients.

A first experiment involving the measurement of tensor polarization observables is underway at the Bates accelerator. In Fig. 63 we show the first results, obtained using a low-duty-cycle accelerator, a water target, and a conventional ^{3}He$(\vec{d},p)$ polarimeter (Schulze *et al.*, 1984). The goal of future experiments of this type will be to reach the region $q\sim 4$ fm^{-1}, where a separation of $C0$ and $C2$ is most interesting. To achieve this, a high duty cycle, a liquid-deuterium target, and a polarimeter more appropriate for high-momentum deuterons (see, for example, Sick, 1984) will be needed.

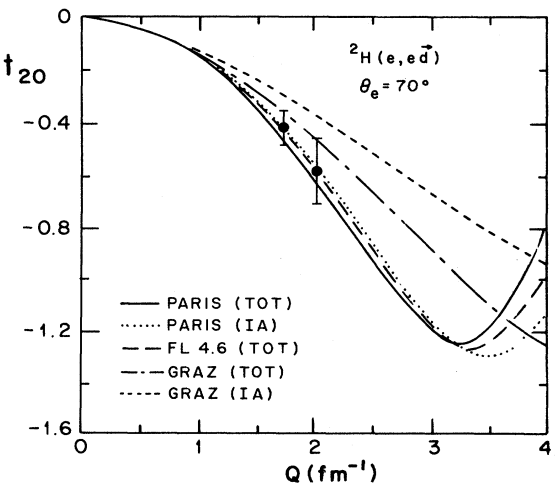

FIG. 63. The experimental results of Schulze *et al.* (1984) compared to predictions calculated using different models for the nucleon-nucleon potential. The curves labeled TOT include the contributions of MEC.

(iv) $J_0=\frac{3}{2}$

Turning now to a more complicated example, here we have multipoles $C0$, $M1$, $C2$, and $M3$, respectively:

$$\begin{aligned} F_0(q)&\equiv\tfrac{1}{2}\langle\tfrac{3}{2}||\hat{M}_0^{\rm Coul}(q)||\tfrac{3}{2}\rangle\ ,\\ F_1(q)&\equiv\tfrac{1}{2}\langle\tfrac{3}{2}||i\hat{T}_1^{\rm mag}(q)||\tfrac{3}{2}\rangle\ ,\\ F_2(q)&\equiv\tfrac{1}{2}\langle\tfrac{3}{2}||\hat{M}_2^{\rm Coul}(q)||\tfrac{3}{2}\rangle\ ,\\ F_3(q)&\equiv\tfrac{1}{2}\langle\tfrac{3}{2}||i\hat{T}_3^{\rm mag}(q)||\tfrac{3}{2}\rangle\ , \end{aligned} \tag{8.41}$$

and form factors

$$\begin{aligned} F_L^2(q)&=F_0^2(q)+F_2^2(q)\ ,\\ F_T^2(q)&=F_1^2(q)+F_3^2(q)\ . \end{aligned} \tag{8.42}$$

Using Eq. (8.11), we obtain the Fano tensors $f_1^{(i)}=3/2\sqrt{5}$, $f_2^{(i)}=\frac{1}{2}$, and $f_3^{(i)}=1/2\sqrt{5}$. The cross section Σ_{fi} takes the same form as in the previous example, except now with

$$\begin{aligned} R_2^0(q,\theta)_{fi}&=-\{v_L[2F_0F_2]+v_T[\tfrac{2}{5}(F_1+\sqrt{3/2}F_3)^2]\}/F^2(q,\theta)\ ,\\ R_2^1(q,\theta)_{fi}&=v_{TL}\left[\frac{2}{\sqrt{5}}F_2(F_1-\sqrt{2/3}F_3)\right]\Big/F^2(q,\theta)\ ,\\ R_2^2(q,\theta)_{fi}&=v_{TT}\left[\frac{1}{5}\left[F_1^2-F_3^2+\frac{1}{\sqrt{6}}F_1F_3\right]\right]\Big/F^2(q,\theta)\ . \end{aligned} \tag{8.43}$$

The polarization cross section now includes rank-3 tensors:

$$\Delta_{fi}=\Sigma_0[P_1(\cos\theta^*)R_1^0(q,\theta)_{fi}+P_1^1(\cos\theta^*)\cos\phi^*R_1^1(q,\theta)_{fi}+P_3(\cos\theta^*)R_3^0(q,\theta)_{fi}+P_3^1(\cos\theta^*)\cos\phi^*R_3^1(q,\theta)_{fi}] \tag{8.44}$$

with

$$
\begin{aligned}
R_1^0(q,\theta)_{fi} &= -v'_T[\tfrac{3}{5}(F_1^2+F_3^2)]/F^2(q,\theta)\ , \\
R_1^1(q,\theta)_{fi} &= -v'_{TL}\left[\frac{6}{\sqrt{5}}\left[(F_0+\tfrac{2}{5}F_2)F_1+\frac{\sqrt{6}}{5}F_2F_3\right]\right]\Big/F^2(q,\theta)\ , \\
R_3^0(q,\theta)_{fi} &= v'_T[\tfrac{1}{5}F_3(F_3+2\sqrt{6}F_1)]/F^2(q,\theta)\ , \\
R_3^1(q,\theta)_{fi} &= v'_{TL}\left[\left[\frac{2}{15}\right]^{1/2}\left[(F_0+\tfrac{3}{5}F_2)F_3+\frac{\sqrt{6}}{5}F_2F_1\right]\right]\Big/F^2(q,\theta)\ .
\end{aligned}
\tag{8.45}
$$

As a specific example of such a case, consider the $\frac{3}{2}^-$ ground state of ^{7}Li (Donnelly, 1983; Donnelly and Raskin, 1984). The form factors F_0, F_1, F_2, and F_3 were calculated using Cohen and Kurath wave functions. Some of the results are displayed in Figs. 64—67. In particular we show curves for the situations when the target nucleus ^{7}Li is polarized with $p_{(i)}(+\frac{3}{2})=1$ along the directions labeled L ("longitudinal," along the incident electron direction), N ("normal," perpendicular to the electron scattering plane, along the direction specified by $\mathbf{u}_N$ in Fig. 62), and S ("sideways," orthogonal to the above so that $\mathbf{u}_S=\mathbf{u}_N\times\mathbf{u}_L$ and $\mathbf{u}_S$ also lies in the scattering plane along with $\mathbf{u}_L$).

To achieve these polarizations, the angles (θ^*,ϕ^*) are chosen so that, even as the direction $\mathbf{q}$ changes, the polarization axes are fixed in the laboratory system. Figure 64 shows the cross section Σ_L obtained by polarizing ^{7}Li along the direction of the incident electron beam (L), but not requiring polarized electrons. A discussion of luminosities obtainable with internal targets and a stretcher ring (Bates, 1984) shows that a practical minimum cross section is of the order of 10^{-33} cm^2 sr^{-1}. With electron energies of order 0.5—1 GeV one can hope to reach beyond $q\sim$400—500 MeV/c. The interesting high-q region ($q>3$ fm^{-1}) may be inaccessible in such experi-

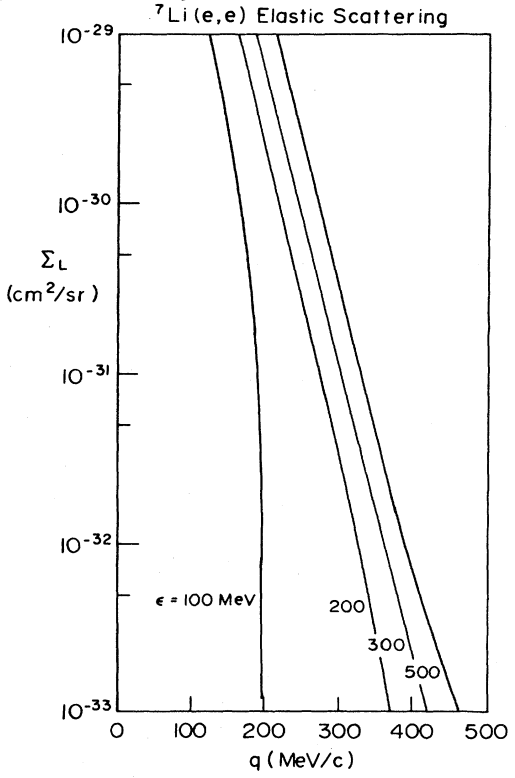

FIG. 64. Elastic scattering from polarized ^{7}Li with unpolarized electrons. The target is assumed to be polarized along the direction of the incident electron ($\mathbf{u}_L$).

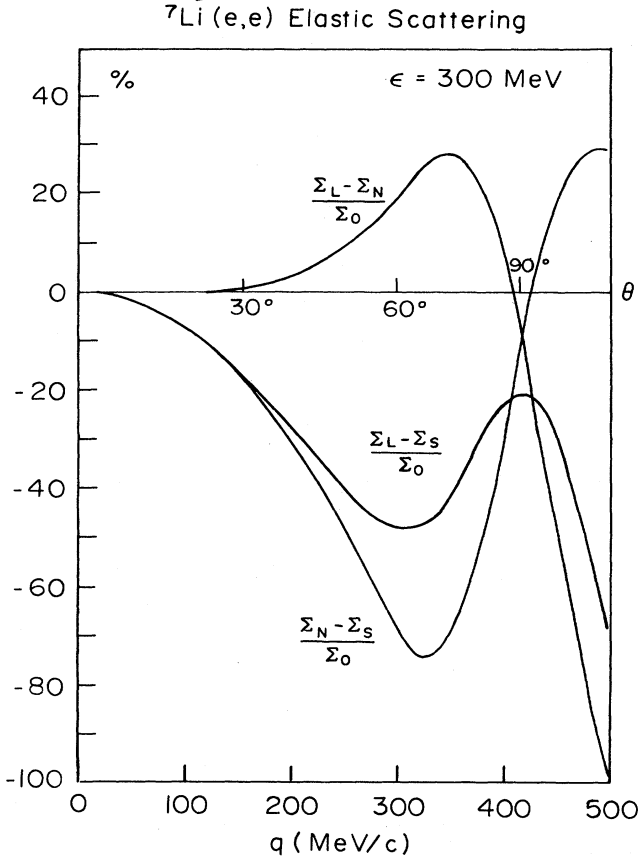

FIG. 65. Unpolarized elastic electron scattering from polarized ^{7}Li at an incident electron energy of 300 MeV. The target is assumed to be polarized along the direction of the incident beam (L, longitudinal), normal to the electron scattering plane (N), or sideways (S: $\mathbf{u}_S=\mathbf{u}_N\times\mathbf{u}_L$). Σ_0 is the usual unpolarized cross section.

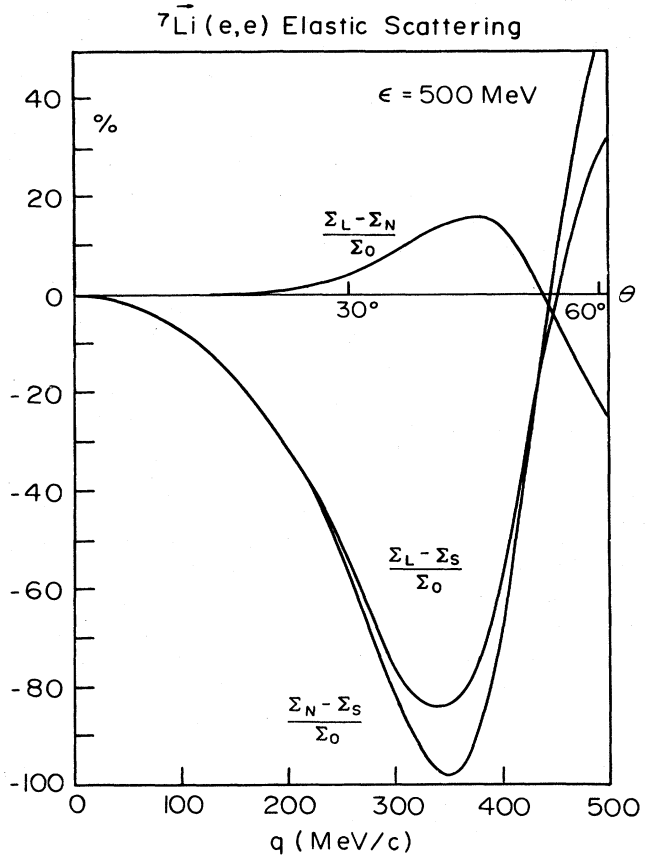

FIG. 66. Same as for Fig. 65, but at $\varepsilon=500$ MeV.

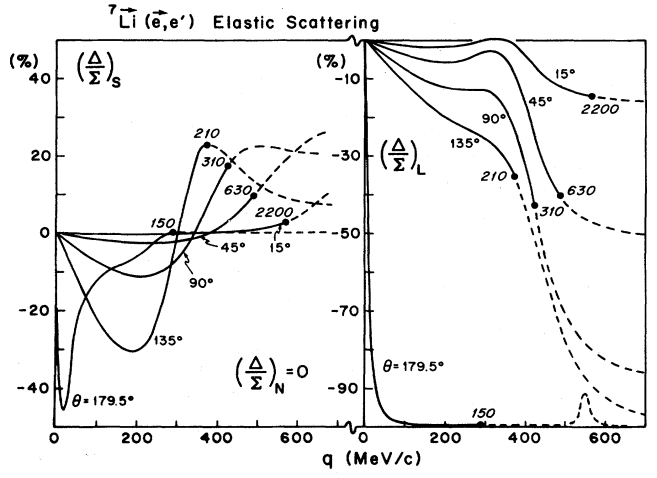

FIG. 67. Scattering of polarized electrons from polarized ^{7}Li. The asymmetries Δ/Σ are shown for sideways (S) and longitudinal (L) polarizations. The curves are labeled with the electron scattering angle θ and have dots on the curves to denote the places at which the cross section drops to 10^{-33} cm^2 sr^{-1}; solid lines correspond to larger cross sections and dashed curves to smaller cross sections. The numbers beside the dots give the electron energies ε corresponding to these conditions.

ments, however. To illustrate the polarization sensitivities we show in Figs. 65 and 66 various asymmetries, for example, $(\Sigma_L-\Sigma_N)/\Sigma_0$, where Σ_0 is the unpolarized cross section [also $\Sigma_0=(\Sigma_L+\Sigma_N+\Sigma_S)/3$ here]. Clearly large asymmetries are present in regions where the cross sections are greater than 10^{-33} cm^2 sr^{-1}. As just one example of what is reasonable for the asymmetries plotted, consider the dip in $(\Sigma_N-\Sigma_S)/\Sigma_0$ at about 325 MeV/c momentum transfer for $\varepsilon=300$ MeV (see Fig. 65). Of the -75% asymmetry, -71.6% comes from the purely Coulomb contributions involving F_0F_2 (see above), $+9.8\%$ comes from the magnetic contributions, involving $(F_1+\sqrt{3/2}F_3)^2$, -4.0% comes from those involving $(F_1^2-F_3^2+1/\sqrt{6}F_1F_3)$, and -9.2% comes from the Coulomb-magnetic interference terms involving $F_2(F_1-\sqrt{2/3}F_3)$. The other curves contain different weighting of these four pieces, and so overall, when these are combined with the usual longitudinal and transverse form factors, F_L^2 and F_T^2, we have six pieces of information from which to extract four form factors at each value of q. Thus the problem is overdetermined even without resorting to experiments with polarized electrons. The asymmetries are large over a significant range of momentum transfer, and all of the various pieces play sufficiently important roles in arriving at the overall asymmetry to suggest that the entire set of elastic form factors may be separately determined. For completeness, in Fig. 67 we show the asymmetry Δ/Σ obtained when polarized electrons are considered along with the ^{7}Li target polarized in the L or S directions (the N-direction polarization yields zero for Δ). Again quite large asymmetries are found in regions where the cross sections exceed 10^{-33} cm^2 sr^{-1}. Both purely magnetic and Coulomb-magnetic interference terms (see above) contribute significantly when the asymmetry is large, with the former generally dominating at high q. From such analyses, still different combinations of the four basic form factors can be obtained.

(v) $J_0>\frac{3}{2}$

The formalism summarized above permits elastic scattering from any target, no matter what its angular momentum, to be analyzed in terms of its component ground-state Coulomb and magnetic form factors. Of course, for large values of J_0 the analysis becomes rather complicated. Nevertheless, as J_0 grows, so does the number of terms in the (associated) Legendre expansions. With sufficient measurements in polarization space, i.e., different values of θ^* and ϕ^*, the experimentally accessible cross sections may in principle be decomposed into the basic nuclear ground-state form factors.

We refrain here from giving further examples for heavier nuclei and higher spins. The choice of nuclei to be studied initially will depend on the technical options of atomic beam sources and polarimeters. The formalism presented above is sufficiently general to treat all these cases.

To conclude this section we summarize some of the points discussed above.

(a) Practically speaking, for energies $\varepsilon\gg m_e$, only lon-

gitudinally polarized electrons appear to be of interest for nuclear physics studies. They may prove difficult to obtain under conditions where such experiments are likely to be most practical, viz., internal targets in electron stretcher rings. In such a case, when electrons are constrained to closed orbits, the spins will precess, and so one will not in general have a beam of longitudinally polarized electrons unless special geometries such as "figure 8" rings are used.

(b) For inclusive scattering with polarized electrons, the cross section Δ_{fi} will vanish unless a nuclear polarization is also known (that is, ignoring parity-violating effects from the weak interaction).

(c) With polarized targets and unpolarized electrons there is new information in the cross sections Σ_{fi}. These contain CJ/CJ', MJ/MJ', and CJ/MJ' interferences in general, in addition to the usual unpolarized cross sections which depend only on $\Sigma(CJ)^2$ and $\Sigma(MJ)^2$, where the different multipole form factors cannot be separated from one another. By varying the direction of polarization of the target, it is possible in principle to determine separately each of the multipole matrix elements for a given transition.

(d) With polarized electrons *and* polarized targets the cross section Δ_{fi} will be accessible. This generally contains MJ/MJ' and CJ/MJ' interferences, which may be separated from one another by varying the direction of polarization as in case (c) above. Σ_{fi} and Δ_{fi} may be separated by taking sums and differences of the overall cross section with electron helicities ± 1. Note that the effects due to Δ_{fi} are diminished by a factor $\tan(\theta/2)$ with respect to Σ_{fi} when the electron scattering angle becomes small. Typically this occurs when ε is large and θ small to fix q at some not-too-large value.

(e) Over a significant range of electron energies and scattering angles the typical cross sections remain above 10^{-33} cm^2 sr^{-1}, and so, from the criteria established in discussions of internal target physics with an electron stretcher ring, appear to yield practical counting rates.

From the above points it appears that nuclear structure studies involving electron scattering from polarized targets may enter a new era once the required experimental facilities become available. The ability to separate all of the various electromagnetic multipole matrix elements as functions of q in a mixed multipole situation is highly desirable and yet is not possible with inclusive electron scattering, lacking information about nuclear polarizations.

IX. CONCLUSIONS

In the preceding sections we have presented an extensive general review both of theoretical developments and of experimental results within the context of magnetic elastic electron-nucleus scattering. For many of the nuclei investigated, we have made relatively detailed comparisons of model calculations (including our own analysis) and experimental data. What overall message can we deduce?

For nuclei with $A > 4$ we have found that magnetic form factors are reasonably well explained in terms of conventional nuclear structure calculations, provided that the model space employed is large enough. The s/d-shell nuclei in particular best demonstrate the degree to which the great variety of different from factors results from the pronounced sensitivity of F_T to the spatial distributions of valence neutrons and protons, and the extent to which they can be understood in terms of shell-model calculations. For a number of cases, however, pronounced differences between calculation and experiment occur at large q. For those few cases where a detailed study has been made, it has become apparent that our understanding of F_T is incomplete. The effects of core polarization and configuration mixing are not satisfactorily understood at present. We believe that only the advent of $2\hbar\omega$ calculations will allow further progress to be made in the understanding of magnetic scattering. We emphasize the need for such calculations; if we want to learn from nuclear systems with $A > 4$ anything about the more "exotic" effects—e.g., MEC or other non-nucleonic degrees of freedom—believable $2\hbar\omega$ calculations are a prerequisite.

We note that, as calculations include more complex configurations, the question of the best interface between theory and experiment becomes more important. The density-matrix formalism developed in this review presents a convenient way to condense the information contained in the wave functions into a few numbers sufficient for calculations with arbitrary one- and two-body observables. A computer code, MAGFO, written for this review to calculate form factors starting from density-matrix elements, is available and provides many of the fitting options needed to interpret experimental data.

For light nuclei ($A \leq 3$) the great sensitivity of the magnetic form factors to ground-state current distributions makes them an ideal tool for the study of non-nucleonic degrees of freedom. While the level of agreement found in comparisons with data testifies to the success of MEC calculations, many questions remain open. In particular, the interplay of MEC and relativistic effects, both in the interaction and in the nuclear wave functions, poses a challenging problem for the future.

A number of topics have not been covered by this review, in order to keep the discussion reasonably coherent in scope and manageable in size. Although $q=0$ properties are covered by a large body of literature, we have given them very little weight; indeed we have concentrated on the q dependence, which is ideally suited to disentangling contributions mixed up in the magnetic moments. The relationship between magnetic form factors and studies of nuclei with hadronic probes has not been pursued either; this field certainly deserves more attention in the future. Nucleon magnetic form factors have not been discussed in any detail. Until QCD becomes generally applicable to calculations of nuclear structure and dynamics, the concepts required to deal with these form factors are very different from those generally of interest for nuclei. Non-nucleonic degrees of freedom beyond the standard MEC and relativistic effects have hardly been

touched upon; these topics will receive more attention once higher momentum transfers become accessible experimentally. The relationships between magnetic form factors and weak interaction processes, although quite close, have not been discussed.

Looking forward, we can identify fields of nuclear physics where magnetic scattering can contribute to the investigation of some exciting problems. "Conventional" nuclear structure studies can be put to much more stringent tests by the measurement of form factors of individual multipolarities, and the investigation of light nuclei at large q opens the possibility of a quantitative study of submesonic degrees of freedom.

Considerable progress in electron-nucleus magnetic scattering can be expected to result from the measurement of polarization observables. This will become a realistic possibility when facilities now in the planning stage go into operation with polarized electron beams, recoil polarimeters, and intense atomic beam sources for use in pulse stretcher rings. The possibility of separating multipolarities and measuring new form factors will give access to the intermediate q range between the maximum of the $M1$ and the highest multipole. The great sensitivity of these form factors to details of nuclear structure predicted by calculations can then be exploited.

Pushing magnetic scattering experiments on light nuclei to very high q will increase the visibility of currents due to constituents other than nucleons or pions. As we reach finer spatial resolution, the quark structure of nuclei—a new frontier for nuclear physics—will become accessible. By analogy with the achievements associated with MEC, we may expect magnetic electron scattering to play a major role.

ACKNOWLEDGMENTS

This review would not have been possible without the help of many individuals and without the material they sent us before publication. In particular, we wish to thank Alex Brown, John Dubach, Alfonsus Bakkum, and Peter Glaudemans for supplying us with density-matrix elements and MEC calculations. We are also grateful to Hartmuth Arenhövel for illuminating correspondence on the few-body problem and to Elvira Moya de Guerra and Alex Dieperink for useful discussions on deformed nuclei. We wish to thank Louk Lapikás for his very thorough reading of the manuscript. We are grateful to Erich Vogt for the hospitality he extended to us at TRIUMF and for his diligent overseeing of our work. We should like to thank the Max-Geldner Stiftung for the support that made the transatlantic collaboration involved in writing this review possible. This work was performed under the auspices of the U. S. Department of Energy (Contract No. DE-AC02-76ER03069) and the Schweizerischer Nationalfonds.

REFERENCES

Adler, R. J., and S. D. Drell, 1964, Phys. Rev. Lett. **13**, 349.
Ajzenberg-Selove, F., and T. Lauritsen, 1974, Nucl. Phys. A **227**, 1.
Arenhövel, H., 1975, Z. Phys. A **275**, 189.
Arenhövel, H., 1979, Nukleonika **24**, 273.
Arenhövel, H., 1983, private communication.
Arenhövel, H., and W. Leidemann, 1983, Nucl. Phys. A **393**, 385.
Arima, A., Y. Horikawa, H. Hyuga, and T. Suzuki, 1978, Phys. Rev. Lett. **40**, 1001.
Arima, A., and H. Hyuga, 1979, in *Mesons in Nuclei,* edited by M. Rho and D. H. Wilkinson (North-Holland, Amsterdam), p. 685.
Arita, K., 1977, in *Proceedings of the International Conference on Nuclear Structure, Tokyo,* edited by T. Marumori (supplement to J. Phys. Soc. Jpn. **44**, 1978), p. 255, and private communication.
Arita, K., A. Enomoto, Y. Mizuno, T. Nakazato, S. Ohsawa, T. Saito, T. Terasawa, and Y. Torizuka, 1981, Phys. Rev. C **23**, 1482.
Arnold, R. G., C. E. Carlson, and F. Gross, 1980, Phys. Rev. C **21**, 1426.
Arnold, R. G., C. E. Carlson, and F. Gross, 1981, Phys. Rev. C **23**, 363.
Auffret, S., J. P. Bazantay, J. M. Cavedon, B. Frois, D. Goutte, M. Huet, P. Leconte, X. H. Phan, S. K. Platchkov, W. Boeglin, and I. Sick, 1984 (to be published).
Bakkum, E. A., and P. W. M. Glaudemans, 1982, private communication.
Barrett, R. C., 1974, Rep. Prog. Phys. **37**, 1.
Barroso, A., and E. Hadjimichael, 1975, Nucl. Phys. A **238**, 422.
Bates Linear Accelerator Laboratory Proposal, 1984.
Benaksas, D., D. Drickey, and D. Frèrejacque, 1964, Phys. Rev. Lett. **13**, 353.
Benaksas, D., D. Drickey, and D. Frèrejacque, 1966, Phys. Rev. **148**, 1327.
Bergstrom, J. C., 1975, Phys. Rev. C **11**, 1514.
Bergstrom, J. C., 1979, Nucl. Phys. A **327**, 458.
Bergstrom, J. C., I. P. Auer, and R. S. Hicks, 1975, Nucl. Phys. A **251**, 401.
Bergstrom, J. C., U. Deutschmann, and R. Neuhausen, 1979, Nucl. Phys. A **327**, 439.
Bergstrom, J. C., S. B. Kowalski, and R. Neuhausen, 1982, Phys. Rev. C **25**, 1156.
Bernabeu, J., and J. Ros, 1974, Nucl. Phys. A **220**, 1.
Bernheim, M., D. Blum, W. McGill, R. Riscalla, C. Trail, and T. Stovall, 1972, Nuovo Cimento Lett. **5**, 431.
Bernheim, M., E. Jans, J. Mougey, D. Royer, D. Tarnowski, S. Turck-Chièze, I. Sick, G. P. Capitani, E. De Sanctis, and S. Frullani, 1981, Phys. Rev. Lett. **46**, 402.
Bertozzi, W. (never to be published).
Bertozzi, W., M. V. Hynes, C. P. Sargent, C. Creswell, P. C. Dunn, A. Hirsch, M. Leitch, B. Norum, F. N. Rad, and T. Sasanuma, 1977, Nucl. Instrum. Methods **141**, 457.
Bertozzi, W., M. V. Hynes, C. P. Sargent, W. Turchinetz, and C. Williamson, 1979, Nucl. Instrum. Methods **162**, 211.
Bertsch, G. F., and T. T. S. Kuo, 1968, Nucl. Phys. A **112**, 204.
Bertsch, G., J. Borysowicz, H. McManus, and W. G. Love, 1977, Nucl. Phys. A **284**, 399.
Blankenbecler, R., and J. F. Gunion, 1971, Phys. Rev. D **4**, 718.
Blatnik, S., and N. Zovko, 1974, Acta Phys. Austriaca **39**, 62.
Bohannon, G., L. Zamick, and E. Moya de Guerra, 1980, Nucl. Phys. A **334**, 278.
Bohr, A., and B. Mottelson, 1975, *Nuclear Structure* (Benjamin, New York), Vol. II.

Bohr, A., and V. F. Weisskopf, 1950, Phys. Rev. **77**, 94.
Bongardt, K., M. Pilkuhn, and H. G. Schlaile, 1974, Phys. Lett. B **52**, 271.
Bornais, R., 1981, Ph.D. thesis (Université de Montréal).
Bosco, B., and A. Piazza, 1970, Phys. Rev. C **1**, 787.
Bouten, M., M. C. Bouten, and H. Depuydt, 1969, Nucl. Phys A **131**, 385.
Box, G., 1976, Ph.D. thesis (Instituut voor Kernphysisch Onderzoek, Amsterdam).
Brandenburg, R. A., Y. E. Kim, and A. Tubis, 1974, Phys. Rev. Lett. **32**, 1325.
Brockmann, R., and W. Weise, 1977, Phys. Rev. C **16**, 1282.
Brody, T. A., and M. Moshinsky, 1960, *Tables of Transformation Brackets* (Monographeas, Instituto de Fisica, Universidad de Mexico, Mexico, D.F.).
Brown, B. A., and B. H. Wildenthal, 1982, private communication.
Brown, B. A., W. Chung, and B. H. Wildenthal, 1980, Phys. Rev. C **22**, 774.
Brown, B. A., R. Radhi, and B. H. Wildenthal, 1983, Phys. Lett. B **133**, 5.
Brown, G. E., J. H. Gunn, and P. Gould, 1963, Nucl. Phys. **46**, 598.
Buchanan, C. D., and M. R. Yearian, 1965, Phys. Rev. Lett. **15**, 303.
Buck, W. W., and F. Gross, 1979, Phys. Rev. D **20**, 2361.
Burzynski, S., M. Baumgartner, H. P. Gubler, J. Jourdan, H. O. Meyer, G. R. Plattner, H. W. Roser, and I. Sick, 1983, Nucl. Phys. A **399**, 230.
Campi, X., 1982, private communication.
Campi, X., and D. W. Sprung, 1972, Nucl. Phys. A **194**, 401.
Cardman, L. S., B. Frois, J. Heisenberg, W. Hersman, R. Hicks, P. Mueller, and C. N. Papanicolas, 1983, Bates Linear Accelerator Laboratory proposal 83-10 (unpublished).
Cardman, L. S., J. W. Lightbody, S. Penner, S. P. Fivozinski, X. K. Maruyama, W. P. Trower, and S. E. Williamson, 1980, Phys. Lett. B **91**, 203.
Castel, B., and K. Goeke, 1979, Phys. Lett. B **82**, 160.
Cavedon, J. M., B. Frois, D. Goutte, M. Huet, P. Leconte, C. N. Papanicolas, X. H. Phan, S. K. Platchkov, S. Williamson, W. Boeglin, and I. Sick, 1982a, Phys. Rev. Lett. **49**, 978.
Cavedon, J. M., B. Frois, D. Goutte, M. Huet, P. Leconte, J. Martino, X. H. Phan, S. K. Platchkov, S. E. Williamson, W. Boeglin, I. Sick, P. K. A. De Witt Huberts, L. S. Cardman, and C. N. Papanicolas, 1982b, Phys. Rev. Lett. **49**, 986.
Chapman, R., J. N. Mo, J. L. Durell, and N. H. Merrill, 1976, J. Phys. G **12**, 951.
Chemtob, M., 1969, Nucl. Phys. A **123**, 449.
Chemtob, M., and A. Lumbroso, 1970, Nucl. Phys. B **17**, 401.
Chemtob, M., E. J. Moniz, and M. Rho, 1974, Phys. Rev. C **10**, 344.
Chemtob, M., and M. Rho 1971, Nucl. Phys. A **163**, 1.
Cheon, I. T., 1981, Nuovo Cimento Lett. **31**, 347.
Cheon, I. T., 1983, Phys. Lett. B **124**, 451.
Chung, W., 1976, Ph.D. thesis (Michigan State University).
Ciofi Degli Atti, C., 1980, Prog. Part Nucl. Phys. **3**, 163.
Clement, C. F., 1973, Nucl. Phys. A **213**, 469.
Cohen, S., and D. Kurath, 1965, Nucl. Phys. **73**, 1.
Collard, H., R. Hofstadter, E. B. Hughes, A. Johansson, M. R. Yearian, R. B. Day, and R. T. Wagner, 1965, Phys. Rev. **138**, 57B.
Coon, S. A., R. J. McCarthy, and J. P. Vary, 1982, Phys. Rev. C **25**, 756.
Dally, E. B., M. G. Croissiaux, and B. Schweitz, 1970, Phys. Rev. C **2**, 2057.
Dechargé, J., and D. Gogny, 1980, Phys. Rev. C **21**, 1568.
deForest, T., and J. D. Walecka, 1966, Adv. Phys. **15**, 1.
De Jager, C. W., H. De Vries, and C. De Vries, 1974, At. Data Nucl. Data Tables **14**, 479.
De Jager, K., *et al.*, quoted by Lapikás, 1979.
Delorme, J., A. Figureau, and P. Guichon, 1981, Phys. Lett. B **99**, 187.
de Shalit, A., and I. Talmi, 1963, *Nuclear Shell Theory* (Academic, New York).
de Shalit, A., and H. Feshbach, 1974, *Theoretical Nuclear Physics* (Wiley, New York), Vol. I.
Desplanques, B., and J. F. Mathiot, 1982, Phys. Lett. B **116**, 82.
Deutschmann, U., G. Lahm, R. Neuhausen, and J. C. Bergstrom, 1980, paper presented at the International Conference on Nuclear Physics, Berkeley, California, August 1980 (unpublished).
De Vries, C., 1978, *Lecture Notes in Physics* (Springer, Berlin), Vol. 86, p. 181.
De Vries, C., C. W. de Jager, L. Lapikás, G. Luijckx, R. Maas, H. De Vries, and P. K. A. De Witt Huberts, 1984, Nucl. Instrum. Methods (to be published).
De Vries, H., 1973, Ph.D. thesis (Instituut voor Kerphysisch Onderzoek, Amsterdam).
De Vries, H., G. J. C. Van Niftrik, and L. Lapikás, 1970, Phys. Lett. B **33**, 403.
De Witt Huberts, P. K. A., J. B. Bellicard, B. Frois, M. Huet, P. Leconte, A. Nakada, Phan Xuan Ho, S. Turck, L. Lapikás, H. De Vries, and I. Sick, 1976, Phys. Lett. B **60**, 157.
De Witt Huberts, P. K. A., L. Lapikás, H. De Vries, J. B. Bellicard, J. M. Cavedon, B. Frois, M. Huet, P. Leconte, A. Nakada, Phan Xuan Ho, S. K. Platchkov, and I. Sick, 1977, Phys. Lett. B **71**, 317.
Dieperink, A. E. L., and I. Sick, 1982, Phys. Lett. B **109**, 1.
Dirac, P. A. M., 1928, Proc. R. Soc. London **117**, 610.
Donné, A. J. H., G. van Middelkoop, L. De Vries, L. Lapikás, A. M. Selig, P. K. A. De Witt Huberts, and I. Zacharov, 1983, paper presented at the International Conference on Nuclear Physics, Florence, Italy (unpublished).
Donné, A. J. H., G. van Middelkoop, L. De Vries, L. Lapikás, J. B. van der Laan, C. De Vries, and J. G. Noomen, 1984, Nucl. Instrum. Methods (to be published).
Donnelly, T. W., 1983, in *Symmetries in Nuclear Structure*, edited by K. Abrahams, K. Allaart, and A. E. L. Dieperink (Plenum, New York), p. 1.
Donnelly, T. W., and A. Gökalp, 1981, Nucl. Phys. A **355**, 403.
Donnelly, T. W., and W. C. Haxton, 1979, At. Data Nucl. Data Tables **23**, 103.
Donnelly, T. W., and W. C. Haxton, 1980, At. Data Nucl. Data Tables **25**, 1.
Donnelly, T. W., and R. D. Peccei, 1979, Phys. Rep. **50**, 1.
Donnelly, T. W., and A. S. Raskin, 1984 (to be published).
Donnelly, T. W., and J. D. Walecka, 1973a Nucl. Phys. A **201**, 81.
Donnelly, T. W., and J. D. Walecka, 1973b, Phys. Lett. B **44**, 330.
Donnelly, T. W., and J. D. Walecka, 1975, Annu. Rev. Nucl. Sci. **25**, 329.
Donnelly, T. W., and J. D. Walecka, 1976, Nucl. Phys. A **274**, 368.
Dubach, J., 1975, Ph.D. thesis (Stanford University).
Dubach, J., 1980, Nucl. Phys. A **340**, 271.
Dubach, J., 1983, private communication.
Dubach, J., and W. C. Haxton, 1982, cited by Hicks *et al.*, 1982.

Dubach, J., J. H. Koch, and T. W. Donnelly, 1976, Nucl. Phys. A **271**, 279.
Dunn, P. C., S. B. Kowalski, F. N. Rad, C. P. Sargent, W. E. Turchinetz, R. Goloskie, and D. P. Saylor, 1983, Phys. Rev. C **27**, 71.
Edmonds, A. R., 1960, *Angular Momentum in Quantum Mechanics* (Princeton University, Princeton, N.J.).
Ehrenberg, H., H. Averdung, B. Dreher, G. Fricke, H. Herminghaus, R. Herr, H. Hultzsch, G. Lührs, K. Merle, R. Neuhausen, G. Nöldeke, H. M. Stolz, V. Walther, and H. D. Wohlfahrt, 1972, Nucl. Instrum. Methods **105**, 253.
Elton, L. R. B., 1950, Proc. Phys. Soc. London, Sect. A **63**, 1115.
Euteneuer, H., H. Rothhaas, O. Schwentker, J. R. Moreira, C. W. De Jager, L. Lapikás, H. De Vries, J. Flanz, K. Itoh, G. A. Peterson, D. V. Webb, W. C. Barber, and S. Kowalski, 1977, Phys. Rev. C **16**, 1703.
Fabian, W., 1975, Ph.D. thesis (University of Mainz).
Fabian, W., and H. Arenhövel, 1976, Nucl. Phys. A **258**, 461.
Fabian, W., H. Arenhövel, and H. G. Miller, 1974, Z. Phys. **271**, 93.
Fetter, A. L., and J. D. Walecka, 1971, *Quantum Theory of Many-Particle Systems* (McGraw-Hill, New York).
Fischer-Woetzmann, M., 1981, Z. Phys. **302**, 15.
Flocard, H., P. Quentin, A. K. Kerman, and D. Vautherin, 1973, Nucl. Phys. A **203**, 433.
Franey, M. A., J. S. Lilley, and W. R. Phillips, 1979, Nucl. Phys. A **324**, 193.
Friar, J. L., 1973, Ann. Phys. **81**, 332.
Friar, J. L., 1979, in *Mesons in Nuclei,* edited by M. Rho and D. H. Wilkinson (North-Holland, Amsterdam), p. 594.
Friar, J. L., 1983, Phys. Rev. C **27**, 2078.
Friar, J. L., E. L. Tomusiak, and J. Dubach, 1982, Phys. Rev. C **25**, 1659.
Friedman, J. I., H. W. Kendall, and P. A. M. Gram, 1960, Phys. Rev. **120**, 992.
Fujita, T., and A. Arima, 1975, Nucl. Phys. A **254**, 513.
Ganichot, D., B. Grossetête, and D. B. Isabelle, 1972, Nucl. Phys. A **178**, 545.
Gari, M., and H. Hyuga, 1976a, Phys. Rev. Lett. **36**, 345.
Gari, M., and H. Hyuga, 1976b, Nucl. Phys. A **264**, 409.
Gari, M., H. Hyuga, and B. Sommer, 1976, Phys. Rev. C **14**, 2196.
Gerstenberger, R. V., and Y. Nogami, 1972, Phys. Rev. Lett. **29**, 233.
Gibson, B. F., 1965, Phys. Rev. **139**, 1153B.
Gilbert, W., 1600, *De Magnete,* translation in the Collectors Series in Science (Basic Books, New York, 1958).
Glaudemans, P. W. M., 1983, in *Symmetries in Nuclear Structure,* edited by K. Abrahams, K. Allaart, and A. E. L. Dieperink (Plenum, New York), p. 119.
Glaudemans, P. W. M., G. Wiechers, and P. J. Brussaard, 1964, Nucl. Phys. **56**, 529.
Goldemberg, J., and C. Schaerf, 1964, Phys. Rev. Lett. **12**, 298.
Goldemberg, J., and Y. Torizuka, 1963, Phys. Rev. **129**, 312.
Goldemberg, J., D. B. Isabelle, T. Stovall, D. Vinciguerra, and A. Bottino, 1965, Phys. Lett. **16**, 141.
Gourdin, M., 1963, Nuovo Cimento **28**, 533.
Gourdin, M., 1974, Phys. Rep. C **11**, 29.
Gourdin, M., and C. A. Piketty, 1964, Nuovo Cimento **32**, 1137.
Green, A. M., and T. H. Schucan, 1972, Nucl. Phys. A **188**, 289.
Griffy, T. A., and D. U. L. Yu, 1965, Phys. Rev. **139**, 880B.
Gross, F., 1978, in *Proceedings of the Conference on Few Body Systems Nuclear Forces, Graz,* Lecture Notes in Physics, No. 82, edited by H. Zingl, M. Haftel, and H. Zankel (Springer, Berlin), Vol. I, p. 46.
Grossetête, B., D. Drickey, and P. Lehmann, 1966, Phys. Rev. **141**, 1425.
Gubler, H. P., G. R. Plattner, I. Sick, A. Traber, and W. Weiss, 1977, Nucl. Phys. A **284**, 114.
Guth, E., 1934, Anz. Akad. Wiss. Wien, Math.-Naturwiss. Kl. **24**, 299.
Hadjimichael, E., and A. Barroso, 1973, Phys. Lett. B **47**, 103.
Hadjimichael, E., B. Goulard, and R. Bornais, 1983, Phys. Rev. C **27**, 831.
Hadjimichael, E., S. N. Yang, and G. E. Brown, 1972, Phys. Lett. B **39**, 594.
Haftel, M. I., L. Mathelitsch, and H. F. K. Zingl, 1980, Phys. Rev. C **22**, 1285.
Hajduk, Ch., P. U. Sauer, and W. Strueve, 1983, Nucl. Phys. A **405**, 581.
Hamamoto, I., J. Lichtenstadt, and G. F. Bertsch, 1980, Phys. Lett. B **93**, 213.
Harper, E. P., Y. E. Kim, A. Tubis, and M. Rho, 1972, Phys. Lett. B **40**, 533.
Heisenberg, J., 1981, Adv. Nucl. Phys. **12**, 61.
Heisenberg, J., J. S. McCarthy, and I. Sick, 1970, Nucl. Phys A **157**, 435.
Hennel, M. A., and L. M. Delves, 1971, Phys. Lett. B **34**, 195.
Hicks, R. S., 1982, Phys. Rev. C **25**, 695.
Hicks, R. S., *et al.,* 1983, private communication.
Hicks, R. S., J. Dubach, R. A. Lindgren, B. Parker, and G. A. Peterson, 1982a, Phys. Rev. C **26**, 339.
Hicks, R. S., R. L. Huffman, R. A. Lindgren, B. Parker, M. A. Plum, G. A. Peterson, P. J. Ryan, J. Dubach, and R. P. Singhal, 1982b, Bates Linear Accelerator Laboratory Proposal 82-11 Update.
Hockert, J., D. O. Riska, M. Gari, and A. Huffman, 1973, Nucl. Phys. **217**, 14.
Hofstadter, R., 1956, Rev. Mod. Phys. **28**, 214.
Hofstadter, R., 1957, Annu. Rev. Nucl. Sci. **7**, 231.
Hofstadter, R., and R. W. McAllister, 1955, Phys. Rev. **98**, 217.
Höhler, G., E. Pietarinen, I. Sabba-Stefanescu, F. Borkowski, G. G. Simon, V. H. Walther, and R. D. Wendling, 1976, Nucl. Phys. B **114**, 505.
Horikawa, Y., T. Fujita, and K. Yazaki, 1972, Phys. Lett. B **42**, 173.
Horowitz, C. J., and B. D. Serot, 1983, Nucl. Phys. A **399**, 529.
Huffman, R. L., R. S. Hicks, J. Dubach, B. Parker, M. A. Plum, G. Lahm, R. Neuhausen, and J. C. Bergstrom, Phys. Lett. B **139**, 249.
Hüfner, J., F. Scheck, and C. S. Wu, 1977, in *Muon Physics,* edited by V. W. Hughes and C. S. Wu (Academic, New York), Vol. I, p. 201.
Hynes, M. V., H. Miska, B. Norum, W. Bertozzi, S. Kowalski, F. N. Rad, C. P. Sargent, T. Sasanuma, W. Turchinetz, and B. L. Berman, 1979, Phys. Rev. Lett. **42**, 1444.
Iachello, F., A. D. Jackson, and A. Lande, 1973, Phys. Lett. B **34**, 191.
Ichimura, M., H. Hyuga, and G. E. Brown, 1972, Nucl. Phys. A **196**, 17.
Jackson, A. D., A. Lande, and D. O. Riska, 1975, Phys. Lett. B **55**, 23.
Jankus, V. Z., 1956, Phys. Rev. **102**, 1586.
Jauch, J. M., 1940, Helv. Phys. Acta **13**, 451.
Jones, E. C., W. L. Bendel, L. W. Fagg, and R. A. Lindgren,

1979, Phys. Rev. C **19**, 610.
Jones, E. C., W. L. Bendel, L. W. Fagg, and R. A. Lindgren 1980, Phys. Rev. C **21**, 1162.
Kabachnik, N. M., and S. I. Grishanova, 1966, Yad. Fiz. **4**, 819 [Sov. J. Nucl. Phys. **4**, 583 (1967)].
Kloet, W. M., and J. A. Tjon, 1971, Nucl. Phys. A **176**, 481.
Kowald, W., 1976, Diplomarbeit (Universität Basel).
Krasnopol'ski, V. M., V. I. Kukulin, P. B. Sazonov, and V. T. Voronchev, 1983, Phys. Lett. B **121**, 96.
Krewald, S., and J. Speth, 1980, Phys. Rev. Lett. **45**, 417.
Kruger, J., and P. Van Leuven, 1969, Nucl. Phys. A **139**, 418.
Kudeyarov, Y. A., I. V. Kurdyumov, V. G. Neudatchin, and Y. F. Smirnov, 1969, Nucl. Phys. A **126**, 36.
Kudeyarov, Y. A., I. V. Kurdyumov, V. G. Neudatchin, and Y. F. Smirnov, 1971, Nucl. Phys. A **163**, 316.
Kuo, T. T. S., 1967, Nucl. Phys. A **103**, 71.
Kuroboshi, E., and Y. Hara, 1958, Prog. Theor. Phys. **20**, 163.
Lacombe, M., B. Loiseau, J. M. Richard, R. Vinh-Mau, P. Pires, and R. de Tourreil, 1975, Phys. Rev. D **12**, 1495.
Lapikás, L., 1978, in *Proceedings of the Conference on Modern Trends in Elastic Electron Scattering, Amsterdam,* edited by C. De Vries (NIKHEF-K, Amsterdam), p. 49.
Lapikás, L., 1979, in *Proceedings of the International Conference on Nuclear Physics with Electromagnetic Interactions, Mainz,* edited by H. Arenhövel and D. Drechsel, *Lecture Notes in Physics* (Springer, Berlin), Vol. 108, p. 41.
Lapikás, L., A. E. L. Dieperink, and G. Box, 1973, Nucl. Phys. A **203**, 609.
Lapikás, L., G. Box and H. De Vries, 1975, Nucl. Phys. A **253**, 324.
Laverne, A., and C. Gignoux, 1973, Nucl. Phys. A **203**, 597.
Leconte, P., 1976, Ph.D. thesis (Université de Paris—Sud).
Leconte, P., J. Mougey, A. Tomasso, P. Barreau, M. Bernheim, A. Bussière de Nercy, L. Cohen, J. C. Comoretto, J. Dupont, S. Frullani, C. Grunberg, J. M. Hisleur, J. Le Devehat, M. Lefévre, G. Lemarchand, J. Millaud, D. Royer, and R. Salvaudon, 1980, Nucl. Instrum. Methods **169**, 401.
Lehman, D. R., and W. C. Parke, 1983a, Phys. Rev. Lett. **50**, 98.
Lehman, D. R., and W. C. Parke 1983b, Phys. Rev. C **28**, 364.
Lejeune, A., 1980, Nucl. Phys. A **339**, 317.
Lejeune, A., and C. Mahaux, 1979, in "What do we know about radial shapes in the Ca-region", Karlsruhe, p. 352.
Li, G. C., I. Sick, J. D. Walecka, and G. E. Walker, 1970, Phys. Lett. B **32**, 317.
Li, G. C., I. Sick, and M. R. Yearian, 1974, Phys. Rev. C **9**, 1861.
Licht, A. L., and A. Pagnamenta, 1970, Phys. Rev. D **2**, 1150.
Lichtenstadt, J., J. Alster, M. A. Moinester, J. Dubach, R. S. Hicks, G. A. Peterson, and S. Kowalski, 1983, Phys. Lett. B **121**, 377.
Likhachev, V. P., N. G. Afanas'ev, A. A. Nemashkalo, G. A. Savitskii, V. M. Khvastunov, and L. D. Yaroshevskii, 1974, Yad. Fiz. **20**, 1113 [Sov. J. Nucl. Phys. **20**, 583 (1975)].
Likhachev, V. P., N. G. Afanas'ev, A. A. Nemashkalo, G. A. Savitskii, V. M. Khvastunov, and L. D. Yaroshevskii, 1975, Ukr. Fiz. Zh. (Russ. Ed.) **20**, 1484.
Likhachev, V. P., N. G. Afanas'ev, A. A. Nemashkalo, G. A. Savitskii, V. M. Khvastunov, L. D. Yaroshevskii, L. G. Lishenko, and A. T. Ushanev, 1976, Yad. Fiz. **23**, 498 [Sov. J. Nucl. Phys. **23**, 261 (1976)].
Lin, C. K., 1983, Ph.D. thesis (Rutgers University).
Lin, C. K., and L. Zamick, 1981, Nucl. Phys. A **365**, 411.
Lock, J. A., and L. L. Foldy, 1974, Phys. Lett. B **51**, 212.
Lock, J. A., and L. L. Foldy, 1975, Ann. Phys. (N.Y.) **93**, 276.
Lock, J. A., L. L. Foldy, and F. R. Buskirk, 1974, Nucl. Phys. A **220**, 103.
Lomon, E. L., 1980, Ann. Phys. (N.Y.) **125**, 309.
Lyman, E. M., A. O. Hanson, and M. B. Scott, 1951, Phys. Rev. **84**, 626.
Ma, Z. Y., and J. Wambach, 1983, Nucl. Phys. A **402**, 275.
Macauley, M. W. S., R. P. Singhal, R. G. Arthur, and E. A. Knight, 1977, Kelvin Laboratory report, quoted in Singhal *et al.*, 1982.
Mairle, G., G. J. Wagner, P. Doll, K. T. Knöpfle, and H. Breuer, 1978, Nucl. Phys. A **299**, 39.
Maize, M. A., and Y. E. Kim, 1983, Nucl. Phys. A **407**, 507.
Maize, M. A., and Y. E. Kim, 1984, Nucl. Phys. A **420**, 365.
Malfliet, R. A., and J. A. Tjon, 1971, Phys. Lett. B **35**, 487.
Martin, F., and R. G. Arnold, B. T. Chertok, E. B. Dally, A. Grigorian, C. L. Jordan, W. P. Schütz, R. Zdarko, and B. A. Mecking, 1977, Phys. Rev. Lett. **38**, 1320.
Massey, H. S. W., 1930, Proc. R. Soc. London **127**, 666.
Mathelitsch, L., and H. F. K. Zingl, 1978, Nuovo Cimento A **44**, 81.
Mathelitsch, L., and H. F. K. Zingl, 1983, private communication.
Mathiot, J. F., 1984, Nucl. Phys. A **412**, 201.
Mathiot, J. F., and B. Desplanques, 1981 Phys. Lett. B **101**, 141.
Mathiot, J. F., and D. O. Riska, 1983, Phys. Lett. B **133**, 23.
McCarthy, J. S., I. Sick, R. R. Whitney, and M. R. Yearian, 1970, Phys. Rev. Lett. **25**, 884.
McCarthy, J. S., I. Sick, and R. R. Whitney, 1977, Phys. Rev. C **15**, 1396.
McVoy, K. W., and L. Van Hove, 1962, Phys. Rev. **125**, 1034.
Meyer, H. O., and G. R. Plattner, 1977, Nucl. Phys. A **279**, 53.
Miessen, H., 1982, Ph.D. thesis (University of Mainz).
Millener, D. J., and D. Kurath, 1975, Nucl. Phys. A **255**, 315.
Miller, L. D., 1974, Phys. Rev. C **9**, 537.
Miska, H., B. Norum, M. V. Hynes, W. Bertozzi, S. Kowalski, F. N. Rad, C. P. Sargent, and T. Sasanuma, 1979, Phys. Lett. B **83**, 165.
Miyazawa, H., 1951, Prog. Theor. Phys. **6**, 801.
Mo, L. W., and Y. S. Tsai, 1969, Rev. Mod. Phys. **41**, 205.
Moreira, J. R., I. C. Nascimento, K. Arita, J. Friedrich, A. Enomoto, T. Terasawa, and Y. Torizuka, 1976, Phys. Rev. Lett. **36**, 566.
Mosconi, B., and P. Ricci, 1974, Nuovo Cimento A **23**, 401
Mott, N. F., 1929, Proc. R. Soc. London **124**, 425.
Moya de Guerra, E., 1980, Ann. Phys. (N.Y.) **128**, 286.
Moya de Guerra, E., and A. E. L. Dieperink, 1978, Phys. Rev. C **18**, 1596.
Moya de Guerra, E., and S. Kowalski, 1979, Phys. Rev. C **20**, 357.
Moya de Guerra, E., and S. Kowalski, 1980, Phys. Rev. C **22**, 1308.
Nascimento, I. C., J. R. Moreira, J. Goldemberg, S. Fukuda, T. Terasawa, T. Saito, K. Hosoyama, and Y. Torizuka, 1974, Phys. Lett. B **53**, 168.
Negele, J. W., 1970, Phys. Rev. C **1**, 1260.
Negele, J. W., and G. Rinker, 1977, Phys. Rev. C **15**, 1499.
Negele, J. W., and D. Vautherin, 1972, Phys. Rev. C **5**, 1472.
Nilsson, S. G. 1955, K. Dan. Vidensk. Selsk. Mat. Fys. Medd. **29**, No. 16.
O'Connell, J. S., T. W. Donnelly, and J. D. Walecka, 1972, Phys. Rev. C **6**, 719.
Osborn, R. K., and L. L. Foldy, 1950, Phys. Rev. **79**, 795.

Papanicolas, C., 1979, Ph.D. thesis (Massachusetts Institute of Technology).
Papanicolas, C. N., J. Heisenberg, J. Lichtenstadt, A. N. Courtemanche, and J. S. McCarthy, 1978, Phys. Rev. Lett. **41**, 537.
Papanicolas, C. N., J. Lichtenstadt, C. P. Sargent, J. Heisenberg, and J. S. McCarthy, 1980, Phys. Rev. Lett. **45**, 106.
Peierls, R. E., and D. J. Thouless, 1962, Nucl. Phys. **38**, 154.
Peierls, R. E., and J. Yoccoz, 1957, Proc. Phys. Soc. London, Sect. A **70**, 381.
Peterson, G. A., 1962, Phys. Lett. **2**, 162.
Peterson, G. A., 1983, private communication.
Peterson, G. A., and W. C. Barber, 1962, Phys. Rev. **128**, 812.
Peterson, G. A., J. B. Flanz, D. V. Webb, H. De Vries, and C. F. Williamson, 1979, Nucl. Instrum. Methods **160**, 375.
Peterson, G. A., K. Hosoyama, M. Nagao, A. Nakada, and Y. Torizuka, 1973, Phys. Rev. C **7**, 1028.
Platchkov, S., J. B. Bellicard, J. M. Cavedon, B. Frois, D. Goutte, M. Huet, P. Leconte, Phan Xuan Ho, I. Sick, P. K. A. De Witt Huberts, and L. Lapikás, 1979, Phys. Lett. B **86**, 1.
Platchkov, S., J. B. Bellicard, J. M. Cavedon, B. Frois, D. Goutte, M. Huet, P. Leconte, Phan Xuan Ho, P. K. A. De Witt Huberts, L. Lapikás, and I. Sick, 1982, Phys. Rev. C **25**, 2318.
Platchkov, S., J. M. Cavedon, J. C. Clemens, B. Frois, D. Goutte, M. Huet, P. Leconte, X. H. Phan, S. Williamson, I. Sick, P. K. A. De Witt Huberts, L. Lapikás, B. Desplanques, and J. F. Mathiot, 1983, Phys. Lett. B **131**, 301.
Poth, H., G. Backenstoss, I. Bergstrom, P. Blum, J. Egger, W. Fetscher, R. Guigas, R. Hagelberg, N. Hassler, C. J. Herrlander, M. Izycki, H. Koch, A. Nilsson, P. Pavlopoulos, H. P. Povel, K. Rolli, I. Sick, L. Simons, A. Schwitter, L. Sztarkier, and L. Tauscher, 1978, Nucl. Phys. A **294**, 435.
Poves, A., 1982, private communication.
Poves, A., A. L. Cedillo, and J. M. G. Gomez, 1977, Nucl. Phys. A **293**, 397.
Pratt, R. H., J. D. Walecka, and T. A. Griffy, 1965, Nucl. Phys. **64**, 677 (based on HEPL Report 272, 1962).
Prepost, R., R. M. Simonds, and B. H. Wiik, 1968, Phys. Rev. Lett. **21**, 1271.
Prescott, C. Y., W. B. Atwood, R. L. A. Cottrell, H. De Staebler, E. L. Garwin, A. Gonidec, R. H. Miller, L. S. Rochester, T. Sato, D. J. Sherden, C. K. Sinclair, S. Stein, R. E. Taylor, J. E. Glendenin, V. W. Hughes, N. Sasao, K. P. Schüler, M. G. Borghini, K. Lubelsmeyer, and W. Jentschke, 1978, Phys. Lett. B **77**, 347.
Prewitt, J. F., and L. E. Wright, 1974, Phys. Rev. C **9**, 2033.
Rad, F. N., W. Bertozzi, S. Kowalski, C. P. Sargent, C. F. Williamson, M. V. Hynes, B. Norum, B. Peterson, T. Sasanuma, and W. Turchinetz, 1980, Phys. Rev. Lett. **45**, 1785.
Rad, F. N., T. Sasanuma, W. Bertozzi, J. Heisenberg, M. V. Hynes, S. Kowalski, H. Miska, B. Norum, C. P. Sargent, W. Turchinetz, and C. F. Williamson, 1978, Phys. Rev. Lett. **40**, 368.
Rand, R. E., R. F. Frosch, C. E. Littig, and M. R. Yearian, 1967, Phys. Rev. Lett. **18**, 469.
Rand, R. E., R. F. Frosch, and M. R. Yearian, 1965, Phys. Rev. Lett. **14**, 234.
Rand, R. E., R. F. Frosch, and M. R. Yearian, 1966, Phys. Rev. **144**, 859.
Rand, R. E., M. R. Yearian, H. A. Bethe, and C. D. Buchanan, 1973, Phys. Rev. D **8**, 3229.
Ravenhall, D. G., and R. L. Mercer, 1976, Phys. Rev. C **13**, 2324.
Reuter, W., G. Fricke, K. Merle, and H. Miska, 1982, Phys. Rev. C **26**, 806.
Rho, M. 1970, in Proc. Nucl. Struct. Symp. 1000 Lakes, Joutsa.
Riska, D. O., 1980, Nucl. Phys. A **350**, 227.
Riska, D. O., 1983, University of Helsinki, Report HU-P-224.
Riska, D. O., and G. E. Brown, 1972, Phys. Lett. B **38**, 193.
Rose, M. E., 1948, Phys. Rev. **73**, 279.
Rosenbluth, M. N., 1950, Phys. Rev. **79**, 615.
Sagawa, H., 1980, Phys. Lett. B **90**, 21.
Sarker, A. Q., 1964, Phys. Rev. Lett. **13**, 375.
Schiff, L. I., 1949, Stanford University, Microwave Laboratory Report 102.
Schiff, L. I., 1964, Phys. Rev. **133**, 802B.
Schiff, L. I., H. Collard, R. Hofstadter, A. Johansson, and M. R. Yearian, 1963, Phys. Rev. Lett. **11**, 387.
Schildknecht, D., 1965, Z. Phys. **185**, 399.
Schulze, M. E., D. Beck, M. Farkhondeh, S. Gilad, R. Goloskie, R. J. Holt, S. Kowalski, R. M. Laszewski, M. J. Leitch, J. D. Moses, R. P. Redwine, D. P. Saylor, J. R. Specht, E. J. Stephenson, K. Stephenson, W. Turchinetz, and B. Zeidman, 1984, Phys. Rev. Lett. **52**, 597.
Schweber, S. S., 1961, *An Introduction to Relativistic Quantum Field Theory* (Harper and Row, New York).
Schwentker, O., 1977, Ph.D. thesis (Universität Mainz).
Selig, A. M., 1984, private communication.
Selig, A. M., L. Lapikás, P. K. A. De Witt Huberts, and T. Suzuki, 1982, Z. Phys. **307**, 247.
Serot, B., 1981, Phys. Lett. B **107**, 253.
Shepard, J. R., E. Rost, E. R. Siciliano, and J. A. Neil, 1984, Dirac Single-Particle Wave Functions in Inelastic Electron Scattering, University of Colorado preprint.
Sick, I., 1973, Nucl. Phys. A **208**, 557.
Sick, I., 1974, Phys. Lett. B **53**, 15.
Sick, I., 1980, Commun. Nucl. Part. Phys. **9**, 55.
Sick, I., 1982, Phys. Lett. B **116**, 212.
Sick, I., 1984, in *Proceedings of the 10th International IUPAP Conference on Few Body Problems in Physics, Karlsruhe,* in Nucl. Phys. A **416**, 605c.
Sick, I., J. B. Bellicard, J. M. Cavedon, B. Frois, M. Huet, P. Leconte, A. Nakada, Phan Xuan Ho, S. Platchkov, P. K. A. De Witt Huberts, and L. Lapikás, 1977, Phys. Rev. Lett. **38**, 1259.
Simon, G. G., C. Schmitt, and V. H. Walther, 1981, Nucl. Phys. A **364**, 285.
Singhal, R. P., J. Dubach, R. S. Hicks, R. A. Lindgren, B. Barka, and G. A. Peterson, 1983, Phys. Rev. C **28**, 513.
Singhal, R. P., A. Watt, and R. R. Whitehead, 1982, J. Phys. G **8**, 1059.
Slight, A. G., T. E. Drake, and G. R. Bishop, 1973, Nucl. Phys. A **208**, 157.
Sprung, D. W., and P. K. Banerjee, 1971, Nucl. Phys. A **168**, 273.
Stichel, P., and E. Werner, 1970, Nucl. Phys. A **145**, 257.
Stovall, T., D. Vinciguerra, and M. Bernheim, 1967, Nucl. Phys. A **91**, 513.
Strueve, W., C. Hajduk, and P. U. Sauer, 1983, Nucl. Phys. A **405**, 620.
Suzuki, T., 1978, Ph.D. thesis (University of Tokyo).
Suzuki, T., 1983, Phys. Lett. B **120**, 27.
Suzuki, T., and H. Hyuga, 1983, Nucl. Phys. A **402**, 491.
Suzuki, T., H. Hyuga, and A. Arima, 1979, Z. Phys. A **293**, 5.
Suzuki, T., H. Hyuga, A. Arima, and K. Yazaki, 1981a, Nucl. Phys. A **358**, 421.
Suzuki, T., H. Hyuga, A. Arima, and K. Yazaki, 1981b, Phys. Lett. B **106**, 19.

Suzuki, T., and M. Oka, 1980, paper presented at the International Conference Nuclear Physics, Berkeley (unpublished).
Tassie, L. J., and F. C. Barker, 1958, Phys. Rev. **111**, 940.
Tjon, J. A., B. F. Gibson, and J. S. O'Connell, 1970, Phys. Rev. Lett. **25**, 540.
Tjon, J. A., and M. J. Zuilhof, 1979, Phys. Lett. B **84**, 31.
Torizuka, Y., 1982, Tohoku University Laboratory for Nuclear Science report (quoted by Singhal *et al.,* 1982).
Torre, J., J. J. Benayoun, and J. Chauvin, 1981, Z. Phys. **300**, 319.
Tsai, Y. S. 1971, SLAC report 848.
Tuan, S. T., L. E. Wright, and D. S. Onley, 1968, Nucl. Instrum. Methods **60**, 70.
Überall, H., 1971, *Electron Scattering from Complex Nuclei* (Academic, New York).
Uckert, J., 1983, Diplomarbeit (Universität Mainz).
Uhrhane, F. J., J. S. McCarthy, and M. R. Yearian, 1971, Phys. Rev. Lett. **26**, 578.
Van Hees, A. G. M., 1982, Ph.D. thesis (Rijksuniversiteit Utrecht).
Van Hees, A. G. M., and P. W. M. Glaudemans, 1984, Z. Phys. A **314**, 323.
Van Niftrik, G. J. C., H. De Vries, L. Lapikás, and C. De Vries, 1971a, Nucl. Instrum. Methods **93**, 301.
Van Niftrik, G. J. C., L. Lapikás, H. De Vries, and G. Box, 1971b, Nucl. Phys. A **174**, 173.
Vanpraet, G. J., and P. Kossanyi-Demay, 1965, Nuovo Cimento **39**, 388.
Vary, J. P., R. H. Belehrad, and R. J. McCarthy, 1980, Phys. Rev. C **21**, 1626.
Vergados, J. D., 1974, Nucl. Phys. A **220**, 259.
Villars, F., 1947, Helv. Phys. Acta **20**, 476.
Villars, F., and N. Schmeing-Rogerson, 1971, Ann. Phys. **63**, 443.
Vinciguerra, D., and T. Stovall, 1969, Nucl. Phys. A **132**, 410.
Von Geramb, H. V., 1983, in *The Interaction Between Medium Energy Nucleons in Nuclei,* AIP Conference Proceedings No. 97, edited by H. O. Meyer (AIP, New York), p. 44.
Walecka, J. D., 1974, Ann. Phys. **83**, 491.
Walecka, J. D., 1975, in *Muon Physics,* edited by V. W. Hughes and C. S. Wu (Academic, New York), Vol. 2, p. 113.
Weber, H. J., and H. Arenhövel, 1978, Phys. Rep. C **36**, 278.
Weigert, L. J., and M. E. Rose, 1964, Nucl. Phys. **51**, 529.
Whitehead, R. R., A. Watt, B. J. Cole, and I. Morrison, 1977, Adv. Nucl. Phys. **9**, 123.
Wildenthal, B. H., 1984, in *Progress in Particle and Nuclear Physics,* edited by D. H. Wilkinson (Pergamon, Oxford), Vol. 2, p. 5.
Wildenthal, B. H., and W. Chung, 1979, in *Mesons in Nuclei,* edited by M. Rho and D. H. Wilkinson (North-Holland, Amsterdam), p. 721.
Williamson, C. F., F. N. Rad, S. Kowalski, J. Heisenberg, H. Crannell, and J. T. O'Brien, 1983, private communication.
Yang, S. N., and A. D. Jackson, 1971, Phys. Lett. B **36**, 1.
York, R. C., and G. A. Peterson, 1979, Phys. Rev. C **19**, 574.
Zamick, L., 1978, Phys. Rev. Lett. **40**, 381.
Zamick, L., 1979, in *Common Problems in Low- and Medium-Energy Nuclear Physics,* edited by B. Castel, B. Goulard, and F. C. Khanna (Plenum, New York), p. 405.
Zamick, L., 1983, private communication.
Zeidmann, B., 1982, "A National CW GeV Electron Microtron Laboratory," Argonne National Laboratory proposal, ANL 82-83, p. 249.
Zuilhof, M. J., and J. A. Tjon, 1980, Phys. Rev. C **22**, 2369.
Zuilhof, M. J., and J. A. Tjon, 1981, Phys. Rev. C **24**, 736.
Zuker, A. P., 1971, in *Proceedings of the Conference on Structure of $1f_{7/2}$ Nuclei, Legnaro,* edited by R. A. Ricci (Editrice Compositori, Bologna), p. 95.